2017

Ultrasonic thickness structural health monitoring of steel pipe for internal corrosion

Thomas John Eason
Iowa State University

Ultrasonic thickness structural health monitoring of steel pipe for internal corrosion

by

Thomas John Eason

A dissertation submitted to the graduate faculty

in partial fulfillment of the requirements for the degree of

DOCTOR OF PHILOSOPHY

Major: Engineering Mechanics

Program of Study Committee:
Leonard J. Bond, Major Professor
Ashraf Bastawros
Paul J. Schafbuch
Kurt R. Hebert
Vinay Dayal

Iowa State University

Ames, Iowa

2017

DEDICATION

I would like to dedicate this work to my wife Therese for her love and support along our unexpected and improbable journey through Ames.

TABLE OF CONTENTS

LIST OF TABLES

LIST OF FIGURES

ACKNOWLEDGEMENTS

I would like to take this opportunity to express my gratitude to those who have helped me during my time as a graduate student.

First and foremost, thank you to Prof. Leonard Bond for his guidance, inspiration, and support throughout the process. I would also like to thank my committee members: Prof. Ashraf Bastawros, Prof. Paul Schafbuch, Prof. Kurt Hebert, and Prof. Vinay Dayal, as well as other Iowa State University colleagues: Prof. Ronald Roberts, Prof. Bill Meeker, Brady Engle, and Dr. Robert Grandin. I would like to express my gratitude to Dr. Mark Lozev, Steve Orwig, Dr. Bruce Cook, and Dr. Andrew Waller for their unwavering commitment to providing me the opportunity to pursue part-time graduate studies; as well as thank Rosary Abot for reviewing this dissertation. I acknowledge that my research was supported by BP Products North America.

I would like to thank my wife, Therese, and our two boys, Connor and Drew, as we have all grown in various ways the past few years. I would also like to thank my parents for their love and support. Finally, I would like to thank my extended family, friends, and colleagues; I am truly blessed for which there are too many to name.

ABSTRACT

The naphthenic acid corrosion that can occur in oil refinery process plants at high temperature (400°C) due to the corrosive nature of certain crude oils during the refining process can be difficult to predict. Therefore, the development of online ultrasonic thickness (UT) structural health monitoring (SHM) technology for high temperature internal pitting corrosion of steel pipe is of interest. A sensor produced by the sol-gel ceramic fabrication process has the potential to be deployed to monitor such pitting corrosion, and to help investigate the mechanisms causing such corrosion. This thick-film transducer is first characterized using an electric circuit model. The propagating elastic waves generated by the transducer are then experimentally characterized using the dynamic photoelastic visualization method and images of the wave-field are compared with semi-analytical modeling results. Next, the classic elastic wave scattering theory for an embedded spherical cavity is reviewed, results are compared with a newer scattering theory from the seismology community, that has been applied to a hemispherical pit geometry. This hemispherical pit theory is extended so as to describe ultrasonic Non-Destructive Evaluation (NDE) applications, for pitting corrosion, with the derivation of a far-field scattering amplitude term. Data from this new scattering theory is compared with experimental results by applying principals from the Thompson-Gray measurement model. The initial model validation provides the basis for a possible new hemispherical pit geometric reference standard for ultrasonic NDE corrosion applications. Next, UT SHM measurement accuracy, precision, and reliability are described with a new weighted censored relative likelihood methodology to consider the propagation of asymmetric uncertainty in quantifying thickness measurement error. This new statistical method is experimentally demonstrated and applied to thickness measurement data obtained in pulse-echo and pitch-catch configurations for various time-of-flight thickness calculation methods. Finally, the plastic behavior of a corroded steel pipe is modeled with analytical and finite element methods to generate prognosis information.

CHAPTER 1. INTRODUCTION

Crude oils from various parts of the world have unique chemical and physical properties. The economics behind the supply of such crude oils fluctuate over short-term and long-term timescales. Over the last few decades, the crudes that are relatively easy to process are being consumed and as a result, are becoming more scarce. The remaining crude supply is trending towards properties of higher density, higher sulfur concentration, higher chloride concentration, and higher acidity [Qing (2010)]. One drawback of processing such crudes is a higher refining energy conversion cost. The energy conversion costs is fairly well understood and can be quantified via unique crude oil distillation curves [Leffler (2008)]. The second drawback of processing such crudes is a higher risk of corrosion [Ropital (2009)]. The risk around corrosion as a result of changing crude oil feedstock properties is more complex and difficult to quantify.

1.1 Corrosion Risk

Unfortunately, there are recent examples in the oil refining industry where the corrosion risk related to crude oil properties were not properly addressed resulting in catastrophic failures: Richmond, California in 2012; Woods Cross, Utah in 2009; and Martinez, California in 1999 [U.S. Chemical Safety Board (2015)]. There can be two approaches to better understanding the corrosion risk associated with a specific crude oil. The first approach is the development or improvement of chemistry based corrosion models that predict corrosion rates at various points in the refinery as a function of crude oil feedstock properties, process conditions, and metallurgical material properties. The second approach is the development or improvement of corrosion rate measurement technology. The corrosion rate measurement must

be at a high enough precision and sampling frequency to allow correlation with the dynamic feedstock properties and process conditions.

The composition of crude oil varies among different reservoirs. The most prominent naturally occurring components in crude oil that can lead to corrosion on refinery distillation units are inorganic chloride salts, organic sulfur compounds, and naphthenic acids [Gutzeit (2006)]. Inorganic chloride salts in the presence of water can become hydrochloric acid and cause general or localized thinning in the primary atmospheric tower overhead piping system at temperatures typically below 150°C. Organic sulfur compounds can cause sulfidic corrosion at temperatures above 260°C resulting in uniform thinning. Naphthenic acids can cause naphthenic acid corrosion at temperatures between 150°C and 400°C and can result in non-uniform corrosion and localized pitting [Garverick (1994); American Petroleum Institute (2011)]. Localized pitting in steel is not unique to naphthenic acid corrosion, and can form under various environmental conditions [Frankel (1998)].

1.2 Naphthenic Acid Corrosion

Crude oils that contain a higher percentage of organic acids are characterized by a high total acid number (TAN) or naphthenic acid number (NAN). Such high TAN crudes can be found in China, Eastern Europe, India, Russia, United States, and Venezuela. Naphthenic crudes contain a wide range of individual acid molecules, but all can be written as $[R\,[CH_2]_n\,COOH]$, where [R] is typically a cyclopentane or cyclohexane ring [Slavcheva et al. (1999)]. The naphthenic acids are present at various molecular weights and become distributed among a distillation unit according to boiling point. Most naphthenic acid corrosion is concentrated in heavy vacuum gas oil sections in the following equipment: furnace tubes, transfer lines, tower internals, tower walls, pump internals, valves, and fittings [Slavcheva et al. (1999); Alvisi and Lins (2011)].

1.2.1 Chemical Reactions

Naphthenic acid corrosion can be described by the chemical reactions in Equations 1.1-1.3 [Slavcheva et al. (1999); Laredo et al. (2004)]. Equation 1.1 shows the direct attack of

naphthenic acid [RCOOH] on the ferrous alloy [Fe] resulting in metal loss through formation of oil soluble iron naphthenate [$Fe(RCOO)_2$] scale. Fluid erosion can increase the spallation and removal of the iron sulphide scale [Wu et al. (2004a)] and Equation 1.2 shows the removal of the iron naphthenate scale by reacting with hydrogen sulphide to regenerate the naphthenic acid and form iron sulphide precipitate. In parallel, Equation 1.3 shows the direct attack from hydrogen sulphide [H_2S] on the ferrous alloy resulting in metal loss through formation of a protective iron sulphide [FeS] scale. In summary, naphthenic acids and sulfur containing compounds react with the steel and each other through the formation and breakdown of various types of scale.

$$Fe_{solid} + 2RCOOH_{liquid} \rightarrow Fe(RCOO)_{2\,solid} + H_{2\,gas} \tag{1.1}$$

$$Fe(RCOO)_{2\,solid} + H_2S_{gas} \rightarrow FeS_{liquid} + 2RCOOH_{liquid} \tag{1.2}$$

$$Fe_{solid} + H_2S_{gas} \rightarrow FeS_{solid} + H_{2\,gas} \tag{1.3}$$

1.2.2 Surface Morphology

The rate and morphology of corrosion as a result of naphthenic acid is dependent on the following variables: metallurgy, acid species, acid concentration, sulfur concentration, process temperature, shear stress, and the extent of a gas phase [Slavcheva et al. (1999)]. In addition, the formation and breakdown of scales have a history dependent influence on corrosion rate. As a result, the naphthenic acid corrosion rate and exact morphology can be difficult to predict in an actual refinery even with precise localized process and environmental information.

A good visual description of all potential corrosion morphologies for various types of mechanisms has been provided [Godard (1984)]. The field observed degradation from naphthenic acid corrosion are a continuum of morphologies from a localized pitting to smooth uniform wall loss. In general, higher acid concentration and lower sulfur concentration may result in more localized corrosion. High sulfur concentration and lower acid concentration may result in more

uniform corrosion. In addition, higher flow rates may result in more localized corrosion as a result of increased rate of iron sulphide scale spallation in areas of higher velocity.

There have been many published laboratory and refinery studies with images and descriptions of the various possible morphologies associated with Naphthenic Acid Corrosion [Wu et al. (2004a); Qu et al. (2005, 2006); Huang et al. (2012)] with clear images of distinct uniform and localized corrosion topology as a result of changing acid concentration, flow rate, and temperature in a lab environment [Wu et al. (2004b)].

A single steel pipe has been removed from service exhibiting uniform degradation in Figure 1.1, isolated single pitting in Figure 1.2, localized pitting clusters in Figure 1.3, and random rough surface corrosion in Figure 1.4. Figures 1.1-1.4 each contain a two dimensional optical image and a three dimensional point cloud surface mesh optical image. The possibility that all three morphologies can occur in the same service make naphthenic acid corrosion a challenging corrosion modeling and measurement problem.

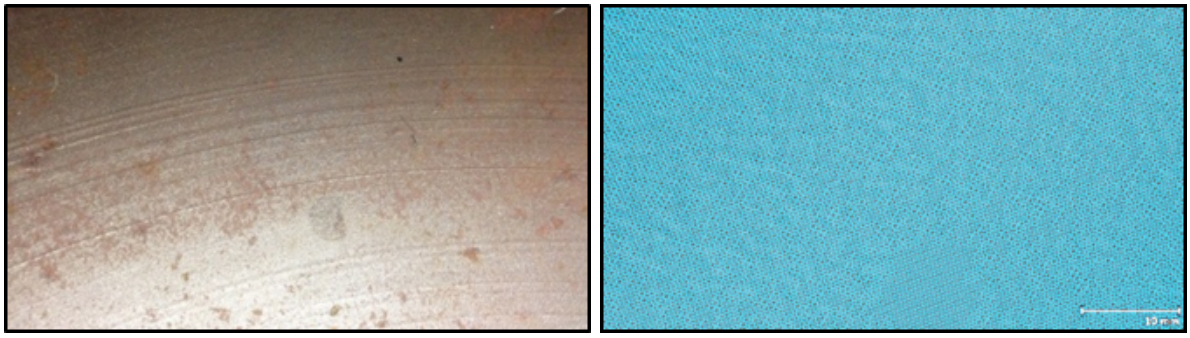

Figure 1.1 Photograph and corresponding optical scan image of naphthenic acid corrosion with uniform degradation. Printed with the permission of BP Products North America Inc.

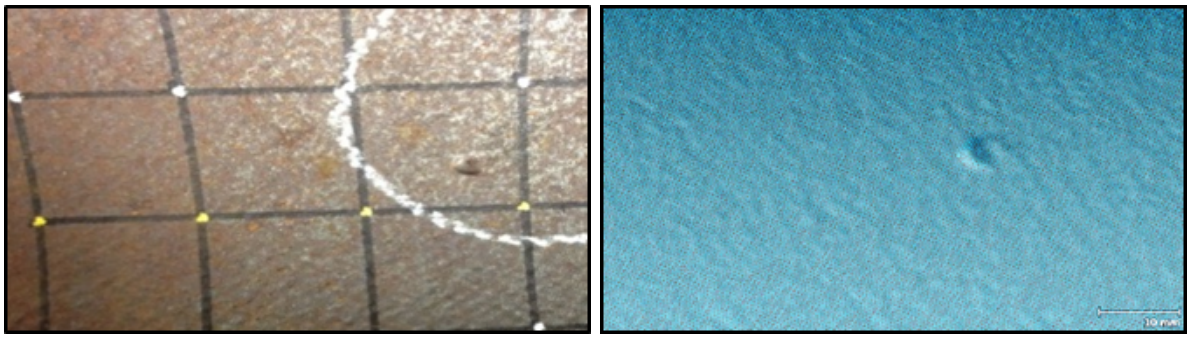

Figure 1.2 Photograph and corresponding optical scan image of naphthenic acid corrosion with isolated single pit degradation. Printed with the permission of BP Products North America Inc.

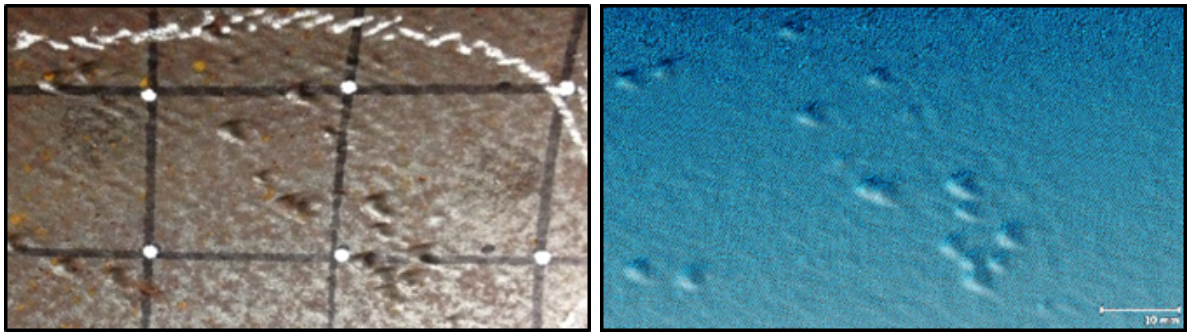

Figure 1.3 Photograph and corresponding optical scan image of naphthenic acid corrosion with localized cluster pitting degradation. Printed with the permission of BP Products North America Inc.

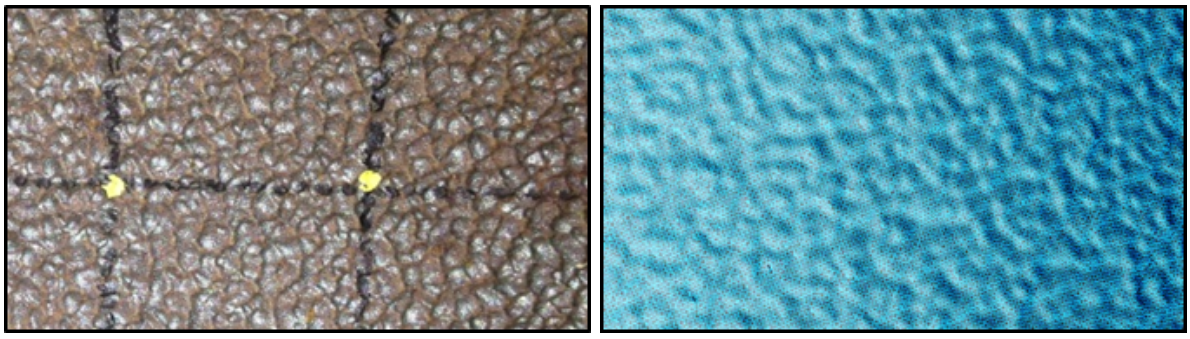

Figure 1.4 Photograph and corresponding optical scan image of naphthenic acid corrosion with rough surface degradation. Printed with the permission of BP Products North America Inc.

1.3 Corrosion Measurement Technology

The ideal measurement technology should satisfy two distinct, but related objectives. The first objective is to collect a high frequency of relative wall thickness measurements in order to help predict future corrosion rates. The relative changes in wall thickness can be correlated with current operational parameters to improve prognostic models resulting in a better prediction of future corrosion rates under future operational conditions. A permanently installed Structural Health Monitoring (SHM) measurement technology may be well suited to provide such high frequency relative thickness measurements. The use of SHM technology may decrease the typical wall thickness measurement interval from "years" down to "days" in order to bring more granularity to improve the validation of corrosion models, and to detect small changes in significant corrosion rate behavior if the thickness measurement precision of the technology can be around 0.05 mm.

The second objective is to find and precisely measure the absolute thinnest points in a system to perform a current state "Fitness-for-service" [American Petroleum Institute (2007)] assessment based on the mechanical design, current dimensions, and current operation conditions. A non-permanent manual Non-Destructive Evaluation (NDE) measurement technology may be well suited to provide a more random sampling of precise thickness measurements over a larger surface area in an attempt to find the thinnest points, but access costs can limit the practical frequency of such manual NDE measurements.

The ideal measurement approach should look to incorporate the positive aspects of both SHM and NDE via improved monitoring technology to have highly repeatable precise thickness measurements with extended pipe surface area coverage. The potential for localized pitting corrosion needs to be considered for monitoring applications such as naphthenic acid corrosion. Finally, there needs to be an intelligent merging of SHM into ongoing NDE activities and a logical monitoring strategy among area and point measurements [Cawley et al. (2013)]. A list of potential target technology design parameters to address both relative and absolute measurement requirements for localized pitting corrosion are shown in Table 1.1.

Table 1.1 Target Design Parameters for Naphthenic Acid Corrosion Monitoring

Parameter	**Potential Design Target**
Temperature	up to 400°C
Thickness Precision	0.05 mm
Spatial Resolution Precision	0.05 mm width × 0.05 mm length
Pipe Wall Thickness	3-25 mm
Pipe Diameter	>114 mm
Metallurgy	Low-Alloy Steel (<9%Cr & <2.5%Mo)

Precise characterization of non-uniform localized pitting corrosion in piping up to 400°C is challenging; regardless, the measurement technology should produce repeatable measurements within a statistically reasonable precision for realistic corrosion surfaces.

1.4 Summary

This first chapter outlined the motivation for the research topic by briefly addressing crude oil trends related to corrosion, principals of naphthenic acid corrosion, and factors to consider when designing corrosion measurement technology.

General Non-Destructive Evaluation (NDE) background material is summarized in Chapter 2 for optical, electromagnetic, radiographic, acoustic emission, ultrasonic, and other methods. Ultimately, a permanently installed bulk wave ultrasonic monitoring technology is one of the most applicable methods to monitor localized high-temperature corrosion, and a review of commercial technology is included. A review of rough surface elastic wave scattering is also provided in Chapter 2.

One potential ultrasonic monitoring technology are piezoelectric transducers produced by the sol-gel ceramic fabrication process; this technology is reviewed in Chapter 3. The thick-film sensors are characterized by experimental generation of a beam profile via photoelastic imaging.

Various bounding case scenarios for the ultrasonic bulk wave corrosion monitoring application are modeled in Chapter 4.

The elastic wave scattering behavior from a single pit is described in Chapter 5. Existing theory is reviewed, and new theory is presented as an extension of recent developments from the seismology community. A combination of experimental measurements and modeling are

completed for a flat surface (in Chapter 5) and for a curved surface (in Chapter 6) for immersion measurement configurations. Contact measurement configuration modeling and experimental results on a curved surface are shown in Chapter 7.

Statistical considerations related to permanently installed sensor accuracy, precision, and reliability are discussed in Chapter 8. A new weighted censored relative likelihood analysis technique is described and demonstrated with experimental data to quantify the propagation of asymmetric measurement uncertainty.

The elastic and plastic failure criteria for steel pipe with uniform and localized pitting corrosion is investigated via analytical and finite element methods in Chapter 9 as prognosis information.

Conclusions and future work are described in Chapter 10.

CHAPTER 2. BACKGROUND

This chapter reviews Non-Destructive Evaluation (NDE) inspection and monitoring methods for piping internal corrosion, and compares the methods for a high-temperature localized corrosion monitoring application. Ultrasonic bulk wave piezoelectric transducer technology has the potential to monitor such high-temperature localized corrosion, and a commercial review of permanently installed bulk wave structural health monitoring ultrasonic thickness (SHM-UT) technology is provided.

2.1 Non-Destructive Evaluation Method Review

This section reviews NDE inspection and monitoring methods for piping internal corrosion. Prior reviews of inspection and monitoring technologies for general corrosion [Beissner and Birring (1988)], upstream riser damage [Lozev et al. (2005)], water pipe condition [Liu and Kleiner (2013)], underwater structures [Rizzo (2013)], in-line pipeline inspection [Bickerstaff et al. (2002)], piping internal corrosion [Eason et al. (2015a)], as well as general NDE [Ness et al. (1996); Gros (1996); Bray and Stanley (1997); ESR Technology (2014); Iowa State University (2014)] are referenced. The individual methods are organized by sensory modality: optical, electromagnetic, radiographic, acoustic emission, ultrasonic, and other.

2.1.1 Optical

Optical technologies have been previously reviewed [Zhu et al. (2011)] and are described for both endoscopic and optical fiber sensing methods.

2.1.1.1 Endoscopy

Endoscopic methods involve insertion of a camera for direct line-of-sight optical observation of corrosion on the inside surface of a pipe. A continuous video feed, described as closed circuit television (CCTV), has been demonstrated as an inspection method for internal pipe corrosion in water [Stanic et al. (2013)] and pipeline industries. A CCTV camera and visible light source are mounted onto a carrier and placed inside the pipe which typically contains at most a minimal amount of liquid. The camera moves through the pipe capturing visual images of the internal surface. The carrier can be propelled externally with a winch and pulley system, or the carrier itself can be an automated robot crawler. CCTV systems can have multiple cameras with pan and tilt functionality and can be oriented to capture a forward view, perpendicular view, or rear view. Some CCTV systems also use wide-angle fisheye lenses. While guidelines do exist to characterize and assess various types of defects, this manual method is inherently qualitative and prone to errors as a result of lack of scale and technician fatigue. Recent work has been completed to improve image feature detection and tracking in an attempt to make CCTV a more quantitative inspection technique [Hansen et al. (2011a,b); Motamedi et al. (2012); Safizadeh and Azizzadeh (2012); Kawasue and Komatsu (2013)]. Quantitative three dimensional topography information and defect characterization can be obtained using various optical equipment configurations mounted on a crawler inside a pipe such as visual odometry [Hansen et al. (2013)] or laser ring triangulation [Duran et al. (2007)].

2.1.1.2 Fiber Bragg Grating

Fiber Bragg gratings are manufactured by creating specific periodic variations of the refractive index of an optical fiber core. The refractive index interfaces in the fiber can be uniformly spaced such that reflected light at a particular wavelength, the Bragg wavelength, will undergo constructive interference in phase resulting in an amplified signal. Any change in temperature of the fiber and any change in the strain of the fiber can be observed as the effective Bragg wavelength shift, $\frac{\lambda_B}{\lambda}$, in Equation 2.1 with λ_B as the Bragg wavelength, α as the thermal expansion, ζ as the thermo-optic coefficient, ΔT as the change in temperature, ρ_e as the pho-

toelastic constant of the fiber core material, and ε as the longitudinal strain [Majumder et al. (2008)]. Monitoring strain in a structure can provide an early indicator for fatigue failure; strain measurements are also proposed to detect an increase in hoop (circumferential) stress as the result of wall thinning due to corrosion in a pipeline [Tennyson et al. (2007)] as shown in Equation 2.2 with t as the average wall thickness, r as the average pipe radius, P as the relative internal pressure, σ as the hoop stress, and E as Youngs modulus.

$$\frac{\lambda_B}{\lambda} = (\alpha + \zeta)\,\Delta T + (1 - \rho_e)\,\varepsilon \tag{2.1}$$

$$t = \frac{rP}{\sigma} = \frac{rP}{\varepsilon E} \tag{2.2}$$

2.1.2 Electromagnetic

Electromagnetic inspection has been previously reviewed [Sophian et al. (2001)] and involves the generation, interaction, and measurement of electromagnetic fields to detect the relative material conductivity and permeability of a test component.

2.1.2.1 Conventional Eddy Current

A periodic magnetizing coil perpendicular to a conductive surface will create a primary magnetic flux, Φ_p, described in Equation 2.3 with N_p as the primary number of coils, I_p as the primary excitation current, ω as angular frequency, and t as time. The oscillating primary magnetic flux induces circulatory eddy currents which in turn create a secondary magnetic flux, Φ_s, in opposition to the primary magnetic flux. The equilibrium flux, Φ_e, described in Equation 2.4, is measured by a change in coil impedance as a result of a change in the surface material conductivity or permeability. The penetration depth in mm, d, is described in Equation 2.5, with ρ as electrical resistivity in Ω-cm, f as excitation frequency, and μ_r as a dimensionless relative permeability.

$$\Phi_p \propto N_p I_p \sin(\omega t) \tag{2.3}$$

$$\Phi_e = \Phi_p - \Phi_s \tag{2.4}$$

$$d = 50\sqrt{\frac{\rho}{f\mu_r}} \tag{2.5}$$

2.1.2.2 Remote Field Eddy Current

The measurement of phase lag from an exciter coil to a pickup coil placed inside a pipe has a linear relationship to wall thickness. The phase lag, θ, is described in Equation 2.6 with x as distance between coils, f as excitation frequency, μ as average permeability, and σ as electrical conductivity between the two coils.

$$\theta = x\sqrt{\pi f \mu \sigma} \tag{2.6}$$

2.1.2.3 Pulsed Eddy Current

In pulsed eddy current for corrosion monitoring [He et al. (2012)], a step function voltage is applied and emits electromagnetic pulses onto the outer pipe surface. The decaying magnetic field induces eddy currents that diffuse through the wall and then rapidly decay at the pipe inside surface. The voltage induced by the eddy currents can be measured in the time domain and correlated to wall thickness based on the point in time at which rapid signal decay occurs.

2.1.2.4 Field Signature Method

In the field signature method [Wold and Sirnes (2007); Gan et al. (2016)], the pipe wall is used as an active electrode area and electric current is fed through contact pins. A decrease in wall thickness will change the electrical resistivity, which can then be monitored by a voltage measurement decrease across the pins.

2.1.3 Radiographic

Radiographic inspection of corrosion [Rokhlin et al. (1999); Zscherpel et al. (2000); Priyada et al. (2011)] involves the transmission, propagation, attenuation, measurement, and interpretation of energy from a source, through an object, and onto a film or detection device.

2.1.3.1 Energy Source

The most typical energy source is electromagnetic photon radiation such as Gamma rays that emit from unstable isotopes, or X-rays that are released from an unstable condition as high speed electrons strike a target. Sub-atomic particle energy sources such as thermal neutrons or protons can be used with limited application.

2.1.3.2 Attenuation

Generated gamma ray intensity is directly related to the number of atoms present in the isotope source material. Generated X-ray intensity is a function of wavelength and tube voltage. The intensity of a beam of radiation exiting a material, I, is shown as Equation 2.7 with I_0 as the radiation beam intensity entering a material, μ as the linear attenuation coefficient, and x as material thickness. The linear attenuation coefficient is further described in Equation 2.8 with N as Avogradros constant, σ as the total atomic attenuation coefficient, ρ as the material density, and A as the atomic mass. The total atomic attenuation coefficient is further described in Equation 2.9 with σ_{pe} as the photoelectric effect, σ_s as Compton scattering and coherent (or Rayleigh) scattering, σ_{pp} as pair production, and σ_{pd} as photodisintegration.

$$I = I_0 e^{-\mu x} \tag{2.7}$$

$$\mu = \frac{N\sigma\rho}{A} \tag{2.8}$$

$$\sigma = \sigma_{pe} + \sigma_s + \sigma_{pp} + \sigma_{pd} \tag{2.9}$$

2.1.3.3 Detectors

Individual grains of traditional radiographic film react and darken with radiation exposure as shown in Equation 2.10 with E as the film exposure, I_f as the radiation intensity on the film, and T as the time of exposure. When viewing film, interpretations are made based on the observed contrast described in Equation 2.11 with D as the density observed on the film, and G_D as the contrast measured at density D. Observed film density is further defined in Equation 2.12 with I_0 as the intensity of the viewing light source, and I_t as the intensity observed on the film.

$$E = I_f T \tag{2.10}$$

$$G_D = \frac{dD}{d\left(\log E\right)} \tag{2.11}$$

$$D = \log \frac{I_0}{I_t} \tag{2.12}$$

2.1.3.4 Computed Radiography

Computed Radiography refers to flexible imaging plates similar to traditional film, but rather the plates are exposed, digitally scanned, and then reused via a photo-stimulable phosphors storage process.

2.1.3.5 Digital Radiography

Digital Radiography, or Real-Time Radiography, is the use of flat or curved panel detectors composed of amorphous silicon (or other scintillating material) arrays, and thin film transistors for immediate display of the radiograph image after exposure without the need for film development.

2.1.3.6 Orientation

The common configuration is to have both source and detector external to the pipe of interest. An orthogonal external orientation places the source perpendicular to the top surface and the detector perpendicular to the bottom surface of the pipe. A tangential external orientation places the source tangential to the pipe as to focus the beam only through an edge chord section of the pipe wall with the detector placed in a tangential receiving orientation, often used in applications with higher material density. A backscatter orientation places the source and detector outside the pipe at an angle best suited to receive Compton scattered photons. An alternative configuration can have the source placed inside the pipe with multiple curved detectors circumferentially outside the pipe.

2.1.3.7 Computed Tomography

With computed tomography, the source and detector are rotated relative to the object to collect multiple cross-section images which are then reconstructed to generate a composite tomographic image.

2.1.4 Acoustic Emission

A pipe deformed under stress will generate elastic waves referred to as acoustic emissions (AE). The source of such pipe stress is mechanical or thermal loading from normal operations; although, additional loading can be applied for short duration AE inspections. During AE monitoring, a baseline environmental noise measurement is collected and subsequent measurements are compared to the baseline. Low amplitude changes from the baseline can be attributed to microstructural changes, chemical reactions related to corrosion, or flaking or removal of corrosion products from a surface [Rettig and Felsen (1976); Lackner and Tscheliesnig (2004); Jirarungsatian and Prateepasen (2010)]. High amplitude changes from the baseline can be generated by the growth of flaw-like cracks that introduce stress in the lattice.

2.1.5 Ultrasonic

Ultrasonic NDE inspection of steel components consists of the transmission and measured reception of acoustic energy using a wide range of possible system configurations [Rose (2004); Ensminger and Bond (2012); Krautkramer and Krautkramer (2013); Schmerr (2016)]. Ultrasonic measurements at higher temperatures present unique challenges that have been reviewed [Kažys et al. (2008); Budimir et al. (2011); Jiang et al. (2014); Weaver et al. (2015)], as well as ultrasonic applications for the oil and gas pipeline industry [Alobaidi et al. (2015)].

It is possible to organize the different configurations of ultrasonic measurements into the following five categories: wave mode, wave coverage, transduction method, transducer motion, and transducer configuration. Listed are some of the potential types of wave modes: bulk longitudinal, bulk shear horizontal, bulk shear vertical, surface longitudinal creeping, surface Rayleigh, guided transverse, guided symmetric lamb, and guided asymmetric lamb; potential types of wave coverage: single point, point array, sparse array, tomographic array, mid-range, and long-range; potential types of transduction methods: piezoelectric, electromagnetic acoustic transduction (EMAT), magnetostrictive, and laser; potential types of transducer motion: manual, semi-automated, fully-automated, and permanent installation; and potential types of transducer configurations: pulse-echo, pitch-catch, and various simultaneous interactions between multiple transducers in an array such as phased array electronic scanning, beam steering, and beam focusing.

2.1.5.1 Bulk Wave Thickness Measurement

An ultrasonic transducer acoustically coupled to the outside of a pipe can be excited with a voltage pulse to transmit a bulk wave from the transducer, through the pipe outside surface interface, through the pipe wall, reflected back from the pipe inside surface interface, back through the pipe wall, back through the pipe outside surface interface, and finally received by the same or another transducer [Matthies (1998)]. A simplified one-dimensional wave equation for elastic bulk wave propagation is shown in Equation 2.13 with ρ as mass density, u as the wave front particle displacement, t as time, c as the speed of sound, and x as distance. The

speed of sound for longitudinal, c_l, and shear, c_s, waves are shown in Equations 2.14 and 2.15 with λ and μ as the first and second Lamé parameters, E as Youngs modulus, ν as Poissons ratio, and G as the shear modulus. The temperature influence on the elastic moduli has been found to be approximately linear as shown in Equation 2.16, with c as the wave speed at a reference temperature, $\frac{dc}{dT}$ as a speed change constant, and ΔT as the temperature change.

$$\rho \frac{\partial^2 u}{\partial t^2} = c^2 \frac{\partial^2 u}{\partial x^2} \tag{2.13}$$

$$c_l = \sqrt{\frac{\lambda + 2\mu}{\rho}} = \sqrt{\frac{E\,(1+\nu)}{(1+\nu)\,(1-2/nu)\,\rho}} \tag{2.14}$$

$$c_s = \sqrt{\frac{\mu}{\rho}} = \sqrt{\frac{G}{\rho}} = \sqrt{\frac{E}{2\,(1+\nu)\,\rho}} \tag{2.15}$$

$$c = c^\circ - \frac{dc}{dT}\Delta T \tag{2.16}$$

The time domain harmonic motion solution to Equation 2.13 is shown as Equation 2.17 with A as the maximum particle displacement amplitude, ω as the angular frequency, and k as the angular wave number. The relation between wavelength, λ, frequency, f, wave speed, c, and wave number, k, are shown as Equation 2.18-2.20.

$$u = Ae^{i(kx-\omega t)} \tag{2.17}$$

$$f = \frac{\omega}{2\pi} \tag{2.18}$$

$$\lambda = \frac{c}{f} = \frac{2\pi c}{\omega} \tag{2.19}$$

$$k = \frac{\omega}{c} \tag{2.20}$$

As a sound wave reaches an interface between two different materials, the proportion reflected depends on the acoustic impedance mismatch between the two materials as shown in

Equation 2.21 and 2.22 with R as the reflection coefficient, z_1 as the incident material acoustic impedance, and z_2 as the transmission material acoustic impedance. Given z_1 as a metal and z_2 as a fluid, $z_1 \gg z_2$ resulting in a strong reflected signal as $R \approx -1$ as is the case of a back-wall reflection from an inside pipe wall surface.

$$z = \rho c \tag{2.21}$$

$$R = \frac{z_2 - z_1}{z_2 + z_1} \tag{2.22}$$

In general, the thickness of the pipe wall d can be computed from Equation 2.23 with c as the bulk (longitudinal or shear) wave speed in the material, and t_r as the total round trip time between transducer excitation and reception for a pulse-echo configuration.

$$d = \frac{ct_r}{2} \tag{2.23}$$

The received voltage signal can be processed using various filtering and envelope wrapping techniques and analyzed using various time-of-flight calculation algorithms; different calculation methods will result in different thickness measurement values [Barshan (2000); Jarvis and Cegla (2012)]. The manual bulk wave method requires the temporary coupling of an ultrasonic sensor to a pipe exterior. Permanently installed piezoelectric ultrasonic bulk wave sensors of various wave mode, frequency, footprint, and coupling design are possible above ambient temperature [GE Sensing & Inspection Technologies (2009); Kobayashi et al. (2009); Cegla et al. (2011)].

2.1.5.2 Guided Waves

The use of guided waves has been broadly reviewed [Rose (2002); Raghavan and Cesnik (2007)] and applied to measure corrosion in pipes [Rose et al. (1996); Lowe et al. (1998); Alleyne et al. (2001); Cawley et al. (2003); Kwun et al. (2003); Demma et al. (2004); Vinogradov (2009); Galvagni and Cawley (2013); Leinov et al. (2016)]. The long range guided waves in a piping system are generated by a circumferential transducer; the waves propagate between the

inside surface boundary and outside surface boundary of the pipe in torsional, longitudinal, or transverse wave modes. The propagating wave can become distorted and have a partial mode conversion when encountering a cross-sectional area change in the pipe wall such as a weld or a region of localized corrosion. In a pulse-echo configuration, lower energy waves are reflected back to the transducer to be received and interpreted. The magnitude of the cross-sectional change associated with a reflection is relative to the received signal amplitude; the longitudinal location of the cross-sectional change can be determined by the signal arrival time; the circumferential location of the cross-sectional change can be determined when using a circumferential array transducer by measuring the relative signal amplitude received by each element in the array. Circumferentially segmented transducers allow the application of various synthetic and adaptive focusing methods [Sun et al. (2005); Li and Rose (2006); Luo and Rose (2007); Mu et al. (2007); Davies and Cawley (2009); Lowe et al. (2016)].

The same principles apply to higher frequency medium range guided wave techniques which generate and propagate waves in a pipe longitudinal and circumferential direction using various types of array configurations over distances generally less than 3 meters. In medium range guided wave, cross-sectional area changes from reflected signals in the sound path can be measured in a pulse-echo configuration, or attenuation can be measured using a pitch-catch configuration, or the average wall thickness of the sound path can be correlated from the appropriate dispersion curve to a change in acoustic velocity measured by a change in signal arrival time in a pitch-catch configuration. A tomographic inversion technique can also be applied in certain medium range guided wave configurations [Leonard and Hinders (2003); Van Velsor et al. (2007); Huthwaite et al. (2013); Nagy et al. (2014); Brath et al. (2017)].

2.1.5.3 Transduction

Different transduction methods can generate and receive elastic waves of different mode, frequency, and amplitude combinations by using various conversion processes between electrical energy and mechanical/vibration/elastic energy. Piezoelectric transducers exhibit the piezoelectric effect as a reversible interaction between electrical charge and mechanical stress on a crystalline or ceramic material and are a common transduction method for industrial applica-

tions. Magnetostrictive transducers utilize magnetostriction as a reversible interaction between an applied electromagnetic field and a dimensional change from domain shifting and rotation in a ferromagnetic material. Electromagnetic Acoustic Transduction (EMAT) transducers induce eddy currents in the surface region which then interact with a permanent magnetic field and generate elastic ultrasonic waves directly in the component via the Lorentz mechanism in conductive materials and by magnetostriction in ferromagnetic materials; both as reversible processes [Thompson (1990); MacLauchlan et al. (2004); Lunn et al. (2017)]. Laser transduction can involves a generation laser and/or a detection laser. The generation laser can quickly heat a small area on the surface causing sudden thermal expansion, and the associated stress reactions can generate elastic waves in the MHz to THz range; the detection laser can measure dimensional changes on the surface from elastic waves via interferometry [Scruby and Drain (1990); Davies et al. (1993); Matsuda et al. (2015)]. A low acoustic impedance interface is necessary between piezoelectric and magnetostrictive transducers and the pipe surface to directly transfer mechanical stresses; rather, this coupling is not necessary for EMAT and laser transduction methods. EMAT, laser, and other loosely contacting transduction methods have been reviewed and compared in regard to minimum detectable surface displacement sensitivity [Cheeke (2012)].

2.1.5.4 Element Arrays

Ultrasonic array technology for NDE has been reviewed along with literature from the medical and sonar fields [Drinkwater and Wilcox (2006)], and fundamentally described [Schmerr (2015)]. The acoustic characteristics of an ultrasonic element phased array probe can be modified electronically by introducing time shifts in signals sent to and received from individual elements. The dynamic control of the beam properties and dynamic focusing can lead to improved measurement precision for various wave modes. Beam manipulations include: electronic scanning achieved by pulsing a group of elements along a transducer in sequence, beam steering achieved by delaying the pulsing of each element at a set rate, and beam focusing achieved by varying the rate of delay of the pulsing of each element. Finally, another technique that can be applied with phased array transducers is Full Matrix Capture (FMC) involving the sequential

excitation of individual elements and reception by all elements in the array followed by the reconstruction of the image using the Total Focusing Method (TFM), or permutations of the TFM, to time-shift each received signal according to the focal laws for each element relative to the inspection field location [Holmes et al. (2005); Zhang et al. (2010)].

A tomographic technique can also be applied using element arrays to collect multiple cross-section signals which are then reconstructed and processed to generate a composite image. Arrays can also be fabricated with a monolithic piezoelectric material and with discrete electrodes, intended for use in a high temperature environment [Kirk et al. (1999)].

2.1.6 Other Modalities

Other methods can be used to monitor corrosion activity. One such measurement is an electrical resistance or a linear polarization resistance immersion probe inserted into the process stream. The probe contains a sacrificial coupon of the same metallurgy of the pipe. In the electrical resistance method [Royer and Unz (2002); Li et al. (2007)], the decrease in electrical resistance of the coupon is directly measured as the coupon losses mass as similar to the more traditional weight loss method. In the linear polarization resistance method, for conductive fluids, a small current is passed between two or three elements of a probe; the voltage and current are measured, and then correlated to the electro-chemical corrosion potential [Scully (1998); Hinds and Turnbull (2010)]. In both immersion probe methods, there is an optimization between corrosion rate sensitivity and duration of measurement before probe replacement. These immersion probe techniques do not directly monitor the pipe wall thickness, but rather provide an indication of the corrosivity of the process environment [Bovankovich (1994)], and can be influenced by deposit buildup [Wolf et al. (2016)].

Hydrogen is a product of corrosion reactions, and can be monitoring via the hydgrogen flux method [Mishael et al. (2004)]. In this method, similar to the immersion probe methods, the pipe wall thickness is not directly measured, but rather the corrosion activity is being monitored.

Certain degradation corrosion mechanisms are highly temperature dependent in ferrous material such as creep and high-temperature hydrogen attack. Temperature is often moni-

tored only at certain points in the process, and an unexpected temperature gradient away from the monitoring location may lead to an accelerated degradation rate. Infrared thermography [Bagavathiappan et al. (2013)] is a method for remote monitoring and visualization of relative temperature differences of process piping, pressure vessel, furnace tube, and storage tank exposed surfaces.

2.2 Non-Destructive Evaluation Method Comparison

The various NDE methods for piping internal corrosion monitoring are compared. The difference between direct and indirect wall thickness measurements is first discussed. Then the NDE measurement method characteristics are compared in order to better understand the relative potential for precise monitoring of high temperature localized corrosion. While many of the NDE methods are suitable for inspection of localized internal corrosion and pitting type defects in piping, fewer methods are suitable for precise in-service monitoring at temperatures up to 400°C.

2.2.1 Direct and Indirect Thickness Measurement Classification

Various measurement technologies can be classified as either directly measuring the wall thickness in a local area, or as indirectly measuring another characteristic to infer the wall thickness in a local area or global region as summarized in Table 2.1. Some ultrasonic, electromagnetic, and radiography methods can be used to directly measure wall thickness in a localized area. Acoustic emission, immersion probe, and hydrogen flux technology do not directly measure the physical wall thickness, but rather monitor the corrosion activity which can then be inferred to make assumptions for the remaining wall thickness. Optical measurement methods can profile a surface and can be combined with other direct measurement methods to determine the wall thickness. Thermography measurement methods can be an indirect indication of wall thickness. Ultrasonic mid-range guided wave in pitch-catch mode can measure an average wall thickness. Ultrasonic long-range guided wave in pitch-catch mode as well as ultrasonic mid-range guided wave in a tomography arrangement can provide information on the cross-sectional area of a pipe system.

Table 2.1 Direct and Indirect Wall Thickness Measurement Methods

	MEASUREMENT	METHOD
DIRECT	**Wall Thickness**	Ultrasonic Bulk Wave Electromagnetic Pulsed Eddy Current Radiography (Profile)
INDIRECT	**Average Wall Thickness**	Ultrasonic Mid-Range Guided Wave – Pitch Catch
	Cross-Sectional Area	Ultrasonic Long-Range Guided Wave – Pulse Echo Ultrasonic Mid-Range Guided Wave – Tomography
	Corrosion Rate	Acoustic Emission Immersion Probe Hydrogen Flux
	Surface Profile	Optical
	Temperature Gradient	Thermography

2.2.2 Measurement Method Characteristics

Characteristics of the previously described NDE measurement methods are summarized in Table 2.2 for the application of high temperature localized corrosion wall thickness monitoring; the methods are classified as either being low-potential, moderate potential, or high potential for the various measurement characteristics [Eason et al. (2015b)]. The temperature characteristic is based on material properties and required access proximity; for example, radiographic methods do not require direct contact with the pipe surface and can be applied at high temperatures, and therefore have high potential for the temperature characteristic. The permanent monitoring characteristic is based on implementation; for example, endoscopic methods require line of sight access to the internal pipe surface and are not well suited for in-service online monitoring, and therefore have low potential for the permanent monitoring characteristic. The direct thickness measurement characteristic is summarized in Table 2.1; as a example, acoustic emission methods may provide an average corrosion rate which can then be used to infer a wall thickness, and therefore have low potential for the direct measurement characteristic, as opposed to directly measuring wall thickness in ultrasonic bulk wave methods, which therefore have high potential for the direct measurement characteristic. The localized measurement characteristic refers to wall thickness measurements in a relatively local region

of interest as described in Table 1.1; for example, fiber Bragg grating methods may provide an average wall thickness over a relatively large area, and therefore have low potential for the localized measurement characteristic.

Table 2.2 Potential Application of Various Non-Destructive Evaluation Methods

Method	**Sub-method**	**400°C Surface Temperature**	**Permanent Monitoring Potential**	**Direct Measure-ment**	**Localized Measure-ment**
Optical	Endoscopy	o	o	o	+
	Fiber Bragg Grating	+	+	o	o
Electro-magnetic	Remote Field Eddy Current	o	o	+	+/o
	Pulsed Eddy Current	+	+	+	+
Radiography	Traditional Film	+	o	+/o	+
	Computed Radiography	+	o	+/o	+
	Digital Radiography	+	+/o	+/o	+
Acoustic Emission		+	+	o	o
Ultrasonic	Bulk Wave Mode	+	+	+	+
	Guided Wave Mode	+	+	o	o
	Piezoelectric Transduction	+	+	+	+
	Electromagnetic Acoustic Transduction	+/o	+	+	+
	Magnetostrictive Transduction	+/o	+	+	+
	Laser Transduction	+	+/o	+	+
o **Low Potential**	+/o **Moderate Potential**			+ **High Potential**	

2.3 Commercial Ultrasonic SHM Technology

Guided wave and bulk wave permanently installed ultrasonic Structural Health Monitoring (SHM) systems are discussed with a commercial technology review of bulk wave systems.

2.3.1 Guided Wave

Regarding localized corrosion, there is a large body of work on ultrasonic guided waves for pipe condition monitoring. In general, long-range guide wave (LRGW) measurements in steel pipes are in the 10–100 kHz range where as bulk wave measurements are around 1–10 MHz. The bulk wave measurements provide a higher level of sensitivity required for direct thickness measurements to be able to correlate with short term corrosion rate changes. There is a need for the intelligent merging of bulk wave SHM-UT local point measurements, SHM-LRGW cross-sectional area measurements, and other manual inspection activities [Cawley et al. (2013)].

2.3.2 Bulk Wave

Permanently installed Structural Health Monitoring Ultrasonic Thickness (SHM-UT) bulk wave sensor technology has the potential for precise wall thickness corrosion monitoring as shown in Table 2.2. Various wave modes, frequencies, footprint sizes, and coupling designs are described for relatively low and high temperatures in Tables 2.3 and 2.4 based on a review of commercially available information [GE Sensing & Inspection Technologies (2009); Cegla et al. (2011); A3 Monitoring (2014); Permasense (2015, 2016); Sensorlink (2015, 2016a,b); Berkeley Springs (2016); Cosasco (2016); Mistras (2016); Sonotec (2016); Sensor Networks (2016); GE Oil & Gas (2017)]. In Tables 2.3 and 2.4, "Channel" is not the total number of parallel channels, but rather the total number of channels available through multiplexing. A single channel is used for pulse-echo configurations, and two (dual) parallel channels are used for pitch-catch configurations. While there is currently no high-temperature SHM-UT array commercial technology, the piezoelectric bulk-wave sol-gel sensor has the potential for permanently installed high temperature transducer arrays [Kobayashi et al. (2009)] for precise thickness monitoring for a naphthenic acid corrosion application as described in Table 1.1.

Table 2.3 Low Temperature Commercial Permanently Installed Bulk Wave Sensors

Commercial Sensor	Design Temperature	Wave Mode Configuration	Footprint	Coupling
Sensor Networks SMART PIMS® XD-101	Low	5 MHz Compression Pulse-Echo	Single Element 6mm Diameter 16 Channels	Magnet/ Adhesive
Sonotec Sonowall S	70°C	Compression Pulse-Echo	Single Element 8 Channels	-
Sensor Networks matPIMS XD-401	80°C	7.5 MHz Compression Pulse-Echo	Linear Array 232mm x 25mm 16 Elements	Magnet/ Adhesive
Sensorlink UltraMonit In Situ	90°C	-	-	-
A3 Monitoring spotOn U	120°C	3-5 MHz Compression Pitch-Catch	Dual Element 2 Channels	Dry
EMERSON® PERMASENSE® ET210	120°C	Pulse-Echo	Single Element ∼50mm Diameter 1 Channel	EMAT
Sensorlink PipeMonit Swarm	125°C	5 MHz Compression Pitch-Catch	Dual Element 10mm Diameter	-
MISTRAS® CALIPERAY® LT	150°C	5 MHz Compression Pitch-Catch	Dual Element 17mm Diameter 8 Channels	Epoxy
COSASCO® ULTRACORR® 2	150°C	Compression Pulse-Echo	Single Element 30mm Diameter 8 Channels	Epoxy
Sensor Networks SMART PIMS® XD-201	150°C	5 MHz Compression Pitch-Catch	Dual Element 10mm Diameter 16 Channels	Magnet/ Adhesive
Sensorlink UltraMonit Retrofit	150°C	-	-	-

Table 2.4 High Temperature Commercial Permanently Installed Bulk Wave Sensors

Commercial Sensor	**Design Temperature**	**Wave Mode Configuration**	**Footprint**	**Coupling**
3-Sci Wi-Corr	200°C	Compression Pulse-Echo	Single Element 32mm Diameter 1 Channel	Epoxy
GE® RIGHTRAX® PM	200°C	5 MHz Compression Pulse-Echo	Single Element 8mm X 8mm 64 Channels	Dry
Berkeley Springs Eagle Array	230°C	0.5-5 MHz Compression Pulse-Echo	Single Element 10-13 mm Diameter 8 Channels	Silicone
GE® RIGHTRAX® HT	350°C	5 MHz Compression Pulse-Echo	Single Element 7-21mm Diameter 1 Channel	Metal Foil
MISTRAS® CALIPERAY® HT	350°C	3-5 MHz Compression Pulse-Echo	Single Element 19mm Diameter 4 Channels	Dry
Sensor Networks SMART PIMS® XD-301	500°C	7 MHz Compression Pulse-Echo	Single Element 10mm Diameter 16 Channels	Dry
EMERSON® PERMASENSE® WT210	600°C	∼2 MHz Shear Horizontal Pitch-Catch	Dual Element ∼15mm x ∼3mm 2 Channels	Dry

2.4 Elastic Wave Scattering - Rough Surface

The surface topography of localized corrosion can be represented by different geometries for the purpose of predicting the bulk elastic wave scattering response as shown in Figure 2.1. Such geometries have been studied in various research communities: flat-bottom-holes by the NDE community, single hemispherical canyons by the seismology community, and random rough-surface scattering by the radar community with vector modeled electromagnetic waves.

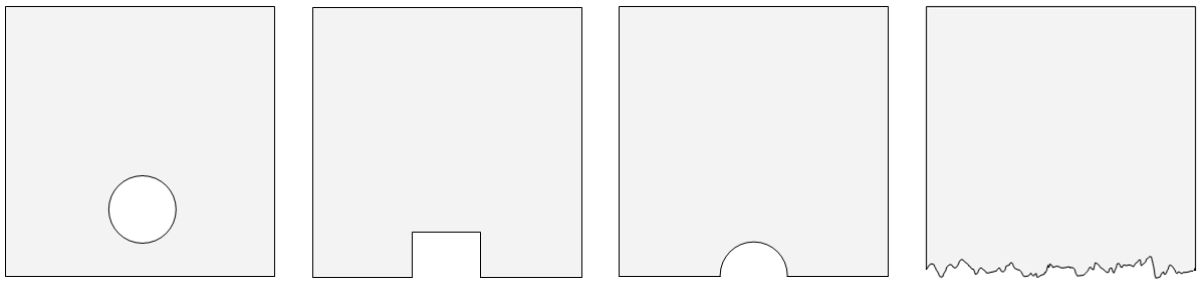

Figure 2.1 Cross-section geometry images representing a sphere or cylinder, flat bottom hole, hemispherical pit, and random rough surface. Figure previously published [Eason et al. (2017a)].

Wave scattering specifically from rough and random surfaces has been studied extensively across many disciplines over at least the past 50 years. While variations exist between the different physical forms and dimensional scales of electromagnetic, acoustic, elastic, and optical wave scattering, many underlying principals are common.

2.4.1 Background

A description of different scattering regimes is first provided followed by rough surface scattering work organized into various categories: i) classical and contemporary texts covering a broad and general range of rough surface scattering, ii) analytical theory methods, iii) numerical solution methods, iv) application of methods to specific problems with experimental result, and v) an aggregate combination of analytical, numerical, and experimental application work.

2.4.1.1 Scattering Regimes

The relative dimensional scale of the feature and incident wavelength for scattering problems is transferable among applications when comparing results with dimensionless variables. One common dimensionless variable is ka, with k as the wavenumber defined as $k = \frac{\omega}{c}$, with ω as the angular frequency defined as $\omega = 2\pi f$, with f as the frequency, c as the wave speed, and a as a dimensional length variable of the feature or flaw radius. The second common dimensionless variable is $\frac{d}{\lambda}$, with d as a dimensional length variable of the feature or flaw diameter, and λ as the wavelength defined as $\lambda = \frac{c}{f}$. An example relating frequency f, wavelength λ, and dimensionless variables ka and $\frac{d}{\lambda}$ is shown in Table 2.5 for $c = 5907$ m/s and $a = 1.0$ mm as an example of values for an NDE flaw detection application in steel material.

Table 2.5 Dimensionless Variable Reference

Variable	**Values**							
Frequency f MHz	0	1	2	5	10	20	50	100
Wavelength λ mm	-	5.9	3.0	1.2	0.59	0.30	0.12	0.059
Dimensionless ka	0	1.1	2.1	5.3	11	21	53	106
Dimensionless $\frac{d}{\lambda}$	0	0.3	0.7	1.7	3.4	6.8	17	34

The relatively low-frequency (long-wavelength) perturbation Rayleigh scattering regime is typically in the $0 < ka < 1$ range, the relatively high-frequency (short-wavelength) ray tracing Geometrical Theory of Diffraction (GTD) scattering regime is typically around $ka > 10$, and the mid-frequency scattering regime has limited closed-form solutions for most geometric features.

In seeking solutions to canonical problems, a range of geometries are of interest and several are shown in Figure 2.1. While there are full-frequency range closed form solutions for three dimensional elastic wave scattering from an embedded spherical and cylindrical geometry, there are no such broadly accepted solutions for scattering by a single hemispherical pit or random rough surface geometries as shown in Figure 2.1.

2.4.1.2 General

Many texts have been authored on the scattering of waves from rough surfaces; the earliest identified discusses the scattering of electromagnetic waves in the context of radio wave reflec-

tions from the earth, moon, and other planets [Beckmann and Spizzichino (1963)]. Another early reference covers wave scattering more broadly with a section of the book dedicated to rough surface scattering [Ishamaru (1978)]. Other earlier books on wave scattering from rough surfaces are also identified [Bass and Fuks (1979); Sobczyk (1985)].

One of the most referenced texts on scattering from rough surface is authored from the perspective of ultrasonic Non-Destructive Evaluation, but written broadly as applicable to other physical forms [Ogilvy (1991)]. Another reference, similar to the Ogilvy text, covers rough surface scattering in general [Voronovich (1994)]. A large encyclopedia type resource broadly covers wave scattering theory, approximations, numerical techniques, mathematical modeling, experimental techniques, technology practices, and experimental comparison with theory for a range of fields and applications [Pike and Sabatier (2001)].

References are available for discipline specific topics: rough surface electromagnetic scattering [Ilyinski and Slepyan (1993); Tateiba and Tsang (1996); Tsang et al. (2000); Tsang and Kong (2001); Fung and Chen (2010); Pinel and Boulier (2013)], rough surface acoustic scattering for underwater applications [Biryukov et al. (1995); Jackson and Richardson (2006)], rough surface seismic scattering for underground applications [Sato and Fehler (1998)], rough surface light scattering from random nanoscales [Bennett and Mattsson (1989); Maradudin (2007)], as well as multi-scale surface scattering applications [Fung (2015)].

2.4.1.3 Analytical Methods

The most extensive and current review paper on rough surface scattering identifies more than 30 different analytical theoretical models [Elfouhaily and Guérin (2004)]. The various models in this paper can be classified into three broad groups and multiple sub-groups as shown in Table 2.6. The first broad group of analytical models are variations of the Small Perturbation Method. The Small Perturbation Methods is generally applicable only to relatively smooth surfaces covering the regime of small roughness in the high frequency regime. The second broad group of analytical models are variations of the Kirchhoff Approximation. The Kirchhoff Approximation is generally applicable to non-smooth surfaces covering the regime of large roughness in the low frequency regime. However, the Kirchhoff Approximation is a local method

based on individual points on the surface and does not take into consideration curvature or multiple scattering. The Small Perturbation Method is generally more accurate in the high frequency regime while the Kirchhoff Approximation is generally the better option in the low frequency regime. The third broad group of analytical models are termed Unifying Theories that attempt to use a single model to satisfy both low and high frequency scattering regimes. Characteristics of the various analytical models are summarized [Elfouhaily and Guérin (2004)].

Table 2.6 Rough Surface Scattering Analytical Models [Elfouhaily and Guérin (2004)]

Group	**Sub-Group**	**Sub-Sub-Group**
Small Perturbation Method	First Order	
	Second Order	
Kirchoff Approx.	Tangent Plane Approx.	Momentum Transfer Expansion
	High-Frequency Regime	Physical Optics
		High-Frequency Kirchoff Approx.
		Geometrical Optics
		Two-Scale Model
	Curvature Corrections	Lynch Variational Method
		Local Parabolic Approx.
Unifying Theory	Meecham-Lysanov Method	
	Phase Perturbation Method	
	Small-Slope Approx.	Quasi-Slope Expansion
		Extended Small-Slope Approx.
		Non-Local Small-Slope Approx.
		Non-Local Curvature Approx.
	Operator Expansion Method	
	Tilt-Invariant Approx.	Local Curvature Approx.
	Local Weight Approx.	
	Weighted Curvature Approx.	
	Weiner-Hermite Approach	
	Unified Perturbation Expansion	
	Full-Wave Approach	Local Spectral Expansion Method
		Correction Current Method
	Improved Green Function Method	
	Volumetric Methods	Born Approx.
		Distorted-Wave Born Approx.
		Mean-Field Theory
	Integral Equation Method	

A new theory for scalar and vector wave scattering from rough surfaces combines an extended Kirchhoff Approximation with both first and second order small slope approximations

that result in approximations similar to the second order small perturbation method [Thompson (2003)]. A new approach termed the curvilinear coordinate method applies a non-orthogonal coordinate system for electromagnetic scattering from a plane wave incident on a one-dimensional random rough surface [Bardier et al. (2004)]. A second kind of boundary integral equation method for the soft-sound case is presented for both isotropic and anisotropic solids [Chandler-Wilde et al. (2006)]. A new model termed the reduced local curvature approximation of third order (RLCA3) is presented similar to the small slope approximation (SSA) but with better agreement in the high-frequency limit [Elfouhaily and Johnson (2007)]. A closed-form first-order solution based off the small perturbation method is presented and applied to electromagnetic scattering from a layered structure with multiple rough surface interfaces [Imperatore et al. (2009)]. Variational formulations theory is presented to address scattering from penetrable rough layers for acoustic and electromagnetic waves [Lechleiter and Ritterbusch (2010)]. A high order small perturbation method (HISPM) for electromagnetic wave scattering from rough surfaces is presented [Guo et al. (2011)]. A closed form of the scattered field cross-spectral density function has been derived using the physical optics approximation and validated against simulated data [Hyde et al. (2013)]. An analytical Kirchoff approximation method has been derived incorporating surface statistics for three dimensional geometry and out of plane SH mode conversion in an ultrasonic bulk wave scattering application [Shi et al. (2016)].

2.4.1.4 Numerical Methods

While the earliest work is on scattering theory, more recent texts discuss numerical methods for rough surface scattering problems [Tsang et al. (2001); Jin (2005)]. A guideline is provided for the selection of key parameters for numerical simulation of electromagnetic scattering from random rough surfaces [Ye and Jin (2005)]. A spectral method is presented using a probabilistic framework applied to the small perturbation method for acoustic wave scattering from rough surfaces [Xiu and Shen (2007)]. A new semi-analytical method is applied to elastic wave fields in isotropic and anisotropic plate structures containing anomalies of any geometry [Banerjee and Kundu (2008)]. An analytical-numerical technique termed the Cylindrical Wave Approach using the Small Perturbation Method is presented and applied to the scattering of a plane

wave from a cylinder buried under a rough surface [Fiaz et al. (2012)]. A text describes the distributed point source method (DPSM) for modeling various engineering problems as a mesh-free computation process having the potential to use less computational resources as compared to element based numerical techniques [Placko and Kundu (2007)]. The DSPM has been applied to ultrasonic waves reflected from an elliptical cavity [Shelke et al. (2010)], as well as elastic wave scattering from a random rough surface with an incident shear horizontal wave mode [Jarvis and Cegla (2014)]. A frequency-domain finite element technique is presented that represents the scattering matrix in the Fourier domain to capture both near-field and far-field behavior [Wilcox and Velichko (2010)] and used to predict the far-field scattering of an arbitrary shaped defect in anisotropic medium, presented for the isotropic case and compared with analytical solutions [Velichko and Wilcox (2010)]. Numerical simulation of scattering from rough surface cracks using the finite element local scattering (FELS) model is presented in the form of a scattering matrix [Zhang et al. (2011)]. Weighted Sobolev spaces are applied to elastic plane wave and spherical wave scattering from diffraction gratings [Elschner and Hu (2015)]. A finite element modeling approach is compared with Kirchoff theory predictions and experimental measurements [Pettit et al. (2015).]

2.4.1.5 Method Application

While not introducing new theoretical or numerical methods, the following references apply existing methods to various applications. The incorporation of rough surface scattering from the tangent plane approximation is applied to a ray propagation model for optical waves [Didascalou et al. (2003)]. The Small-Slope Approximation (SSA) is applied to electromagnetic scattering at penetrable random rough interfaces [Gilbert and Johnson (2003)]. A finite element method and Monte Carlo simulation are applied to an electromagnetic wave incident at a low grazing angle over a randomly rough sea surface [Liu and Jin (2004)]. An approach to combine the method of fictitious sources and the scattering-matrix method is presented for electromagnetic problems in two dimensions [Tayeb and Enoch (2004)]. The weighted curvature approximation (WCA) has been compared numerically to the method of moments (MoM) based results for Gaussian random surfaces showing that WCA is accurate beyond the typical

range where Small Slope and Kirchhoff Approximations are valid [Guérin et al. (2004)]. A finite difference numerical analysis of seismic wave scattering from randomly rough interfaces in a multi-layered medium compares the differences between two dimensional and three dimensional simulations [Makinde et al. (2005)]. A one-dimensional comparison of Weighted Curvature Approximation (WCA), Local Curvature Approximation (LCA), First Order Small Slope Approximation (SSA-1), and Second Order Small Slope Approximation (SSA-2) backscattering models is presented for an electromagnetic application [Bourlier et al. (2005)]. The incorporation of electromagnetic scattering using the Kirchhoff approximation is applied to a three dimensional ray tracing software package [Cocheril and Vauzelle (2007)]. The elastodynamic finite integration technique (EFIT) has been applied to acoustic scattering from an aluminum cylinder near a rough interface [Calvo et al. (2010)]. A Small Perturbation Method is applied to the scattering of acoustic waves at rough solid-solid interfaces [Sun and Pipe (2012)]. A finite difference time domain solver is applied to electromagnetic surface scattering at low angles by comparing to the Surface Integral Equation (SIE) approach [Liao and Dogaru (2012)].

2.4.1.6 Aggregate Methods

A combination of analytical methods, numerical methods, and applications include: scattering of acoustic and electromagnetic waves under various boundary conditions for rough surfaces in two and three dimensions [Thomas (2006)], the detection of surface corrosion by ultrasonic backscatter [Retaureau (2006)], wave propagation over large rough surfaces at low grazing angles [Lai (2007)], scattering from layered rough surfaces [Kuo (2008); Tabatabaeenejad (2008)], high frequency scattering from rough surfaces [Kurkcu (2008)], scattering of a plane wave by an embedded corrugated surface [Yu (2008)], comparison of acoustic rough surface scattering in two and three dimensions [Joshi (2011); Tran (2013)], simulation of high temperature ultrasonic data for the characterization of rough surface corrosion [Jarvis (2013)], and application of the physical optics approximation for partially coherent illumination [Spencer (2014)].

The characterization, measurement, and statistical description of rough surfaces has been described [Thomas (1982); Brune (1997); Whitehouse (2002); Zhao et al. (2000)], including specific work on fractal surfaces [Russ (1994); Li et al. (2003); Franceschetti and Riccio (2006)].

2.4.2 Theory

The most basic description of a rough surface is variation of surface height relative to a flat reference plane. Consider a scenario shown in Figure 2.2 with two points on a flat reference plane along a one dimensional line at position x_1 and x_2. The surface heights corresponding to the points are h_1 and h_2. Consider a sinusoid wave transmitted at the same angle, θ_1, and at the same distance perpendicular to the reference plane for each point. Based on the difference in time of travel, the phase difference of the reflected wave between the two points on the surface, $\Delta\phi$, is described in Equation 2.24 with k as the wavevector modulus (related to wavelength) and θ_2 the reflection angle [Ogilvy (1991)].

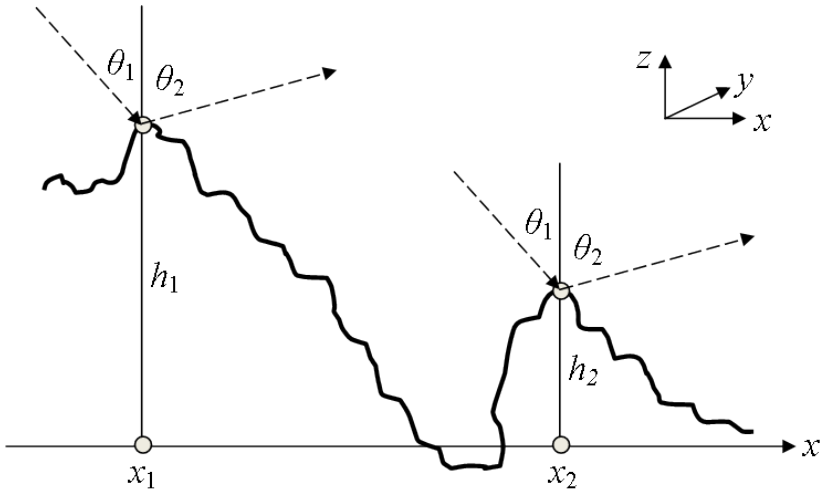

Figure 2.2 Schematic showing surface roughness observed by the phase difference of reflected signals. The phase difference is related to the incident wavelength, incident angle, and height difference between points. Based on similar figure previously published [Ogilvy (1991)].

$$\Delta\phi = k\left[(h_1 - h_2)\left(\cos\theta_1 + \cos\theta_2\right) + (x_2 - x_2)\sin\theta_1 - \sin\theta_2\right] \tag{2.24}$$

By simplifying the scenario, and assuming that the reflected signal is of the same mode as the transmitted signal, then the reflection angle will be the same as the incident angle and can

be considered specular scattering at each of the two points. With this simplification, $\theta_1 = \theta_2$, and Equation 2.24 reduces to Equation 2.25 [Ogilvy (1991)].

$$\Delta\phi = k\Delta h \cos\theta_1 \tag{2.25}$$

The phase difference will cause destructive interference if $\Delta\phi \approx \pi$ resulting in an aggregate decrease in reflected signal amplitude from the two points. The phase difference will be constructive if $\Delta\phi \ll \pi$ resulting in an aggregate increase in reflected signal amplitude from the two points. A surface can be considered smooth if the phase change does not result in destructive interference with $\Delta\phi < \frac{\pi}{2}$ [Ogilvy (1991)]. The Rayleigh parameter, R_a, is used to describe surface roughness as shown in Equation 2.26 with σ as a measure of surface height variation with Root-Mean-Square (RMS) deviation [Ogilvy (1991)]. A surface can be considered smooth if $R_a < \frac{\pi}{4}$; a surface can be considered rough if $R_a \geq \frac{\pi}{4}$.

$$R_a = k\sigma \cos\theta_1 \tag{2.26}$$

In summary, surface roughness can be observed by the phase difference of a reflected signal. The phase difference is related to the incident wavelength, incident angle, and height difference between points. Only the height difference is an intrinsic material characteristic; the incident wavelength and the incident angle are characteristics of the measurement technique. Therefore, rough surface scattering behavior is dependent on the physical surface height profile as well as on the applied measurement technique.

2.4.2.1 Coherent and Diffuse Fields

Moving beyond two points, consider an entire surface under three different scenarios. The first scenario is a smooth surface, the second scenario is a slightly rough surface, and the third scenario is a very rough surface [Ogilvy (1991)].

For the smooth surface scenario, the height of every point on the surface is considered to be the same with $h_1 = h_2$ everywhere. The result from Equation 2.25 is no phase change, $\Delta\phi = 0$, caused by surface roughness in the reflected wave field. This reflected wave field from the flat

surface is in the specular direction and termed the coherent field. By definition, the coherent field at the same phase and at the same specular angle direction as compared to the incident wave. For a smooth surface scenario, the coherent field is very strong and dominates the total reflected wave field.

For the slightly rough surface scenario, the height of every point on the surface is not considered to be the same with $h_1 \neq h_2$ everywhere. The result from Equation 2.25 is some phase change, $\Delta\phi \neq 0$, caused by surface roughness in the reflected wave field. Again, the reflected wave field in the specular direction is termed the coherent field with the same phase and as the incident wave. While the coherent field reflected from a smooth surface is very strong, the coherent field reflected from a slightly rough surface is weaker and no longer dominates the reflected wave field. This reduction in amplitude can be described by $e^{-\frac{g}{2}}$ with g as a backscattering term described in Equation 2.27 [Ogilvy (1991)]. The scattered component of the reflected signal not in the specular direction is termed the diffuse field. Assuming the surface roughness profile is random, the diffuse field is scattered in random angle directions and is not of the same phase as the incident wave; the diffuse field consists of random phase components. For a slightly rough surface scenario, the diffuse field is present, but still weak and contributes to part of the total reflected wave field along with the weak coherent field.

$$g = 4k^2\sigma^2 \cos^2\theta_1 = 4{R_a}^2 \tag{2.27}$$

For the very rough surface scenario, the height of every point on the surface is not considered to be the same with $h_1 \neq h_2$ everywhere. When the surface is very rough, the coherent field can disappear and the diffuse field becomes very strong and dominates the total reflected wave field. Again, the diffuse field from a random surface will reflect in random angle directions and be of random phase. The amplitude of the diffuse field must be calculated from only the intensity of the field components and ignoring the phase of the field components as the summation of random phases will be zero.

2.4.2.2 Polarization Modality

Wave scattering from rough surfaces can be applied to problems of various physical forms resulting in the presence of different polarization modalities. For example, acoustic waves consist of only a single longitudinal wave reflection mode. Electromagnetic waves consist of two elliptically polarized reflection modes. Elastic waves consist of three bulk wave reflection modes: longitudinal, vertical polarization, and horizontal polarization. In the case of elastic waves, the influence of a two dimensionally rough surface can cause three reflected modes, where a smooth surface assumption results in only two reflected modes.

Models described as scalar wave scattering are applicable for acoustic wave problems. Models described as vector wave scattering are applicable for electromagnetic wave problems, but are also applied to elastic wave problems, possibly without a complete representation of all three polarizations: compression, shear horizontal, and shear vertical.

2.5 Summary

This chapter reviewed NDE inspection and monitoring methods for piping internal corrosion, and compared the methods for a high-temperature localized corrosion monitoring application. Ultrasonic bulk wave piezoelectric transducer technology has the potential to monitor such high-temperature localized corrosion, and a commercial review of SHM-UT technology was provided. There is currently no high-temperature permanently installed bulk wave ultrasonic array commercial technology; however, transducers manufactured from the "sol-gel" ceramic fabrication process have potential in this space. Finally, a background discussion and review on random rough surface scattering was presented.

The hypothesis under investigation is to understand if sol-gel sensor technology can monitor localized high-temperature corrosion with measurement precision as defined in Table 1.1. This will be explored by characterizing sol-gel transducers (Chapter 3), understanding the measurement application bounding cases (Chapter 4), elastic wave scattering behavior from a single hemispherical pit (Chapters 5-7), ultrasonic thickness measurement statistical considerations (Chapter 8), and pipe stress analysis methods to obtain prognosis information (Chapter 9).

CHAPTER 3. SOL-GEL TRANSDUCER CHARACTERIZATION

Transducers manufactured from the ‟sol-gel″ ceramic fabrication process have potential as high-temperature permanently installed bulk wave ultrasonic array commercial technology to satisfy the measurement application as described in Table 1.1. This chapter provides a description and review of prior work on sol-gel sensors, characterization of such sensors by acoustic/electric circuit models, as well as characterization of transducer incident beam profiles by utilizing photoelastic imaging.

3.1 Sol-Gel Fabrication Process

The sol-gel ceramic fabrication process can be applied to produce the piezoelectric material [Barrow et al. (1996)] used in thick-film ultrasonic transducers for bulk wave wall thickness measurements [Kobayashi et al. (2009)]. This transducer design has the potential to provide a strong and reliable permanent acoustic bond to the pipe wall surface, has customizable sensor element array configurations to expand into larger areas of measurement coverage, and also has the potential for installation in high temperature environment [Shih et al. (2010); Kobayashi and Jen (2012)].

The term ‟sol-gel″ refers to a ceramic fabrication process to manufacture piezoelectric transducers involving the following steps i) preparation of solution material and powder material, ii) mixing of the two materials with sufficient shear forces within the fluid to maintain the mixture as a suspension, iii) deposition of the materials onto a surface of interest, one method is aerosol deposition with use of a mask, iv) thermal curing of the initial layer v) deposition and curing of subsequent layers vi) final geometric changes such as slicing, vii) polarization, and viii) wiring and encapsulation.

An optimization problem exists between the number and thickness of individual deposition layers in order to achieve the final thickness for the desired transducer central frequency. Thicker individual layers can be more prone to cracking as a result of higher residual stress within each individual layer. Thinner individual layers require more deposition steps, increasing the time and cost of fabrication. Also, material properties such as brittleness, elasticity, and porosity can be controlled by the various fabrication process parameters. These properties influence the transducer bandwidth and durability.

There are different variations on the fabrication process regarding piezoelectric materials, particle size, curing temperature, curing time, number of layers, individual layer thickness, and total layer thickness for various sensing applications. Integration of a microwave processing method into the sol-gel fabrication process was demonstrated to fabricate transducers for active vibration control of a flexible structures [Ounaies (1995)]. The influence of sol-gel particle size and heat treatment has been studied for gas sensor performance [Liu et al. (1997)]. A sol-gel fabrication spin-coating process is described [Tanase et al. (2004)]. A vacuum filling sol-gel precursor is described and presented along with SEM cross-section images showing the porous nature of a sol-gel ceramic [Zhang et al. (2006)]. Annular array sol-gel transducers have been fabricated by micromaching techniques in combination with sol-gel processing [Dorey et al. (2007)]. Flexible singe-element and multi-element array transducers have been fabricated by the sol-gel process [Ono et al. (2007); Wu et al. (2010); van der Heijden et al. (2016)] and evaluated at high temperatures up to 420°C [Veilleux et al. (2013)]. Actuators, in addition to flexible sensors, have been fabricated by the sol-gel process [Hsueh and Wu (2010)]. Sol-gel thick-film electrical impedance and other material properties have been characterized [Pardo et al. (2010)]. A process to control the particle size of sol-gel power is described with the intention of a piezoelectric material 3D printing application [Huang et al. (2014)]. Ferroelectric properties of ceramics fabricated from sol-gel powders of different chemistry have been evaluated up to a temperature of 350°C [Mahmood et al. (2015)]. Improvements in the sol-gel fabrication process for high temperature ultrasonic thickness transducers have been recently published [Searfass et al. (2016)]. Sol-gel sensors have been used in an ultrasonic thickness

structural health monitoring application to demonstrate the photoelastic visualization method as well as statistical uncertainty quantification methods [Eason et al. (2015a,b, 2016a,b)].

3.2 Circuit Modeling

Modeling the performance of thick-film sol-gel piezoelectric transducer behavior is based on general transducer characterization methods [Kino (1987); Meeker (1996); Lu (2012); Sherrit and Mukherjee (2012)] and specific examples of air-backed thick-film transducer impedance characterization [Maréchal et al. (2006); Dorey et al. (2007); Pardo et al. (2010); Ali et al. (2015); Mahmood et al. (2015)]. There are various circuit models available to characterize an air backed thick-film sol-gel transducer: Three-Port-Network, Mason Circuit, Redwood, KLM, Reeder Winslow [Reeder and Winslow (1969)], and a model specifically for air-back thick-film sol-gel transducers [Lukacs et al. (1999, 2000)].

The Three-Port-Network and Lukacs Models are reviewed and analyzed for an air-backed thick-film sol-gel transducer application. The Three-Port-Network Model appears to have a realistic pattern for real and imaginary impedance values. The Lukacs Model analysis is not applicable as only the real material parameters were used instead of the required complex material parameters. The circuit modeling details are shown in APPENDIX A.

3.3 Photoelastic Imaging

Elastic wave propagation can be visualized in a transparent material by observing polarized light refracted from pressure gradients via the schlieren method [Baborovsky et al. (1973)], or from localized regions of stress via the photoelastic method. While the schlieren method can be more sensitive to acoustic waves in liquids, the photoelastic method can observe the shear stress mode [Yamamoto (2012)]. The earliest publication of the photoelastic method [Heidemann and Hoesch (1937)] occurred decades prior to the first applications to ultrasonic visualization [Hanstead (1972, 1974); Wyatt (1972, 1974, 1975); Hall (1977, 1982); Sachse (1979)]. This physical model imaging technique has not been adopted as broadly as computer based models that started to gain favor from the mid 80's. However, modern equipment is causing

the photoelastic imaging technique to be revisited. More current efforts are around image digitization and quantification [Ginzel and Stewart (2004); Ginzel and Zhenshun (2006); Schmitte et al. (2012); Washimori et al. (2012); An et al. (2014)] are in part a result of improved camera and LED light source technology. A commercial photoelastic imaging system was used for this study [Eclipse Scientific (2014)].

3.3.1 Visualization Images

The elastic wave propagation beam profiles from a manual ultrasonic contact transducer and from a thick-film sol-gel ultrasonic transducer are characterized using a photoelastic visualization imaging technique.

3.3.1.1 Manual Contact Transducer

To provide reference images for comparison with a sol-gel transducer, a 5.0 MHz flat 6.35 mm circular PANAMETRICS® V110 [Serial #61566] manual ultrasonic contact transducer is investigated. This transducer frequency is common for manual wall thickness measurements of steel pipe. The transducer was applied to a 19 × 65 × 110 mm soda lime glass block with SOUNDSAFE® water based ultrasonic couplant and a dead weight contact pressure of approximately 9 kPa. The transducer was excited with a 120 V square wave. The strobe delay was adjusted to capture photoelastic images at various points in time of the initial beam propagation. The individual images are analogous to a single frame of a beam propagation video. A sampling of four frames are shown in Figure 3.1. The primary longitudinal wave mode as well as the edge effect shear wave mode are observable with color intensity proportional to acoustic amplitude; lighter color correlating to a positive amplitude and darker color correlating to a negative amplitude.

The photoelastic image frames are processed to generate the maximum absolute amplitude beam profile as shown in Figure 3.2. The maximum and minimum pixel values are identified in each frame for each spatial coordinate in Figures 3.2a and 3.2b. The final frame in Figure 3.2c is subtracted to normalize the maximum and minimum amplitude images in Figures 3.2d and 3.2e. The normalized maximum amplitude image is then filtered to remove noise below a constant

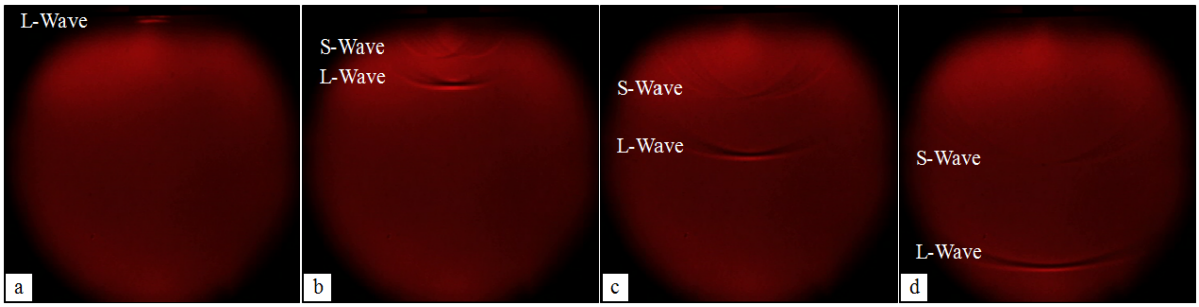

Figure 3.1 Photoelastic images of the incident longitudinal and shear elastic waves propagating from a manual contact transducer at a) 1 μs, b) 3 μs, c) 6 μs, and d) 11 μs. Figure previously published [Eason et al. (2016b)].

value of 4 as shown in Figure 3.2f. The normalized and filtered maximum amplitude image is then smoothed with a 2D convolution function applying a 3 $\times$ 3 [.05 .1 .05; .1 .4 .1; .05 .1 .05] smoothing matrix at 100 iterations as shown in Figure 3.2g. An isosurface plot is shown in Figure 3.2h analogous to a region of focus defined by a dB threshold.

3.3.1.2 Sol-Gel Transducer

A proprietary 7.5 MHz flat 4 mm $\times$ 4 mm square ultrasonic thick-film sol-gel transducer with a 55% -6 dB bandwidth was investigated. The transducer was applied to thin stainless steel film which was then coupled to the same glass block with the same couplant and a dead weight contact pressure of approximately 3 kPa. The transducer was excited with a 120V square wave. A sampling of frames are shown in Figure 3.3. The color intensity change is much less obvious making it difficult to identify the primary longitudinal wave mode.

The photoelastic image frames are processed the same way to generate the maximum absolute amplitude beam profile as shown in Figure 3.4. The maximum and minimum pixel values are identified in each frame for each spatial coordinate in Figures 3.4a and 3.4b. The final frame in Figure 3.4c is subtracted to normalize the maximum and minimum amplitude images in Figures 3.4d and 3.4e. The normalized minimum amplitude image is then filtered to remove noise below a constant value of 3.5 as shown in Figure 3.4f. The normalized and filtered minimum amplitude image is then smoothed with a two dimensional convolution function applying

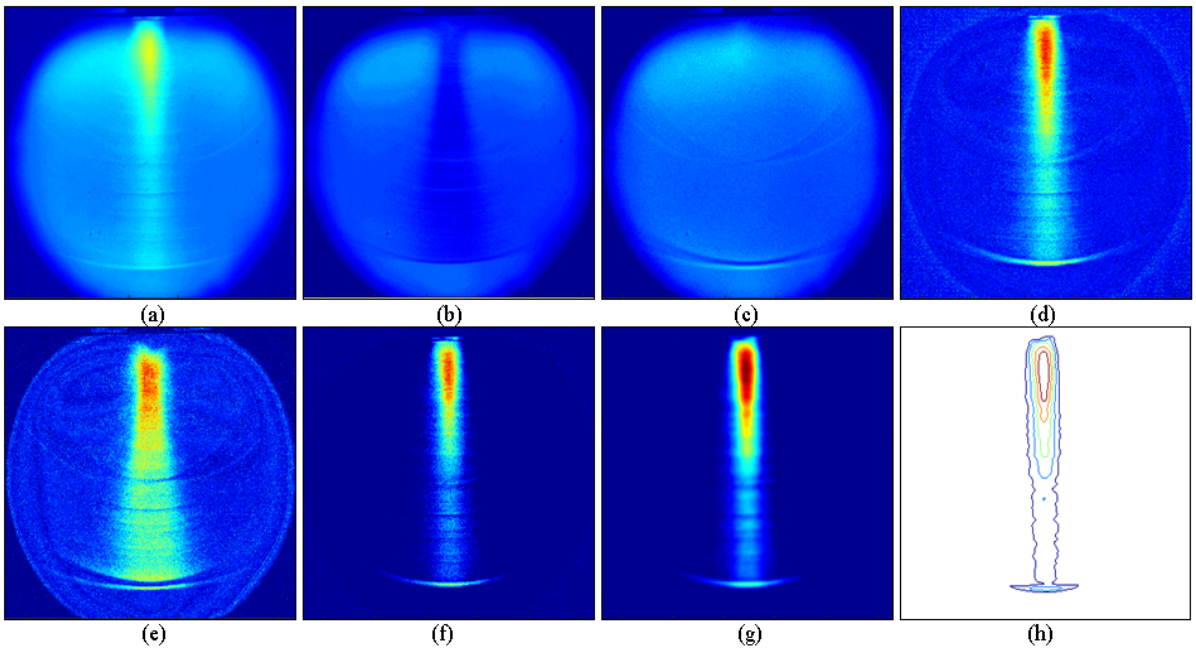

Figure 3.2 Photoelastic beam profile construction of a 5.0 MHz PANAMETRICS® V110 manual transducer for: a) maximum spatial amplitude, b) minimum spatial amplitude, c) final frame image, d) normalized maximum amplitude, e) normalized minimum amplitude, f) filtered normalized maximum amplitude, and g) filtered smoothed normalized maximum amplitude, and h) isosurface plot. Figure previously published [Eason et al. (2015b)].

a 3 × 3 [.05 .1 .05; .1 .4 .1; .05 .1 .05] smoothing matrix at 100 iterations as shown in Figure 3.4g. An isosurface plot is shown in Figure 3.4h analogous to a region of focus defined by a dB threshold.

3.3.2 Visualization Comparison

The photoelastic generated beam profile is compared with calculated near-field values and CIVA [Calmon et al. (2006)] modeling results for the manual contact and sol-gel transducers.

3.3.2.1 Manual Contact Transducer

The classic normalized near-field length is described in Equation 3.1 [Krautkramer and Krautkramer (2013)], with N_0 as the normalized near-field, D as the transducer diameter, f as the acoustic frequency, and c as the wave speed. For the 5.0 MHz flat 6.35 mm circular

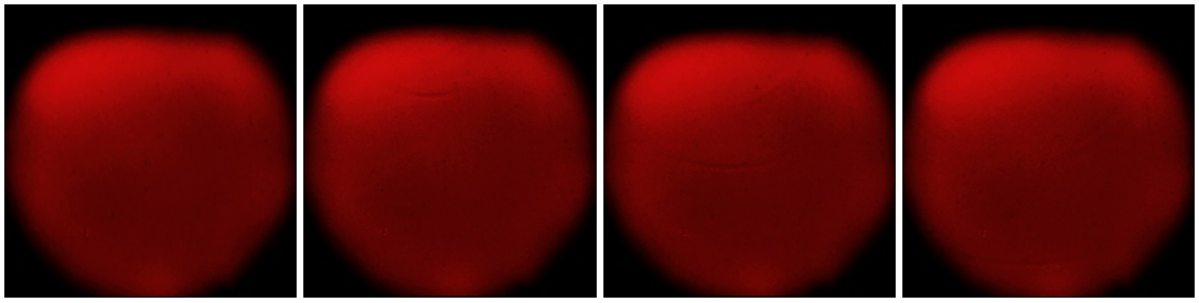

Figure 3.3 Photoelastic images of the incident elastic waves propagating from a proprietary 7.5 MHz thick-film sol-gel transducer. The propagating waves are difficult to observe; improved sol-gel transducer characterization results are shown in Figure 3.8. Figure previously published [Eason et al. (2015b)].

PANAMETRICS® V110 [Serial #61566] manual ultrasonic contact transducer: $D = 6.35$ mm, $f = 5$ MHz, and $c = 5840$ m/s in soda-lime glass resulting in a near-field length of 8.6 mm.

$$N_0 = \frac{D^2 f}{4c} \tag{3.1}$$

The transduction beam profile was modeled with CIVA commercial software [Calmon et al. (2006)] that simulates elastodynamic wave propagation behavior based on electromagnetic wave theory [Deschamps (1972)]. The model configuration is shown in Figure 3.5 with a soda lime glass block specimen of 110 mm × 19 mm × 65 mm with density of 2.24 g/cm^3, longitudinal wave speed of 5840 m/s, a shear wave speed of 2460 m/s, no roughness, and no attenuation.

The manual contact transducer was modeled using CIVA as a single circular 6.35 mm diameter contact transducer with flat focus and a Gaussian frequency spectrum centered at 5 MHz with 100% bandwidth at -6 dB. The inspection was established with a water couplant with a density of 1 gm/cm^3 and a longitudinal wave speed = 1485 m/s. The simulation was run as a three dimensional computation in a two dimensional zone scaled to match the photoelastic imaging window and with a uniform 0.5 mm spatial resolution.

The calculated near-field length of 8.6 mm from Equation 3.1 and CIVA model results are shown in Figure 3.6 with a comparison to the corresponding photoelastic beam profile image from Figure 3.2g. The beam profile from the calculated near-field, elastodynamic simulation, and photoelastic image match relatively well.

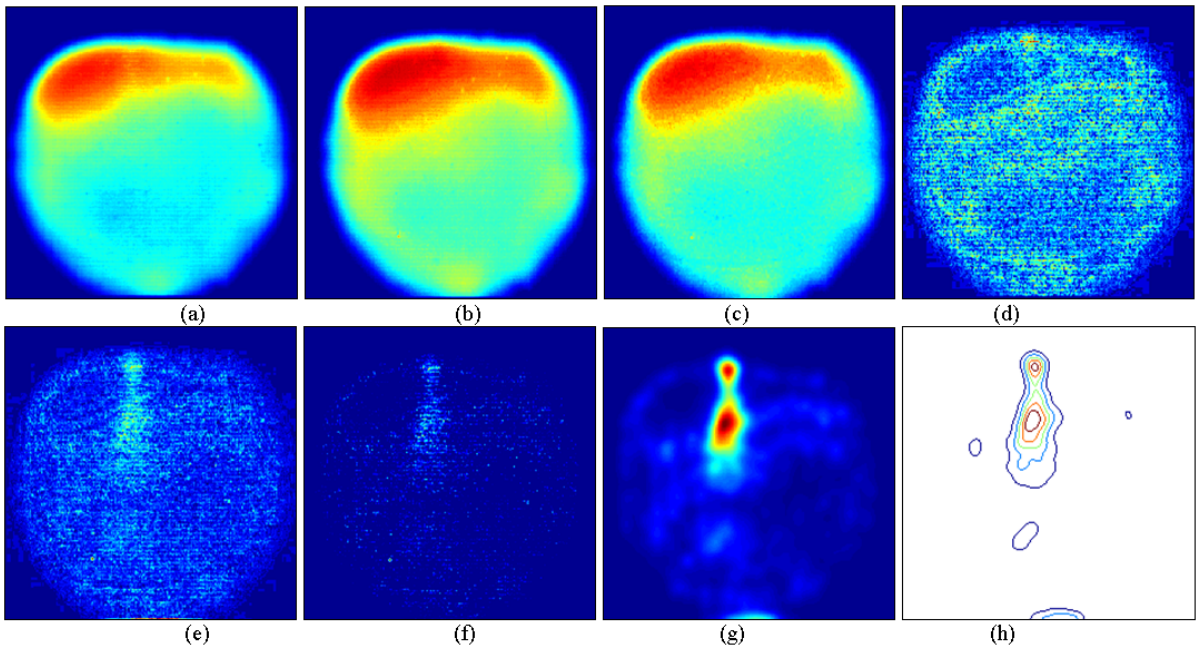

Figure 3.4 Photoelastic beam profile construction of a proprietary 7.5 MHz thick-film sol-gel transducer for: a) maximum spatial amplitude, b) minimum spatial amplitude, c) final frame image, d) normalized maximum amplitude, e) normalized minimum amplitude, f) filtered normalized minimum amplitude, and g) filtered smoothed normalized minimum amplitude, and h) isosurface plot. Figure previously published [Eason et al. (2015b)].

3.3.2.2 Sol-Gel Transducer

When applying Equation 3.1 to the proprietary 7.5 MHz thick-film sol-gel transducer with $D = 4.0$ mm, $f = 7.5$ MHz, and $c = 5840$ m/s, the resulting near-field length is 5.0 mm. The same elastodynamic simulation parameters from the manual contact transducer are used except with a single element 4 mm $\times$ 4 mm rectangular contact transducer with flat focus and a Gaussian frequency spectrum centered at 7.5 MHz with 100% bandwidth at -6 dB.

The calculated near-field length of 5.0 mm from Equation 3.1 and CIVA model results are shown in Figure 3.7 with a comparison to the corresponding photoelastic beam profile image from Figure 3.2g. The beam profile from the calculated near-field and elastodynamic simulation match well, however the photoelastic image does not. This is likely a limitation of the photoelastic image measurement being unable to distinguish the beam profile from

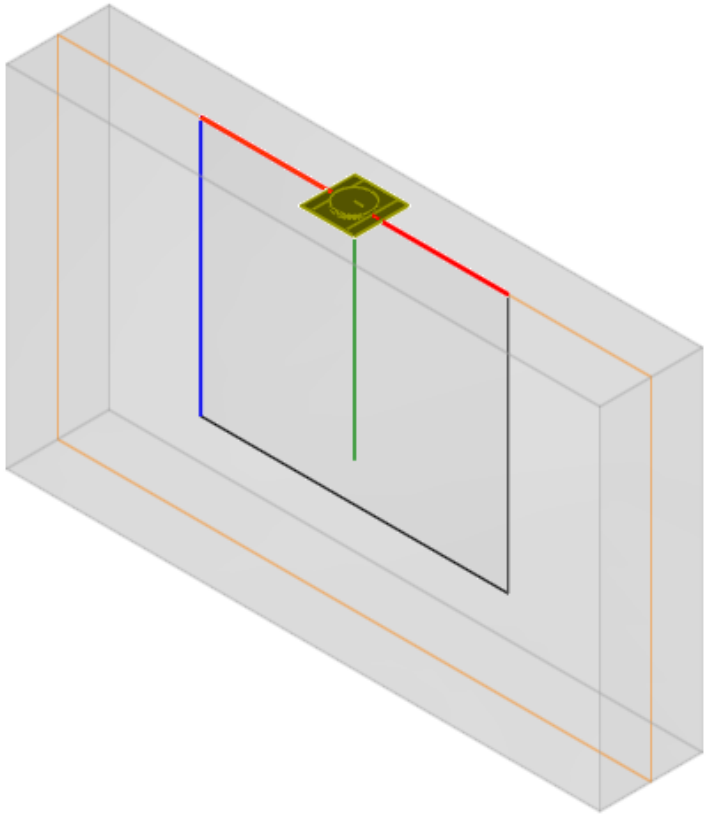

Figure 3.5 CIVA elastodynamic wave propagation model specimen and transducer configuration. Figure previously published [Eason et al. (2015b)].

background noise. This region of higher background noise observed at the top of the image in Figure 3.4c appears to coincide inversely with the beam profile void observed in Figure 3.7. Additional work was necessary to improve light source alignment, optimize lens orientations, increase coupling force, and investigate other sol-gel sensors to better visualize the elastic wave propagation behavior from a thick-film sol-gel type transducer.

3.3.2.3 Improved Sol-gel Transducer Results

The sol-gel transducer visualization results are improved by optimizing the lens orientation to increase the optical signal to noise ratio, and further improved by using automatic motor control to incrementally adjust the strobe delay. Improved results are shown in Figure 3.8c.

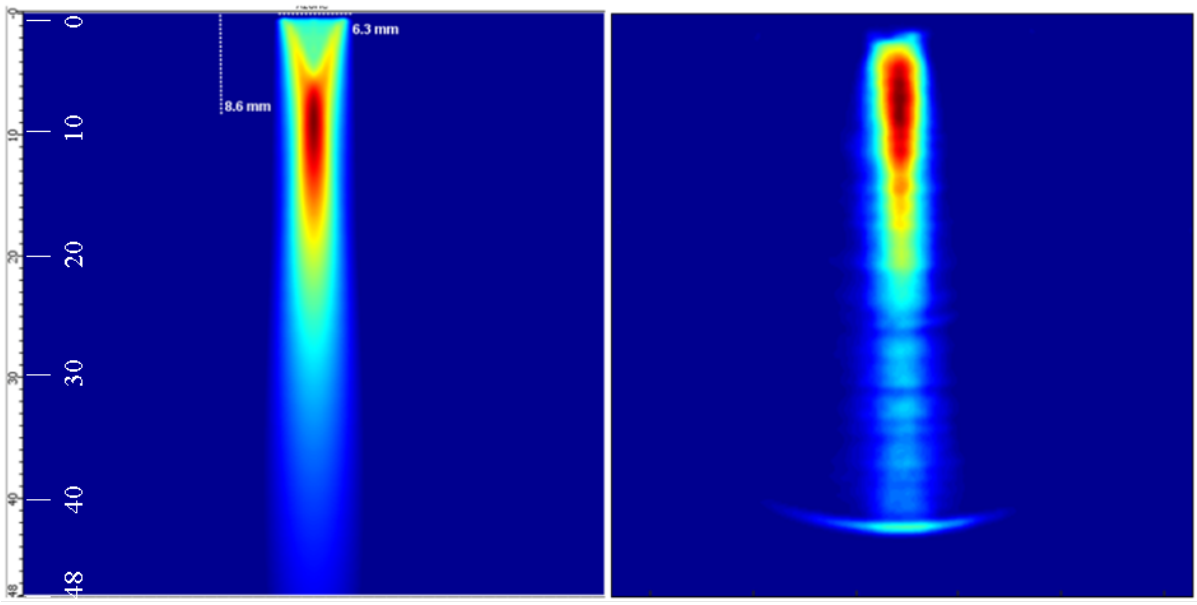

Figure 3.6 Beam profile of manual contact transducer from the CIVA elastodynamic simulation results and 8.6 mm near-field from Equation 3.1 (left), and the photoelastic image from Figure 3.2g (right). The length scale [mm] is equal and proportional. Figure previously published [Eason et al. (2015b)].

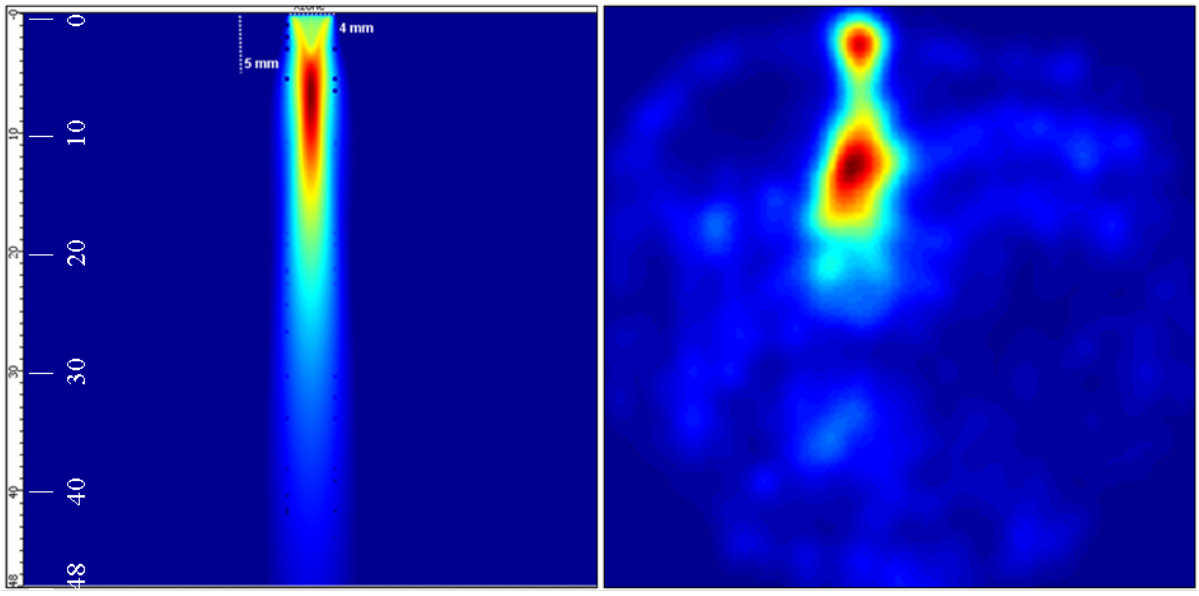

Figure 3.7 Beam profile of thick-film sol-gel transducer from the CIVA elastodynamic simulation results and 5.0 mm near-field from Equation 3.1 (left), and the photoelastic image from Figure 3.4g (right). The length scale [mm] is equal and proportional. Figure previously published [Eason et al. (2015b)].

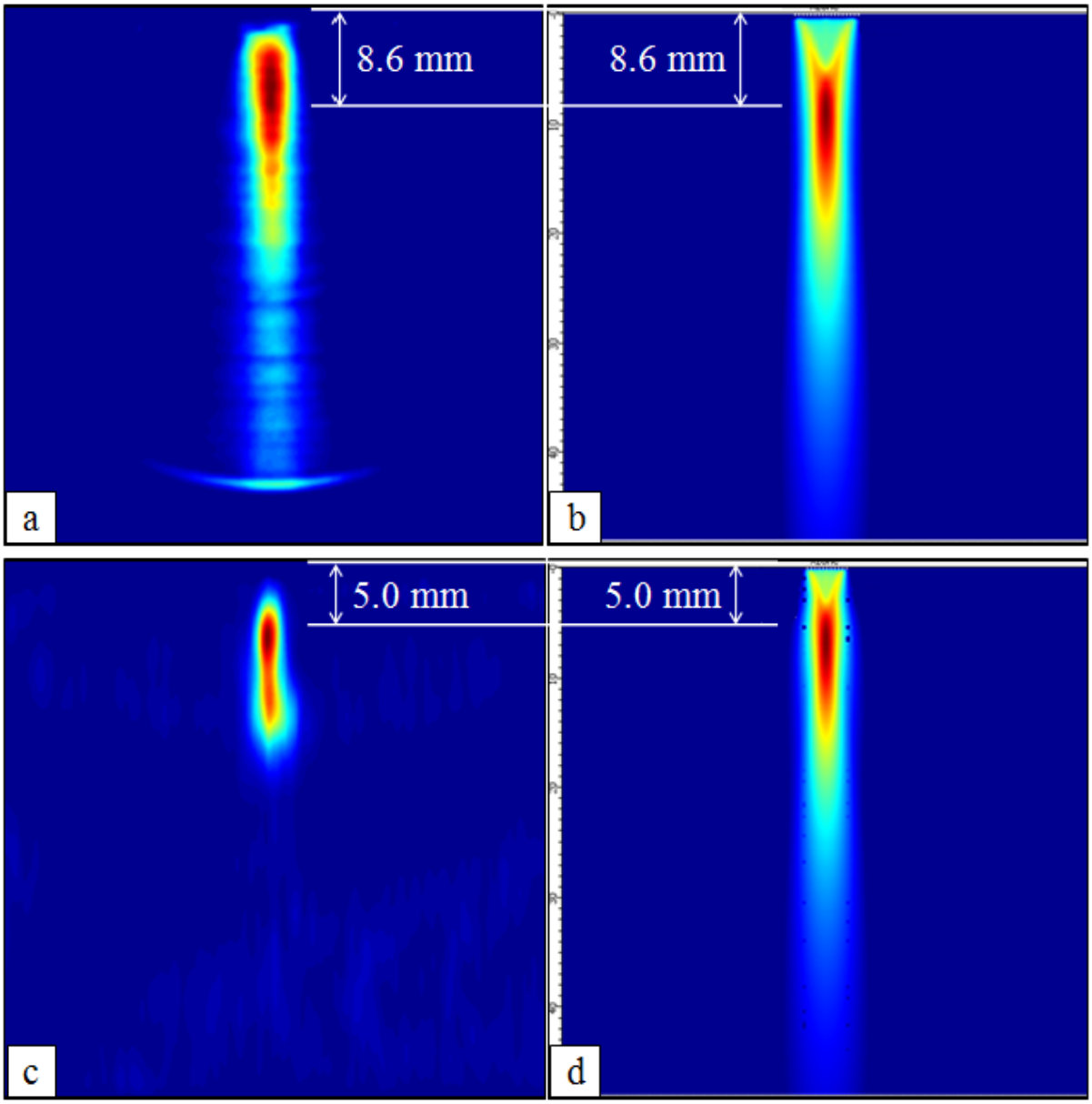

Figure 3.8 Comparison of the manual transducer calculated near-field of 8.6 mm with the a) photoelastic image and the b) CIVA elastodynamic model image. Comparison of the sol-gel transducer calculated near-field of 5.0 mm with the c) photoelastic image and the d) CIVA elastodynamic model image. Figure previously published [Eason et al. (2016b)].

3.4 Summary

This chapter provided a description and review of prior work on sol-gel sensors, addressed an acoustic/electric circuit approach to characterize thick-film air backed transducers, and presented a photoelastic imaging technique to characterize the incident beam profile of such transducers. The generated beam profile from a calculated near-field, elastodynamic simulation, and photoelastic imaging technique match well for both manual contact transducer and thick-film sol-gel transducer. The next few chapters discuss characterization of the reflected and scattered elastic waves from corrosion surfaces.

CHAPTER 4. ELASTIC WAVE SCATTERING - FLAT SURFACE - CASES

Various ultrasonic bulk wave bounding case scenarios for a corrosion pitting contact measurement application are presented to validate the quasi-plane wave approximation. Each case is modeled using CIVA [Calmon et al. (2006)] semi-analytical elastodynamic commercial ultrasonic simulation tool using Auld reciprocity, ray tracing, and a pencil beam model technique.

4.1 Modeling Results

The test specimen is a steel plate of 100 mm wide, 100 mm long, and either 3 mm or 25 mm thick with a density of 7.8 gm/cm^3, longitudinal wave speed of 5900 m/s, and a shear wave speed of 3230 m/s. The probe is a single circular element flat contact longitudinal wave transducer of diameters 1 mm or 10 mm. The probe has a flat 0 degree wedge of the same diameter as the transducer, thickness of 0.01 mm, and same material properties as the test specimen. The transducer has 100% bandwidth at -3 dB with a central frequency of 1 MHz or 10 MHz with a Gaussian filter and 512 sampling points per signal with a 0 degree phase offset. The coupling material is water with a density of 1 gm/cm^3 and longitudinal wave speed of 1483 m/s. The bottom and top surface medium is air with a density of 0.001 gm/cm^3 and longitudinal wave speed of 3330 m/s. The simulation uses a two dimensional computation of longitudinal and shear waves considering direct mode, mode conversion, back-wall reflection, and internal reflection. The computation zone has a 0.05 mm step size for the 3 mm thickness and a 0.25 mm step size for the 25 mm thickness. Neither attenuation nor noise is considered. A total of eight bounding cases are shown as spatial amplitude plots for various points in time and as the maximum spatial amplitude among all points in time in Figures 4.1-4.8.

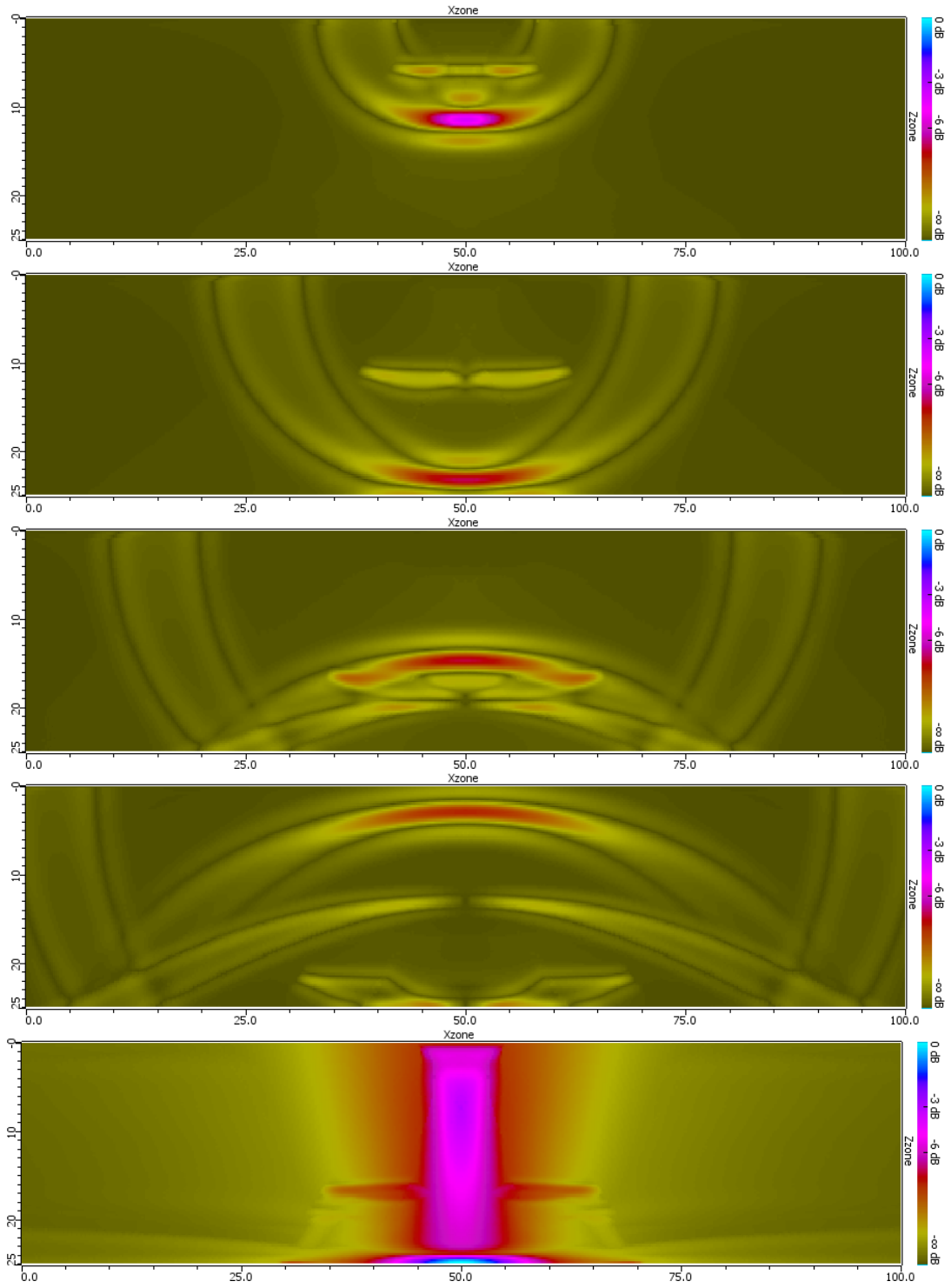

Figure 4.1 Simulation results for 25 mm thick specimen, 10 mm probe diameter, and 1 MHz center frequency showing amplitude at 2 μs, 4 μs, 6 μs, 8 μs, and maximum amplitude over time.

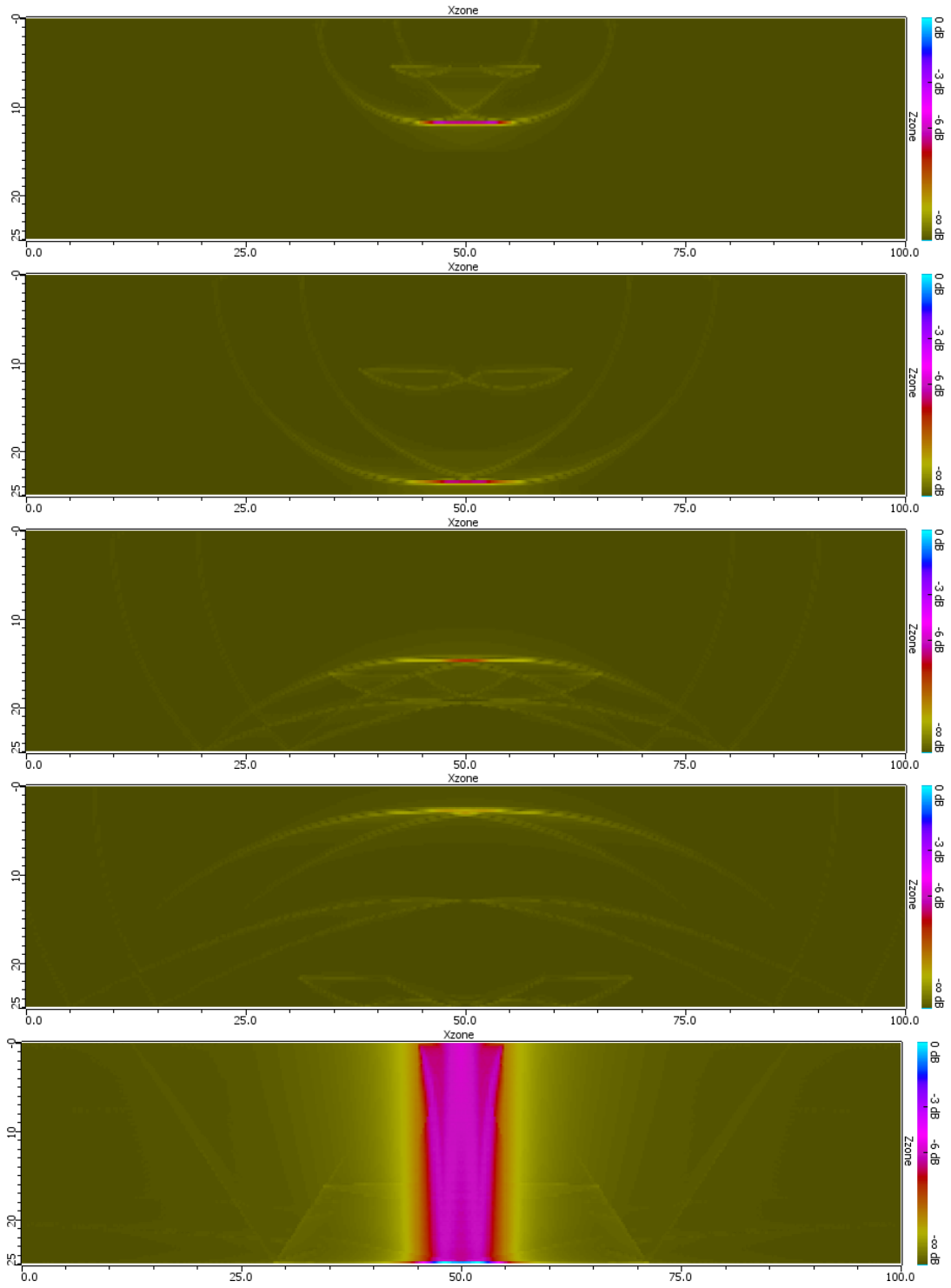

Figure 4.2 Simulation results for 25 mm thick specimen, 10 mm probe diameter, and 10 MHz center frequency showing amplitude at 2 μs, 4 μs, 6 μs, 8 μs, and maximum amplitude over time.

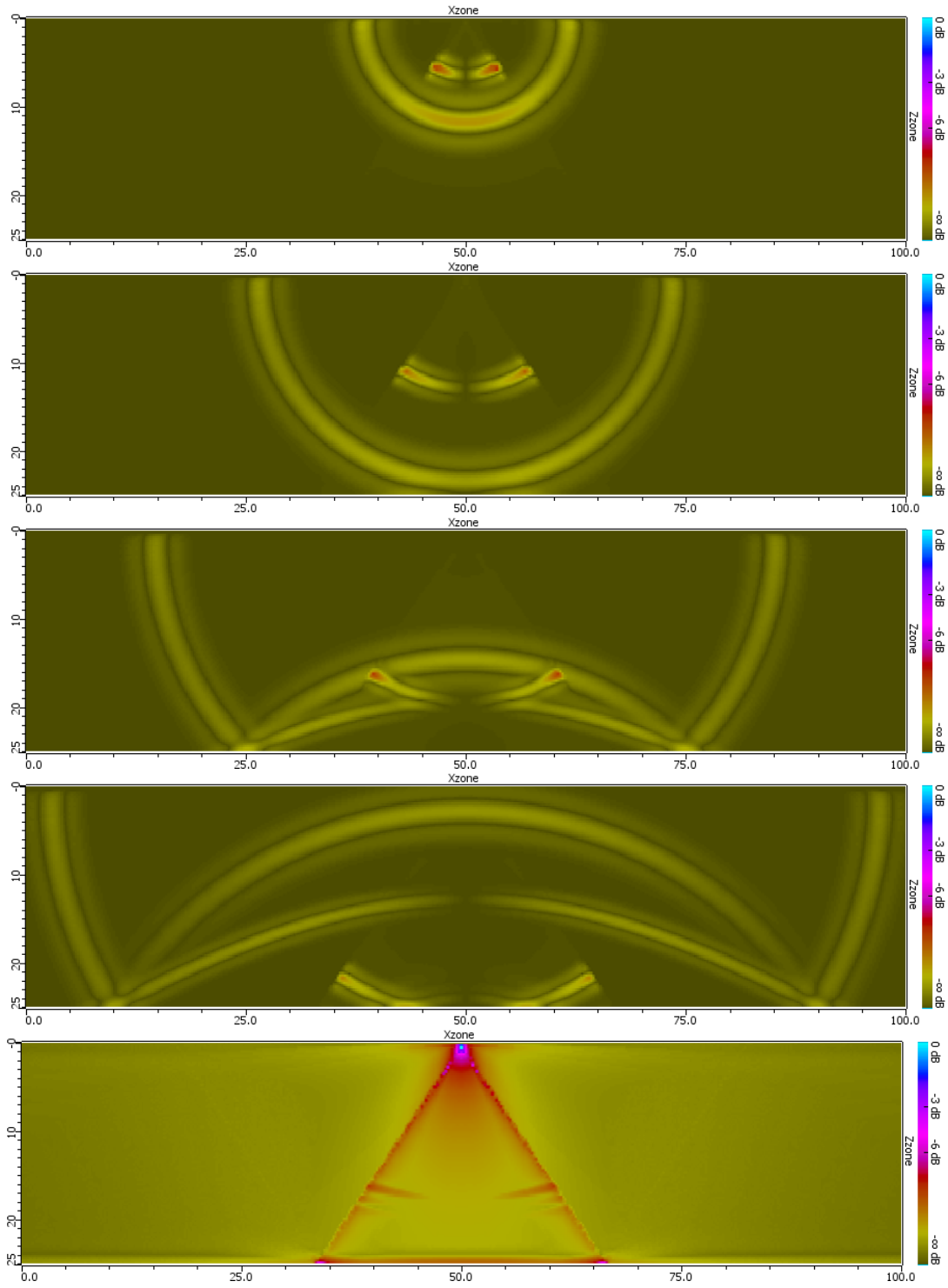

Figure 4.3 Simulation results for 25 mm thick specimen, 1 mm probe diameter, and 1 MHz center frequency showing amplitude at 2 μs, 4 μs, 6 μs, 8 μs, and maximum amplitude over time.

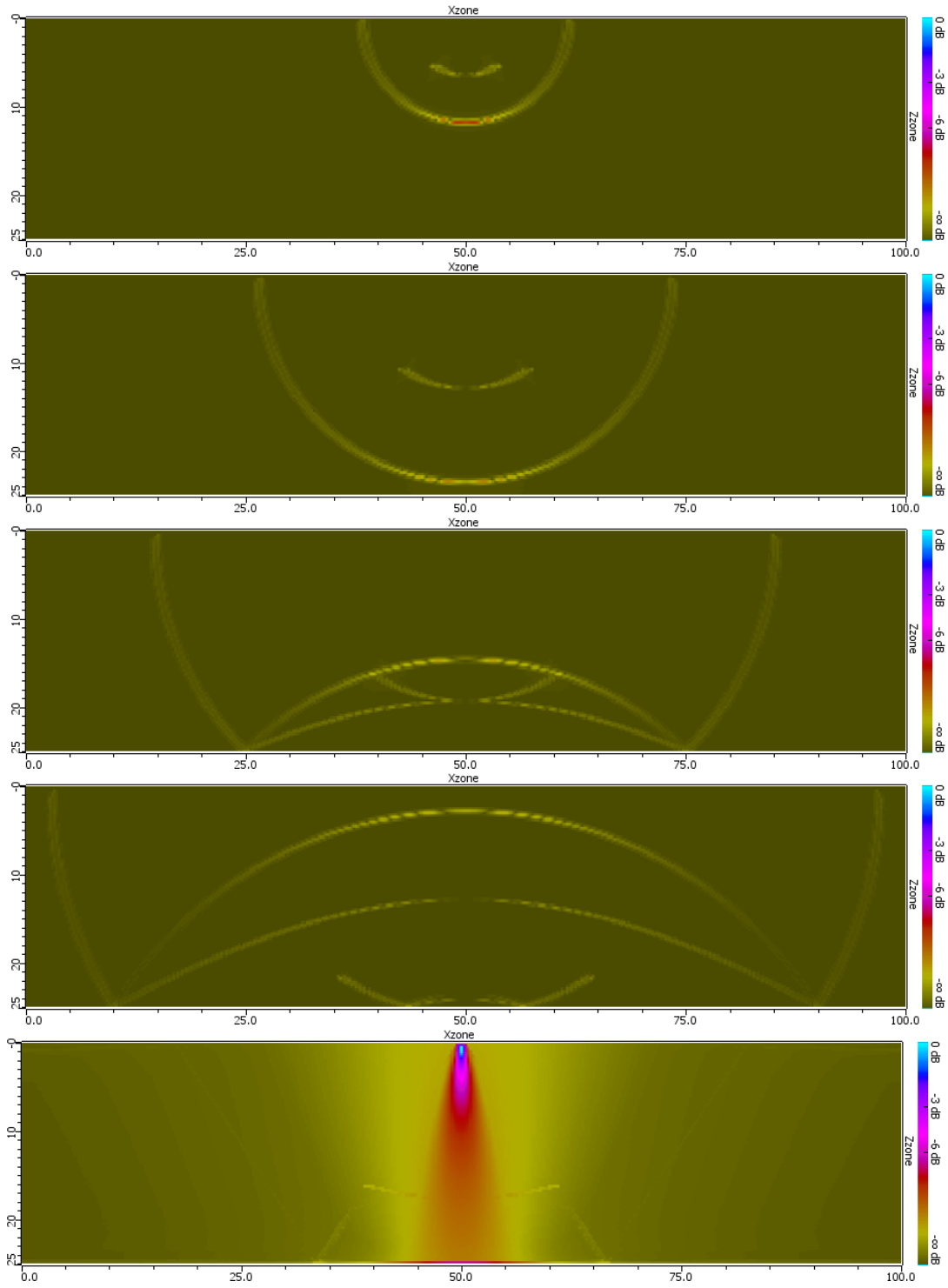

Figure 4.4 Simulation results for 25 mm thick specimen, 1 mm probe diameter, and 10 MHz center frequency showing amplitude at 2 μs, 4 μs, 6 μs, 8 μs, and maximum amplitude over time.

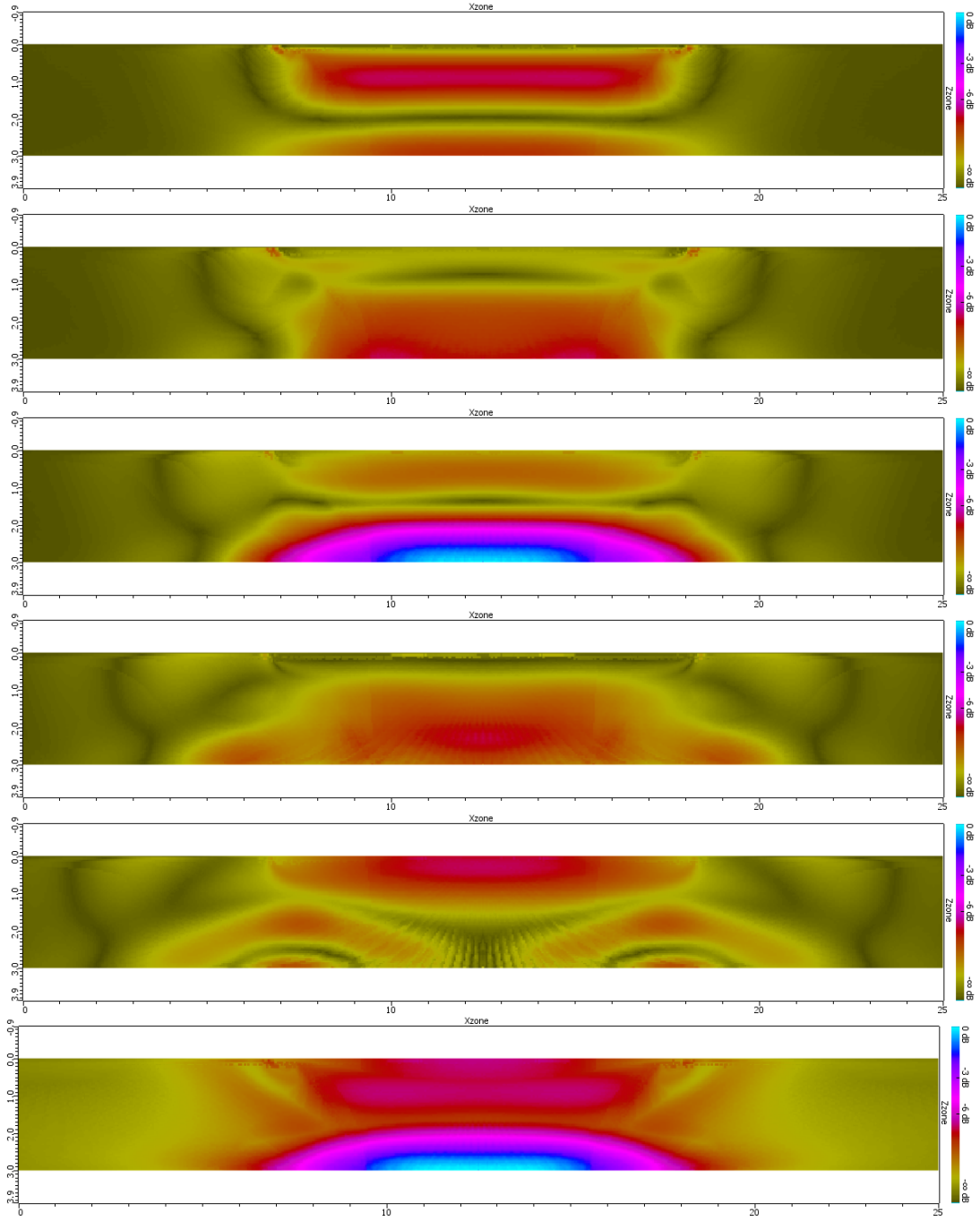

Figure 4.5 Simulation results for 3 mm thick specimen, 10 mm probe diameter, and 1 MHz center frequency showing amplitude at 0.2 μs, 0.4 μs, 0.6 μs, 0.8 μs, 1.0 μs and maximum amplitude over time.

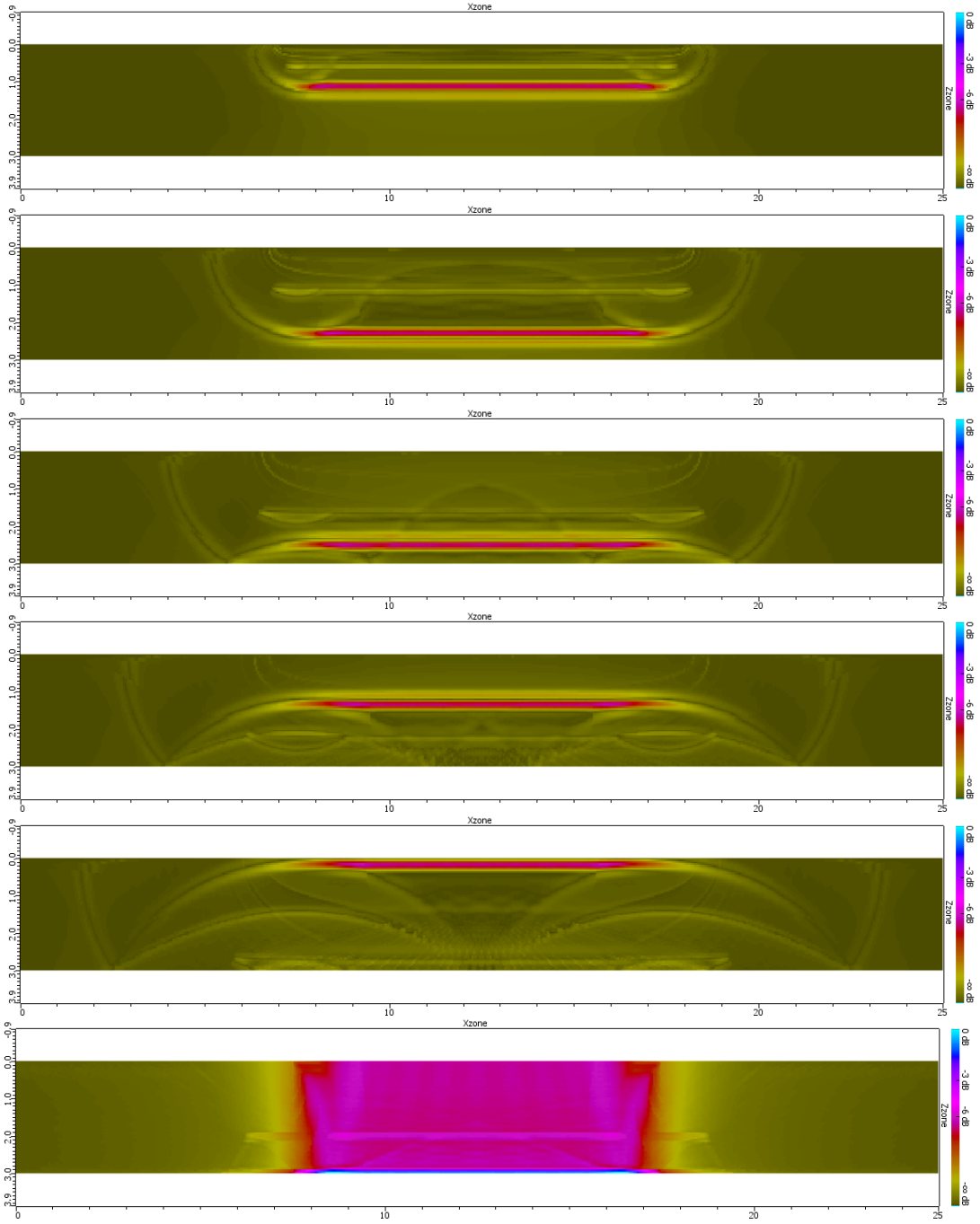

Figure 4.6 Simulation results for 3 mm thick specimen, 10 mm probe diameter, and 10 MHz center frequency showing amplitude at 0.2 μs, 0.4 μs, 0.6 μs, 0.8 μs, 1.0 μs and maximum amplitude over time.

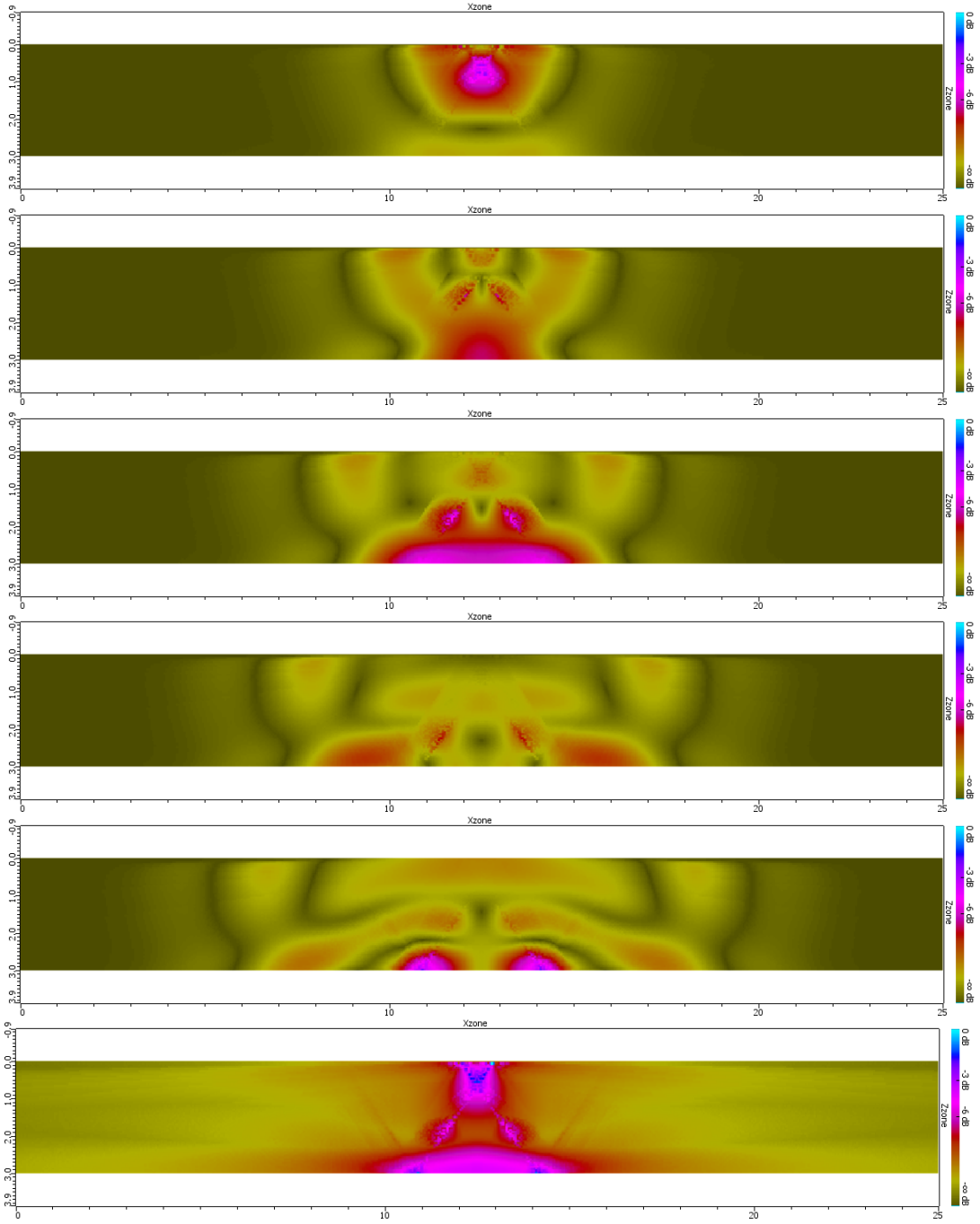

Figure 4.7 Simulation results for 3 mm thick specimen, 1 mm probe diameter, and 1 MHz center frequency showing amplitude at 0.2 μs, 0.4 μs, 0.6 μs, 0.8 μs, 1.0 μs and maximum amplitude over time.

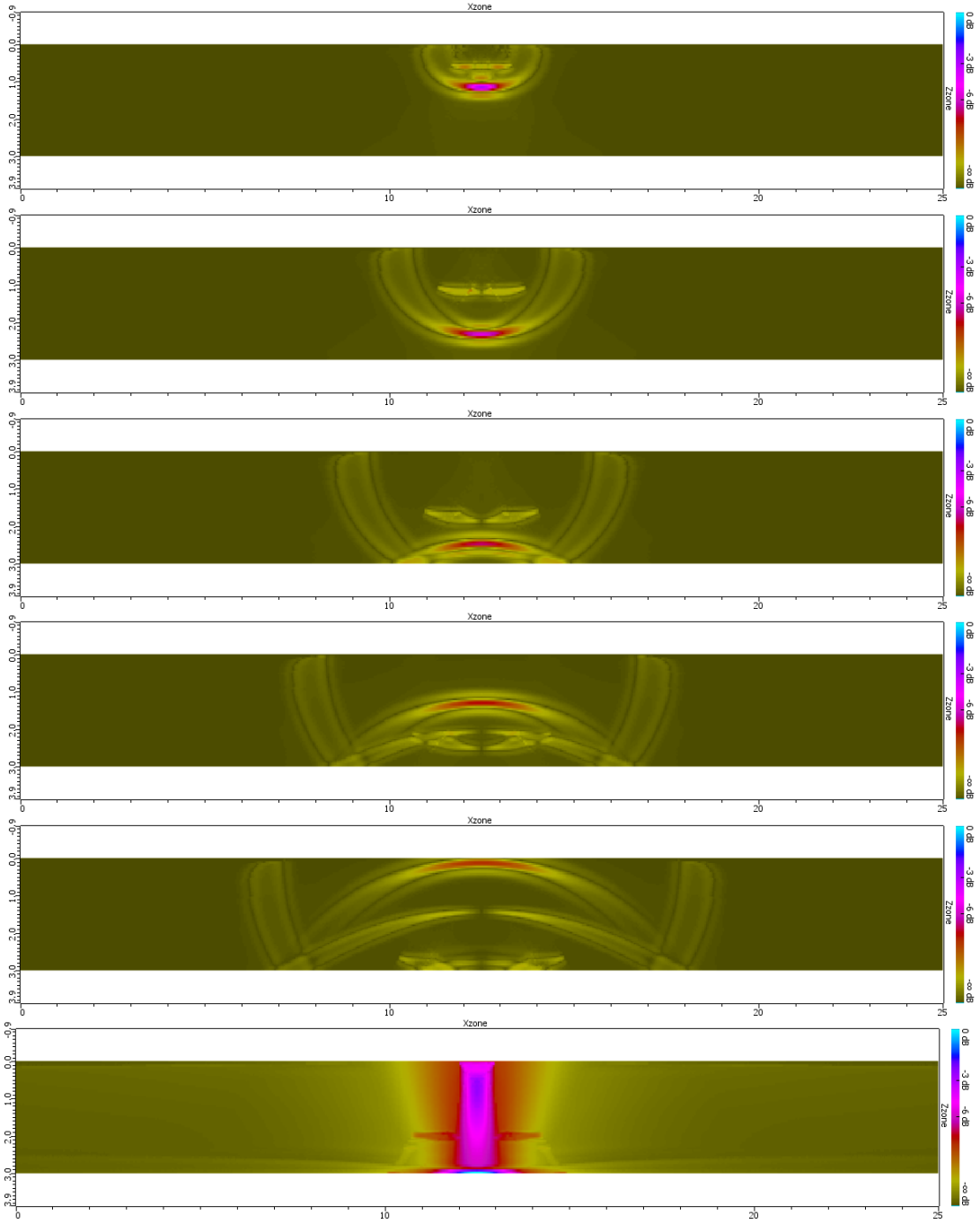

Figure 4.8 Simulation results for 3 mm thick specimen, 1 mm probe diameter, and 10 MHz center frequency showing amplitude at 0.2 μs, 0.4 μs, 0.6 μs, 0.8 μs, 1.0 μs and maximum amplitude over time.

4.2 Summary

A total of eight bounding case scenarios for bulk wave propagation in a steel corrosion monitoring application are presented as CIVA semi-analytical simulation results. The limits of the quasi-plane wave approximation is understood and used for the scattering theory work in Chapters 5-7.

CHAPTER 5. ELASTIC WAVE SCATTERING - FLAT SURFACE - SINGLE FLAW

In many cases in chemical plants an ultrasonic instrument is used to measure pipe wall thickness. Such measurements give a nominal wall thickness that may not adequately report and reflect discrete features such as some forms of pitting corrosion. Adequate characterization of the topography of corrosion on the inner surface of pipes remains a challenge. Improving this characterization of wall thickness and corrosion profile may improve safe operating pressure estimations and remaining life assessments.

A canonical problem is the characterization of a hemispherical pit in the inner surface of a pipe. Past studies have used numerical models to analyze this geometry. Description of elastic wave scattering by individual pits with an analytical solution, has until recently been elusive. Work in the seismology community has however proposed a solution to give surface displacements near a canyon or valley for various wave modes [Lee and Zhu (2014)].

The foundational analytical theory for elastic wave scattering from an embedded spherical cavity is reviewed. An approach gave a new closed-form full-frequency analytical scattering theory for normally incident longitudinal wave modes onto a three dimensional hemispherical canyon [Lee and Zhu (2014)]. This approach is extended to generate new half-space far-field scattering amplitude terms for a single hemispherical pit geometry representative of isolated pitting corrosion. The resulting data are presented in a wavelength to feature scale in ka (wavenumber space) where canyon and corrosion pit to wavelength relationships are similar.

Model results were then tested against experimental data. The experimental data are put into the framework and modality for extracting far-field scattering amplitude theoretical values by applying principals from the Thompson-Gray measurement model [Thompson and Gray (1983); Schmerr and Song (2007); Schmerr (2016)]. The new theory is for the full-

frequency *ka* range, however measurements are focused on the mid-frequency scattering region, which is of particular interest as it is between that covered by relatively low-frequency (long-wavelength) perturbation solutions and relatively high-frequency (short-wavelength) ray theory. Experimental attenuation data are measured and reported that are in good agreement with literature values. Modeling results are then compared with experimental scattering amplitudes in the 6-10 *ka* scattering regime for the case of a 2 mm diameter hemispherical pit in a flat steel block.

5.1 Background

The geometry of a hemispherical pit in a plate and canyon/valley in half-spaces have been studied by the NDE and seismology communities respectively for various incident wave modes to investigate scattering and surface displacement behavior. In seeking solutions to canonical problems, a range of geometries are of interest and several are shown in Figure 2.1. In seeking analytical solutions, attention first considered the spherical cavity, remote from a far surface. Attention then considered the flat bottom hole and moved to address the hemispherical pit, while still recognizing that the ultimate challenge is the general rough surface. A general review of elastic waves in solids that includes a section on diffraction and scattering of elastic waves is provided [Pao (1983)]. Two specific geometries are considered, the embedded spherical cavity and the single hemispherical pit.

5.1.1 Embedded Spherical Cavity

The earliest work on elastic (vector) wave scattering from a spherical inclusion [Clebsch (1863)] preceded the foundational treatise by Rayleigh that addressed, among other topics, impinging acoustic (scalar) plane waves on spherical and circular cylindrical obstacles [Rayleigh (1877)]. Sezawa later described acoustic and elastic wave scattering by a variety of rigid and cavity objects of circular cylindrical, elliptical cylindrical, and spherical shape [Sezawa (1927)].

The theory advanced when Ying and Truell derived the analytical solution for elastic scattering of an incident longitudinal wave on an isotropically elastic sphere [Ying and Truell (1956)] that was then followed by the derivation for the case of an incident shear wave [Einspruch et al.

(1960)]. Scattering cross section results were subsequently presented as a function of normalized wavelength for a selection of materials [Johnson and Truell (1965); Kraft (1971)]. Pao and Mow then presented a more elegant matrix form with common terms among the general elastic solution and the specific rigid, cavity, fluid filled sphere, and acoustic scattering solutions [Pao and Mow (1962, 1963); Mow and Pao (1971)]. This matrix form is now the common notation for the wave coefficient separation of variables solution for scattering from an elastic sphere in an elastic medium [Graff (1975); Schmerr (2016)] with many examples in the literature comparing analytical, experimental, and numerical results [Zhang and Bond (1989); Ness (1994)]. In reviewing the literature, early papers do contain some inconsistencies in some equations; more recently, an attempt was made to review and re-derive the analytical solution for scattering of elastic waves by a single spherical obstacle [Avila-Carrera and Sanchez-Sesma (2006)].

5.1.2 Single Hemispherical Pit

Trifunac first presented a closed-form analytical solution for the normal incident in-plane shear horizontal (SH) wave mode for a two dimensional geometry [Trifunac (1971, 1973)]. This problem was then addressed by Lee who formulated a wave equation coefficient matrix, which is then solved by truncation and inversion for the incident longitudinal, shear vertical, and shear horizontal wave modes for various incident angles for a three dimensional geometry [Lee (1978, 1982, 1984)]. Sanchez-Sesma et al. applied various iterations of a boundary integral method initially for the incident shear horizontal wave mode for a two dimensional geometry [Sanchez-Sesma and Esquivel (1979); Sanchez-Sesma and Rosenblueth (1979)], and later expanded this approach to the incident longitudinal and shear wave modes for various angles as well as the incident Rayleigh wave mode for a three dimensional geometry [Sanchez-Sesma (1983); Sanchez-Sesma and Campillo (1991); Sanchez-Sesma and Luzón (1995)]. Khair et al. applied a numerical approach using both finite element and boundary integral methods for the incident longitudinal and shear vertical wave modes with various incident angles for a three dimensional geometry [Khair et al. (1989a,b)].

Albach and Bond, were among the first to consider this geometry as an NDE problem for scattering by pitting corrosion [Albach and Bond (1990)]. They applied a boundary method for

the 60 degree incident longitudinal wave mode and the normal incident shear wave mode for a three dimensional geometry. Their data and that by Sanchez-Sesma were in good agreement. Related work by Zhu, Bond, and Albach [Zhu et al. (1992)] reported experimental measurements of surface displacements of the scattered far-field Rayleigh wave mode for the incident longitudinal wave mode for various incident angles. Since that time there seems to have been limited work on fundamental aspects of scattering by pitting/canyons.

In more recent work, Lee and Zhu have now reported a closed-form analytical expression for the wave equation coefficients obtained by using a superposition of two models with a coordinate system transform. This model only considers the odd orders of the spherical Bessel and Legendre Polynomial functions for a normally incident longitudinal wave mode for a three dimensional geometry [Lee and Zhu (2014)].

5.1.3 Scattering Amplitude Validation

Data in seismology have typically been reported in terms of surface displacements, given that local amplification effects near topography is a key topic of interest. Some studies have considered perturbation techniques for low ka values [Gilbert and Knopoff (1960)], and ray theory for high ka values [Lee and Langston (1983)]. The particular challenge is in the mid-frequency scattering regime.

To test the validity of new model data, the process to extract the theoretical far-field scattering amplitudes from measured or modeled experimental voltage response values can be completed using principals derived from the Thompson-Gray measurement model [Thompson and Gray (1983); Schmerr and Song (2007); Schmerr (2016)]. This approach is used to isolate the scattering source from the feature of interest, from other physical and experimental influences on the scattered data, which enables wavenumber space ka scattering amplitudes to be reported. For the case of a hemispherical pit, the scattering amplitude term is modified to account for the presence of a stress-free half-space [Eason et al. (2017a,b)].

5.2 Theory

The analysis for the scattering from a hemispherical pit is an extension of that for the spherical cavity and the present work has been reported in a series of publications [Eason et al. (2017a,b,c)].

5.2.1 Embedded Spherical Cavity

For the sake of completeness, the theory presented in this section has been summarized from previous work [Ying and Truell (1956); Johnson and Truell (1965); Pao and Mow (1963); Mow and Pao (1971); Schmerr (2016)] and is presented correcting inconsistencies and applying a common notation.

5.2.1.1 Wave Potential Model

Consider the spherical coordinates system shown in Figure 5.1 for a plane wave impinging on a spherical cavity. The elastic wave displacement vector $\mathbf{u}$ is described in Equation 5.1 with Φ as the longitudinal wave potential (not to be confused with the ϕ coordinate) and Ψ as the shear wave potential.

$$\mathbf{u} = \nabla\Phi + \nabla \times \left(\frac{\partial \Psi}{\partial \theta}\mathbf{e}_{\phi}\right) \tag{5.1}$$

The solution to Equation 5.1, considering a harmonically periodic wave, is shown in Equations 5.2 and 5.3 as the Helmholtz equations with k_l as the longitudinal wavenumber and k_s as the shear wavenumber as defined in Equations 5.4 and 5.5 with Λ_l as the longitudinal wavelength, Λ_s as the shear wavelength, ω as the angular frequency, ρ as the material density, and λ and μ as the Lamé parameters as defined in Equations 5.6 and 5.7 with c_l as the longitudinal wave speed and c_s as the shear wave speed.

$$\nabla^2\Phi + {k_l}^2\Phi = 0 \tag{5.2}$$

$$\nabla^2\Psi + {k_s}^2\Psi = 0 \tag{5.3}$$

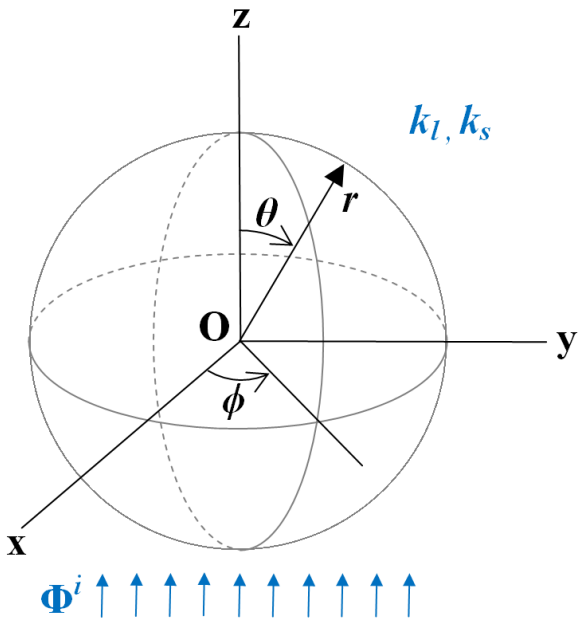

Figure 5.1 Coordinates for impinging plane wave on a spherical cavity. Figure previously published [Eason et al. (2017a)].

$$k_l = \frac{2\pi}{\Lambda_l} = \omega\sqrt{\frac{\rho}{\lambda + 2\mu}} \tag{5.4}$$

$$k_s = \frac{2\pi}{\Lambda_s} = \omega\sqrt{\frac{\rho}{\mu}} \tag{5.5}$$

$$\lambda = \rho\left({c_l}^2 - 2{c_s}^2\right) \tag{5.6}$$

$$\mu = \rho {c_s}^2 \tag{5.7}$$

For the case of an incident longitudinal wave, the total longitudinal wave potential Φ is a sum of the incident longitudinal wave potential Φ^i and the scattered longitudinal wave potential Φ^s as shown in Equation 5.8; the total shear wave potential Ψ consists of only the scattered shear wave potential Ψ^s as shown in Equation 5.9.

$$\Phi = \Phi^i + \Phi^s \tag{5.8}$$

$$\Psi = \Psi^s \tag{5.9}$$

The incident longitudinal wave potential Φ^i can be represented in planar coordinates as shown in Equation 5.10 with z as linear distance and $k_l\Phi_0$ as the incident wave amplitude. Alternatively, the incident longitudinal wave potential can be represented in spherical coordinates as shown in Equation 5.11 with j_n as the spherical Bessel function of the first kind of order n, and P_n as the 0th order Legendre polynomial of degree n. The scattered longitudinal and shear wave potentials are shown in Equations 5.12 and 5.13 with A_n as the longitudinal wave equation coefficient, B_n as the shear wave equation coefficient, and h_n as the spherical Bessel function of the third kind (which is also the spherical Hankel function of the first kind) of order n. The relation between Bessel and spherical Bessel functions are shown in Equations 5.14 and 5.15.

$$\Phi^i = \Phi_0 e^{i(k_l z - \omega t)} \tag{5.10}$$

$$\Phi^i = \Phi_0 \sum_{n=0}^{\infty} i^n \left(2n+1\right) j_n \left(k_l r\right) P_n \left(\cos\theta\right) \tag{5.11}$$

$$\Phi^s = \sum_{n=0}^{\infty} A_n h_n \left(k_l r\right) P_n \left(\cos\theta\right) \tag{5.12}$$

$$\Psi^s = \sum_{n=0}^{\infty} B_n h_n \left(k_s r\right) P_n \left(\cos\theta\right) \tag{5.13}$$

$$j_n \left(\zeta\right) = \sqrt{\frac{\pi}{2\zeta}} J_{n+\frac{1}{2}} \left(\zeta\right) \tag{5.14}$$

$$h_n \left(\zeta\right) = \sqrt{\frac{\pi}{2\zeta}} H_{n+\frac{1}{2}} \left(\zeta\right) \tag{5.15}$$

5.2.1.2 Scattering Cross-section

In characterization of a scattering response and in inverse problems, one metric or signature is the scattering cross-section γ which is the ratio of total scattered energy per unit time (power)

to the incident wave energy per unit time per unit area (intensity) as shown in Equation 5.16. The normalized scattering cross-section γ_N is shown in Equation 5.17 with a as the sphere radius.

$$\gamma = 4\pi \sum_{n=0}^{\infty} \frac{1}{2n+1} \left(|A_n|^2 + n\,(n+1)\,\frac{k_l}{k_s} |B_n|^2 \right) \tag{5.16}$$

$$\gamma_N = \frac{\gamma}{\pi a^2} \tag{5.17}$$

5.2.1.3 Wave Equation Coefficients

The boundary conditions for the case of a spherical cavity can be applied, and the wave equation coefficients A_n and B_n from Equation 5.16 have been defined [Ying and Truell (1956)] solely as a function of k_l and k_s in Equations 5.18-5.20.

$$A_n = (-i)^{(n-1)}\,(2n+1)\,\frac{1}{k_l}\frac{{A_n}'}{\Delta_n} \tag{5.18}$$

$$B_n = (-i)^{(n-1)}\,(2n+1)\,\frac{1}{k_l}\frac{2\,(n-1)\,(n+2) - (k_s a)^2}{k_l a}\frac{1}{\Delta_n} \tag{5.19}$$

$$\begin{aligned}
\begin{Bmatrix} {A_n}' \\ \Delta_n \end{Bmatrix} = {} & (k_s a)^2 \left((1-n)\,(2n+1) + \tfrac{1}{2}\,(k_s a)^2 \right) \begin{Bmatrix} j_n\,(k_l a) \\ h_n\,(k_l a) \end{Bmatrix} h_n\,(k_s a) \\
& + k_s a \left(2n\,(n-1)\,(n+2) - (k_s a)^2 \right) \begin{Bmatrix} j_n\,(k_l a) \\ h_n\,(k_l a) \end{Bmatrix} h_{n+1}\,(k_s a) \\
& + 2k_l a \left((n^2-1)\,(n+2) - (k_s a)^2 \right) \begin{Bmatrix} j_{n+1}\,(k_l a) \\ h_{n+1}\,(k_l a) \end{Bmatrix} h_n\,(k_s a) \\
& - 2\,(k_l a)\,(k_s a)\,(n-1)\,(n+2) \begin{Bmatrix} j_{n+1}\,(k_l a) \\ h_{n+1}\,(k_l a) \end{Bmatrix} h_{n+1}\,(k_s a)
\end{aligned} \tag{5.20}$$

A more elegant form of the wave equation coefficients utilize the relationship between stress and displacement as shown in Equation 5.21 in dyadic notation with $\boldsymbol{\sigma}$ as the stress tensor and $\mathbf{I}$ as the identity tensor. The boundary conditions for the case of a spherical cavity can be

applied such that the wave equation coefficients are alternatively defined in Equations 5.22-5.30 with the individual E matrix terms defined [Pao and Mow (1963); Mow and Pao (1971)] solely as a function of k_l and k_s.

$$\boldsymbol{\sigma} = \lambda \left(\nabla \cdot \mathbf{u}\right) \mathbf{I} + 2\mu \left(\nabla \mathbf{u} + \mathbf{u} \nabla\right) \tag{5.21}$$

$$\begin{bmatrix} E_{31} & E_{32} \\ E_{41} & E_{42} \end{bmatrix} \begin{bmatrix} A_n \\ B_n \end{bmatrix} = \Phi_0 \begin{bmatrix} E_3 \\ E_4 \end{bmatrix} \tag{5.22}$$

$$A_n = \Phi_0 \frac{E_{42}E_3 - E_{32}E_4}{E_{31}E_{42} - E_{32}E_{41}} \tag{5.23}$$

$$B_n = \Phi_0 \frac{E_{31}E_4 - E_{41}E_3}{E_{31}E_{42} - E_{32}E_{41}} \tag{5.24}$$

$$E_{31} = \left(n^2 - n - \frac{k_s^2 a^2}{2}\right) h_n \left(k_l a\right) + 2k_l a h_{n+1} \left(k_l a\right) \equiv E_{11}^{(3)} \tag{5.25}$$

$$E_{32} = -n \left(n+1\right) \left[\left(n-1\right) h_n \left(k_s a\right) - k_s a h_{n+1} \left(k_s a\right)\right] \equiv E_{12}^{(3)} \tag{5.26}$$

$$E_{41} = \left(n-1\right) h_n \left(k_l a\right) - k_l a h_{n+1} \left(k_l a\right) \equiv E_{41}^{(3)} \tag{5.27}$$

$$E_{42} = -\left(n^2 - 1 - \frac{k_s^2 a^2}{2}\right) h_n \left(k_s a\right) - k_s a h_{n+1} \left(k_s a\right) \equiv E_{42}^{(3)} \tag{5.28}$$

$$E_3 = -i^n \left(2n+1\right) \left[\left(n^2 - n - \frac{k_s^2 a^2}{2}\right) j_n \left(k_l a\right) + 2k_l a j_{n+1} \left(k_l a\right)\right] \equiv \frac{E_{11}^{(1)}}{-i^n \left(2n+1\right)} \tag{5.29}$$

$$E_4 = -i^n \left(2n+1\right) \left[\left(n-1\right) j_n \left(k_l a\right) - k_l a j_{n+1} \left(k_l a\right)\right] \equiv \frac{E_{41}^{(1)}}{-i^n \left(2n+1\right)} \tag{5.30}$$

5.2.1.4 Scattering Amplitude

For the case of the radial scattering of an incident longitudinal wave in the z direction, the normalized longitudinal wave far-field scattering amplitude $\mathbf{A}^{L;L}(\mathbf{e}_z;\mathbf{e}_r)$ and normalized shear wave far-field scattering amplitude $\mathbf{A}^{S;L}(\mathbf{e}_z;\mathbf{e}_r)$ are related to the incident wave amplitude $k_l\Phi_0$ and corresponding wave equation coefficients as a function of θ as shown in Equations 5.31 and 5.32 [Schmerr (2016)].

$$\mathbf{A}^{L;L}(\mathbf{e}_z;\mathbf{e}_r) = \left[\frac{1}{k_l\Phi_0}\sum_{n=0}^{\infty}(-i)^{n+1}A_nP_n(\cos\theta)\right]\mathbf{e}_r \tag{5.31}$$

$$\mathbf{A}^{S;L}(\mathbf{e}_z;\mathbf{e}_r) = \left[\frac{1}{k_l\Phi_0}\sum_{n=0}^{\infty}(-i)^{n+1}B_nP^1{}_n(\cos\theta)\right]\mathbf{e}_\theta \tag{5.32}$$

5.2.1.5 Solution Convergence

The analytical solution for the wave equation is in the form of an infinite series that will converge if solved with terms of sufficient order. Plots which show the converging solutions evaluated numerically have been presented in literature as a function of normalized wavelength [Johnson and Truell (1965); Kraft (1971)] from Equation 5.17. These solutions have been regenerated, and then over-layed on top of the classical plots as shown in Figures 5.2 and 5.3 [Eason et al. (2017c)]. The new data has converged and is in very close agreement with prior results; one exception in Figure 5.3 where the data appears to be inconsistent is an exchange in ˜Hypothetical Material˝ and ˜Polyethylene˝ for ka greater than 1.

In addition to the normalized scattering cross-section plots, the same method has been applied to demonstrate a converging solution in Figure 5.4 for the far-field scattering amplitude term from Equation 5.31. The current work used 50 terms to achieve convergence such that the maximum partial sum of the highest order of any solution was infinitesimally small at $< 10^{-30}$ for a ka value up to 20. The convergence shown in Figures 5.2-5.4 and agreement with prior data shown in Figures 5.2 and 5.3 validate the current code used for an embedded spherical cavity; the code used for a single hemispherical pit is very similar.

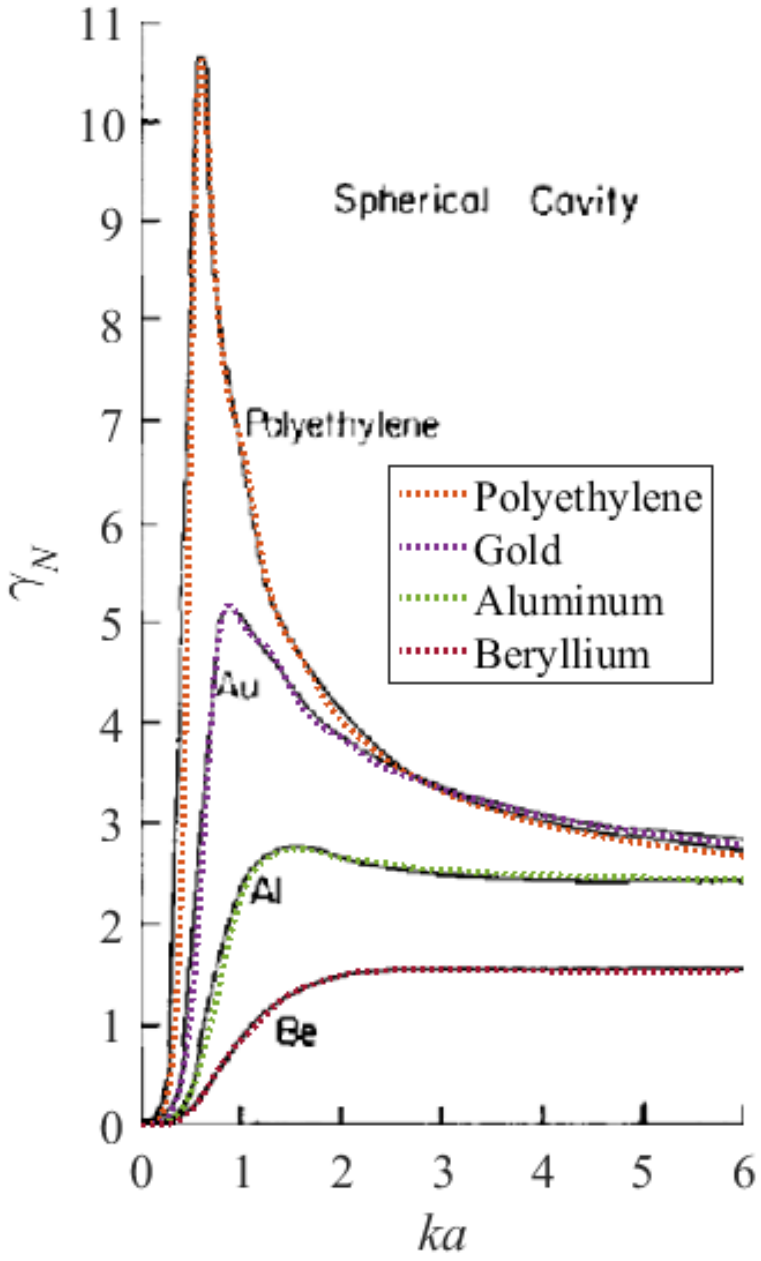

Figure 5.2 Normalized scattering cross-sectional area for an embedded cylinder for various elastic materials. Original plot [Johnson and Truell (1965)] overlayed with current author's solution to show convergence. Figure previously published [Eason et al. (2017a)].

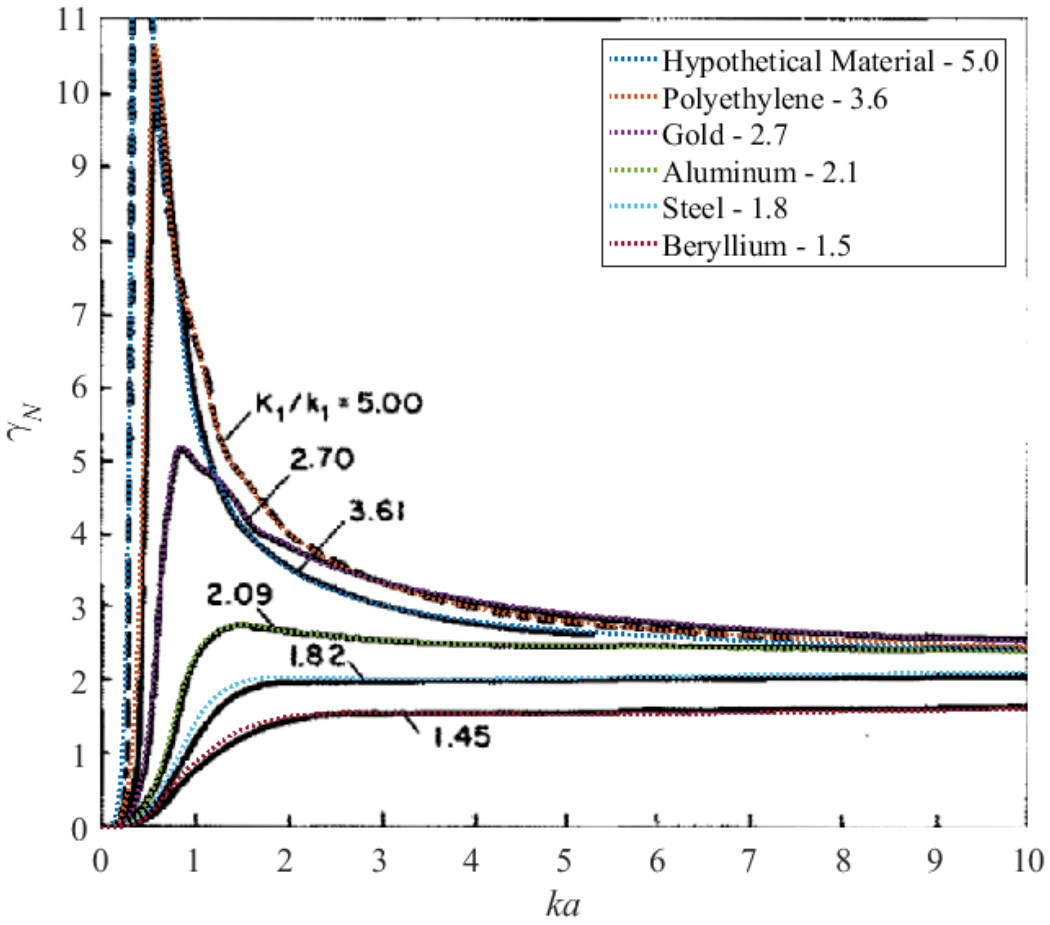

Figure 5.3 Normalized scattering cross-sectional area for an embedded cylinder for various elastic materials. Original plot [Kraft (1971)] overlayed with current author's solution to show convergence. Slight difference in "Hypothetical Material" and "Polyethylene" for ka greater than 1 may likely be an original plotting error. Listed values are material wavenumber ratio k_l/k_s. Figure previously published [Eason et al. (2017c)].

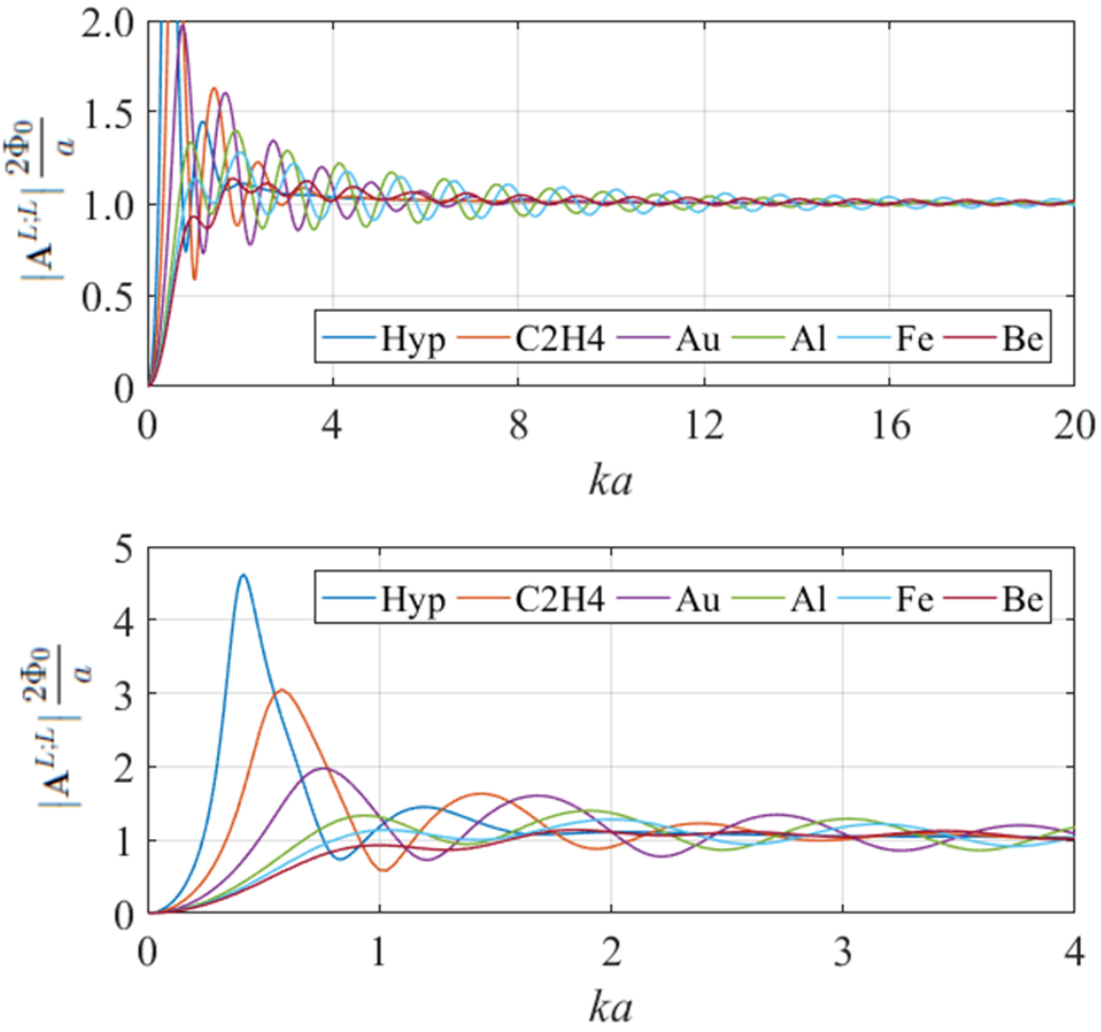

Figure 5.4 Existing normalized far-field scattering amplitude theory $\left|\mathbf{A}^{L;L}\right| \frac{2\Phi_0}{a}$ for an embedded spherical cavity from Equation 5.31. Solution shown to converge for various material wavenumber ratios k_l/k_s: Hypothetical Material "Hyp" = 5.0, Polyethylene "C2H4" = 3.6, Gold "Au" = 2.7, Aluminum "Al" = 2.1, Steel "Fe" = 1.8, and Beryllium "Be" = 1.5.

5.2.2 Single Hemispherical Pit

The theory presented in this section is derived from previously published work [Lee and Zhu (2014)]; there is an adjustment to two variable definitions ($E_{13}^{(3)} \rightarrow E_{32}$ and $E_{43}^{(3)} \rightarrow E_{42}$) to be consist with earlier work [Pao and Mow (1962, 1963); Mow and Pao (1971)], and also the introduction of a simpler notation to account for the odd integer index term. These closed-form analytical expressions were originally used in the seismology community to study surface displacements. The expressions are expanded here to give far-field scattering amplitude terms of interest to the NDE community for the case of a normally incident longitudinal wave for a three dimensional pit geometry.

5.2.2.1 Wave Potential Model

Consider two full-space models of an incident longitudinal wave on an embedded spherical cavity: an ‵upward″ incident wave model and a ‵downward″ incident wave model. The models are symmetric about the x-y plane as shown in Figures 5.5 and 5.6 with ‵u″ and ‵d″ subscripts for coordinate system and wave potential variables. The incident and scattered wave potentials are described in Equations 5.33-5.38 for the corresponding model spherical coordinates system.

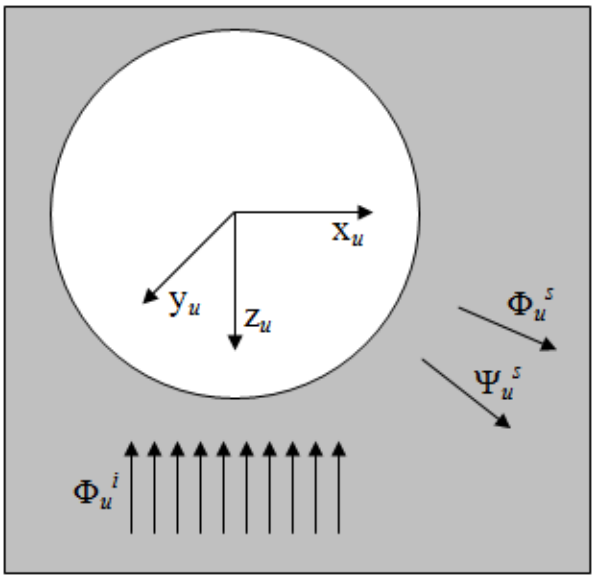

Figure 5.5 Upward incident longitudinal wave model for an embedded spherical cavity. Figure previously published [Eason et al. (2017a)].

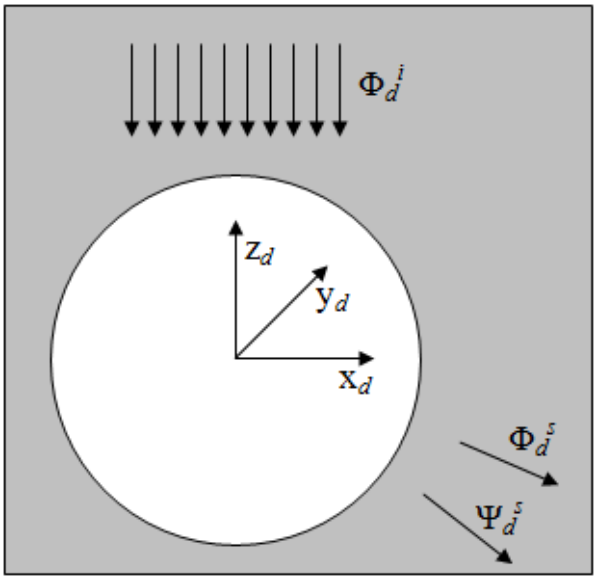

Figure 5.6 Downward incident longitudinal wave model for an embedded spherical cavity. Figure previously published [Eason et al. (2017a)].

$$\Phi_u{}^i = \Phi_0 \sum_{n=0}^{\infty} i^n \left(2n+1\right) j_n \left(k_l r_u\right) P_n \left(\cos\theta_u\right) \tag{5.33}$$

$$\Phi_u{}^s = \sum_{n=0}^{\infty} A_n h_n \left(k_l r_u\right) P_n \left(\cos\theta_u\right) \tag{5.34}$$

$$\Psi_u{}^s = \sum_{n=0}^{\infty} B_n h_n \left(k_s r_u\right) P_n \left(\cos\theta_u\right) \tag{5.35}$$

$$\Phi_d{}^i = \Phi_0 \sum_{n=0}^{\infty} i^n \left(2n+1\right) j_n \left(k_l r_d\right) P_n \left(\cos\theta_d\right) \tag{5.36}$$

$$\Phi_d{}^s = \sum_{n=0}^{\infty} A_n h_n \left(k_l r_d\right) P_n \left(\cos\theta_d\right) \tag{5.37}$$

$$\Psi_d{}^s = \sum_{n=0}^{\infty} B_n h_n \left(k_s r_d\right) P_n \left(\cos\theta_d\right) \tag{5.38}$$

The coordinate systems are transformed as described in Equations 5.39 and 5.40 resulting in new terms for the downward model longitudinal and shear scattered wave potentials as described in Equations 5.41 and 5.42.

$$r_d = r_u = r \tag{5.39}$$

$$\cos\theta_d = -\cos\theta_u = -\cos\theta \tag{5.40}$$

$$\Phi_d{}^s = \sum_{n=0}^{\infty} A_n h_n\left(k_l r\right)(-1)^n P_n\left(\cos\theta\right) \tag{5.41}$$

$$\Psi_d{}^s = \sum_{n=0}^{\infty} B_n h_n\left(k_s r\right)(-1)^n P_n\left(\cos\theta\right) \tag{5.42}$$

Now consider a half-space model shown in Figure 5.7 as a superposition of the two full-space upward and downward models. The resulting longitudinal and scattered wave potentials are described in Equations 5.43-5.48 as functions of the odd order terms of the spherical Bessel and Legendre functions [Lee and Zhu (2014)].

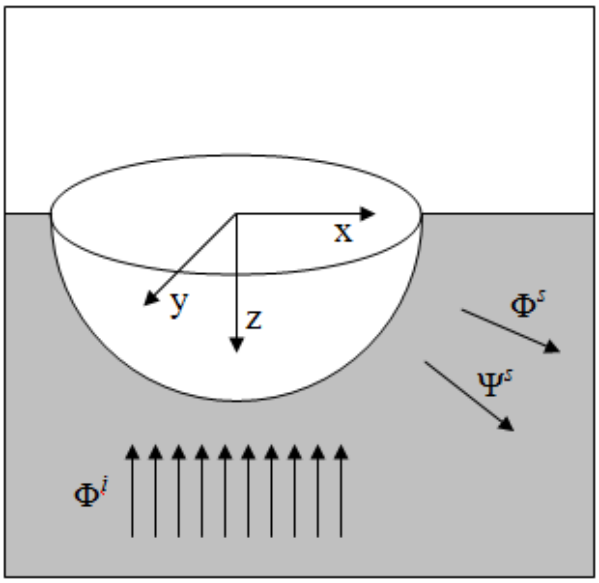

Figure 5.7 Incident longitudinal wave model on a hemispherical half-space. Figure previously published [Eason et al. (2017a)].

$$\Phi^s = {\Phi_u}^s - {\Phi_d}^s \tag{5.43}$$

$$\Phi^s = \sum_{n=0}^{\infty} A_n h_n\left(k_l r\right) P_n\left(\cos\theta\right) - \sum_{n=0}^{\infty} A_n h_n\left(k_l r\right)\left(-1\right)^n P_n\left(\cos\theta\right) \tag{5.44}$$

$$\Phi^s = \sum_{n=0}^{\infty} 2A_{2n+1} h_{2n+1}\left(k_l r\right) P_{2n+1}\left(\cos\theta\right) \tag{5.45}$$

$$\Psi^s = {\Psi_u}^s - {\Psi_d}^s \tag{5.46}$$

$$\Psi^s = \sum_{n=0}^{\infty} B_n h_n\left(k_s r\right) P_n\left(\cos\theta\right) - \sum_{n=0}^{\infty} B_n h_n\left(k_s r\right)\left(-1\right)^n P_n\left(\cos\theta\right) \tag{5.47}$$

$$\Psi^s = \sum_{n=0}^{\infty} 2B_{2n+1} h_{2n+1}\left(k_s r\right) P_{2n+1}\left(\cos\theta\right) \tag{5.48}$$

5.2.2.2 Wave Equation Coefficients

Appropriate zero normal stress and zero shear stress boundary conditions are applied on the half-space surface ($z = 0$, $\theta = \frac{\pi}{2}$) and on the pit surface ($r = a$) to determine solutions for the wave equation coefficients. An odd index term is applied as shown in Equation 5.49 to simplify notation with the resulting longitudinal and shear wave equation coefficients being shown in Equations 5.50 and 5.51 resolving some inconsistencies as well as making notation adjustments as compared to that previously reported [Lee and Zhu (2014)].

$$m = 2n + 1 \tag{5.49}$$

$$A_m = 2A_{2n+1} = 2\Phi_0 \left(\frac{E_{42}E_3 - E_{32}E_4}{E_{31}E_{42} - E_{32}E_{41}} \right)_m \tag{5.50}$$

$$B_m = 2B_{2n+1} = 2\Phi_0 \left(\frac{E_{31}E_4 - E_{41}E_3}{E_{31}E_{42} - E_{32}E_{41}} \right)_m \tag{5.51}$$

5.2.2.3 Scattering Amplitude

As a result of the superposition, it was determined that the corresponding half-space far-field scattering amplitudes should be normalized by an additional $k_l a$ term as shown in Equations 5.52 and 5.53 [Eason et al. (2017a,b)]. As a result of the half-space, the superscript notation "h" is added to distinguish these relationships from those in Equations 5.31 and 5.32.

$$\mathbf{A}^{L;L}\left(\mathbf{e}_z;\mathbf{e}_r\right)^{\mathrm{h}} = \left[\frac{1}{k_l a}\frac{1}{k_l \Phi_0}\sum_{n=0}^{\infty}(-i)^{m+1} A_m P_m\left(\cos\theta\right)\right]\mathbf{e}_r \tag{5.52}$$

$$\mathbf{A}^{S;L}\left(\mathbf{e}_z;\mathbf{e}_r\right)^{\mathrm{h}} = \left[\frac{1}{k_l a}\frac{1}{k_l \Phi_0}\sum_{n=0}^{\infty}(-i)^{m+1} B_m P^1{}_m\left(\cos\theta\right)\right]\mathbf{e}_\theta \tag{5.53}$$

This new theoretic relationship between the spherical cavity and the hemispherical pit half-space scattering amplitudes differs by a factor of $k_l a$ as is shown in Equation 5.54 [Eason et al. (2017a,b)] with simplified notation to consider only normal incident longitudinal and normal reflected longitudinal wave modes.

$$\mathbf{A}^{\mathrm{h}} = \frac{\mathbf{A}}{k_l a} \tag{5.54}$$

5.2.2.4 Solution Convergence

The far-field scattering amplitude for a hemispherical pit are shown in Figure 5.8 with the same materials and scaling shown for the embedded spherical cavity in Figure 5.4. A direct comparison of the embedded spherical cavity far-field scattering amplitude and the half-space hemispherical pit far-field scattering amplitude for steel material is shown in Figure 5.9.

The code used for the hemispherical pit is very similar to the code used for an embedded spherical cavity, the latter being validated by convergence and agreement with prior data. Similar to the embedded spherical cavity, the hemispherical pit work used 50 terms to achieve convergence such that the maximum partial sum of the highest order of any solution was infinitesimally small at $< 10^{-30}$ for a ka value up to 20. While convergence is achieved for the hemispherical pit code, unfortunately there is no prior scattering amplitude data available

for a comparison. Therefore, experimental work is required to generate new data for the hemispherical pit scattering amplitude model validation.

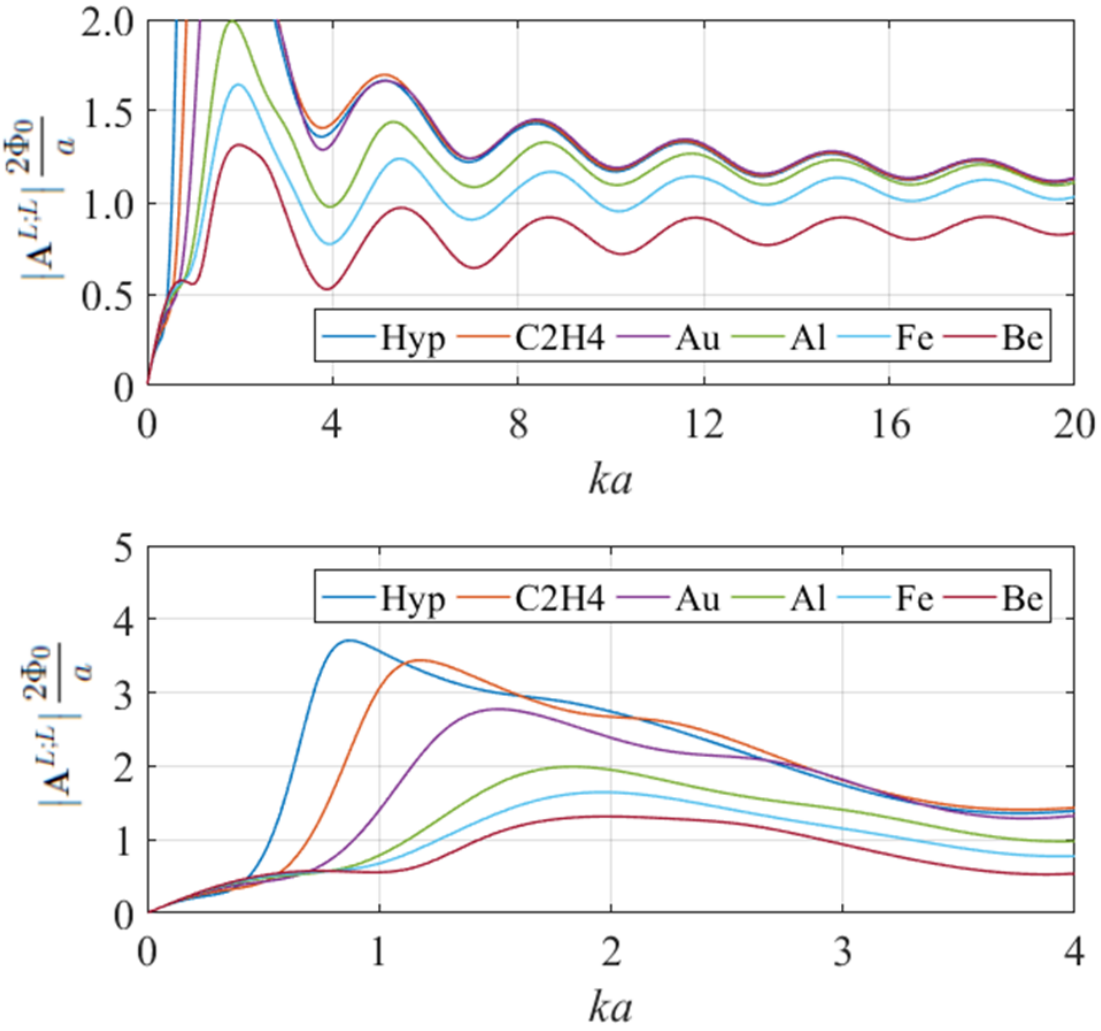

Figure 5.8 New normalized far-field scattering amplitude theory $\left|\mathbf{A}^{L;L}\right| \frac{2\Phi_0}{a}$ for a half-space hemispherical pit from Equation 5.52. Solution shown to converge for various material wavenumber ratios k_l/k_s: Hypothetical Material "Hyp" = 5.0, Polyethylene "C2H4" = 3.6, Gold "Au" = 2.7, Aluminum "Al" = 2.1, Steel "Fe" = 1.8, and Beryllium "Be" = 1.5.

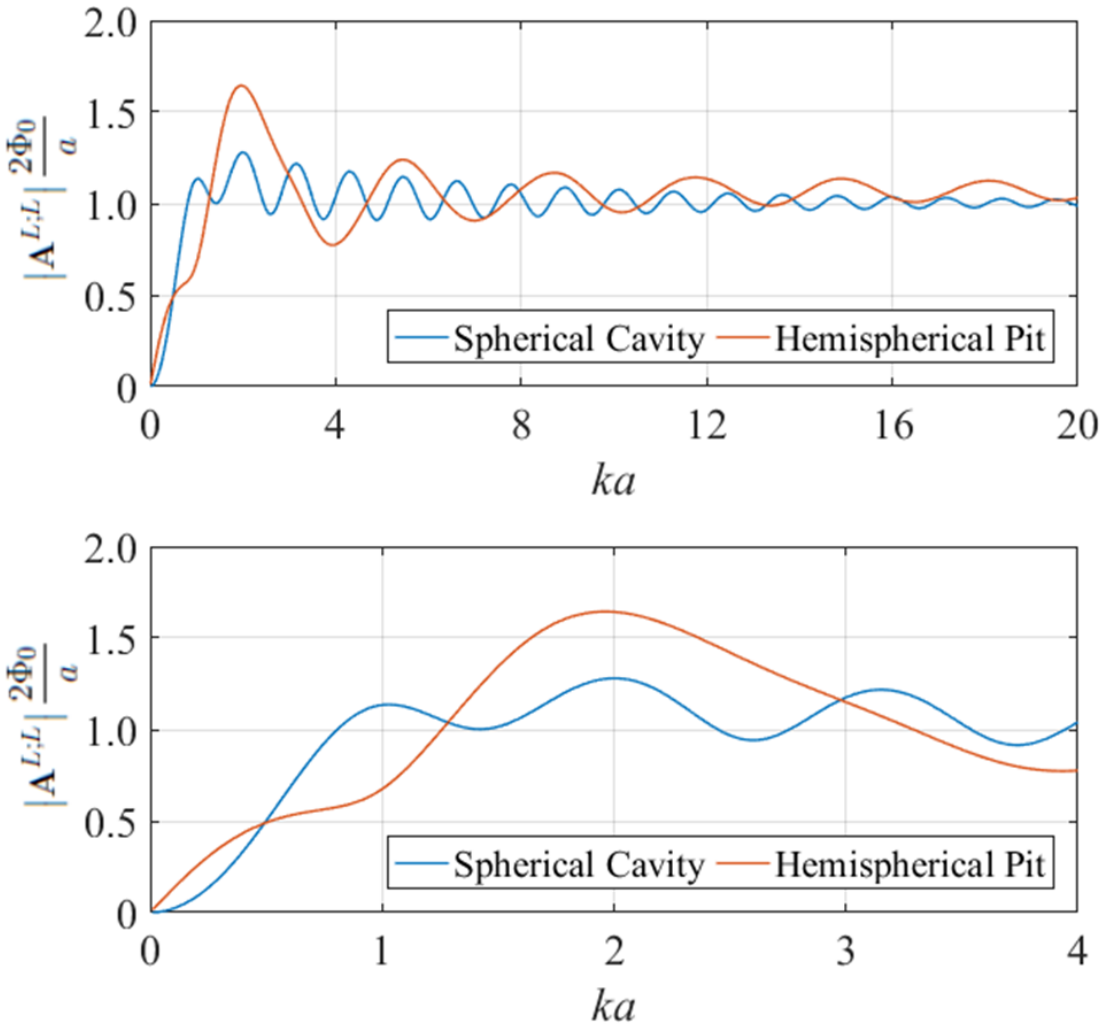

Figure 5.9 New normalized far-field scattering amplitude theory $\left|\mathbf{A}^{L;L}\right| \frac{2\Phi_0}{a}$ for an embedded spherical cavity from Equation 5.31, and for a half-space hemispherical pit from Equation 5.52. Solution shown to convergence for steel material with a wavenumber ratio $k_l/k_s = 1.8$.

5.2.3 Scattering Amplitude Validation

Any theory that provides scattering amplitude values can, potentially, be tested and validated by experimental measurements as is described in the follow process compiled and summarized from various chapters in Schmerr's texts [Schmerr and Song (2007); Schmerr (2016)] with an extension to the process specific to half-space scattering amplitude [Eason et al. (2017a)]. The hemispherical pit scattering amplitude model is tested and validated with experimental measurements collected and analyzed by the process described in this section.

5.2.3.1 Measurement System

An ultrasonic measurement system includes: a source voltage $V_i(\omega)$, that is transformed by the sound generation process. It is then altered by the acoustic/elastic interactions including wave propagation and scattering, further transformed by the sound reception process, and finally measured as a received output voltage $V_R(\omega)$. The system can be modelled in the frequency domain as shown in Equation 5.55 with the sound generation transfer function $t_G(\omega)$, the acoustic/elastic transfer function $t_A(\omega)$, and the sound reception transfer function $t_R(\omega)$ [Schmerr and Song (2007)].

$$V_R(\omega) = V_i(\omega)\, t_G(\omega)\, t_A(\omega)\, t_R(\omega) \tag{5.55}$$

One component of interest is the acoustic/elastic transfer function, and fortunately, the other terms in Equation 5.55 are combined into a single system function $s(\omega)$ as shown in Equation 5.56.

$$s(\omega) = V_i(\omega)\, t_G(\omega)\, t_R(\omega) \tag{5.56}$$

The received output voltage is then a product, in the frequency domain, of the acoustic/elastic transfer function and the system function as shown in Equation 5.57.

$$V_R(\omega) = t_A(\omega)\, s(\omega) \tag{5.57}$$

5.2.3.2 Acoustic/Elastic Transfer Function

In the case of an immersion pulse-echo front-wall inspection of a steel specimen in water, the reference acoustic/elastic transfer function can be described in Equation 5.58 with R_{12} described in Equation 5.59 and $\tilde{D}_l$ described in Equation 5.60. The acoustic/elastic transfer function can be determined from a transducer of radius a, at a distance D from an elastic material (steel) of density ρ_2 and longitudinal wave speed c_{l2}, and water material properties: density ρ_1, wave speed c_{l1}, wavenumber $k_{l1} = \frac{\omega}{c_{l1}}$, and frequency dependent attenuation $\alpha_1(\omega)$ or $\alpha_1(f)$. J_0 is the zeroth order Bessel function of the first kind, and J_1 as the first order Bessel function of the first kind.

$$t_A(\omega) = \tilde{D}_l\left(\frac{k_{l1}a^2}{2D}\right) R_{12} e^{2ik_{l1}D} e^{-2\alpha_1(f)D} \tag{5.58}$$

$$R_{12} = \frac{\rho_2 c_{l2} - \rho_1 c_{l1}}{\rho_2 c_{l2} + \rho_1 c_{l1}} \tag{5.59}$$

$$\tilde{D}_l(u) = 2\left[1 - e^{iu}\left(J_o(u) - iJ_1(u)\right)\right] \tag{5.60}$$

5.2.3.3 System Function

The system function can be determined with an experimental reference measurement from the measured voltage $V_R^{ref}(\omega)$ and reference acoustic/elastic transfer function $t_A(\omega)$ as shown in Equation 5.61 based on a division of terms from Equation 5.57. The structure of Equation 5.61 is a Weiner filter necessary to remove the large difference obtained when dividing two small numbers. The ϵ_s is a scalar value to represent a percentage of the maximum signal amplitude of the divisor term; this can be related to signal noise.

$$s(\omega) = \frac{V_R^{ref}(\omega)\, t_A^{ref^*}(\omega)}{\left|t_A^{ref}(\omega)\right|^2 + {\epsilon_s}^2 \max\left\{\left|t_A^{ref}(\omega)\right|^2\right\}} \tag{5.61}$$

The system function $s(\omega)$ and system efficiency factor $\beta(\omega)$ are proportional for a pulse-echo configuration using the same transducer for generation and reception as shown in Equation 5.62.

$$s(\omega) = \frac{1}{2}\beta(\omega) \tag{5.62}$$

5.2.3.4 Reference Spectrum

Once the system function or system efficiency factor have been determined from an initial calibration experimental reference measurement, then the measurement of the hemispherical pit on the back-wall can be completed. In this case, the response voltage $V_R(\omega)$ is related to the reference spectrum $G(\omega)$, scattering amplitude $A(\omega)$, and reference flaw length L (spherical flaw radius) as shown in Equation 5.63.

$$V_R(\omega) = G(\omega)\frac{A(\omega)}{L} \tag{5.63}$$

The reference spectrum is as defined in Equation 5.64 with $E(\omega)$ defined in Equation 5.65 for a pulse-echo configuration with an incident beam such that the quasi-plane wave approximation is valid as described in Chapter 4. For this case, the flaw is small enough such that beam variations across the flaw surface can be neglected with $\hat{V}_0^{(1)}$ as the incident velocity field and $Z_r^{T;a}$ as the transducer radiation impedance in water further described in Equation 5.66.

$$G(\omega) = s(\omega)E(\omega) \tag{5.64}$$

$$E(\omega) = \left[\hat{V}_0^{(1)}(\omega)\right]^2\left[\frac{4\pi\rho_2 c_{l2}}{-ik_{l2}Z_r^{T;a}}\right] \tag{5.65}$$

$$Z_r^{T;a} = \rho_1 c_{l1}\pi a \tag{5.66}$$

In an immersion configuration on an elastic solid specimen, the incident velocity field $\hat{V}_0^{(1)}(\omega)$ is described in Equation 5.67 with $\alpha_{l2}(\omega)$ as frequency dependent longitudinal wave mode attenuation in the elastic solid, z_2 as the elastic solid specimen thickness, and $\frac{V_{li}}{v_0}$ as the

ideal velocity field at the flaw location normalized by the normal velocity v_0 on the face of the transducer.

$$\hat{V}_0^{(1)}(\omega) = e^{-\alpha_1(\omega)D} e^{-\alpha_{l2}(\omega)z_2} \left(\frac{V_{li}}{v_0}\right) \tag{5.67}$$

The ideal velocity field $\frac{V_{li}}{v_0}$ from Equation 5.67 is the velocity field for a viscosity-free ideal fluid, neglecting any attenuation material losses. At an acoustic impedance interface, without tangential components of the velocity field, the normal velocity field $\mathbf{v} \cdot \mathbf{n}_s$ is related to the normal derivative of the pressure field $\nabla p \cdot \mathbf{n}_s$ as shown in Equation 5.68 [Schmerr and Song (2007)] with p as the pressure, $\mathbf{n}_s$ as the unit normal to the interface, ρ_0 as the material density, $\mathbf{u}$ as the displacement vector, and $\mathbf{v}$ as the velocity vector.

$$-\nabla p \cdot \mathbf{n}_s = \rho_0 \frac{\partial^2 (\mathbf{u} \cdot \mathbf{n}_s)}{\partial t^2} = \rho_0 \frac{\partial (\mathbf{v} \cdot \mathbf{n}_s)}{\partial t} \tag{5.68}$$

5.2.3.5 Multi-Gaussian Beam Model

The ideal velocity field through a multi-axis curved acoustic impedance interface can be determined by using the multi-Gaussian beam model [Schmerr and Song (2007)] as a function of the following parameters:

- Frequency
- Propagating wave type: in fluid (longitudinal) and in elastic solid (longitudinal or shear)
- Transducer properties: diameter d and geometric focal length
- Geometric properties: distance traveled in fluid D, distance traveled in steel z_2, in-plane vertical perpendicular distance from central ray axis x_2, out-of-plane horizontal perpendicular distance from central ray axis y_2, angle of incidence θ_x θ_y, and radius of curvature R_x R_y in both perpendicular planes
- Material properties: densities ρ_1 ρ_2 and wave speeds c_{l1} c_{l2} c_{s2} in both materials

5.2.3.6 Scattering Amplitude

The scattering amplitude as obtained from an experimental flaw measurement is shown in Equation 5.69 with ϵ_A as a Weiner filter constant.

$$\frac{A(\omega)}{L} = \frac{V_R(\omega) G^*(\omega)}{|G(\omega)|^2 + \epsilon_A{}^2 \max\left\{|G(\omega)|^2\right\}} \tag{5.69}$$

The measured scattering amplitude from a flaw in the surface of a half-space $A(\omega)^{\mathrm{h}}$ may be normalized by a $(k_l a)^p$ factor as shown in 5.70. This is similar to the $k_l a$ factor normalizing the theoretical scattering amplitude $\mathbf{A}$ previously described in Equation 5.54 where p is typically a scalar between 0 and 1 [Eason et al. (2017a)].

$$A(\omega)^{\mathrm{h}} = A(\omega)(k_l a)^p \tag{5.70}$$

The experimentally determined far-field scattering amplitude $A(\omega)$ should be equivalent to the theoretical normalized scattering amplitude $\mathbf{A}$ over the measured frequency range; this is shown in Equation 5.71 for the case of a hemispherical pit in a half-space. Determining the comparative relation in Equation 5.71 is the ultimate objective for the experimental validation of a scattering theory.

$$A(\omega)^{\mathrm{h}} \stackrel{?}{=} \mathbf{A}^{\mathrm{h}} \tag{5.71}$$

5.3 Measurement and Analysis

Experiments performed in an ultrasonic immersion system provide data for scattering of longitudinal waves by a hemispherical pit. Data records are analyzed with post processing to provide data in a form to test model results.

5.3.1 Calibration Test Block

An A106B carbon steel calibration block with 25.4 mm thickness, 101.6 mm length, and 50.8 mm width was prepared with a hemispherical pit with a 2.00 mm diameter machined into,

what would be the bottom surface in experiments. A schematic of the calibration block is shown in Figure 5.10.

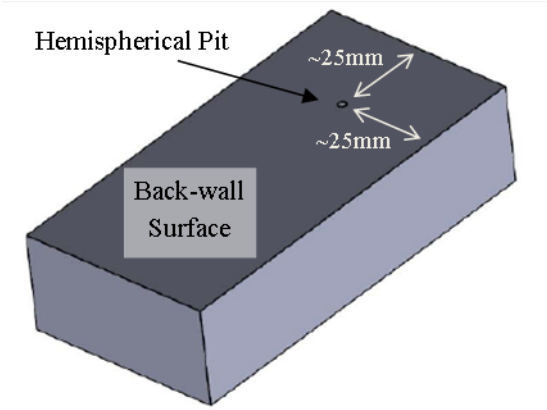

Figure 5.10 Schematic drawing of calibration test block specimen with hemispherical pit on the back-wall surface. Figure previously published [Eason et al. (2017a)].

In designing the experiments, the immersion measurement experimental setup was modeled using UTSim2 ultrasonic beam model, ray-tracing, and flaw response simulation software [Grandin and Gray (2017)] to ensure that practically all energy is reflected from the front-wall and back-wall surfaces, and not influenced by the test block edges. The simulation specimen had dimensions of 75 mm × 75 mm × 25 mm of steel material with a density of 7860 kg/m^3, an isotropic longitudinal wave speed of 6186 m/s, an isotropic shear wave speed of 3330 m/s, and no attenuation. The circular transducer element shape was simulated to be 3.175 mm radius with an infinite focal length with a 8.5 MHz central frequency at 80% bandwidth to try and match the characteristics of a PANAMETRICS® V312 Serial #19014 probe. The transducer was positioned approximately 100 mm from the specimen front-wall surface and surrounded in water with a density of 997.6 kg/m^3, an isotropic longitudinal wave speed of 1490.8 m and power law attenuation of $\alpha = 0.00253f^2$ where α units are neper/cm, and f units are MHz. The simulation calculated an incident field in the steel specimen at 0.5 mm spacing resolution in x, y, and z dimensions in a 50 mm × 50 mm × 25 mm area. The beam model was selected to be Gauss-Hermite with 50 series expansion terms for longitudinal, shear vertical polarization, and shear horizontal polarization wave modes, although only the longitudinal wave

mode is present for this simulation. The spectrum was simulated from 0-20 MHz at a 1 MHz increment. The results in Figure 5.11 show that the immersion experiment configuration is such that practically all acoustic energy is reflected from the front-wall and back-wall surfaces and not influenced by the test block edges.

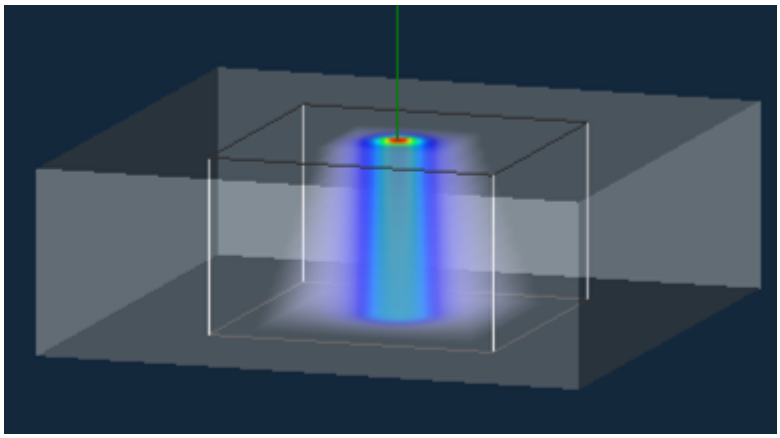

Figure 5.11 Simulation results from UTSim2 showing flat plate immersion configuration adequate to avoid edge effects.

5.3.2 Experiment Setup

The test block was placed in an immersion tank, set to be level and covered with about 30 cm of water. A picture of the immersion setup is shown in Figure 5.12. An electronics system block diagram is shown in Figure 5.13. Measurements were made using a 10 MHz, 6.35 mm (0.25 inch) diameter longitudinal wave immersion probe [PANAMETRICS® V312 Serial #190141] which was driven by a pulser-receiver [Peak MicroPulse LT8] at 150V with a pulse width of 16 ns, at a 1 kHz pulse repetition rate. Data records were recorded at a series of gain settings: 0, 11, 40, 41, and 70 dB. The received signals were collected a 100 MHz sampling frequency and measurements were made with settings of a 2.5 MHz high pass filter and an 18 MHz low pass filter. All data records were averaged 256 times to improve the signal to noise ratio.

After aligning the transducer normal to the front-wall surface, the initial calibration reference measurement was performed in pulse-echo mode collecting data from the block at a

location away from the hemispherical pit. This was then followed by a measurement made with the transducer axis directly above the pit.

The measurements were performed and data collected in a period of one hour. The temperature of the water was measured and monitored at 21.6 ± 0.1 °C resulting in a calculated wave speed of 1487 ± 1 m/s [Lubbers and Graaff (1998)]. The measured arrival time of the echo from the front surface, at normal incidence, was 76.9 μs which gave a water path of 114.4 ± 0.1 mm. The calculated near-field per Equation 3.1 is 34 mm at 5 MHz, 67 mm at 10 MHz, and 102 mm at 15 MHz. All response signals were adjusted with a screen height to voltage conversion of 0.5% and a mean subtraction to cancel any DC voltage offset.

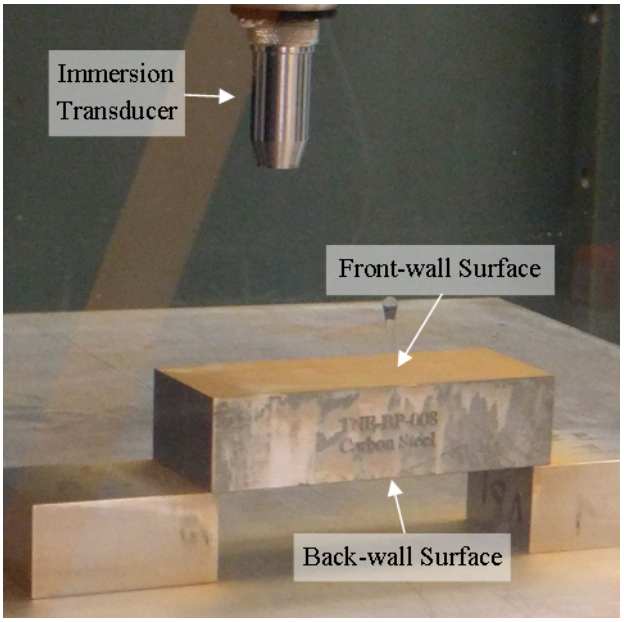

Figure 5.12 Picture of immersion experiment setup showing transducer and calibration test block specimen. Figure previously published [Eason et al. (2017a)].

5.3.3 Reference Measurements

Reference measurements were performed and data collected to enable the system function described in Equation 5.56 to be determined and to ultimately provide the reference spectrum described in Equation 5.64. The voltage response signal was collected with an 11 dB gain to achieve maximum amplitude without saturation of the front-wall response, and then again, but

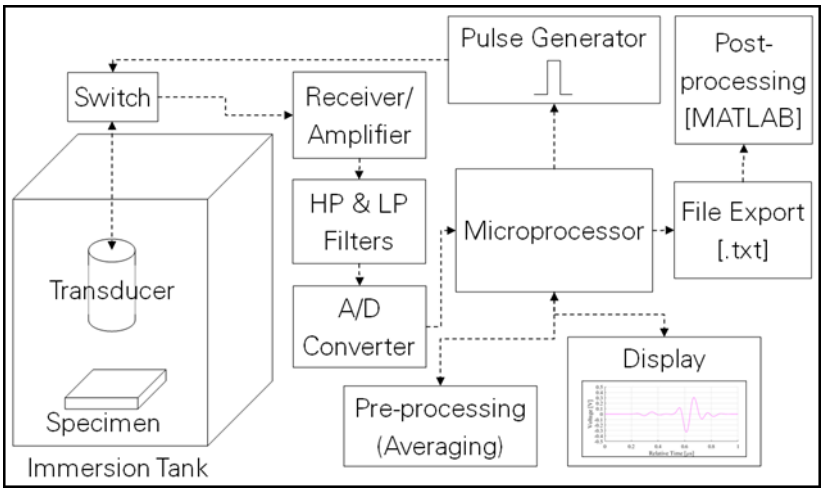

Figure 5.13 Immersion experiment measurement electronics system block diagram.

with a 40 dB gain, to achieve maximum amplitude without saturation of the first back-wall response. These voltage response signals are shown in Figure 5.14 for the full signal showing data record times up to the fourth back-wall reflection (approximately 112 μs) as well as the segment of the data record for the front-wall and first back-wall on an expanded scale.

5.3.3.1 Longitudinal Wave Speed

The longitudinal wave speed in the steel block was determined using the difference in peak arrival times between multiple back-wall reflection features for the data record recorded at a 40 dB gain setting. These positive and negative peak features are shown in Figure 5.15 as a "$\circ$" symbol. The data record for the front-wall features at approximately 77 μs is not usable due to signal saturation, however, the arrival time difference τ_l between the second ($\approx$86 μs) and third ($\approx$94 μs) back-wall longitudinal features were used as a divisor in Equation 5.72 to calculate a longitudinal wave speed c_l for both positive and negative peaks with $t = 25.4$ mm as the calibration block thickness. This process is repeated for the subsequent back-wall longitudinal features resulting in a mean longitudinal wave speed of 5907 $\pm$ 12 m/s.

$$c_l = \frac{2t}{\tau_l} \tag{5.72}$$

5.3.3.2 Shear Wave Speed

The shear wave speed in the steel block was determined using the difference in peak arrival times from the multiple mode converted back-wall reflection features obtained at a 40 dB gain setting. The features in the positive and negative peaks are shown in Figures 5.15 and 5.16 as a "×" symbol. The features seen at approximately 89 μs are from a mode converted signal where the incident mode on the first back-wall is longitudinal and the reflected mode is shear, or the incident mode on the first back-wall is shear and the reflected mode is longitudinal, which gives a response where one path is as a longitudinal wave mode and one as a shear wave mode. The second back-wall mode converted features occur at approximately 98 μs when three out of the four paths within the steel are traveled as a longitudinal wave mode and one path is as a shear wave mode. The arrival time difference τ_s between the first back-wall mode converted features which occur at approximately 89 μs and front-wall features which occur at approximately 77 μs are not usable due to front-wall signal saturation. However, the arrival time difference τ_s between the second back-wall mode converted features which occur at approximately 98 μs and first back-wall longitudinal features which occur at approximately 86 μs are used in Equation 5.73 to calculate the shear wave speed as defined in Equation 5.74 with τ_L as the longitudinal path arrival time and c_L as the previously determined longitudinal wave speed of 5907 m/s. This process is repeated for the subsequent back-wall mode converted features resulting in a mean shear wave speed of 3253 ± 23 m/s. The longitudinal to shear wave speed ratio is 1.82 in the steel calibration flat block.

$$c_s = \frac{t}{\tau_s - \tau_L} \tag{5.73}$$

$$\tau_L = c_L t \tag{5.74}$$

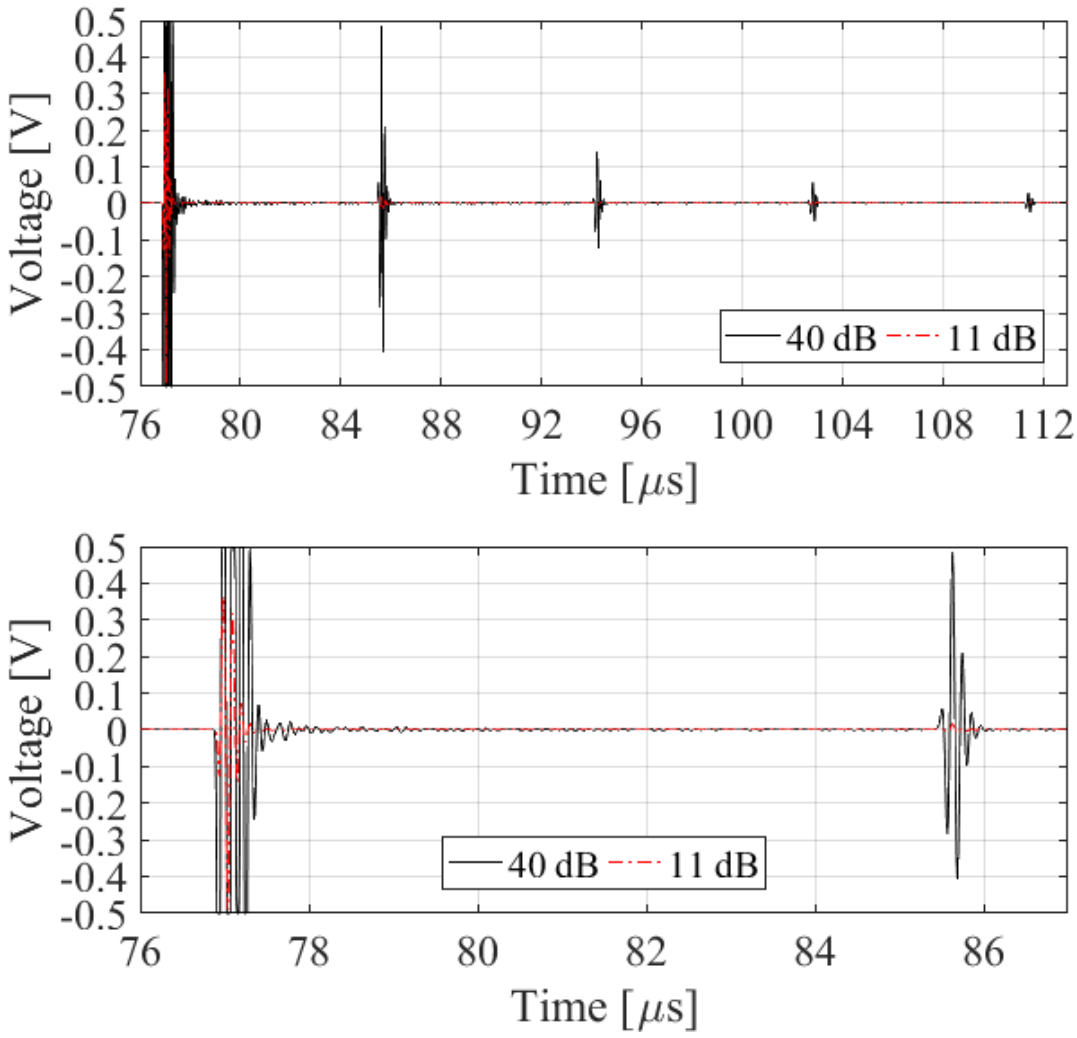

Figure 5.14 Reference measurement time domain voltage signal responses. To avoid saturation, the front-wall response is observed at 11dB gain and the first back-wall response is observed at 40 dB gain. Figure previously published [Eason et al. (2017a)].

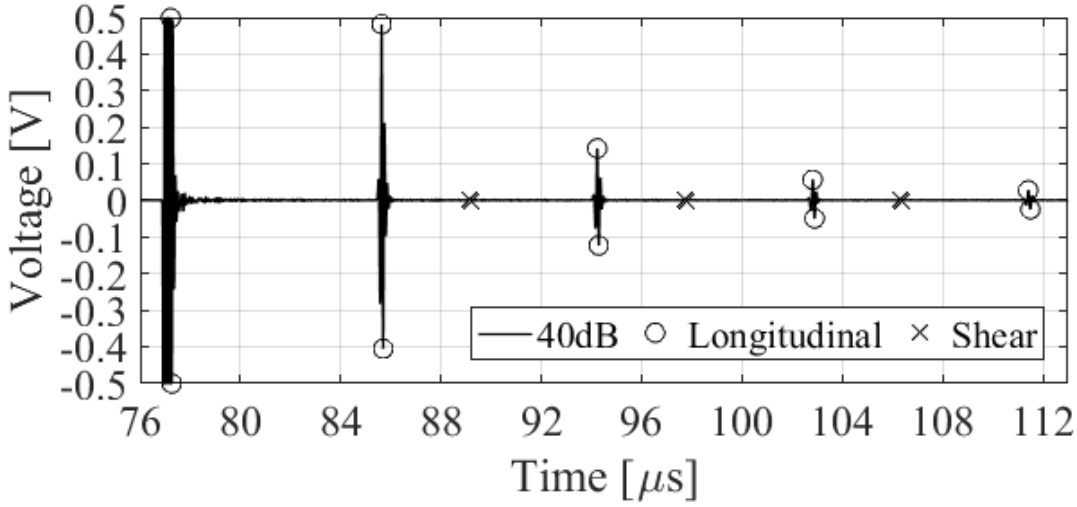

Figure 5.15 Reference measurement time domain voltage signal response with 40 dB gain showing the longitudinal mode signal features used to calculate the longitudinal wave speed in the steel block. Figure previously published [Eason et al. (2017a)].

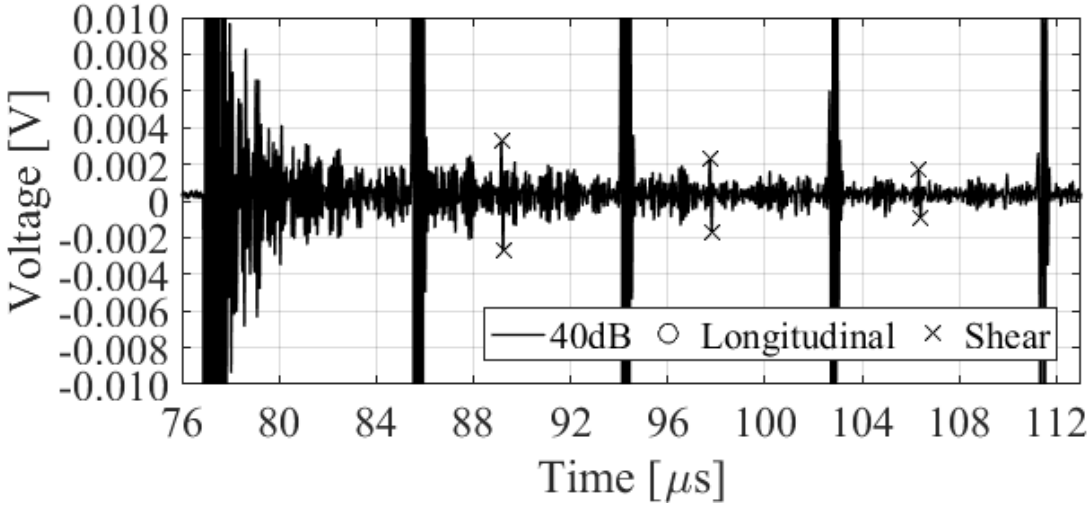

Figure 5.16 Reference measurement time domain voltage signal response with 40 dB gain showing the mode converted signal features used to calculate the shear wave speed in the steel block. Figure previously published [Eason et al. (2017a)].

5.3.3.3 Frequency Domain

The front and back-wall time domain pulse-echo response signals were identified and a gate applied to give 62 individual voltage data points at a 0.01 μs interval over a 0.62 μs time period. For each data record the following process was implemented: (i) each gated signal was subtracted from its mean to remove any DC offset, (ii) a Tukey window function [Harris (1978)] was applied to each signal in order to smooth the transitions to a zero voltage level. The Tukey window had 25% as a transition from 0 to 1, 50% equal to 1, and 25% as a transition from 1 to 0, (iii) 9938 zeros were added to pad the record to provide a record length of 100 μs and retaining the 0.01 μs interval, and (iv) each signal was subtracted from its mean again. The resulting processed time domain signals for the 40 dB first back-wall, 11 dB front-wall, and 11 dB first back-wall responses are shown in Figures 5.17-5.19.

Once the time domain signal is obtained, a Fast Fourier Transform (FFT) was applied to convert each signal to the frequency domain. The process was performed by applying the ‟ifft″ function in MATLAB®, multiplying by the 100 μs signal length, and taking the absolute value [Schmerr (2016)]. The full frequency domain results contain 10000 points from 0-100 MHz at a 0.01 MHz interval, however only the values from 0-20 MHz are considered and displayed in Figures 5.17-5.19. The spectral peaks are identified with‟∘″ symbols and are typically between 8-9 MHz.

The -6 dB amplitude bandwidth is defined as the voltage values within 50.1% of the spectral peak voltage; bandwidth limits are identified with‟+″ symbols and the ranges are between 5 and 12 MHz. The peak and -6 dB amplitude bandwidth values of the reference measurement 11 dB front-wall, reference measurement 11 dB first back-wall, and pit measurement 40 dB first back-wall are listed in Table 5.1 as the spectra of interest. Following data review, the bandwidth range for which the data were used was set to consistently be between 6.10 and 10.30 MHz.

Table 5.1 Reference and Pit Experiment Amplitude Bandwidth

Response Signal	**Peak [MHz]**	**Bandwidth [MHz]**
Reference 11 dB Front-wall	9.03	6.10–11.38
Reference 11 dB 1st Back-wall	8.27	5.48–10.37
Pit 40 dB 1st Back-wall	8.38	5.36–10.30
Available Bandwidth Range		6.10–10.30

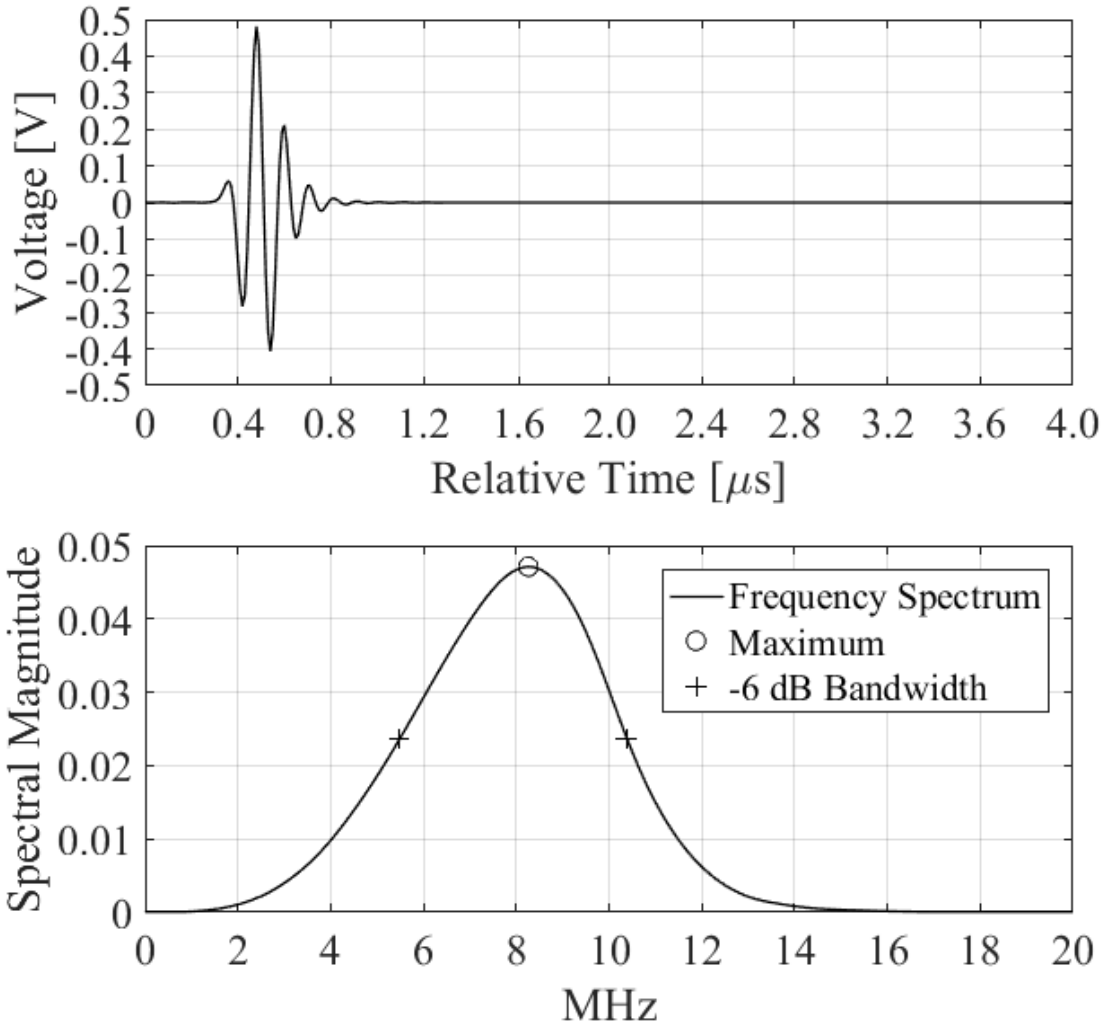

Figure 5.17 Reference measurement gated time and frequency domain first back-wall response signal with 40 dB gain. Figure previously published [Eason et al. (2017a)].

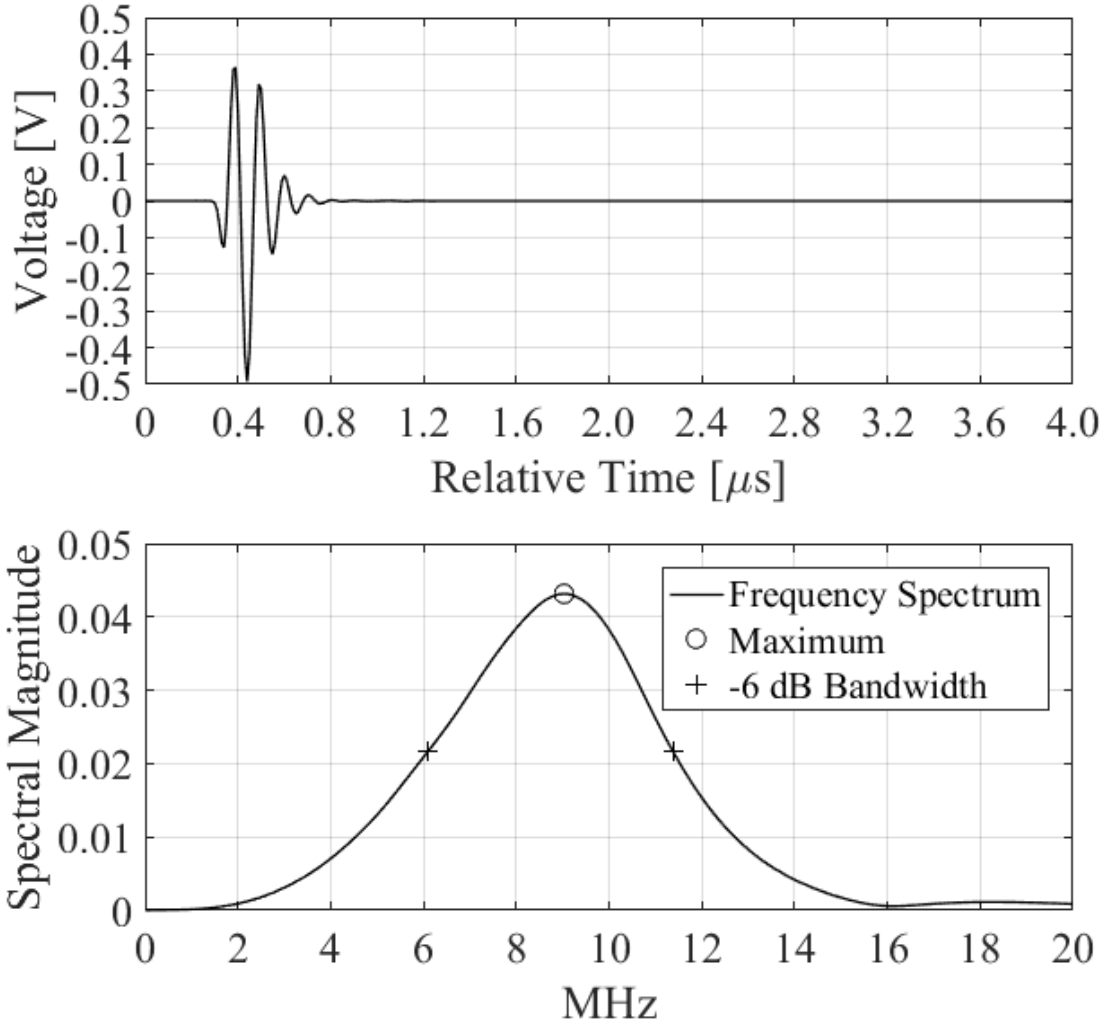

Figure 5.18 Reference measurement gated time and frequency domain front-wall response signal with 11 dB gain. Figure previously published [Eason et al. (2017a)].

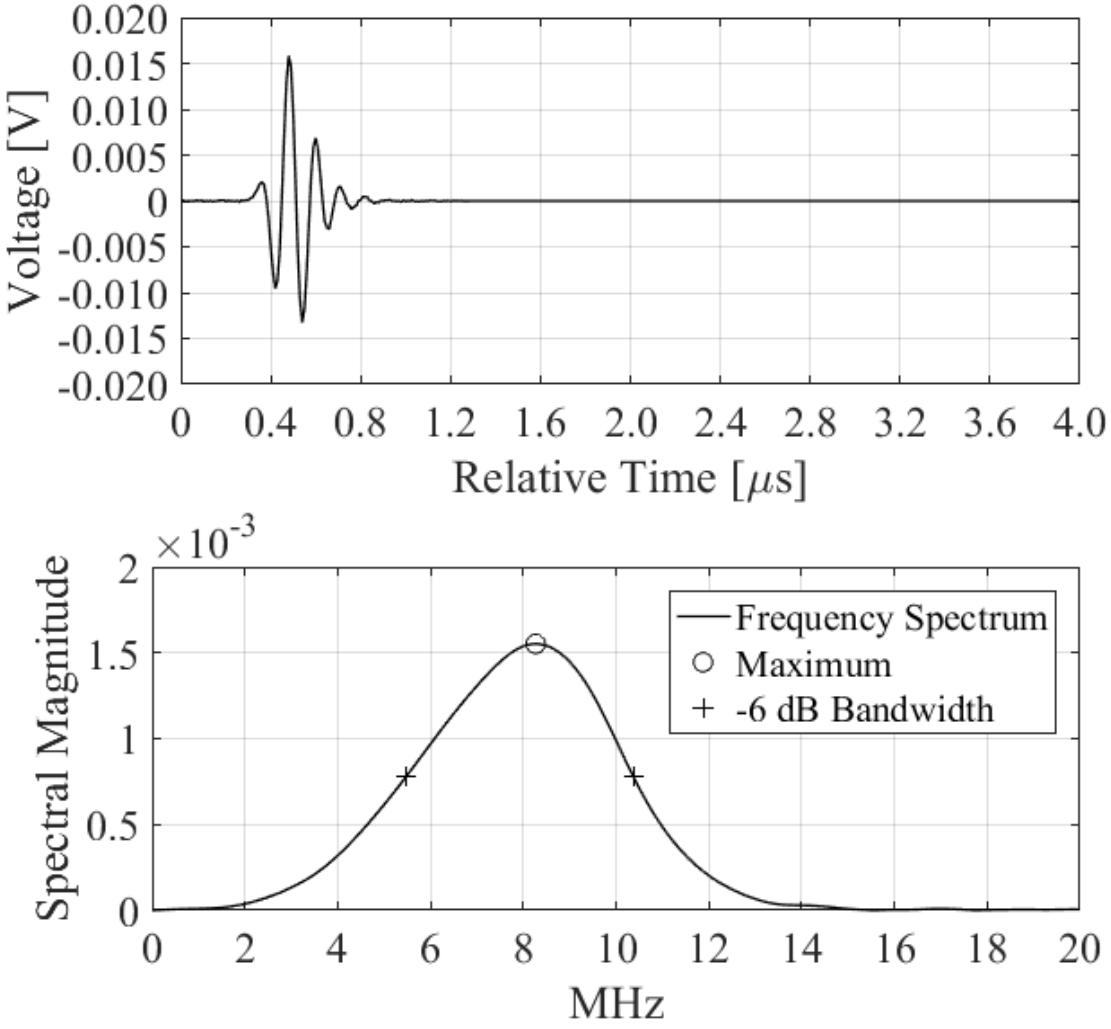

Figure 5.19 Reference measurement gated time and frequency domain first back-wall response signal with 11 dB gain. Figure previously published [Eason et al. (2017a)].

5.3.3.4 Acoustic/Elastic Transfer Function

The acoustic/elastic transfer function as described in Equation 5.58 is calculated for the experimental immersion measurements. The absolute value of the acoustic elastic transfer function is shown in Figure 5.20 using the following values: $\rho_1 = 998$ kg/m^3, $\rho_2 = 7860$ kg/m^3, $c_{l1} = 1487 \pm 1$ m/s, $c_{l2} = 5907 \pm 12$ m/s, $R_{12} = 0.94$, $a = .003$ m, ω evaluated over a range of 0-3.18 $\times 10^6$ angular frequency [rad/s] equivalent to f over a range of 0-20 MHz, $D = 114.4 \pm 0.1$ mm, and $\alpha_1(f) = 25.3 \times 10^{-3} f^2$ Nepers/m. The uncertainty of the longitudinal wave speed in water c_{l1} ($\pm$ 1 or 0.07%) is smaller than the uncertainty of the longitudinal wave speed in the steel block c_{l2} ($\pm$ 12 or 0.2%). The water uncertainty is based on the reported error in the equation used to calculate the wave speed as a function of ambient temperature [Lubbers and Graaff (1998)]; the steel uncertainty is based on the limited experimental wave speed measurements.

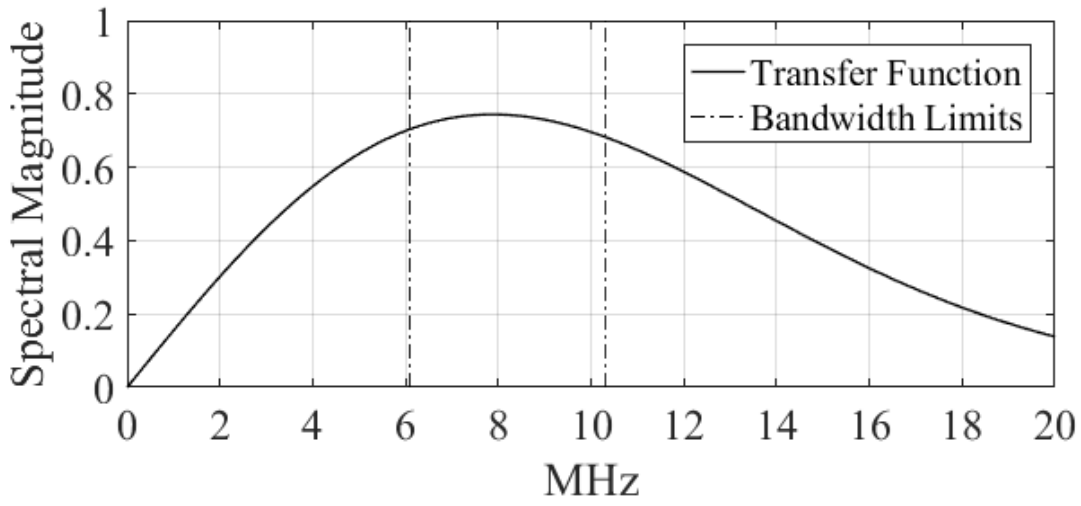

Figure 5.20 Acoustic/elastic transfer function t_A from Equation 5.58. Figure previously published [Eason et al. (2017a)].

5.3.3.5 System Function

The system function described in Equation 5.61 is shown in Figure 5.21 when using the 11dB front-wall response signal with a Weiner constant filter value of $\epsilon_s = 0.5$.

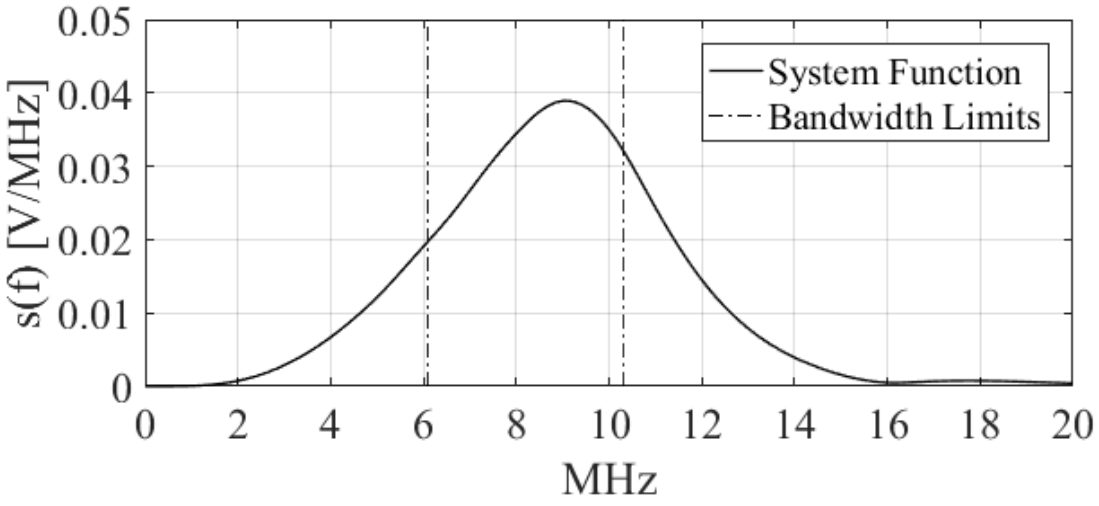

Figure 5.21 System function s from Equation 5.61. Figure previously published [Eason et al. (2017a)].

5.3.3.6 Attenuation in Steel Sample

The attenuation due to grain scattering within the sample can be calculated as described in Equation 5.75 where α is in units of dB per unit length of sample thickness t with $F(\omega)$ as the front-wall spectrum, $B(\omega)$ as the first back-wall spectrum, and ϵ_α as a Weiner filter constant [Schmerr (2016)].

$$\alpha = -\frac{1}{2t} \ln \left[\frac{|B(\omega)|\,|F(\omega)|}{|F(\omega)|^2 + {\epsilon_\alpha}^2} \right] \times 8.686 \tag{5.75}$$

The spectra for the front-wall and first back-wall response from the data records obtained with 11dB gain are shown in Figures 5.18 and 5.19 and are applied to Equation 5.75 for $\epsilon_\alpha = 0.004$ as shown in Figure 5.22. A least squares linear fit is applied to the data within the bandwidth range from 6.10 to 10.30 MHz also shown in Figure 5.22. This frequency domain data is at a 0.01 MHz interval as result of the FFT process. The $R^2 = 0.93$ value indicates an increasing linear relation between frequency and attenuation coefficient, however, the linear approximation is not used in lieu of the actual measured attenuation coefficient values. These measured attenuation coefficient values are in agreement with previously reported results in the range of 0.5-1.0 dB/mm at 10 MHz [Smith et al. (1981)].

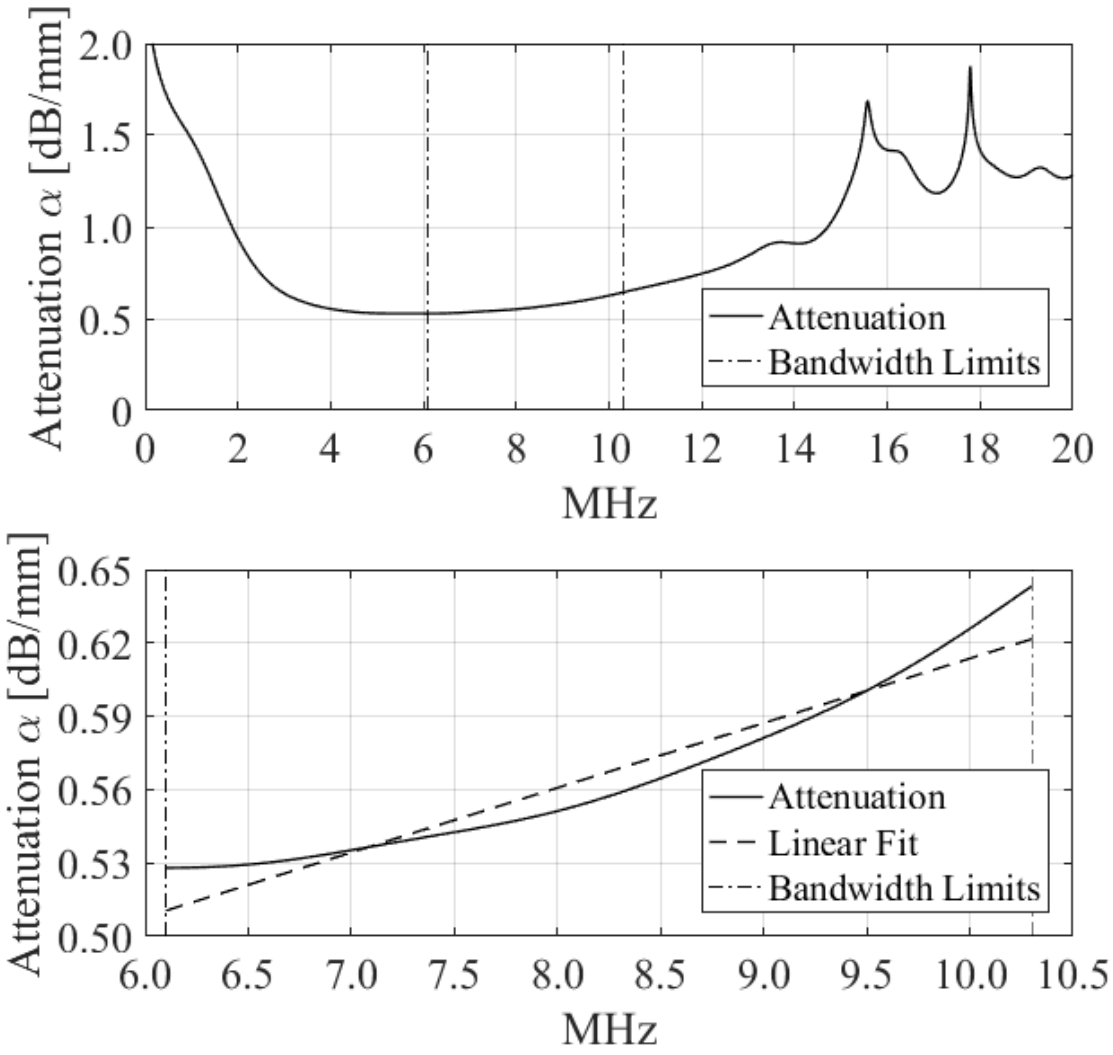

Figure 5.22 Attenuation α from Equation 5.75. Figure previously published [Eason et al. (2017a)].

5.3.3.7 Multi-Gaussian Beam Model

The ideal velocity ratio field term from Equation 5.67 can be determined from the Multi-Gaussian beam model [Schmerr and Song (2007)]. The transducer was positioned at a normal angle of incidence. The longitudinal wave mode for material 1 (water) and the longitudinal wave mode for material 2 (steel) were used with the previously mentioned density and wave speed material property values. The transducer diameter was $d = 6.35$ mm and assumed to be plane-wave infinite focal length. The distance traveled in the water was $D = 114.4$ mm and in the steel it was $z_2 = t = 25.4$ mm. The model was set with an infinite geometric curvature, indicating a flat surface. Ideal velocity ratio field values were calculated over a range of -50 mm to +50 mm in the vertical (Y direction) and horizontal (X direction) perpendicular distances from the central ray axis.

The ideal velocity ratio was evaluated at the location of the flaw at $z_2 = t$ for only the first ten Wen and Breazeale Coefficients over a frequency range from 0-20 MHz for a range of spatial resolution values of 10 mm (121 points), 5 mm (441 points), 2 mm (2601 points), 1 mm (10201 points), and 0.5 mm (40401 points). Different methods were considered to determine the ideal velocity ratio values from 0-20 MHz. The first method was simply the ideal velocity field value at the central ray location (which is also the maximum ideal velocity at each frequency) with data shown in Figure 5.23 as a solid line. The second method was the average ideal velocity ratio above the -6 dB amplitude bandwidth of the maximum ideal velocity at each frequency with data shown as a dashed line in Figure 5.23. The third method was a numerically evaluated trapezoid integral to determine the average ideal velocity ratio above a noise floor of 10% of the maximum ideal velocity at at each frequency with data shown as a dash-dot line in Figure 5.23. The fourth method was the average ideal velocity ratio above a noise floor of 10% of the maximum ideal velocity at each frequency with data shown as a dotted line in Figure 5.23. Also spatial domain plots of the velocity ratio field for the case of 1 mm resolution are shown in Figure 5.24 at the lower bandwidth frequency limit of 6.10 MHz, in Figure 5.25 at the peak frequency of the reference measurement 11 dB first back-wall response signal of 8.27 MHz, and in Figure 5.26 at the upper bandwidth frequency limit of 10.30 MHz.

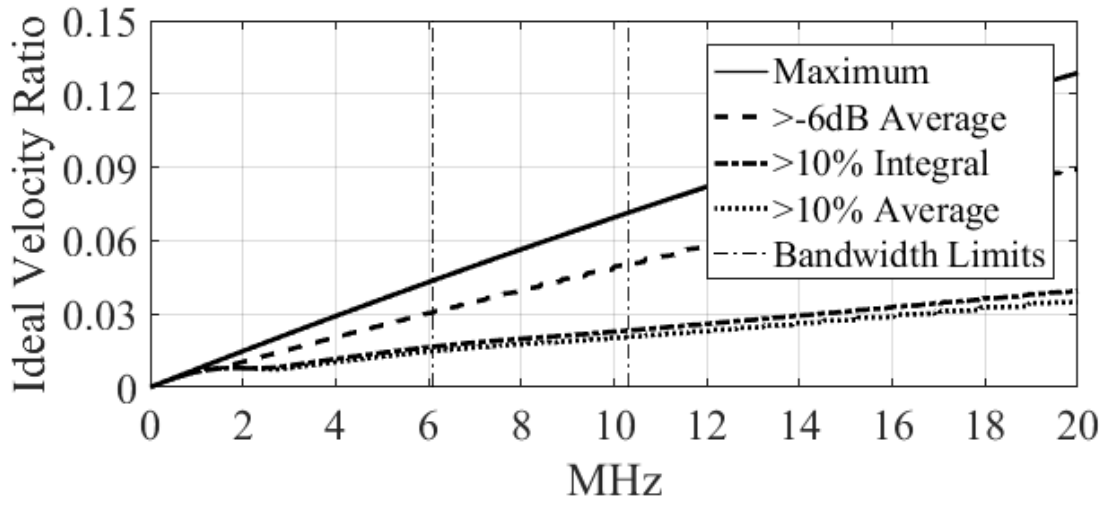

Figure 5.23 Ideal velocity ratio calculation methods from the Multi-Gaussian beam model at the flaw location. Figure previously published [Eason et al. (2017a)].

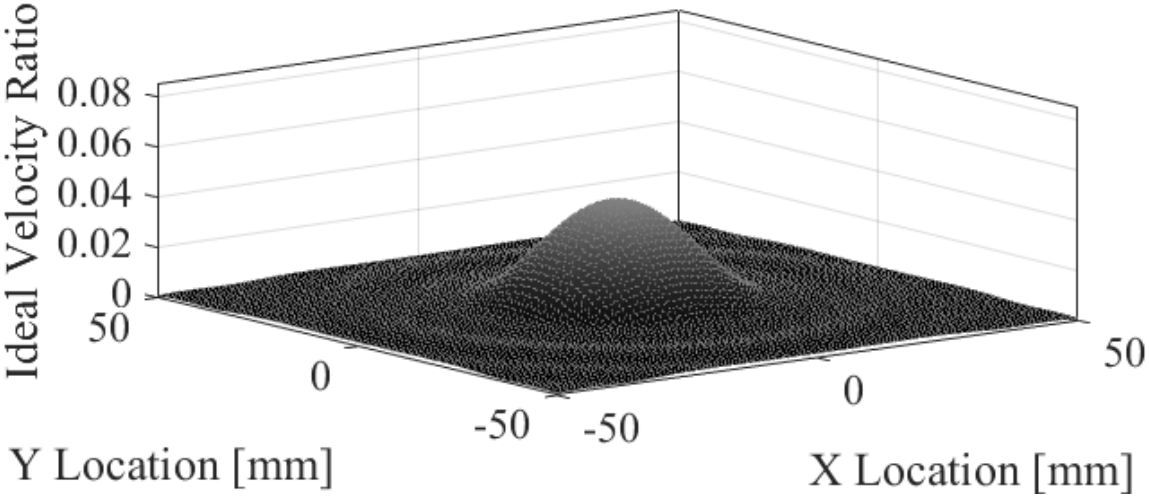

Figure 5.24 Multi-Gaussian beam model ideal velocity ratio field at the flaw location at the lower bandwidth frequency limit of 6.10 MHz with 1 mm spatial resolution. Figure previously published [Eason et al. (2017a)].

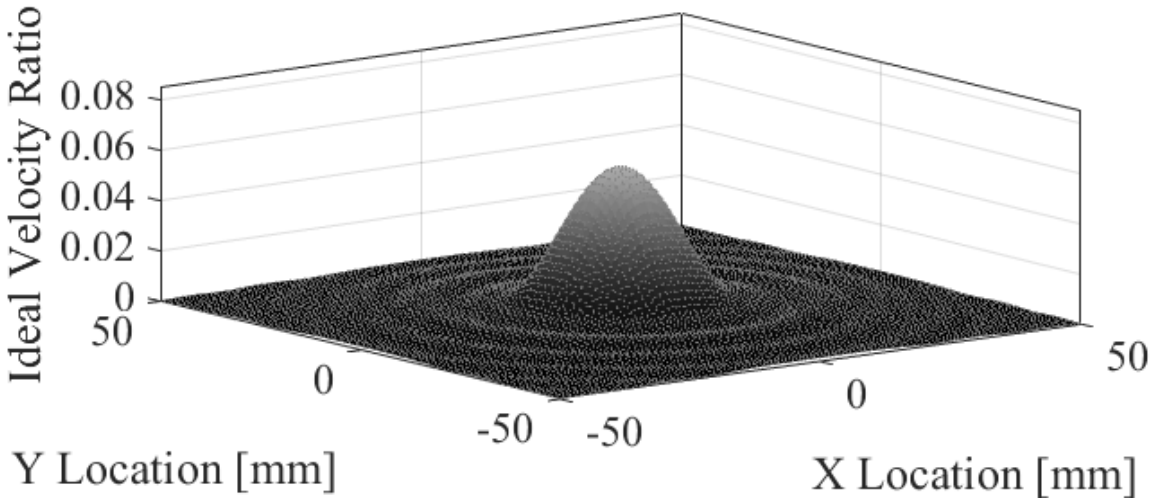

Figure 5.25 Multi-Gaussian beam model ideal velocity ratio field at the flaw location at the reference measurement 11 dB first back-wall response signal peak frequency of 8.27 MHz with 1 mm spatial resolution. Figure previously published [Eason et al. (2017a)].

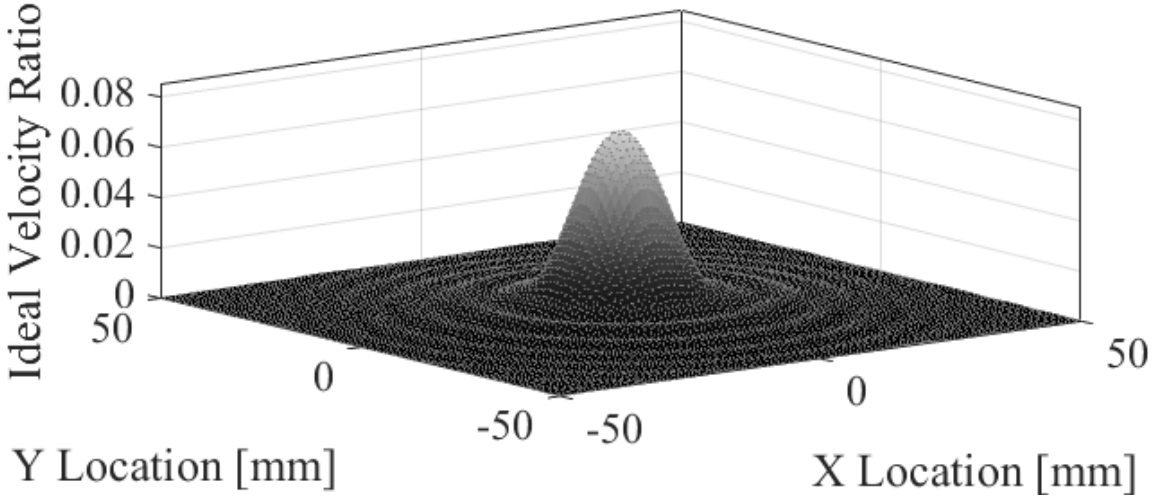

Figure 5.26 Multi-Gaussian beam model ideal velocity ratio field at the flaw location at the upper bandwidth frequency limit of 10.30 MHz with 1 mm spatial resolution. Figure previously published [Eason et al. (2017a)].

A common assumption is that the ideal velocity ratio does not vary significantly over the response surface of the flaw and to use the central axis (maximum) ideal velocity ratio. However, the new hemispherical pit scattering theory includes scattering from the half-space boundary as well as from the hemispherical pit surface, and the common assumption for a constant ideal velocity ratio over this larger region may not be rigorously valid, but appears to be an adequate approximation. The maximum ideal velocity ratio may be too large, and a -6 dB average, >10% integral average, or other ideal velocity ratio values may be a better approximation. Although not completely rigorously correct, for consistency, the maximum ideal velocity ratio is used.

5.3.3.8 Reference Spectrum

The incident velocity $\hat{V}_0^{(1)}(\omega)$ at the flaw location is required to determine the reference spectrum $G(\omega)$ at the flaw location described in Equations 5.64-5.66. The velocity field is related to the normal derivative of the pressure field as defined in Equation 5.68. The incident velocity (at the flaw location) is a product of three parameters: attenuation in water, attenuation in steel, and the ideal velocity ratio at the flaw location as described in Equation 5.67. The values of each of the three parameters are shown for comparison in Figure 5.27 with the resulting incident velocity at the flaw location shown in Figure 5.28. The corresponding reference spectrum at the flaw location from Equation 5.64 is shown in Figure 5.29.

5.3.4 Pit Measurements

Data records for measurements were made directly above and normal to the hemispherical pit. The pulse-echo voltage response signals were recorded with a 40 dB gain setting to achieve maximum amplitude without saturation of the first back-wall response, and at a 70 dB gain to achieve maximum amplitude without saturation for the pit response. The signals are shown in Figure 5.30, together with the corresponding reference measurement response signals at 40 dB and 70 dB gain settings with expanded scales for segments of the data record showing just the pit and first back-wall response. The signal from the waves scattered from the pit is observable by a decrease in amplitude in the first back-wall reflection at approximately 85.7 μs, and with an early arrival just before the first back-wall signal at 85.3 μs.

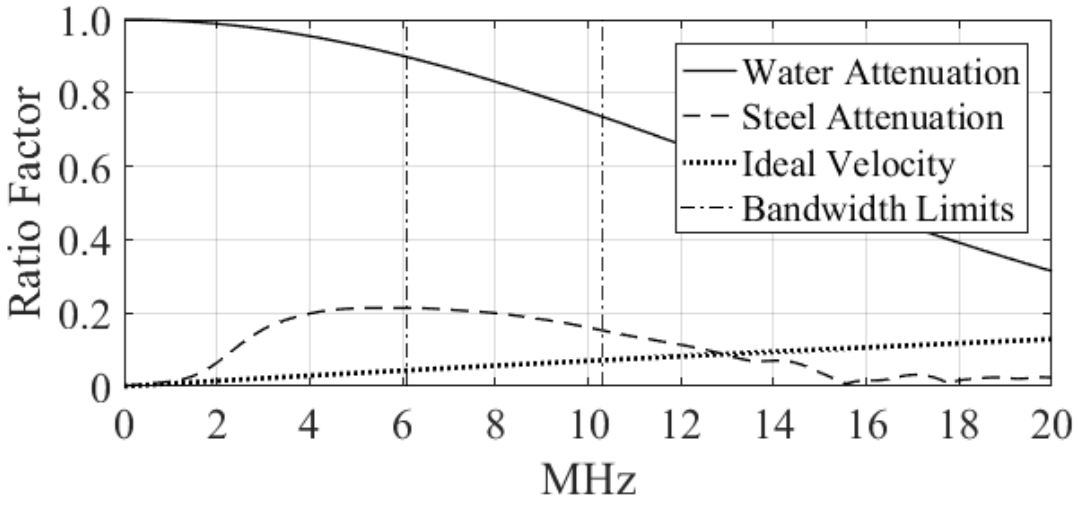

Figure 5.27 Parameters that influence the incident velocity $\hat{V}_0^{(1)}(\omega)$ at the flaw location are shown as water attenuation $e^{-\alpha_1(\omega)D}$, steel attenuation $e^{-\alpha_{l2}(\omega)z_2}$, and ideal velocity $\frac{V_{li}}{v_0}$ at the flaw location. Figure previously published [Eason et al. (2017a)].

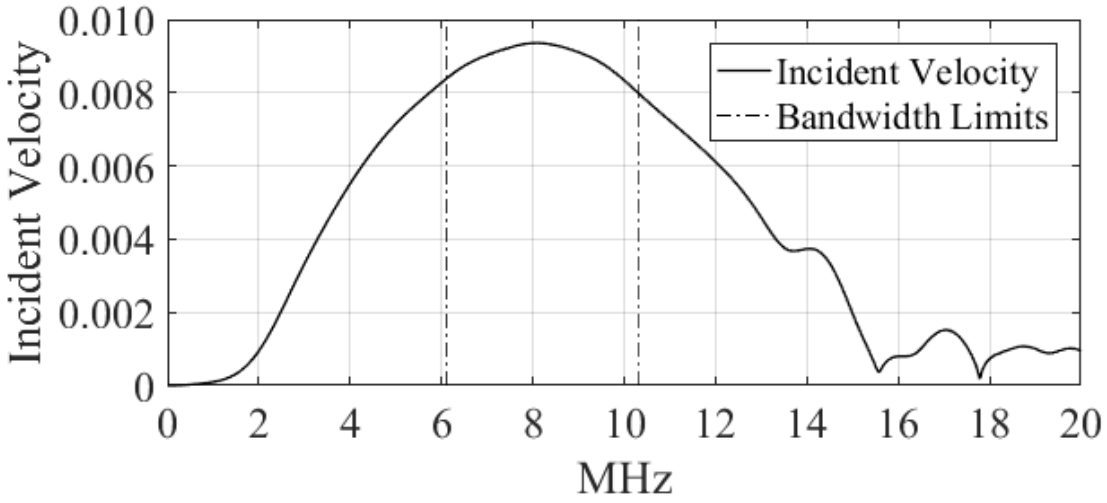

Figure 5.28 Incident velocity $\hat{V}_0^{(1)}(\omega)$ at flaw location from Equation 5.67. Figure previously published [Eason et al. (2017a)].

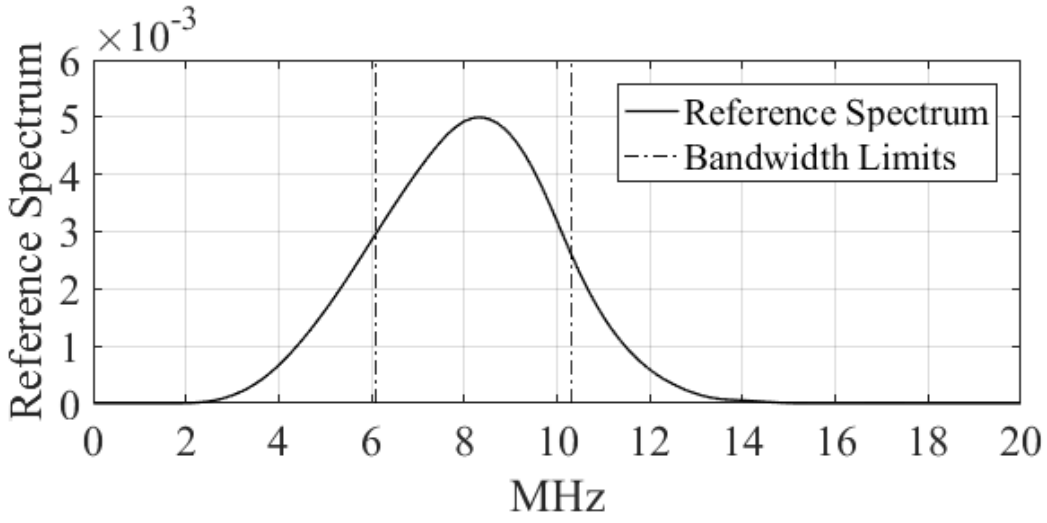

Figure 5.29 Reference spectrum $G(\omega)$ at flaw location from Equation 5.64. Figure previously published [Eason et al. (2017a)].

5.3.4.1 Frequency Domain

The time and frequency domain signals for the first back-wall pulse-echo signal are shown in Figure 5.31. This time domain signal includes scattering from the pit and the back-wall. The same signal processing methods are applied to achieve the frequency data in Figure 5.31.

5.4 Results

Applying Equations 5.69 and 5.70 results in the half-space far-field scattering amplitude $A(\omega)^{\mathrm{h}}$. The reference spectrum $G(\omega)$ was determined from the data obtained from the reference front-wall and reference first back-wall signal with a gain setting of 11 dB. The pit measurement response $V_R(\omega)$ was determined from the spectrum for the pit first back-wall response at a gain setting of 40 dB. None of the signals used to generate the reference spectrum or the pit measurement voltage response were saturated. The measurement system exhibits linearity in its performance at these different gain levels over the frequency range of interest. The system linearity enables scaling and shifting factors to be applied to the scattering amplitude $A(\omega)^{\mathrm{h}}$ via the normalizing variable L in Equation 5.69.

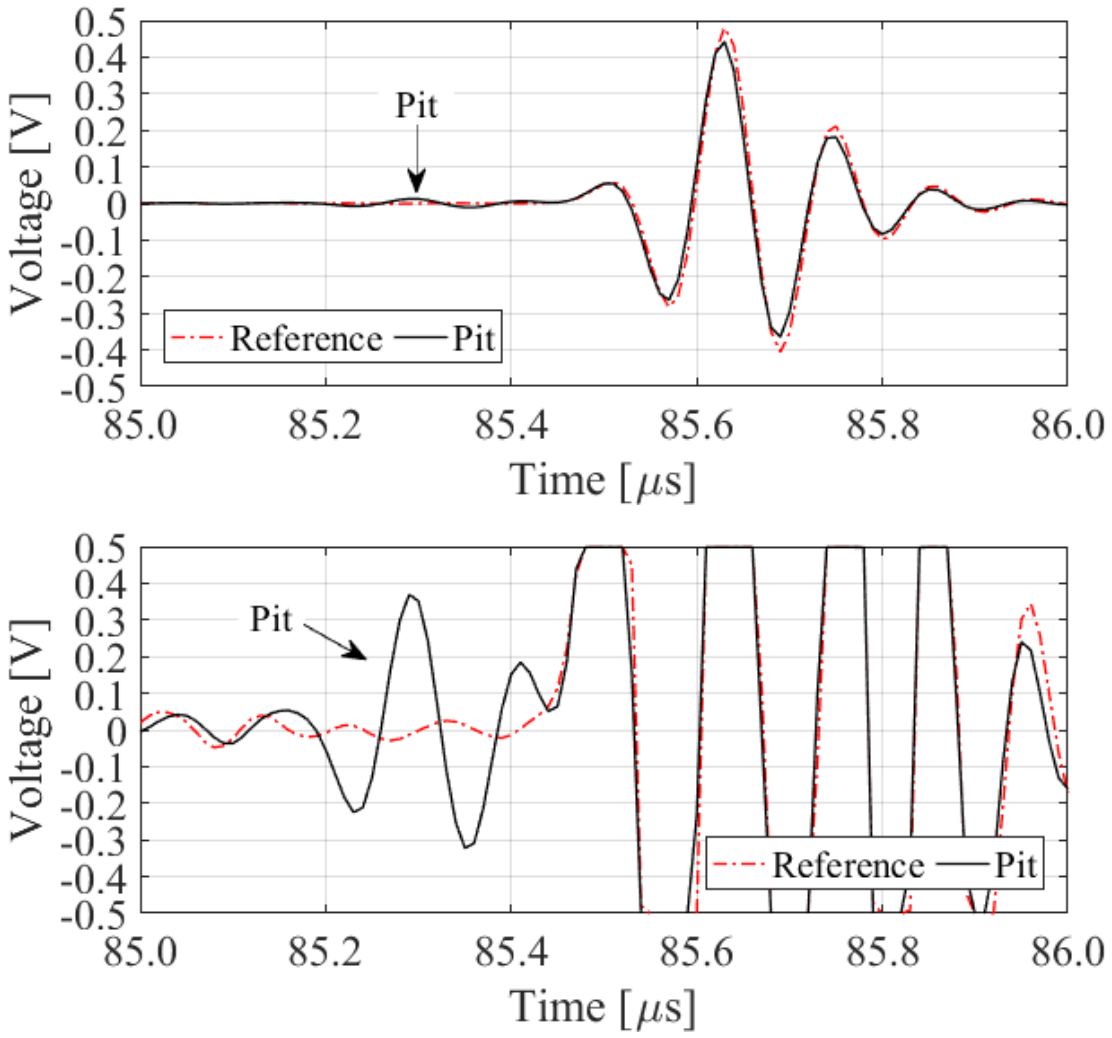

Figure 5.30 Reference and pit measurement time domain voltage signal responses. The top response is at 40 dB gain to avoid saturation of the first back-wall, the bottom response is at 70 dB gain to avoid saturation of the pit. Figure previously published [Eason et al. (2017a)].

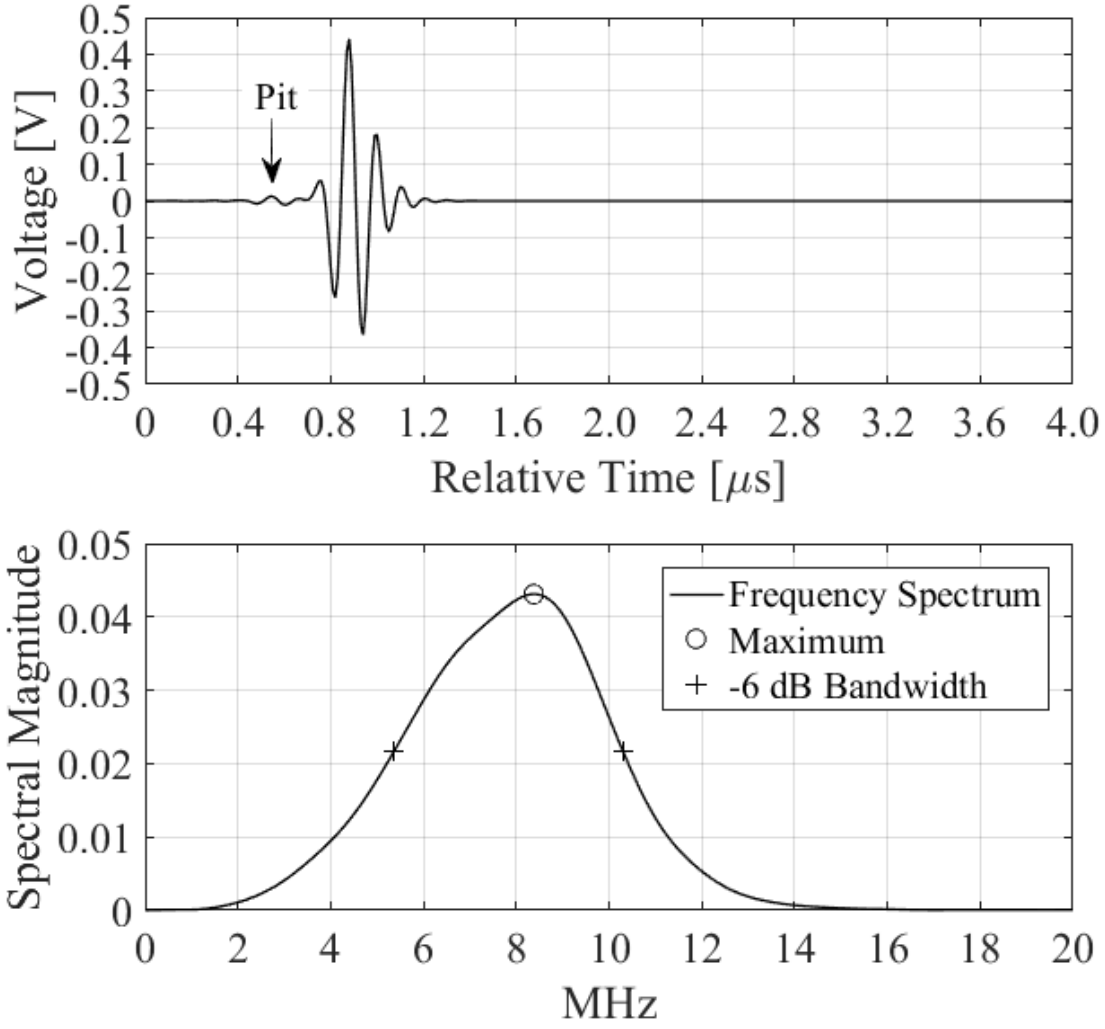

Figure 5.31 Pit measurement experiment gated time and frequency domain first back-wall response signal with 40 dB gain. Figure previously published [Eason et al. (2017a)].

The measured half-space far-field scattering amplitude $A(\omega)^{\mathrm{h}}$ is shown in Figure 5.32 with $\epsilon_A = 0.06$, $p = 0$, a scale factor of -0.42, and a shift factor of 1.08. The measured scattering amplitude is compared with the theoretical scattering amplitude for the longitudinal to shear wave speed ratio of 1.82 measured in the experiment. The estimated error bands are shown as measurement sensitivity limits based on an uncertainty range for a $\pm 10\%$ variation in the measured longitudinal wave speed, scaling factor p, and Weiner filter constants ϵ_s, ϵ_α, and ϵ_A. The measured scattering amplitude in Figure 5.32 shows good agreement in the ka range between 6.5 and 8. There remain differences between theory and experiment at higher ka values.

A modified filtering and scaling approach using modified constants is shown in Figure 5.33 with $\epsilon_s = 0.8$, $\epsilon_\alpha = 0.5$, $\epsilon_A = 0.09$, $p = 0.7$, a scale factor of -0.03, and a shift factor of 1.05. Again, the measured scattering amplitude is compared with the theoretical scattering amplitude for the longitudinal to shear wave speed ratio of 1.82 measured in the experiment. The theoretical and experimental data are in good agreement between 6.5 and 9 ka. Again, the estimated error bands are shown as measurement sensitivity limits based on an uncertainty range for a $\pm 10\%$ variation in the measured longitudinal wave speed, scaling factor p, and Weiner filter constants ϵ_s, ϵ_α, and ϵ_A.

The experimental results from $9 < ka < 11$ do not match the hemispherical pit scattering theory as observable in 5.33. The higher frequency components of the signal, while within the usable bandwidth, may not have been captured sufficiently if the sampling frequency was too low. The Nyquist sampling criterion requires at least 2 times the sampling frequency of the highest frequency component of interest; however this criterion is a lower limit, and often in practice, a sampling frequency of 10 times is conservatively applied [Schmerr (2016)]. A Nyquist criterion limit of 11.3 times is shown in Figure 5.34 corresponding to $ka = 9.4$ and a frequency of 8.9 MHz for a 100 MHz sampling frequency. Also shown in Figure 5.34 are the relatively low-frequency (long-wavelength) fourth power Rayleigh scattering theory and the relatively high-frequency (short-wavelength) ray tracing Geometrical Theory of Diffraction (GTD).

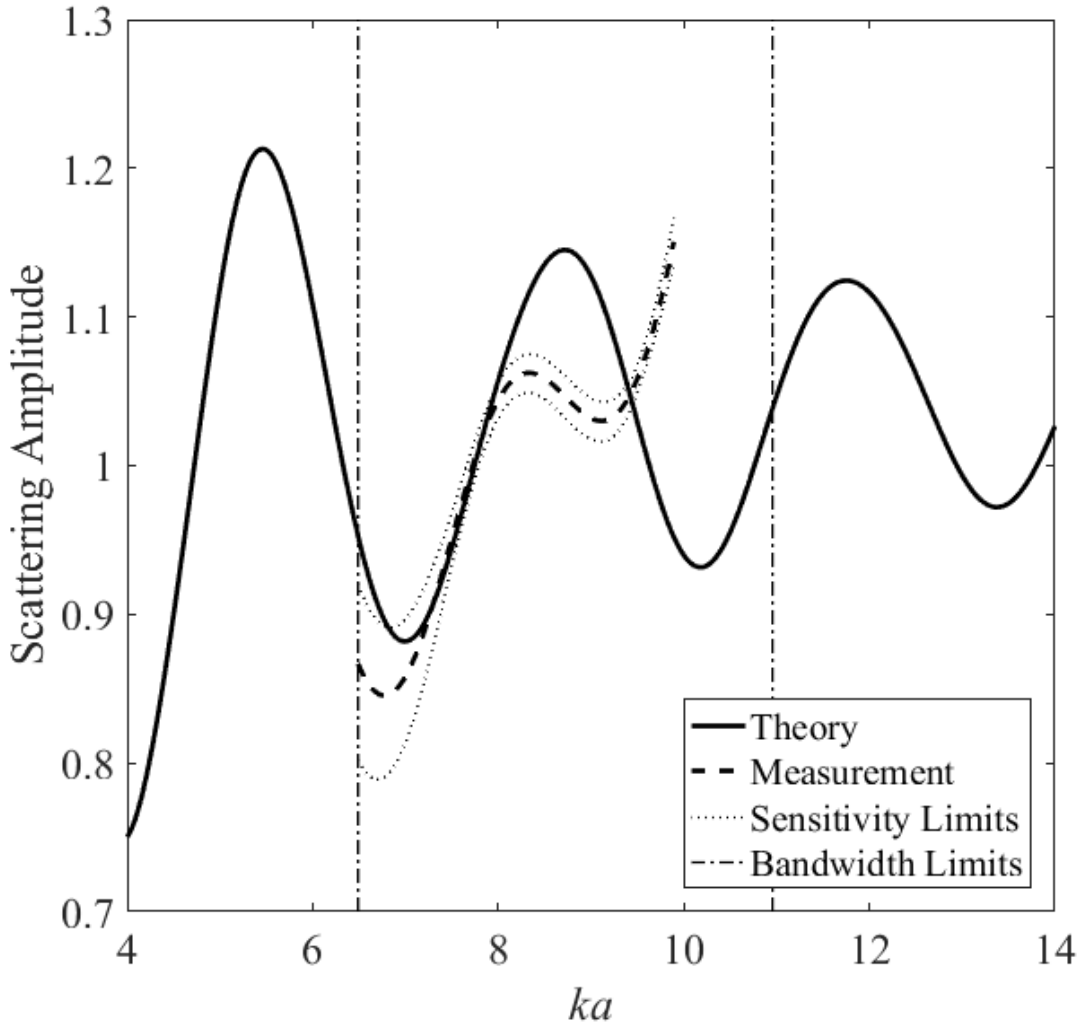

Figure 5.32 Far-field scattering amplitude for a hemispherical pit theory $\mathbf{A}^{\mathrm{h}}$ compared to the measurement $A(\omega)^{\mathrm{h}}$. Figure previously published [Eason et al. (2017a)].

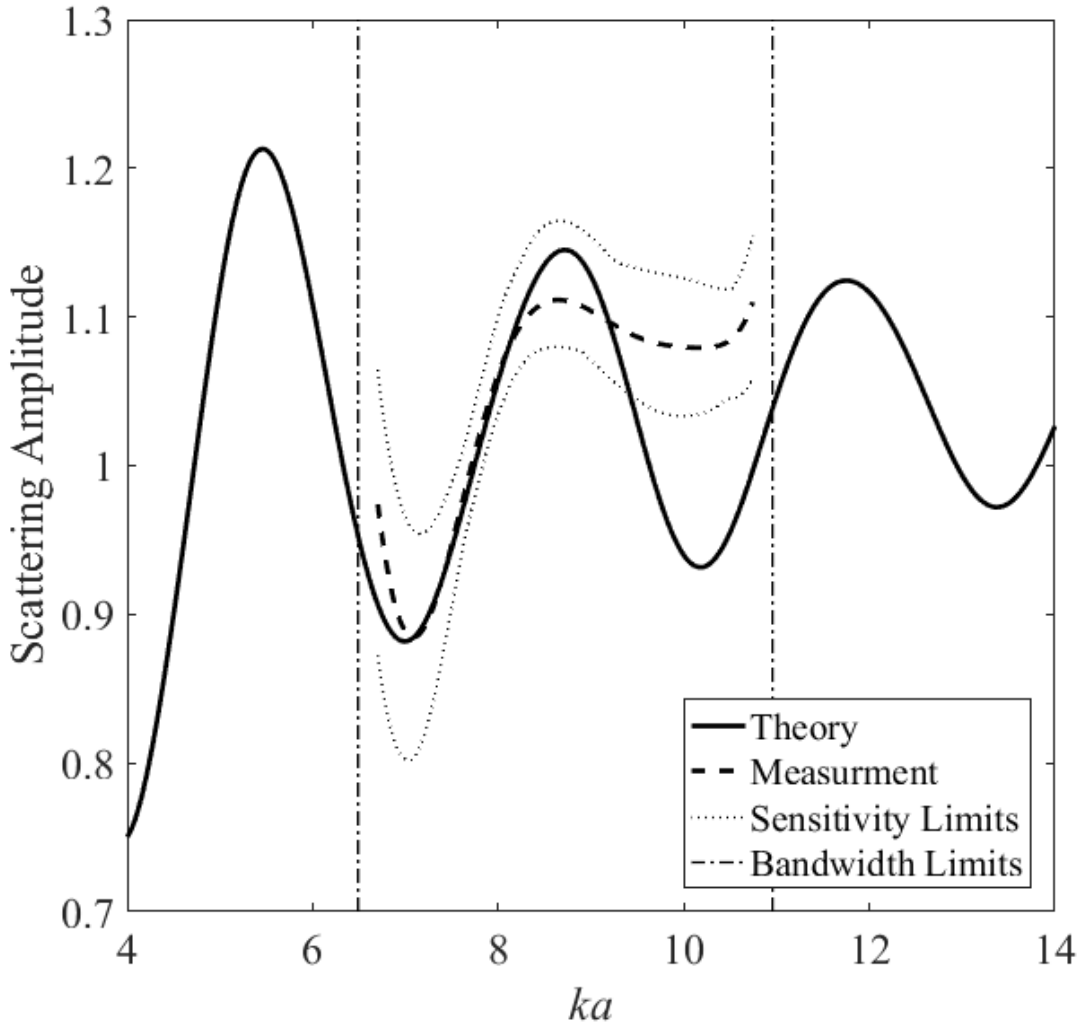

Figure 5.33 Far-field scattering amplitude for a hemispherical pit theory $\mathbf{A}^{\mathrm{h}}$ compared to the measurement $A(\omega)^{\mathrm{h}}$ with different filtering and scaling factors. Figure previously published [Eason et al. (2017a)].

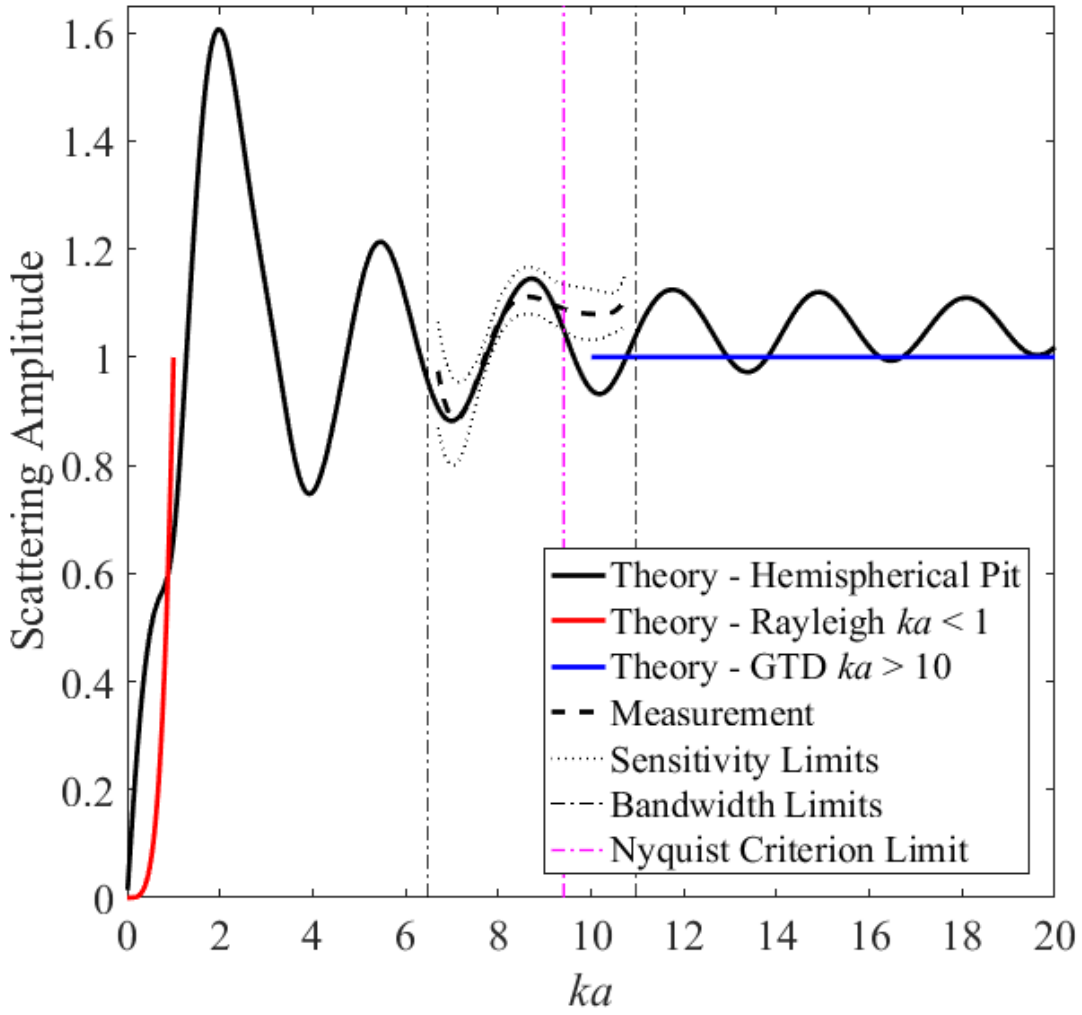

Figure 5.34 The far-field scattering amplitude for a hemispherical pit theory $\mathbf{A}^{\mathrm{h}}$, the Rayleigh scattering theory, and the Geometrical Theory of Diffraction (GTD) are compared to the measurement $A(\omega)^{\mathrm{h}}$ with different filtering and scaling factors along with a conservative Nyquist criterion limit of 11.3 times at $ka = 9.4$ (8.9 MHz).

Another possible explanation for the discrepancy between the scattering amplitude model and the experimental measurement at higher ka values may be potential inconsistency regarding the use of the water path distance as compared to the physical distance between the transducer and flat plate front surface. In the experimental measurements, the water path distance of 114.4 mm is twice the physical distance of 57.2 mm in a pulse-echo configuration. The physical distance or water path distance is applied at various steps in the scattering amplitude validation process for i) the initial calibration block design simulation, ii) generating of the acoustic/elastic transfer function, iii) defining the Multi-Gaussian beam model, iv) determining the reference spectrum, v) collecting the reference measurement, and vi) collecting the pit measurement; this distance may have been defined or applied inconsistently at one or more steps in the process. Preliminary work to try and resolve this possibly inconsistency shows potential for improved agreement between the model and measurement at the larger ka values. This may be explained in part due the frequency dependent location of the near-field. The calculated near-field per Equation 3.1 is 34 mm at 5 MHz, 67 mm at 10 MHz, and 102 mm at 15 MHz. It may be possible that all the steps in the process are outside of the near-field at lower ka values regardless of the use of water path distance or physical distance, however, some steps in the process may fall within the near-field at higher ka values depending on whether the use of water path distance or physical distance is applied.

5.5 Summary

A new theory for the scattering response for a hemispherical pit in a half-space, originally developed in the seismology community, was extended to give the far-field scattering amplitude model for the scattering response of a hemispherical pit in the far wall of a plate. The initial model and experimental data are found to be in good agreement in the ka range from 6.5 to 9. Consideration of the Nyquist sampling criterion may explain why the model and experiment do not match at higher frequency still within the usable bandwidth in the ka range from 9 to 11. If fully validated, the solution to this canonical problem of a half-space with a hemispherical pit could potentially become a new standard geometric reference feature for use in ultrasonic NDE that is more representative of pitting type corrosion.

CHAPTER 6. ELASTIC WAVE SCATTERING - CURVE SURFACE - SINGLE FLAW

The approach developed and reported in Chapter 5 to describe scattering by a hemispherical pit on a flat surface is extended to scattering by a hemispherical pit on a curved surface by applying similar experimentation and analysis methods. Scattering amplitude results are presented for a hemispherical pit on a curved surface from an immersion experiment. The work is extended even further for contact measurement simulation and experiments as described in Chapter 6.

6.1 Measurement and Analysis

This section describes data generated from an immersion transducer experiment in an attempt to validate the hemispherical pit scattering theory on a curved pipe surface.

6.1.1 Experimental Setup

An immersion experiment was conducted on an A106B carbon steel 4-inch nominal calibration pipe specimen of 9.0 ± 0.5 mm thickness and 114.3 ± 1.3 mm outside diameter with a machined hemispherical pit of 2.00 ± 0.005 mm diameter. A picture of the immersion setup is shown in Figure 6.1. A 10 MHz, 0.25 inch diameter immersion probe [PANAMETRICS® V312 S/N 190141] was driven at 150V with a pulse width of 10 ns, at a 1000 Hz pulse repetition rate, with applied gain values of 0 dB, 3 dB, 7 dB, 25 dB, 28dB, and 47dB. The received signals were collected at a 250 MHz sampling frequency with a 1 MHz high pass filter and 20 MHz low pass filter and averaging 128 signals. After normalizing alignment to the pipe surface, an initial system calibration reference experiment was collected at a vertical distance away from

the hemispherical pit, followed by a measurement directly above the pit. The measurements were collected over a 1 hour period where the temperature of the water was monitored to be 22.9°C resulting in a calculated wave speed of 1490.8 m/s [Lubbers and Graaff (1998)]. The measured arrival time of the front surface was 77.0 μs resulting in a water path distance of 114.8 mm. The calculated near-field per Equation 3.1 is 34 mm at 5 MHz, 67 mm at 10 MHz, and 102 mm at 15 MHz.

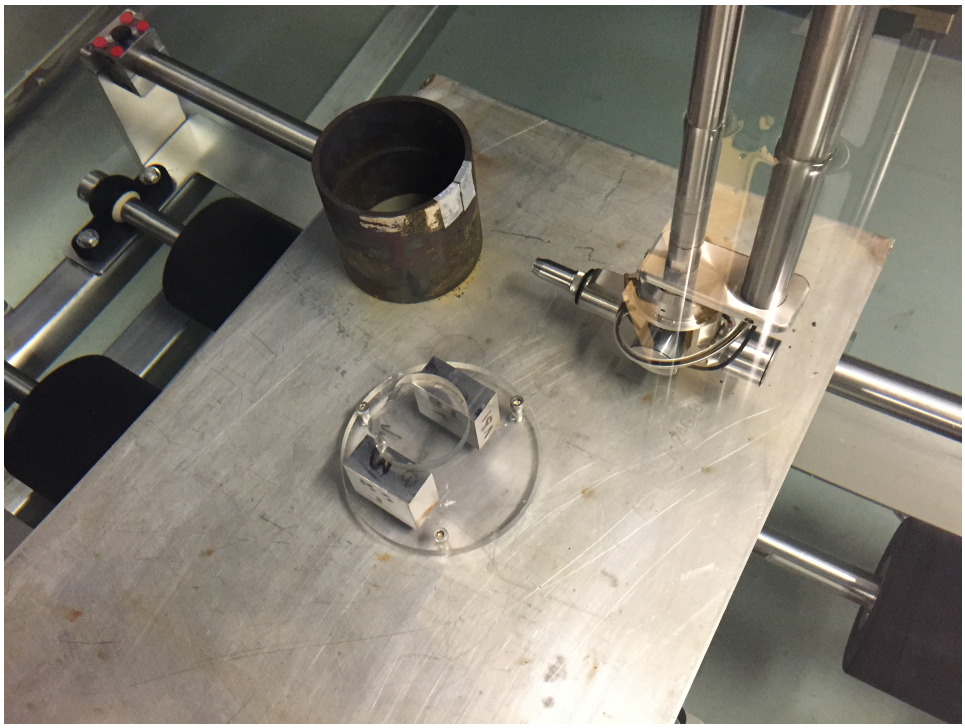

Figure 6.1 Picture of immersion experiment setup showing transducer and calibration test pipe specimen.

6.1.2 Reference Measurements

A reference experiment was completed to establish the system function as described in Equation 5.56. The response signal was collected with a 3 dB gain to achieve maximum amplitude without saturation of the front-wall reflection, and again with a 25 dB gain to achieve maximum amplitude without saturation of the first back-wall reflection. These voltage response signals are shown in Figure 6.2 for the full signal showing up to seven back-wall reflections as well as a region showing just the front-wall and first back-wall.

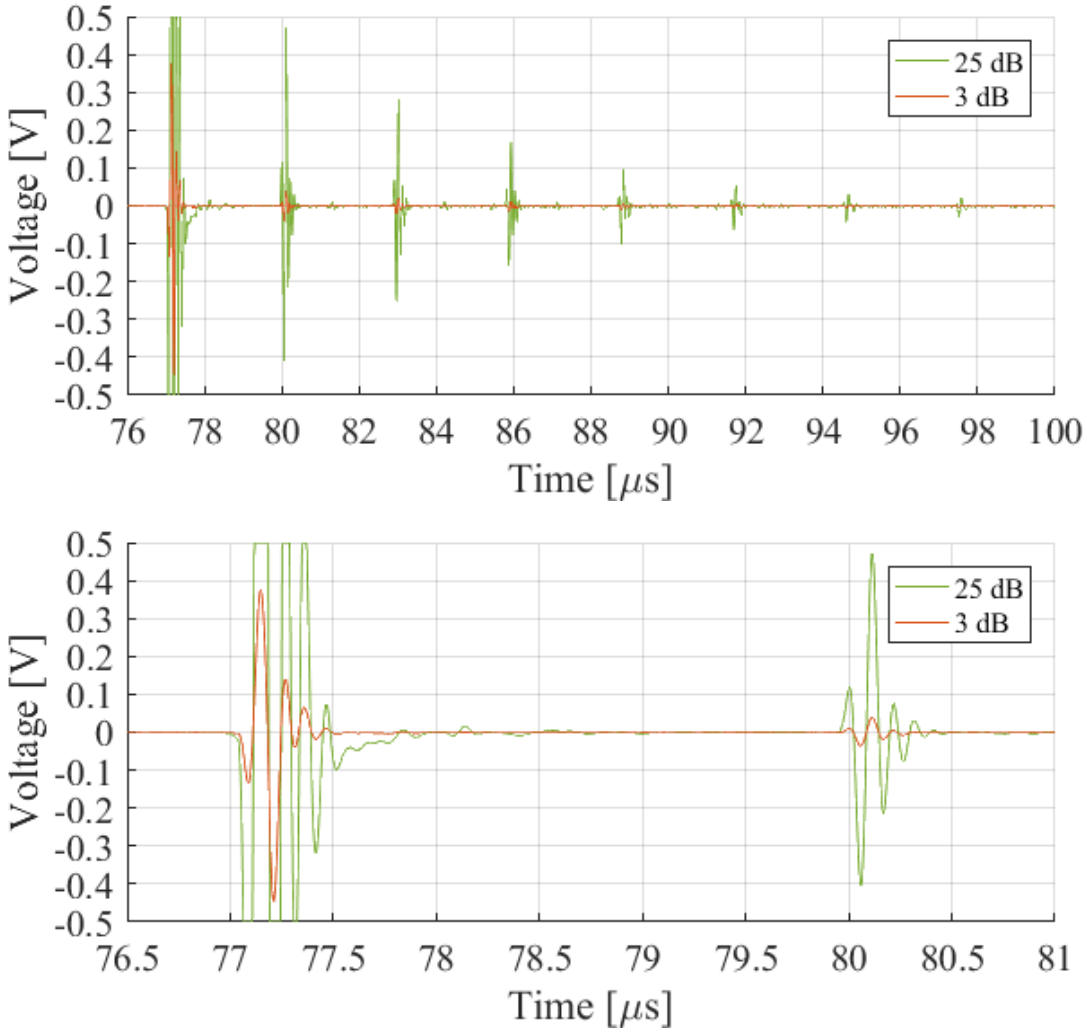

Figure 6.2 Reference measurement time domain voltage signal responses. To avoid saturation, the front-wall response is observed at 3 dB gain and the first back-wall response is observed at 25 dB gain.

6.1.2.1 Longitudinal Wave Speed

The longitudinal wave speed in the steel was calculated from the difference in peak arrival time from multiple back-wall reflection features from the 25 dB signal. These positive and negative peak features are shown as red and blue "o" in Figure 6.3. The front-wall features around 77 μs are not usable due to signal saturation, however, the arrival time difference τ_l between the second ($\approx$80 μs) and third ($\approx$83 μs) back-wall longitudinal features are a divisor in Equation 5.72 to calculate the second back-wall reflection number longitudinal wave speed c_l for both positive and negative peaks per Equation 5.72 with $t = 9.0$ mm as the pipe wall thickness. This process is repeated for the subsequent back-wall longitudinal features with resulting longitudinal wave speeds shown in Figure 6.4. The seventh back-wall longitudinal features are ignored as slightly outlying data points, the remaining values are averaged resulting in a calculated longitudinal wave speed of 6186 m/s.

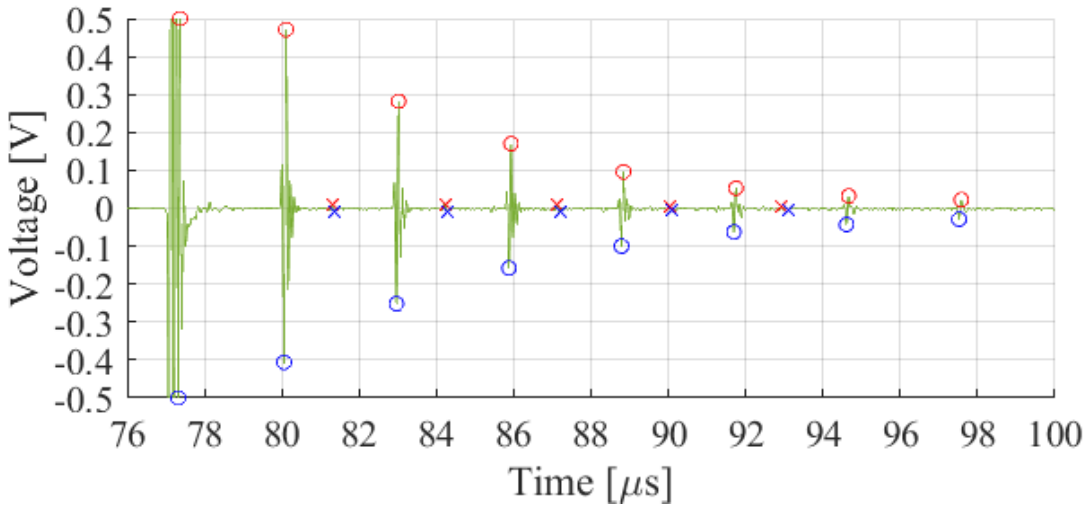

Figure 6.3 Reference measurement time domain voltage signal response with 25 dB gain showing the longitudinal mode signal features used to calculate the longitudinal wave speed in the steel pipe.

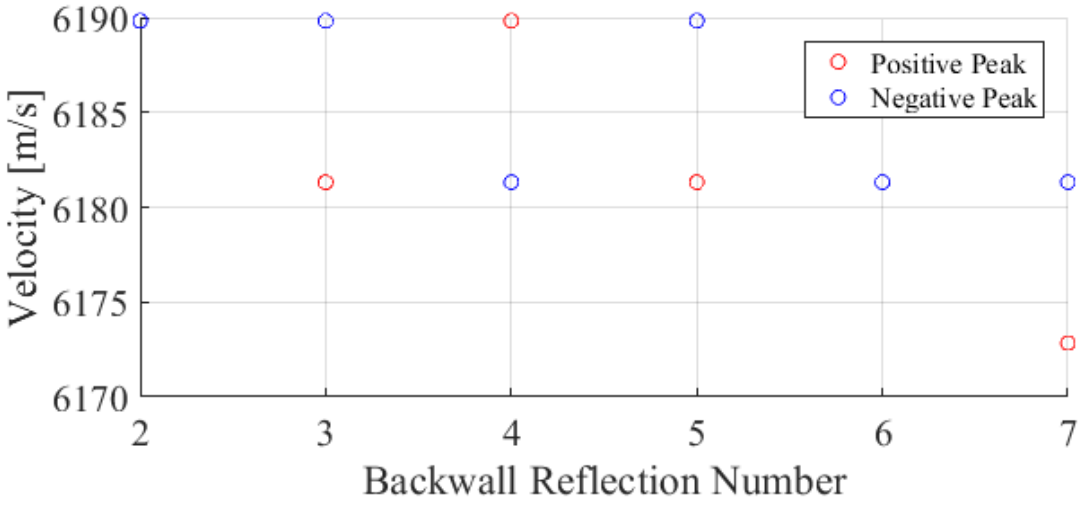

Figure 6.4 Calculated individual wave speed values from each back-wall reflection used to determine the longitudinal wave speed in the steel pipe.

6.1.2.2 Shear Wave Speed

The shear wave speed in the steel was calculated from the arrival time of multiple mode converted back-wall refection features from the 25 dB signal. These positive and negative peak features are shown as red and blue "×" in Figure 6.5. The features around 81 μs are from a mode converted signal where the incident mode on the first back-wall is longitudinal and the reflected mode is shear, or the incident mode on the first back-wall is shear and the reflected mode is longitudinal, summarized as having one path longitudinal and one path shear. The second back-wall mode converted features around 84 μs are when three out of the four paths within the steel are of longitudinal mode and one path is of shear mode. The arrival time difference τ_s between the first back-wall mode converted features ($\approx$81 μs) and front-wall features ($\approx$77 μs) are not usable due to front-wall signal saturation, however, the arrival time difference τ_s of the second back-wall mode converted features ($\approx$84 μs) and first back-wall longitudinal features ($\approx$80 μs) are used in Equation 5.73 to calculate shear wave speed with τ_L as the longitudinal path arrival time defined in Equation 5.74 with c_L as the previously determined longitudinal wave speed of 6186 m/s. This process is repeated for the subsequent back-wall mode converted features with resulting shear wave speeds shown in Figure 6.6. The fifth back-wall mode converted features

are ignored as slightly outlying data points, the remaining values are averaged resulting in a calculated shear wave speed of 3330 ± 24 m/s. The longitudinal to shear wave speed ratio is 1.86 for the steel calibration pipe; this value is slightly greater than the flat plate material in Chapter 5 with a longitudinal to shear wave speed ratio of 1.82.

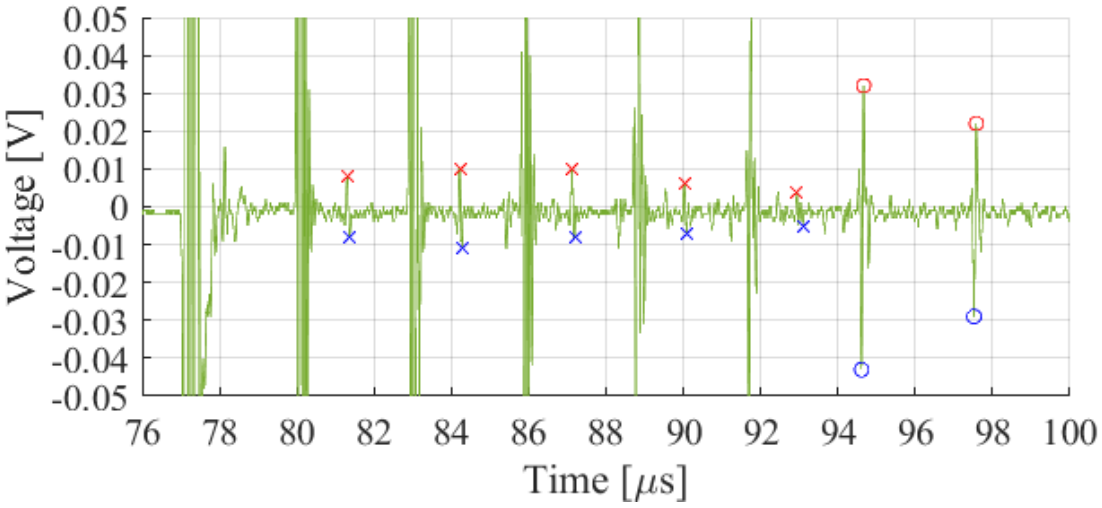

Figure 6.5 Reference measurement time domain voltage signal response with 25 dB gain showing the mode converted signal features used to calculate the shear wave speed in the steel pipe.

6.1.2.3 Frequency Domain

The front-wall and all back-wall reflection signals were gated to have 152 voltage measurements at a 0.004 μs interval over a 0.608 μs time period. First, each signal was subtracted from its mean to remove any DC offset. Next, a Tukey window function [Harris (1978)] was applied to each signal in order to smooth the transitions to a zero voltage level. The Tukey window had 25% as a transition from 0 to 1, 50% equal to 1, and 25% as a transition from 1 to 0. Next, 24848 zeros were padded to the end of each signal to bring the total signal length to 100 μs while retaining the 0.004 μs interval. Finally, each signal was subtracted from its mean again. The resulting processed time domain signals for the front-wall and back-wall reflections are shown in Figures 6.7 and 6.8 for 25 dB and 3 dB signals. The 25 dB front-wall signal is not shown due to saturation.

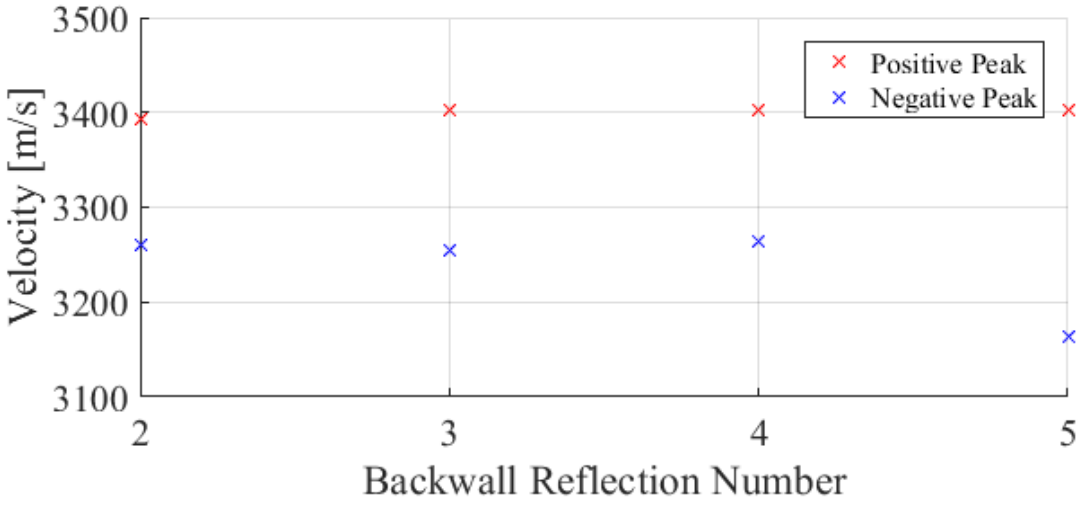

Figure 6.6 Calculated individual wave speed values from each back-wall reflection used to determine the shear wave speed in the steel pipe.

A FFT function was applied to convert each time domain signals to frequency domain spectral magnitude by applying the "ifft" function in MATLAB®, multiplying by the 100 μs signal length, and taking the absolute value [Schmerr (2016)]. The full frequency domain results contain 250000 points from 0-250 MHz at a 0.01 MHz interval, however only the values from 0-20 MHz are considered and plotted in Figures 6.7 and 6.8 for the 25 dB and 3 dB signals. The 25 dB front-wall signal is not shown due to saturation. The plots identify the spectral peaks as "o" and are typically between 9-10 MHz. The -6 dB amplitude bandwidth is defined as the voltage values within 50.1% of the spectral peak voltage; the plots identify the bandwidth limits as "+" and the ranges are typically between 5-11 MHz.

Only the reference experiment 3 dB front-wall, 3 dB first back-wall, and 25 dB first back-wall frequency domain signals are used to determine the system function. The -6 dB amplitude bandwidth values for these signals are listed in Table 6.1 for the reference experiment as well as the 25 dB first back-wall signal from the pit experimental measurement. The conservative bandwidth range is consistently used on all frequency domain plots from the curved pipe sample.

Table 6.1 Reference and Pit Experiment Amplitude Bandwidth

Experiment	Signal	Lower Limit	Maximum	Upper Limit
Reference	3 dB Front-wall	3.42 MHz	8.51 MHz	11.03 MHz
Reference	3 dB 1st Back-wall	4.50 MHz	9.06 MHz	11.53 MHz
Reference	25 dB 1st Back-wall	4.64 MHz	9.10 MHz	11.55 MHz
Pit	25 dB 1st Back-wall	4.47 MHz	9.22 MHz	11.02 MHz
Conservative Range		**4.64 MHz**		**11.02 MHz**

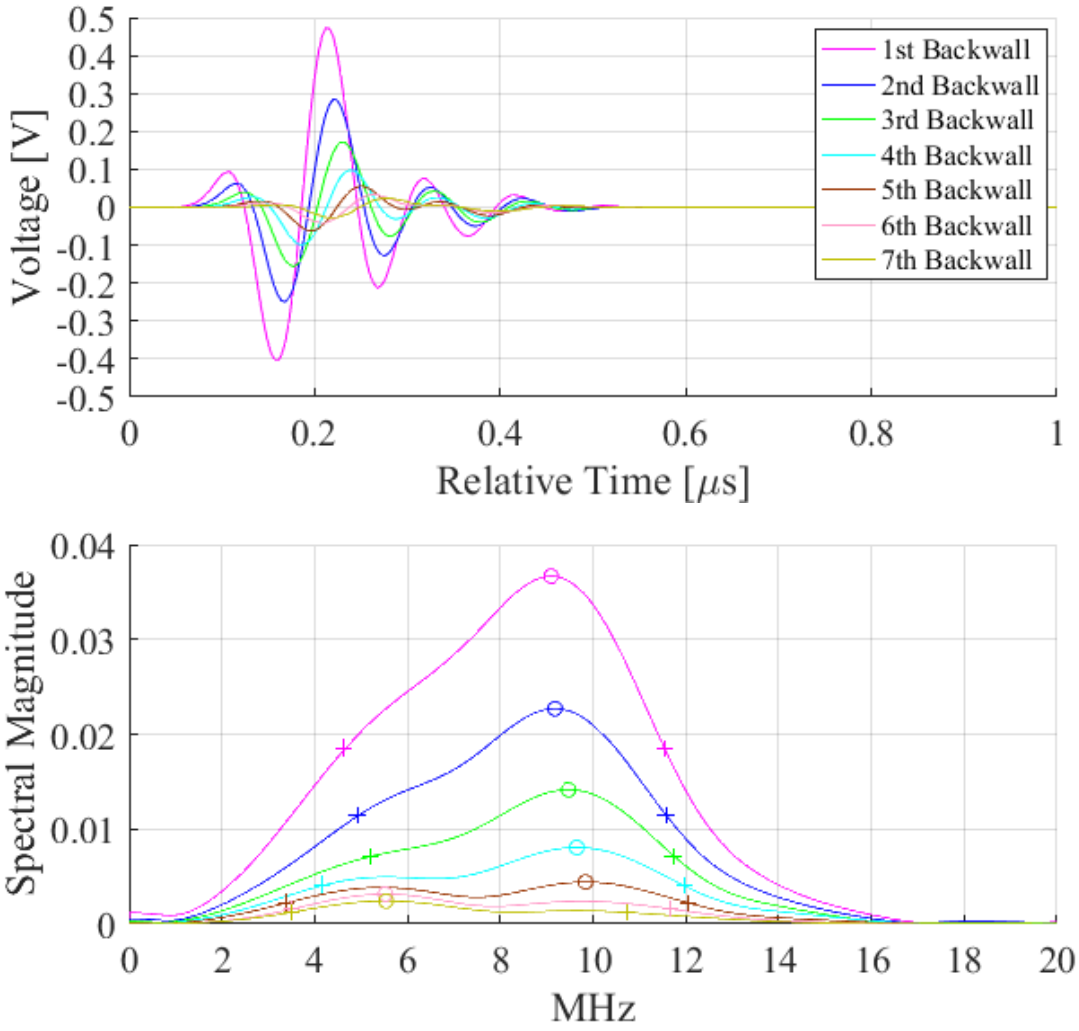

Figure 6.7 Reference measurement gated time and frequency domain for multiple back-wall response signals with 25 dB gain. The front-wall response signal is not shown due to signal saturation.

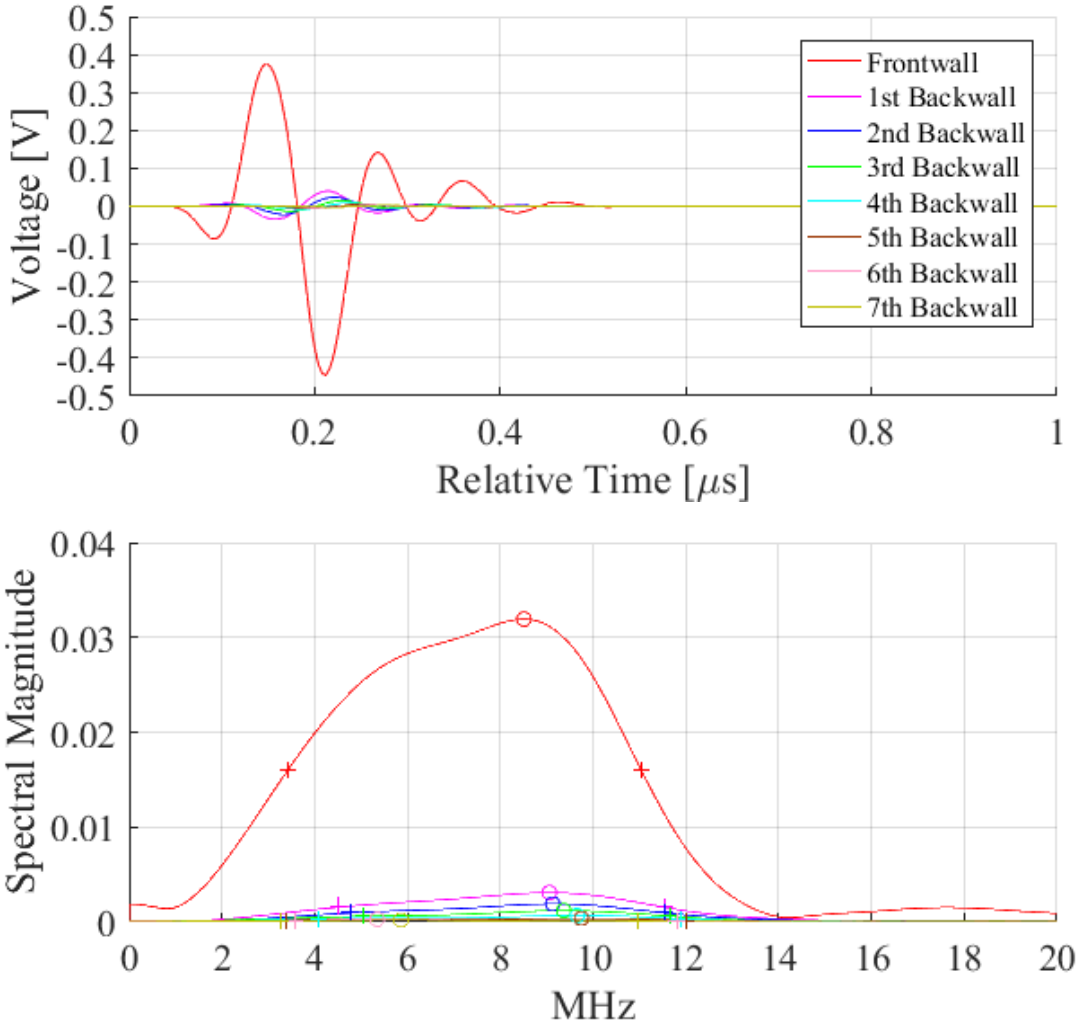

Figure 6.8 Reference measurement gated time and frequency domain for front-wall and multiple back-wall response signals with 3 dB gain.

6.1.2.4 Acoustic/Elastic Transfer Function

The reference acoustic/elastic transfer function as described in Equation 5.58 is calculated for the immersion transducer experiment. The absolute value of the acoustic elastic transfer function is shown in Figure 6.9 using the following values: $\rho_1 = 997.6$ kg/m^3, $\rho_2 = 7860$ kg/m^3, $c_{11} = 1490.8$ m/s, $c_{l2} = 6185.5$ m/s, $R_{12} = .94$, $a = 0.003$ m, ω evaluated over the same range from 0-3.18 $\times 10^6$ angular frequency [rad/s] equivalent to f over a range of 0-20 MHz, $D = 0.1448$ m, and $\alpha_1(f) = 25.3 \times 10^{-3} f^2$ Nepers/m. The calibration pipe specimen density ρ_1 was not measured, but provided from a standard reference table; coincidentally, this value is very similar to the flat block specimen measured material density of 999 kg/m^3 as described in Chapter 5.

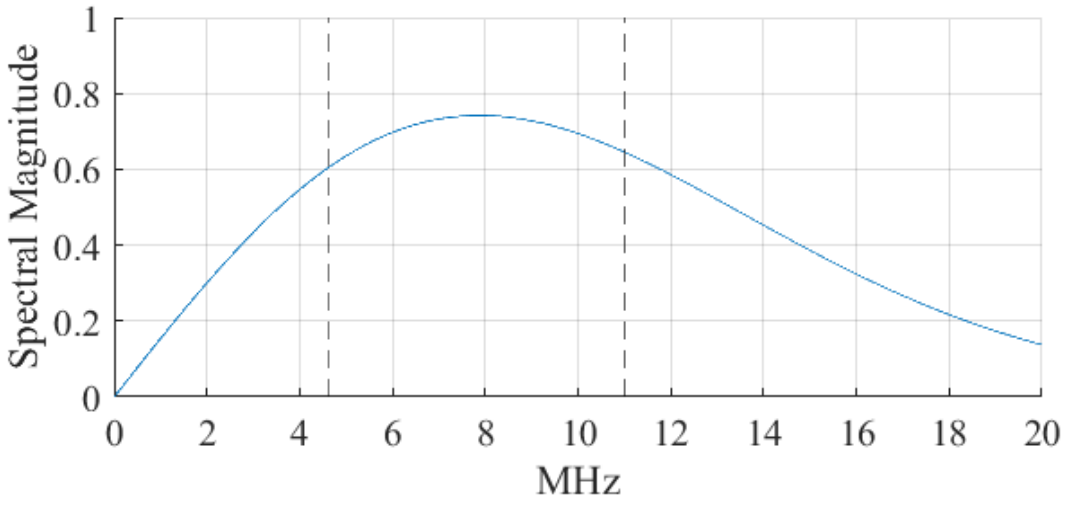

Figure 6.9 Acoustic/elastic transfer function t_A from Equation 5.58.

6.1.2.5 System Function

The system function described in Equation 5.61 is shown in Figure 6.10 using the 25 dB first back-wall reflected signal for various Weiner filter constant values. The system function with a Weiner filter constant value of $\epsilon_s = 0.10$ was used.

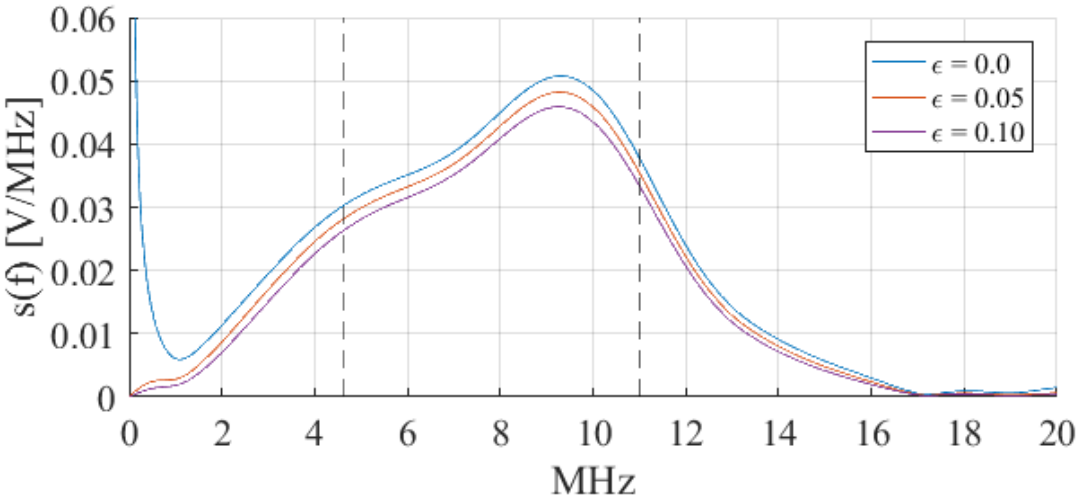

Figure 6.10 System function s from Equation 5.61. Specific immersion setup system function for Weiner filter noise level constant values of $\epsilon_s = 0.0$, $\epsilon_s = 0.05$, and $\epsilon_s = 0.10$.

6.1.2.6 Attenuation in Steel Sample

The front-wall and first back-wall frequency domain values from the 3dB signal shown in Figure 6.8 are applied to Equation 5.75 for three ϵ_α values as shown in Figure 6.11. A linear fit is applied to the curves within the bandwidth range from 4.64 to 11.02 MHz. The $\epsilon_\alpha = 0.02$ Weiner filter constant provides the best least squares regression linear fit; the resulting longitudinal attenuation coefficient for this particular steel is the empirical Equation 6.1 for the tested bandwidth range in dB/mm.

$$\alpha_2 = -0.0443f + 1.5283 \tag{6.1}$$

While the attenuation coefficient values should be increasing with frequency, the measured results are relatively flat to slightly decreasing. This may be due to unaccounted curvature effects exacerbated by the relatively large ratio of curvature to sample thickness. However, while the trend is incorrect, the values are close to previously reported attenuation coefficients [Smith et al. (1981)]. The actual attenuation values for $\epsilon_\alpha = 0.02$ will be used as opposed to the linear approximation.

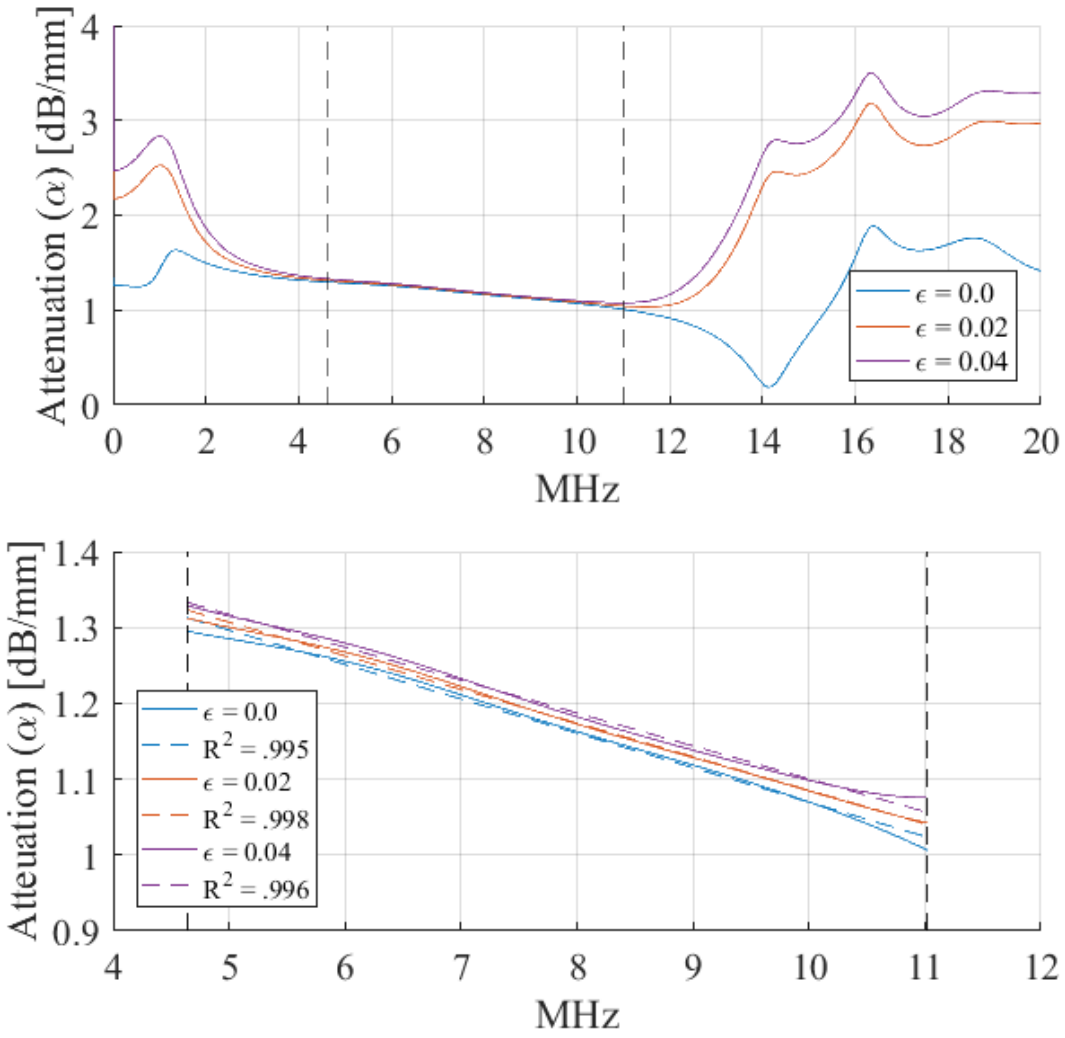

Figure 6.11 Attenuation α from Equation 5.75 for Weiner fileter noise level constant values of $\epsilon_\alpha = 0.0$, $\epsilon_\alpha = 0.02$, and $\epsilon_\alpha = 0.04$.

6.1.2.7 Multi-Gaussian Beam Model

The ideal velocity ratio field term from Equation 5.67 was determined from the Multi-Gaussian beam model. The longitudinal wave mode for material 1 (water) and the longitudinal wave mode for material 2 (steel) was used with the previously mentioned density and wave speed material property values. The transducer diameter was $d = 6$ mm with an infinite focal length. The distance traveled in the water was $D = 114.8$ mm and in the steel was $z_2 = t = 9$ mm. The geometric curvature was a radius of 51.75 mm along the vertical perpendicular direction. Velocity ratio measurements were calculated over a range of -50 mm to +50 mm in the vertical (Y direction) and horizontal (X direction) perpendicular distances from the central ray axis. The transducer was positioned at a normal angle of incidence.

The ideal velocity ratio was evaluated at the flaw location at $z_2 = t$ for only the first ten Wen and Breazeale Coefficients over a frequency range from 0-20 MHz as shown in Figures 6.12, 6.16, 6.20, 6.24, and 6.28 for a corresponding range of spatial resolution values of 10 mm (121 points), 5 mm (441 points), 2 mm (2601 points), 1 mm (10201 points), and 0.5 mm (40401 points). The solid black lines indicate the velocity ratio for each individual spatial location. The black dotted line indicates the velocity ratio at the central ray location (which is also the maximum velocity ratio at each frequency). The green dotted line indicates the average velocity ratio for values above the -6 dB amplitude bandwidth of the maximum velocity ratio at each frequency. The blue dotted line indicates the average velocity ratio for values above a noise floor of 10% of the maximum velocity ratio at each frequency. The red dotted line indicates a numerically evaluated trapezoid integral method to determine the average velocity ratio for values above a noise floor of 10%. Spatial domain velocity ratio field plat at the flaw location for the conservative lower bandwidth limit (4.64 MHz), the peak frequency value of the 25 dB system first back-wall response (9.10 MHz), and the conservative upper bandwidth limit (11.02 MHz) are shown in Figures 6.13-6.15, 6.17-6.19, 6.21-6.23, 6.25-6.27, and 6.29-6.31.

A common assumption is such that the velocity ratio does not vary much over the response surface of the flaw and that the central axis (maximum) velocity ratio is used. However, the new hemispherical pit scattering theory incorporates scattering from the stress-free half-

space boundary surface in addition to scattering from the pit surface. In this application, the maximum velocity ratio may be too large, and a -6dB average, >10% integral average, or other velocity ratio values may be a better approximation. Regardless, for consistency, the maximum velocity ratio is used in this study, but additional work may be necessary to explore other options.

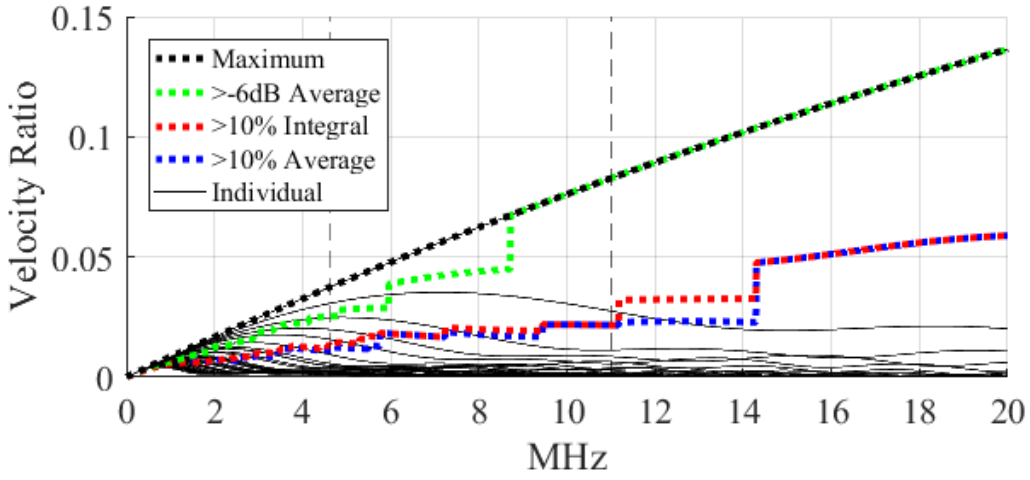

Figure 6.12 Ideal velocity ratio calculation methods from the Multi-Gaussian beam model at the flaw location with 10 mm spatial resolution.

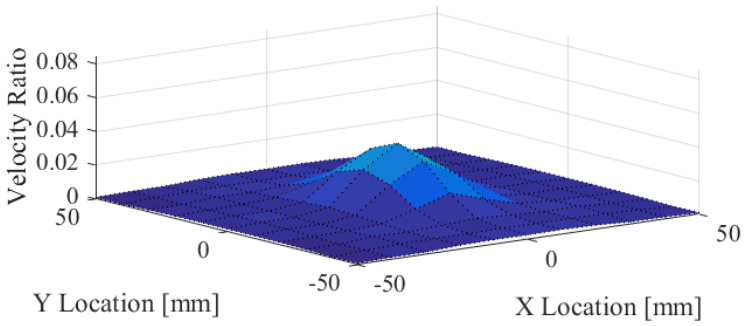

Figure 6.13 Multi-Gaussian beam model ideal velocity ratio field at the flaw location at the lower bandwidth frequency limit of 4.64 MHz with 10 mm spatial resolution.

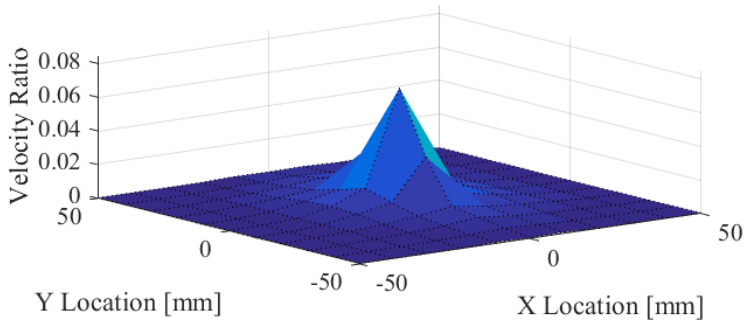

Figure 6.14 Multi-Gaussian beam model ideal velocity ratio field at the flaw location at the reference measurement 25 dB first back-wall response signal peak frequency of 9.10 MHz with 10 mm spatial resolution.

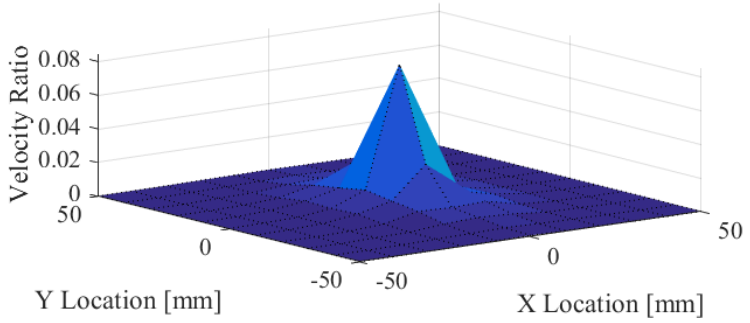

Figure 6.15 Multi-Gaussian beam model ideal velocity ratio field at the flaw location at the upper bandwidth frequency limit of 11.02 MHz with 10 mm spatial resolution.

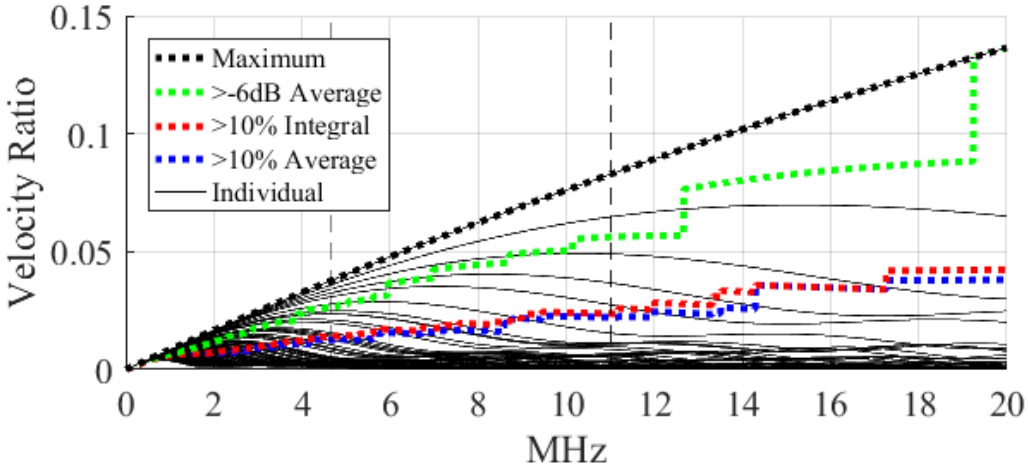

Figure 6.16 Ideal velocity ratio calculation methods from the Multi-Gaussian beam model at the flaw location with 5 mm spatial resolution.

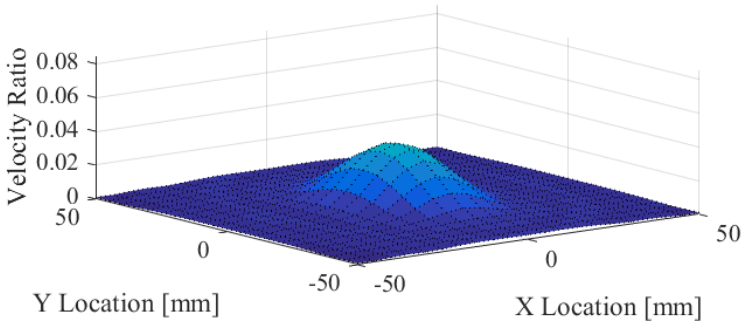

Figure 6.17 Multi-Gaussian beam model ideal velocity ratio field at the flaw location at the lower bandwidth frequency limit of 4.64 MHz with 5 mm spatial resolution.

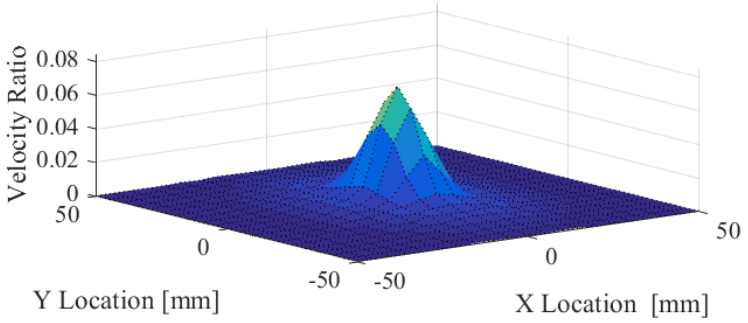

Figure 6.18 Multi-Gaussian beam model ideal velocity ratio field at the flaw location at the reference measurement 25 dB first back-wall response signal peak frequency of 9.10 MHz with 5 mm spatial resolution.

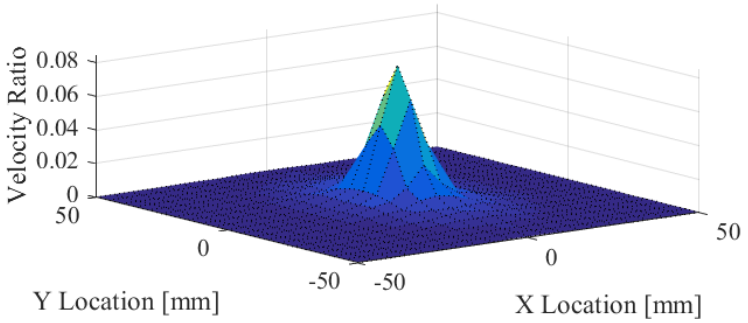

Figure 6.19 Multi-Gaussian beam model ideal velocity ratio field at the flaw location at the upper bandwidth frequency limit of 11.02 MHz with 5 mm spatial resolution.

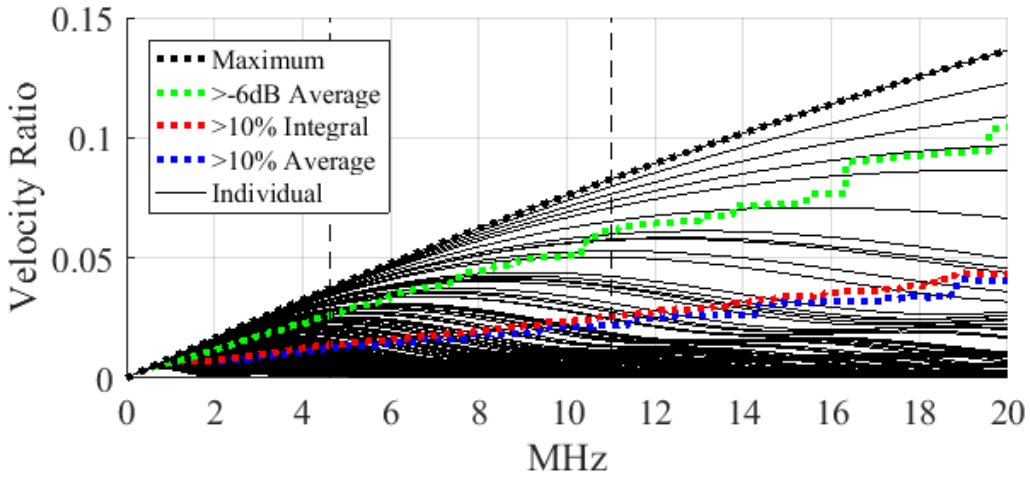

Figure 6.20 Ideal velocity ratio calculation methods from the Multi-Gaussian beam model at the flaw location with 2 mm spatial resolution.

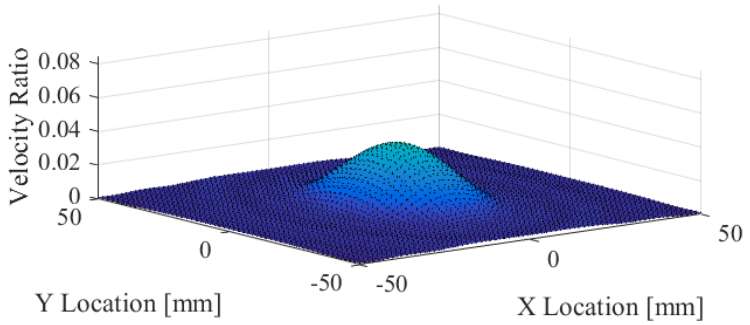

Figure 6.21 Multi-Gaussian beam model ideal velocity ratio field at the flaw location at the lower bandwidth frequency limit of 4.64 MHz with 2 mm spatial resolution.

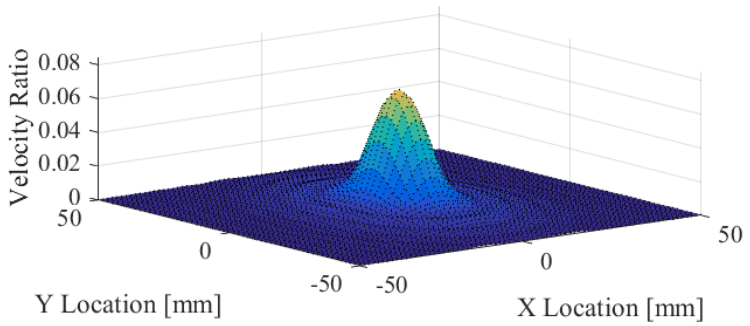

Figure 6.22 Multi-Gaussian beam model ideal velocity ratio field at the flaw location at the reference measurement 25 dB first back-wall response signal peak frequency of 9.10 MHz with 2 mm spatial resolution.

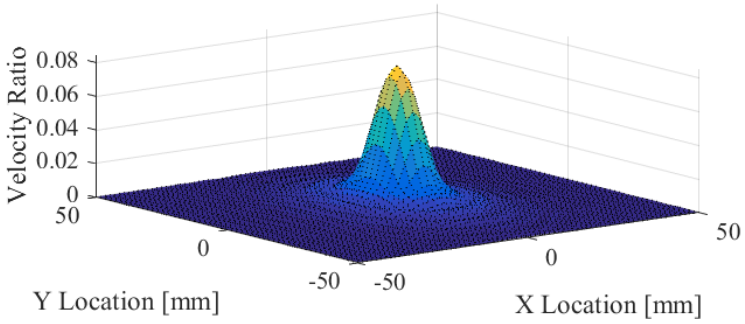

Figure 6.23 Multi-Gaussian beam model ideal velocity ratio field at the flaw location at the upper bandwidth frequency limit of 11.02 MHz with 2 mm spatial resolution.

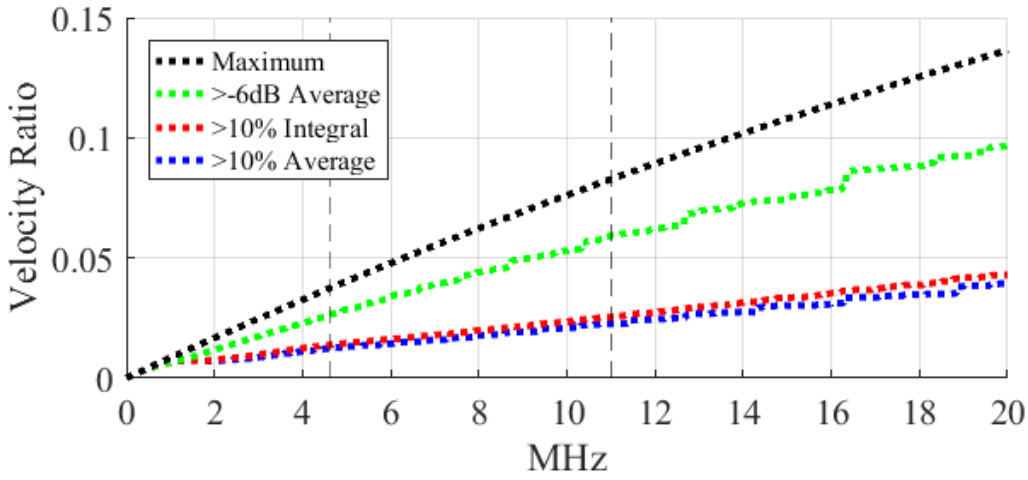

Figure 6.24 Ideal velocity ratio calculation methods from the Multi-Gaussian beam model at the flaw location with 1 mm spatial resolution.

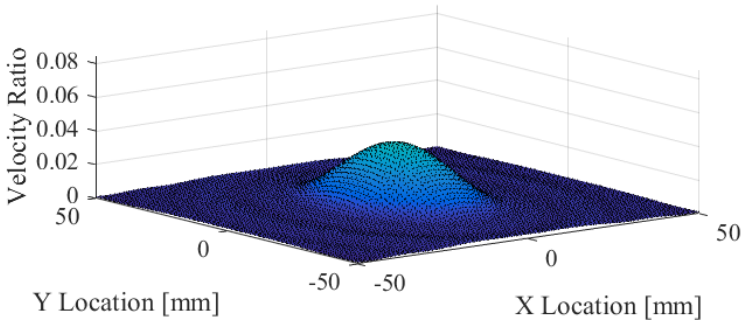

Figure 6.25 Multi-Gaussian beam model ideal velocity ratio field at the flaw location at the lower bandwidth frequency limit of 4.64 MHz with 1 mm spatial resolution. Figure previously published [Eason et al. (2017b)].

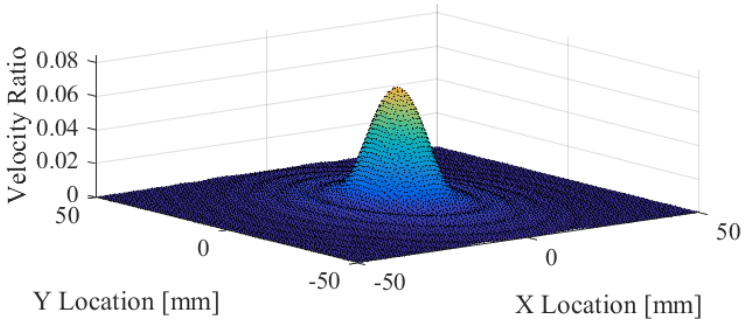

Figure 6.26 Multi-Gaussian beam model ideal velocity ratio field at the flaw location at the reference measurement 25 dB first back-wall response signal peak frequency of 9.10 MHz with 1 mm spatial resolution.

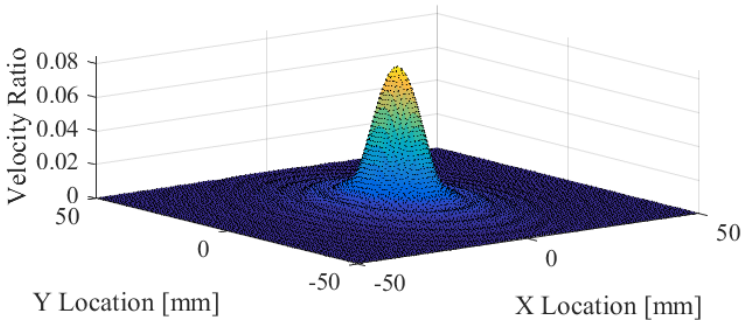

Figure 6.27 Multi-Gaussian beam model ideal velocity ratio field at the flaw location at the upper bandwidth frequency limit of 11.02 MHz with 1 mm spatial resolution. Figure previously published [Eason et al. (2017b)].

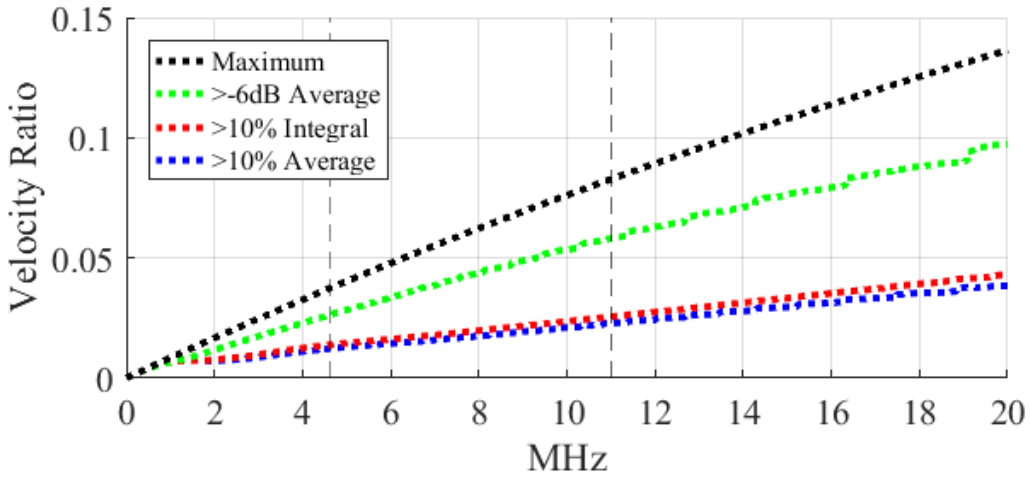

Figure 6.28 Ideal velocity ratio calculation methods from the Multi-Gaussian beam model at the flaw location with 0.5 mm spatial resolution.

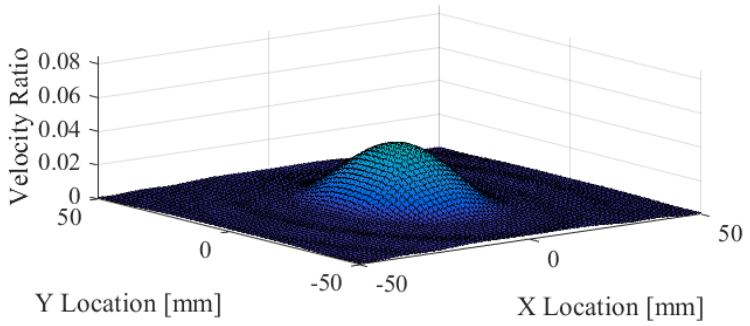

Figure 6.29 Multi-Gaussian beam model ideal velocity ratio field at the flaw location at the lower bandwidth frequency limit of 4.64 MHz with 0.5 mm spatial resolution.

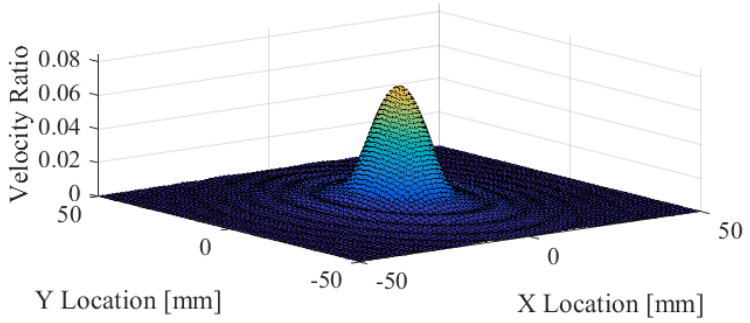

Figure 6.30 Multi-Gaussian beam model ideal velocity ratio field at the flaw location at the reference measurement 25 dB first back-wall response signal peak frequency of 9.10 MHz with 0.5 mm spatial resolution.

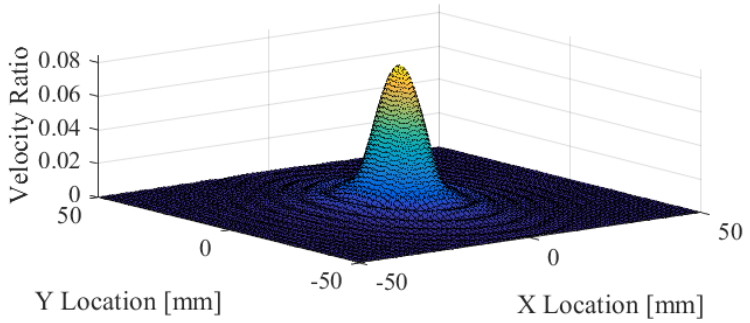

Figure 6.31 Multi-Gaussian beam model ideal velocity ratio field at the flaw location at the upper bandwidth frequency limit of 11.02 MHz with 0.5 mm spatial resolution.

6.1.2.8 Reference Spectrum

The incident velocity $\hat{V}_0^{(1)}(\omega)$ at the flaw location is required to determine the reference spectrum $G(\omega)$ at the flaw location described in Equations 5.64-5.66. The velocity field is related to the normal derivative of the pressure field as defined in Equation 5.68. The incident velocity (at the flaw location) is a product of three parameters: attenuation in water, attenuation in steel, and the ideal velocity ratio at the flaw location as described in Equation 5.67. The values of each of the three parameters are shown for comparison in Figure 6.32 with the resulting incident velocity at the flaw location shown in Figure 6.33. The corresponding $E(\omega)$ and reference spectrum $G(\omega)$at the flaw location from Equations 5.65 and 5.64 are shown in Figures 6.34 and 6.35 correspondingly. The water attenuation term used in Equation 5.67 is defined as $\alpha_1(f) = 25.3 \times 10^{-3} f^2$ Nepers/m [Schmerr (2016)]; the steel attenuation term from Equation 5.67 is determined experimentally as described in Equation 5.75 [Schmerr (2016)]. The 22.9°C water temperature is not a factor in the water attenuation calculation. Similarly, the 22.9°C steel temperature is not a factor in the experimental determined steel attenuation, but this attenuation value may not be applicable at other temperatures.

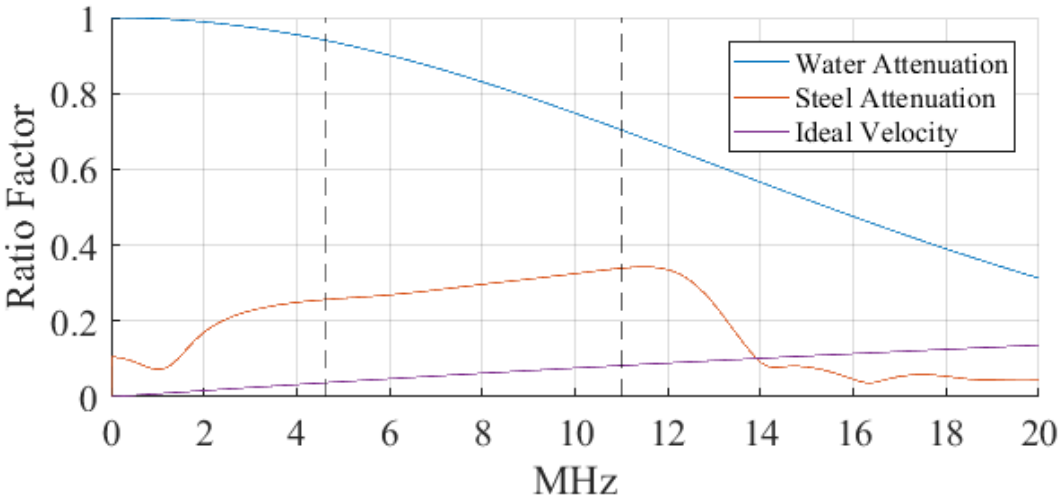

Figure 6.32 Parameters that influence the incident velocity $\hat{V}_0^{(1)}(\omega)$ at the flaw location are shown as water attenuation $e^{-\alpha_1(\omega)D}$, steel attenuation $e^{-\alpha_{l2}(\omega)z_2}$, and ideal velocity $\frac{V_{li}}{v_0}$ at the flaw location.

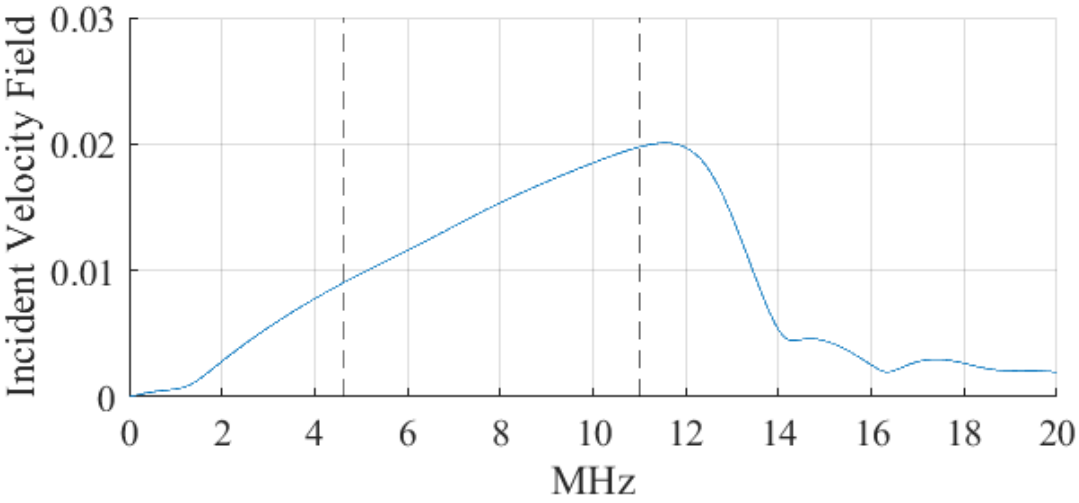

Figure 6.33 Incident velocity $\hat{V}_0^{(1)}(\omega)$ at flaw location from Equation 5.67.

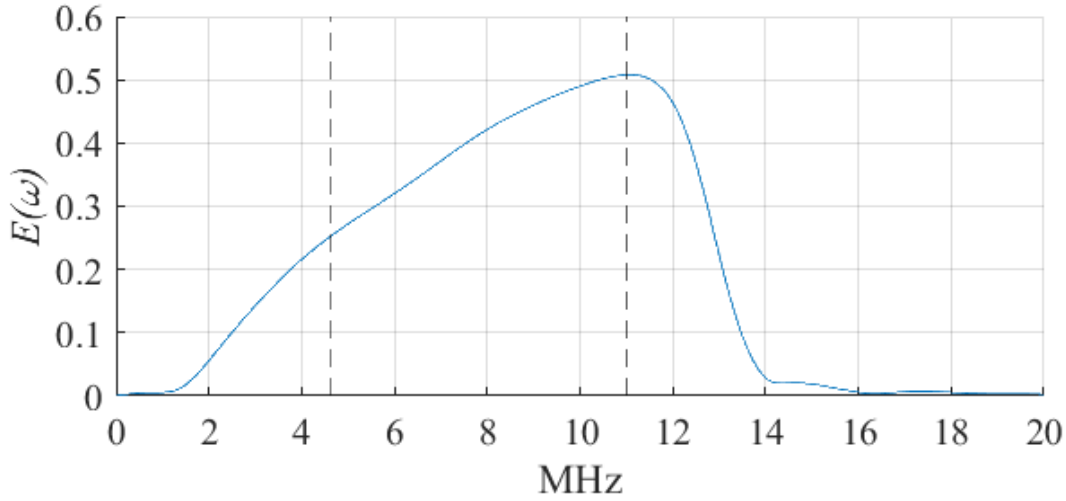

Figure 6.34 $E(\omega)$ at flaw location from Equation 5.65.

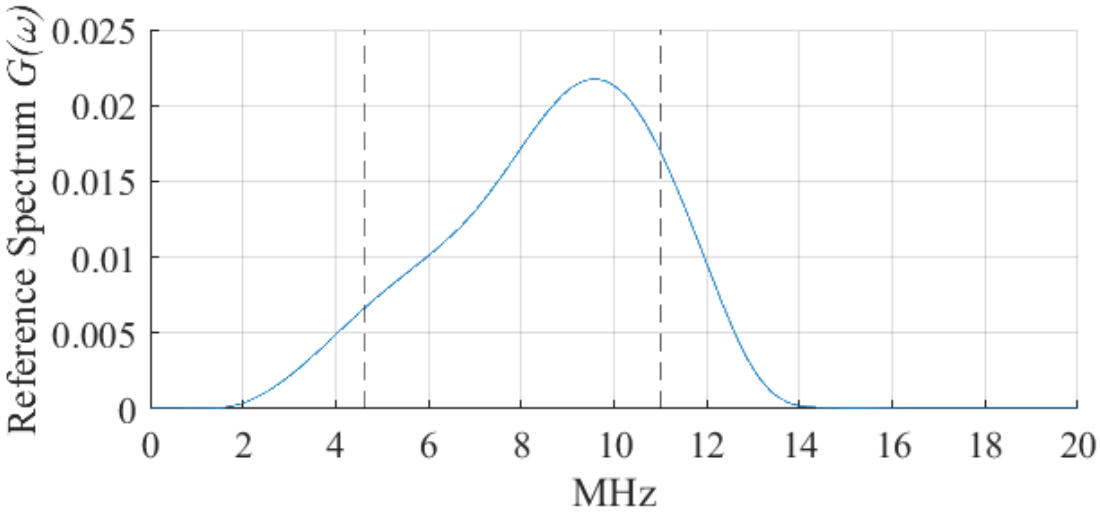

Figure 6.35 Reference spectrum $G(\omega)$ at flaw location from Equation 5.64.

6.1.3 Pit Measurements

After the reference spectrum has been established at the location of the flaw from the reference experiment, the next step is to analyze the data collected from the pit measurement experiment. The data is presented in the time domain comparing the reference measurement response at 25 dB gain and the pit measurement response at 25 dB gain as shown in Figure 6.36. The pit measurement was shifted by 44 ns for better alignment. The signal scattered from the pit is observable as a decrease in amplitude in first back-wall reflection at 80.25 μs as well as the appearance of a smaller response just before the first back-wall at 79.75 μs.

6.1.3.1 Frequency Domain

The time and frequency domain of the first back-wall response is shown in Figure 6.37. This time domain window includes scattering from the pit as well as the back-wall as consistent with the hemispherical pit scattering theory. The same signal processing methods are applied to achieve the frequency domain plot with similar -6 dB from peak usable bandwidth range.

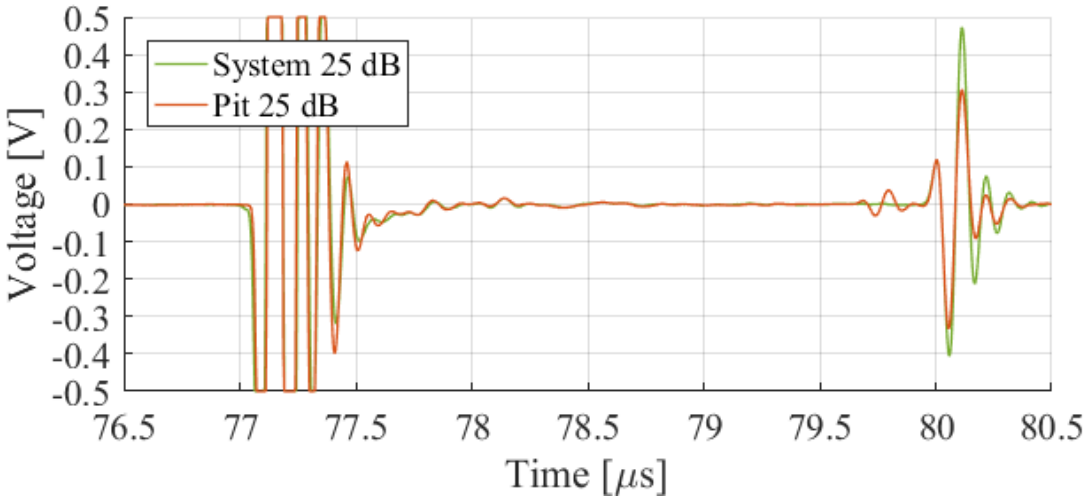

Figure 6.36 Reference and pit measurement time domain voltage signal responses at 25 dB gain. Figure previously published [Eason et al. (2017b)].

6.2 Results

The curved surface scattering amplitude results and a curvature effects comparison of the attenuation and scattering amplitude measurements are discussed.

6.2.1 Scattering Amplitude

Applying Equations 5.69 and 5.70 result in the far-field scattering amplitude $A(\omega)^{\mathrm{h}}$ for $L = 0.1$ cm (1 mm) pit radius flaw size as shown in Figure 6.38 for various ϵ values. The value of $\epsilon_A = 0.04$ was used as a reasonable noise filter level. The far-field scattering amplitude results are compared with theory as shown in Figure 6.39 for the longitudinal to shear wave speed ratio of 1.86 measured in the experiment. While the measured hemispherical pit curved surface scattering amplitude is not an exact match to the theory, the periodicity of the hemispherical pit curved surface measurement is similar to that of the hemispherical pit theory, as compared to the embedded spherical cavity theory. A frequency domain shift of $ka = 1$ of the measured results brings a much closer alignment with theory as shown in Figure 6.40, but still with some discrepancy in the upper $9 \leq ka \leq 11$ range. This discrepancy could be a result of measurement error, incorrect theory, or incorrect methods to transfer the received voltage to a scattering

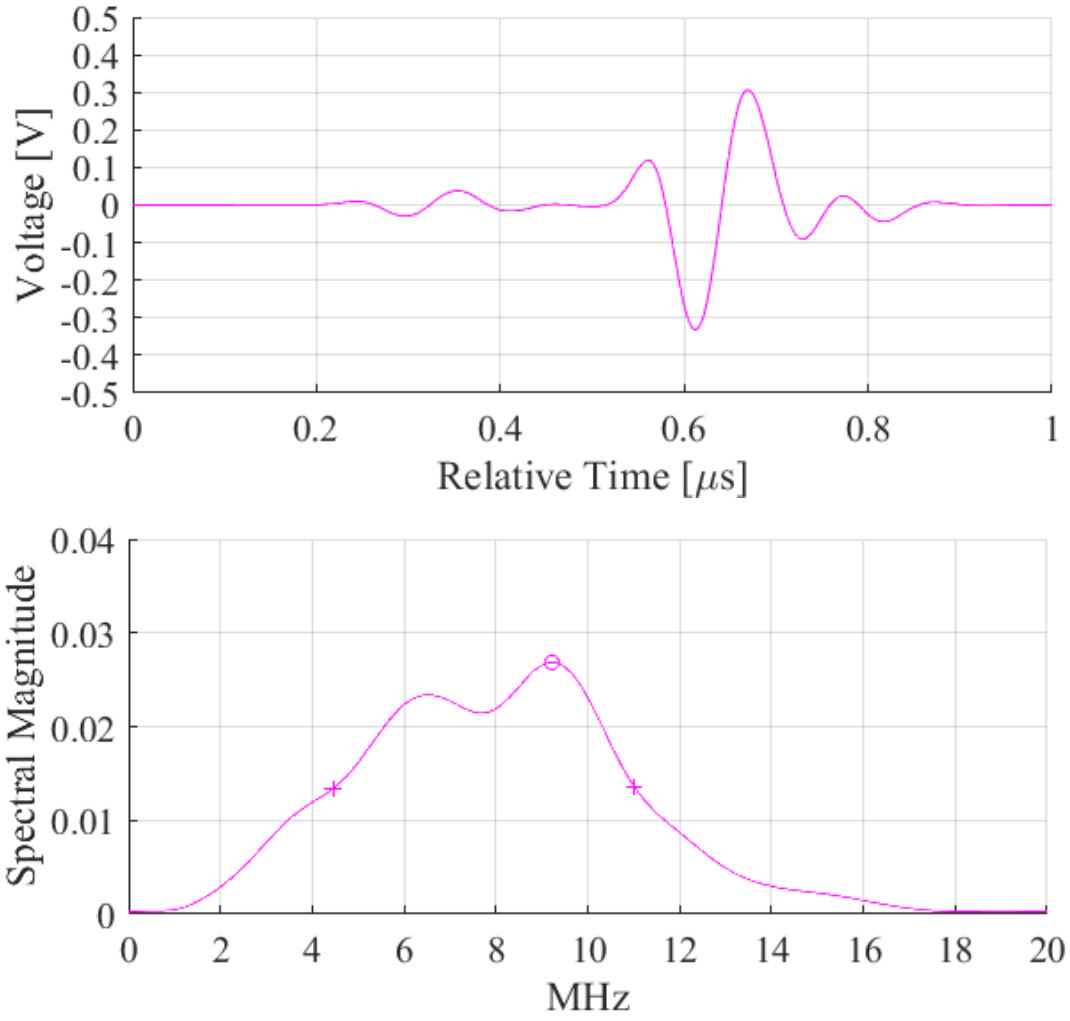

Figure 6.37 Pit measurement experiment gated time and frequency domain first back-wall response signal with 25 dB gain. Figure previously published [Eason et al. (2017b)].

amplitude. This last discrepancy source is possibly most significant as surface curvature was not accounted for in the acoustic/elastic transfer function, and the ratio of specimen radius to beam cross-sectional area may not be insignificant; curvature effects are discussed in the next section. Other less significant possible sources of discrepancy are described in Chapter 10.

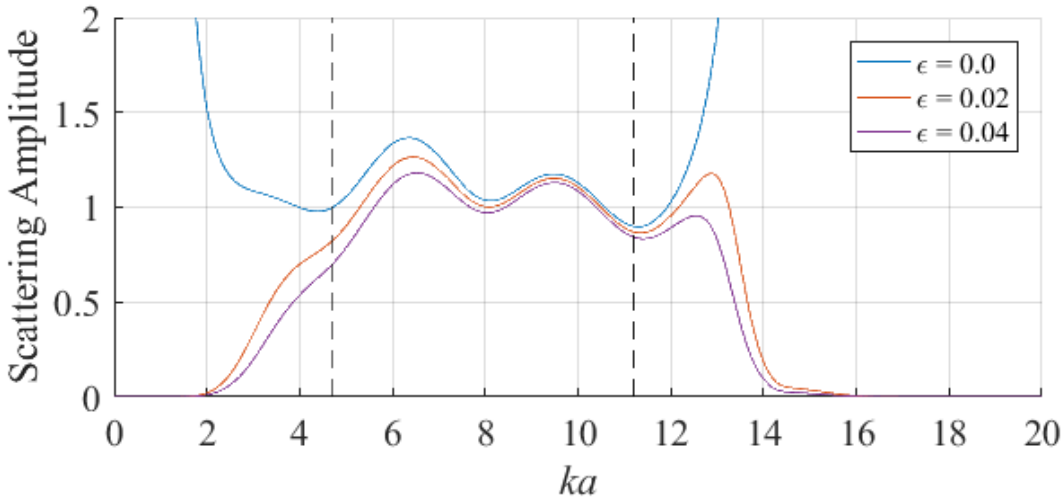

Figure 6.38 Far-field scattering amplitude measurement value $A(\omega)^{\mathrm{h}}$ from Equations 5.69 and 5.70.

6.2.2 Curvature Effects

While the angle of the incident acoustic beam impinging onto the curved pipe surface is normal exactly below the transducer, the transducer aperture and beam spreading will result in non-normal incident angles at locations away from beam centerline. Consider the Gauss-Hermite beam simulation shown in Figure 5.11 with a 6.35 mm transducer at a distance of 114.8 mm away from the surface. The resulting region containing significant acoustic energy will be of about 25 mm in diameter. Considering the outer edge of this region, and provided that the pipe diameter is 114.3 mm, the outer edge of the beam will impinge the surface at an angle of $\cos^{-1}\left(\frac{12.5}{57.15}\right) = 12.6°$ as shown in Figure 6.41. Snell's law as shown in Equation 6.2 can be used to calculate the transmission angle with c_1 as the water wave speed at 1490.8 m/s, c_2 as the steel longitudinal mode wave speed at 6186 $\pm$ 13 m/s, θ_1 as the incident angle from normal, and θ_2 as the transmission angle from normal of 58.9° as shown in Figure 6.41. The corresponding angle of deflection from vertical is 46.3° as shown in Figure 6.41. This transmission angle will vary depending on the pipe curvature, transducer diameter and frequency, and material wave speeds.

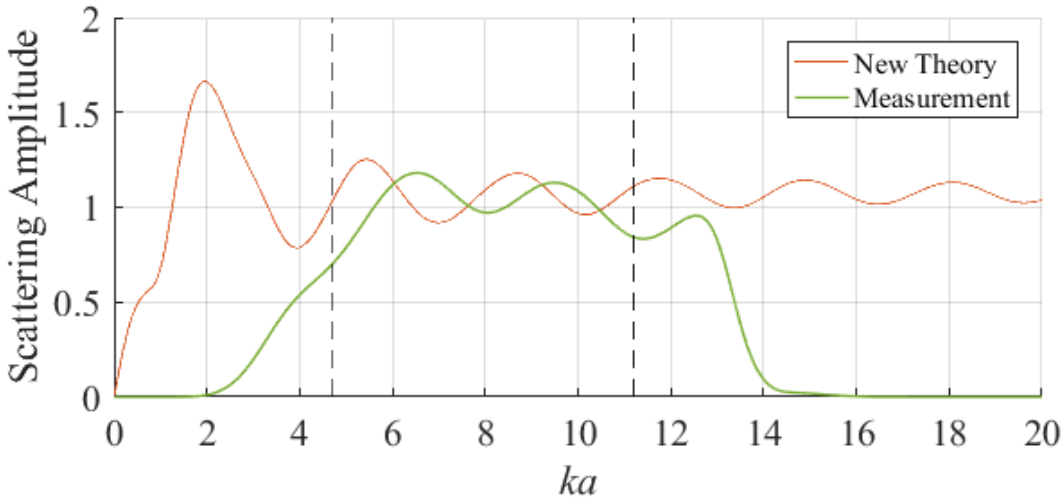

Figure 6.39 Far-field scattering amplitude for a hemispherical pit theory $\mathbf{A}^{\mathrm{h}}$ is compared to the measurement value $A(\omega)^{\mathrm{h}}$.

The presence of curvature at the fluid to elastic material interface may have a significant effect on the attenuation and scattering amplitude measurement results.

$$\frac{\sin(\theta_1)}{c_1} = \frac{\sin(\theta_2)}{c_2} \tag{6.2}$$

6.2.2.1 Attenuation

Attenuation is the loss of acoustic energy when progressing through a medium as a result of scattering and diffraction. The specimen thickness to curvature ratio must be adequately large when taking attenuation measurements, otherwise, the curvature interface can cause significant additional diffraction leading to an increase in measured material attenuation at lower frequencies [Papadakis (1966)]. This increase in attenuation at lower frequencies is observable in Figure 6.42. In this case, a curvature correction could be explored for attenuation measurements so that the contribution of curvature diffraction can be separated from the contribution of material attenuation.

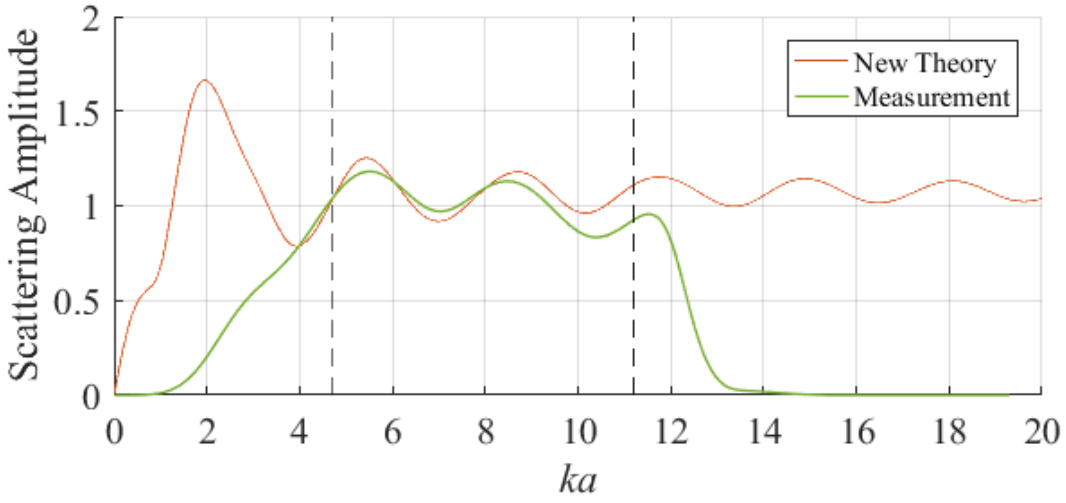

Figure 6.40 Far-field scattering amplitude for a hemispherical pit theory $\mathbf{A}^{\mathrm{h}}$ is compared to the measurement value $A(\omega)^{\mathrm{h}}$ with a $ka = 1$ frequency domain shift applied. Figure previously published [Eason et al. (2017b)].

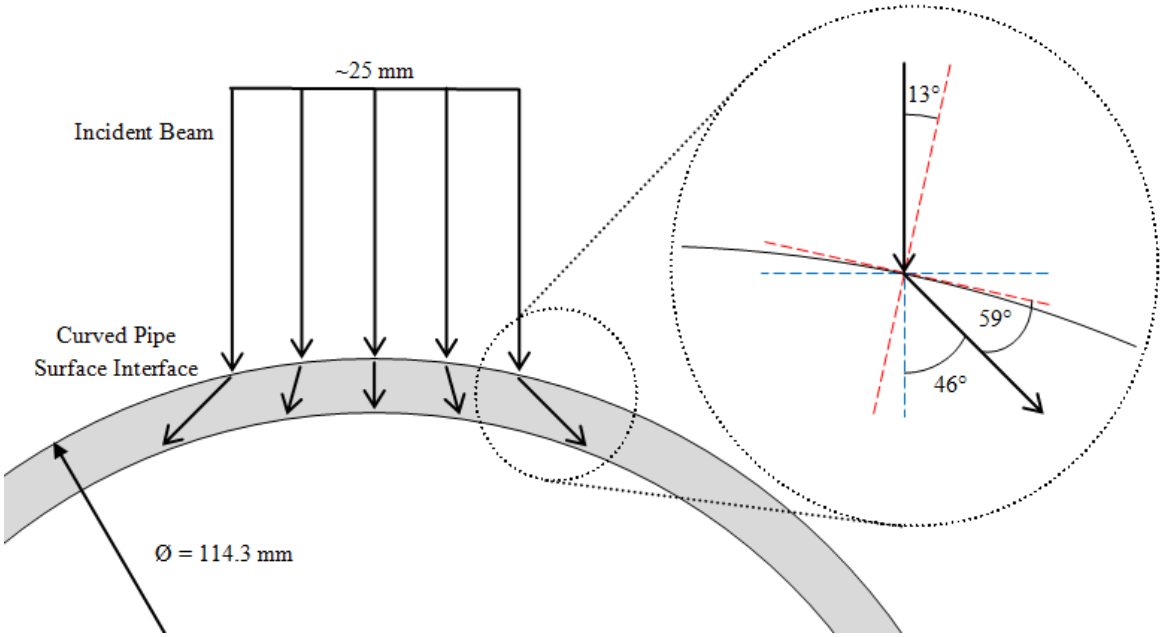

Figure 6.41 Snell's law showing divergent beam. Blue axes are normal to vertical incident beam. Red axes are normal to pipe outside surface tangent line at end of illuminated 25 mm diameter area per beam propagation simulation.

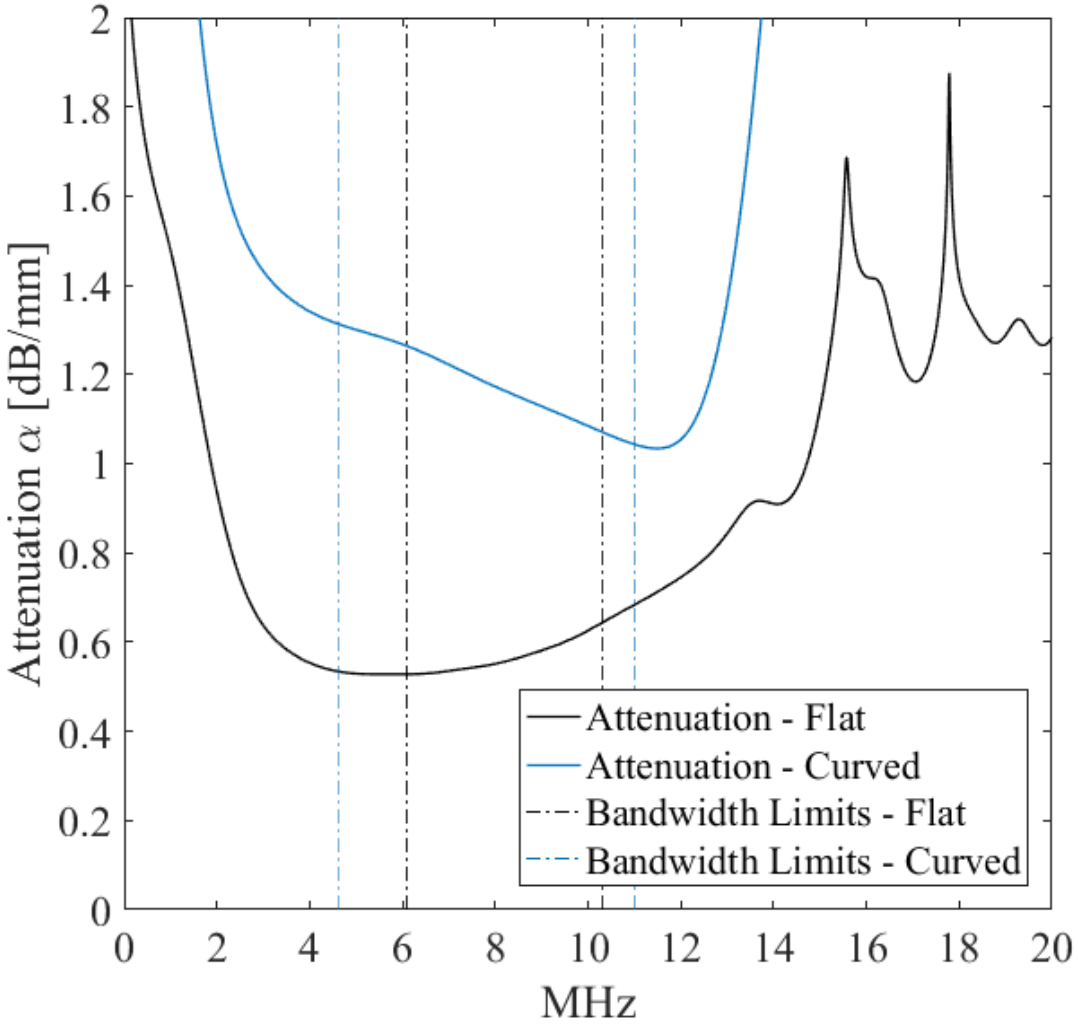

Figure 6.42 Comparing the attenuation measurements from the flat surface with $\epsilon_\alpha = 0.004$ and the curved surface with $\epsilon_\alpha = 0.02$.

6.2.2.2 Scattering Amplitude

A full comparison of scattering amplitude theory and measurements for hemispherical pits in flat and curved surfaces are shown in Figure 6.43. The two specimens were fabricated from steels with slightly different material properties resulting in slightly different theoretical scattering amplitude curves; the flat material had a longitudinal to shear wave speed ratio of $\frac{k_l}{k_s} = 1.82$, and for the curved material $\frac{k_l}{k_s} = 1.86$. The same bandwidth limits and Nyquist criterion from Figures 5.34 and 6.40 are also shown in Figure 6.43 for both materials.

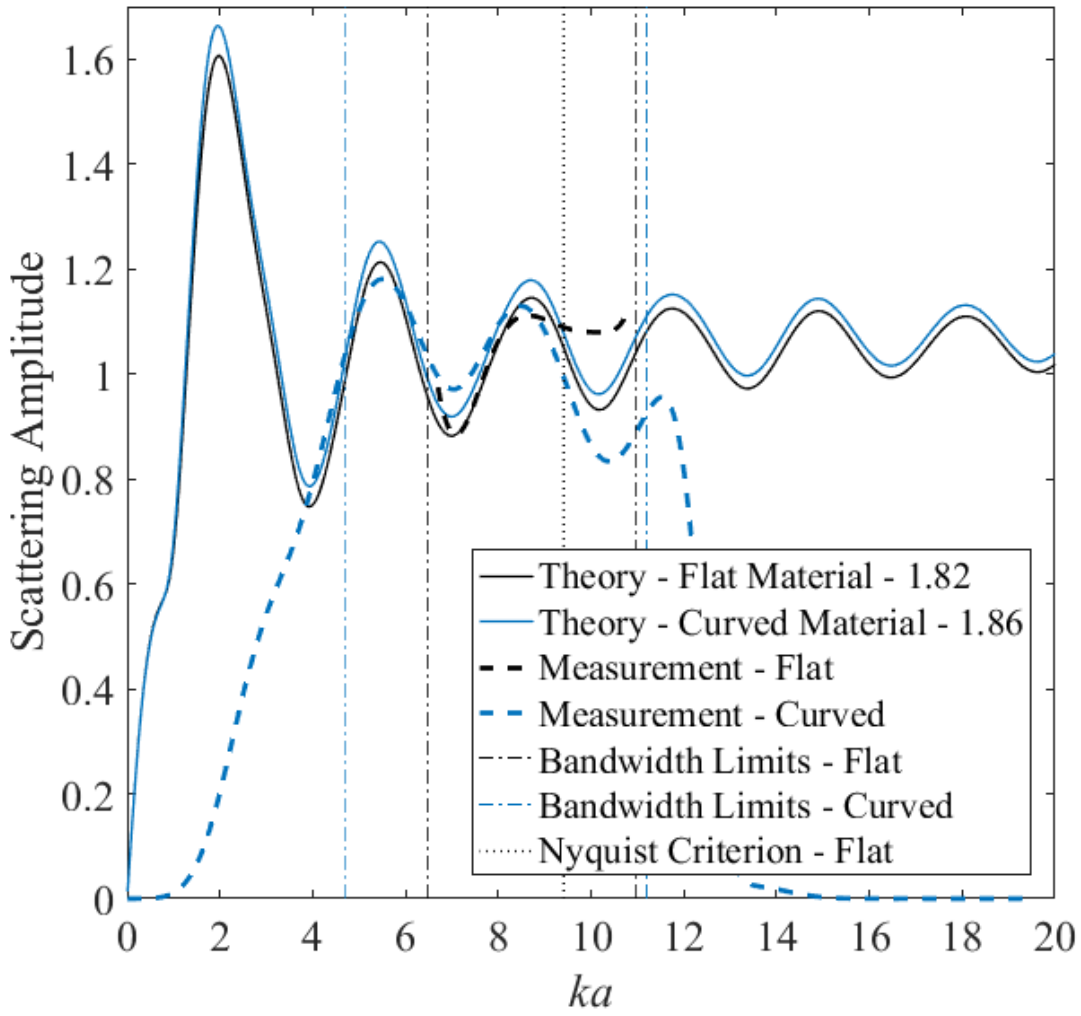

Figure 6.43 Comparison of scattering amplitude theory and measurements for flat and curved surfaces.

6.3 Summary

The work in Chapter 5 on hemispherical pit scattering on a flat surface was extended to hemispherical pit scattering on a curved surface by applying similar experimentation and analysis methods. Scattering amplitude results were presented for a hemispherical pit on a curved surface from an immersion experiment and curvature effects were discussed. The work is extended further for contact measurement simulation and experiments in Chapter 7.

CHAPTER 7. ELASTIC WAVE SCATTERING - CURVE SURFACE - CONTACT MEASUREMENT

A contact transducer simulation and experimental measurements are provided to evaluate the scattering of a hemispherical pit on a curved surface.

7.1 Simulation

The CIVA semi-analytical elastodynamic commercial ultrasonic simulation tool with Auld reciprocity, ray tracing, and pencil beam model techniques [Calmon et al. (2006)] was used to model the incident wave propagation and flaw scattering behavior.

7.1.1 Wave Propagation

The test specimen is a steel cylinder of 114.3 mm outside diameter, 9 mm thickness, 75 mm length, and a 90 degree angular section with a density of 7.8 gm/cm^3, longitudinal wave speed of 5900 m/s, and a transverse wave speed of 3230 m/s. The probe is a single circular flat contact longitudinal wave 6 mm diameter transducer. The probe has a flat 0 degree wedge of the same diameter as the transducer, a thickness of 0.01 mm, and the same steel material as the test specimen. The transducer has 100% bandwidth at -3 dB with a central frequency of 10 MHz with a Gaussian filter and 512 sampling points per signal with a 0 degree phase offset. The coupling material directly below the probe is water with a density of 1 gm/cm^3 and a longitudinal wave speed of 1483 m/s. The bottom and top surface medium is air with a density of 0.001 gm/cm^3 and a longitudinal wave speed of 330 m/s. A simulation is setup as a three dimensional computation of both longitudinal and transverse waves considering the direct mode, mode conversion, back-wall reflection, and internal reflection. The computation

zone was set at a 0.25 mm step size. Neither attenuation nor noise is considered in the specimen, wedge, or coupling mediums. The initial model without a pit is shown in Figure 7.1 with the three dimensional wave propagation results at various points in time shown in Figures 7.2-7.7.

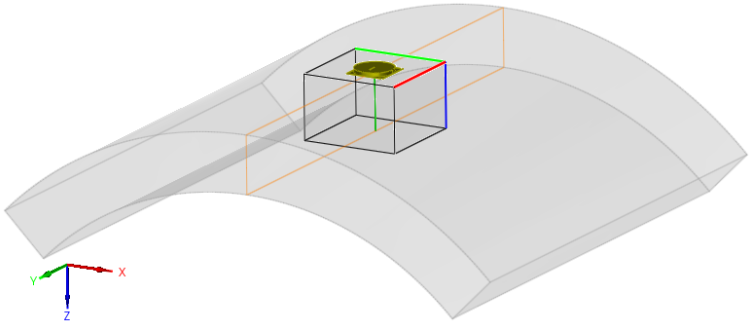

Figure 7.1 Model configuration without flaw.

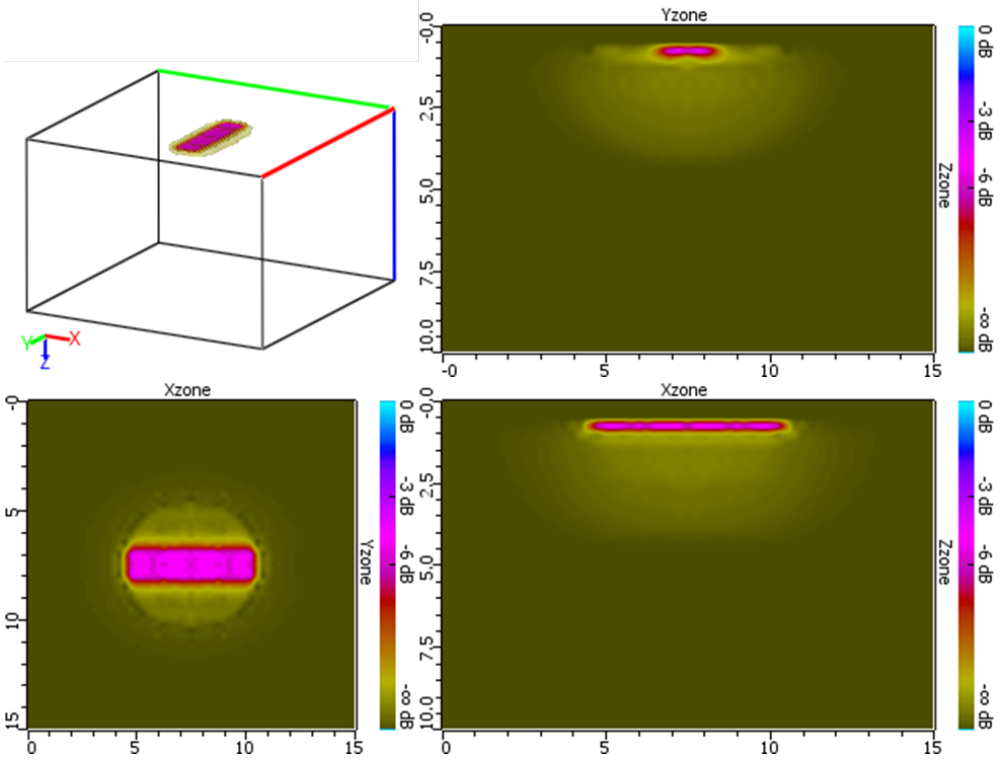

Figure 7.2 Simulation results at 0.07 μs. Figure previously published [Eason et al. (2017c)].

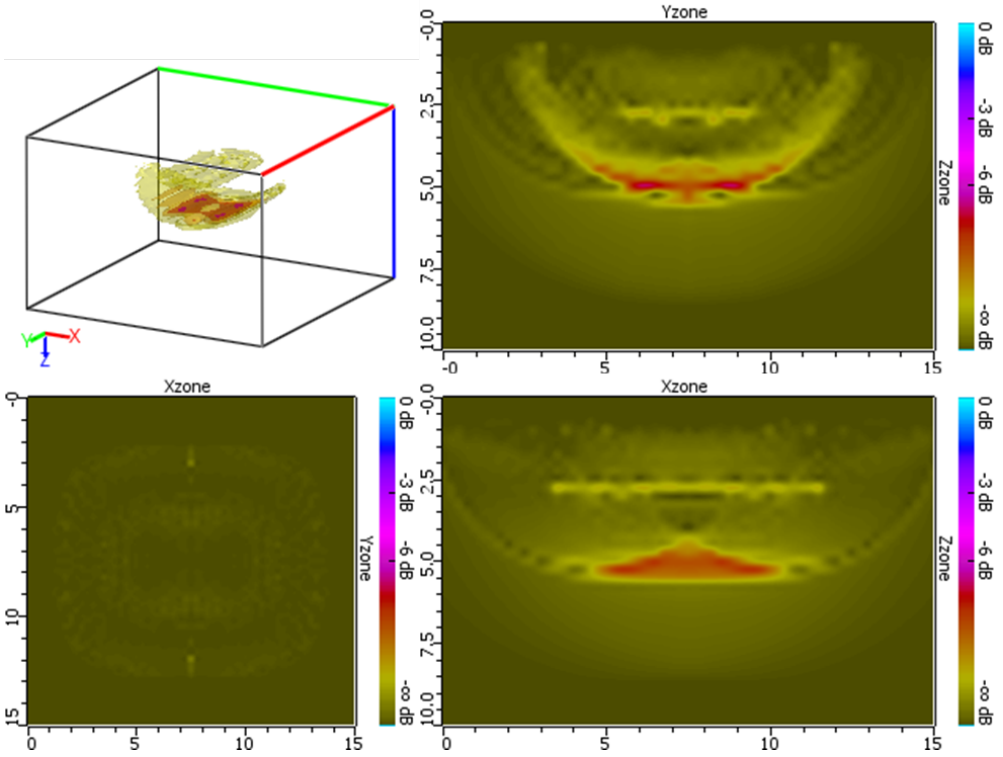

Figure 7.3 Simulation results at 0.81 μs. Figure previously published [Eason et al. (2017c)].

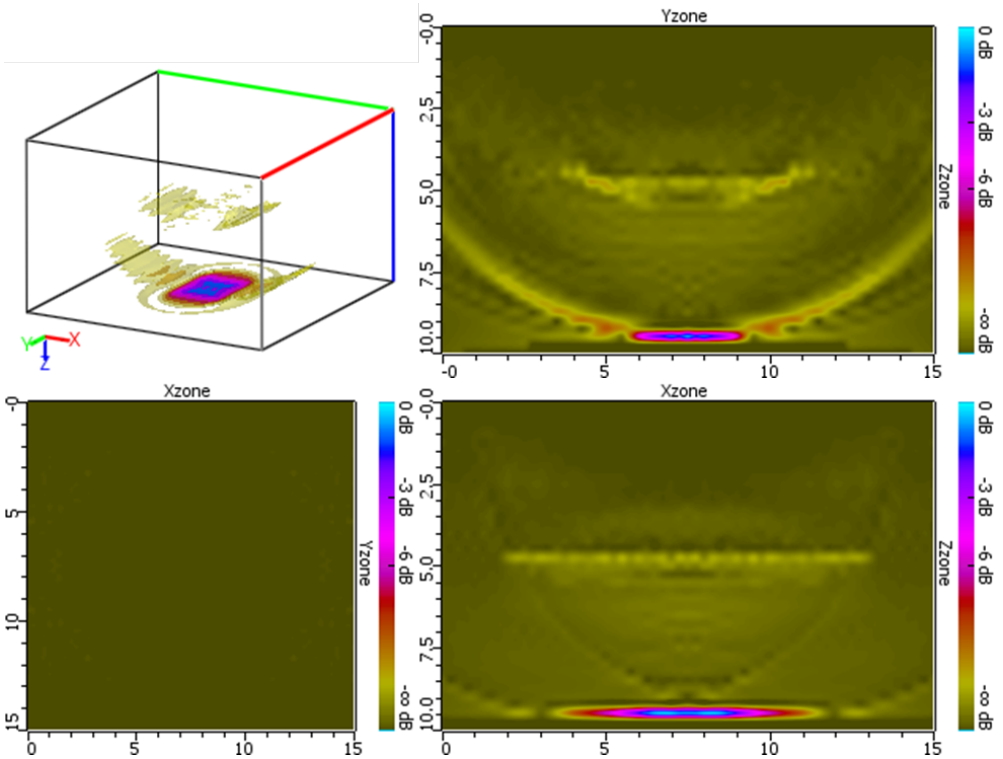

Figure 7.4 Simulation results at 1.55 μs. Figure previously published [Eason et al. (2017c)].

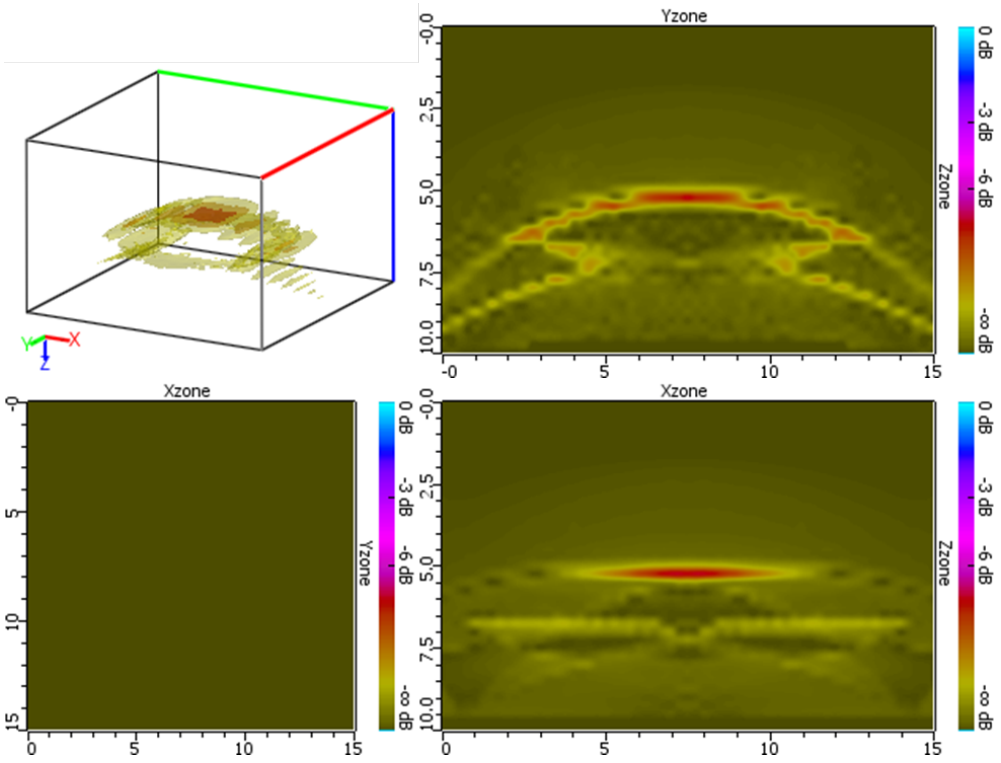

Figure 7.5 Simulation results at 2.27 μs. Figure previously published [Eason et al. (2017c)].

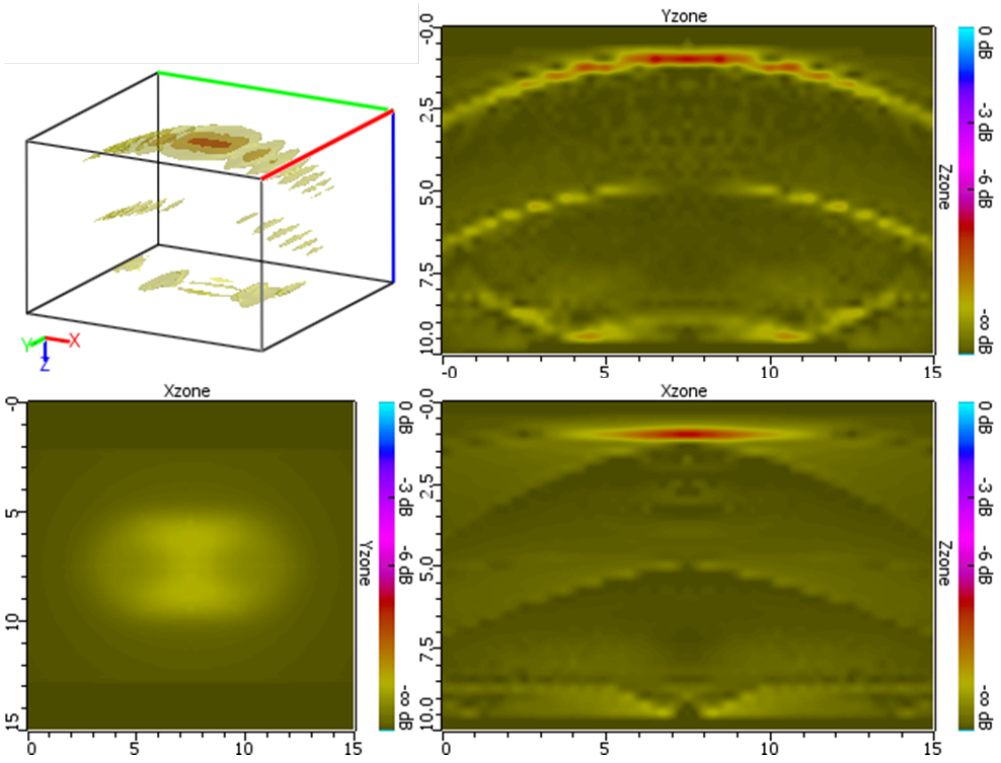

Figure 7.6 Simulation results at 2.99 μs. Figure previously published [Eason et al. (2017c)].

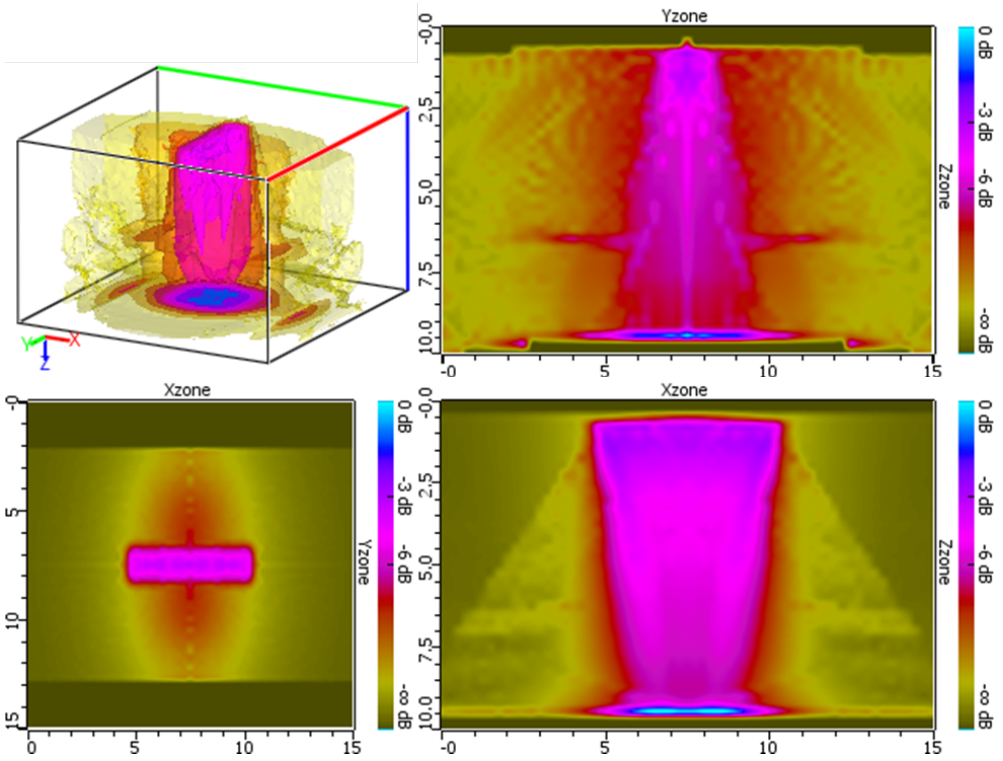

Figure 7.7 Maximum amplitude results. Figure previously published [Eason et al. (2017c)].

7.1.2 Flaw Scattering

A 2 mm diameter spherical flaw was added directly below the transducer centered on the inside pipe diameter as shown in Figure 7.8 to simulate a hemispherical pit. The reflection from the front and back-wall surfaces was analyzed as a Kirchoff reflection. The back-wall response was combined with the scattering response from the pit considering four scenarios: i) no flaw, ii) spherical flaw with separation of variables (SOV), iii) spherical flaw with Kirchoff approximation, and iv) hemispherical flat bottom hole (FBH) with a Kirchoff approximation. The simulated time domain voltage amplitude response for all factors are shown in Figure 7.9. There is no significant difference in the amplitude response among the three pit defects. The spherical flaw SOV responses are subtracted from the baseline as shown in Figure 7.10. The time domain signals were adjusted for a DC offset, multiplied by a Tukey windowing function, zero padded, adjusted again for an offset, and taken through a Fourier transform resulting in the frequency domain plots also shown in Figure 7.10.

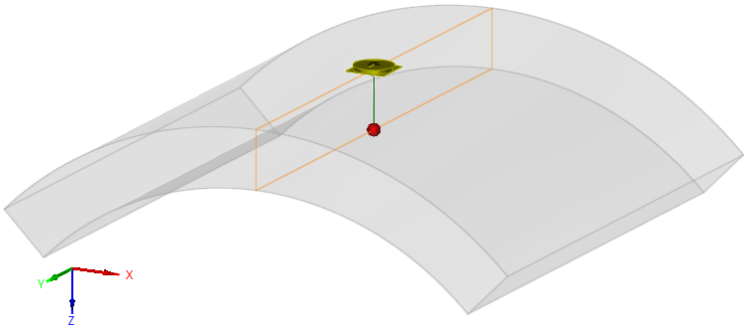

Figure 7.8 Model configuration with a 2 mm diameter pit flaw.

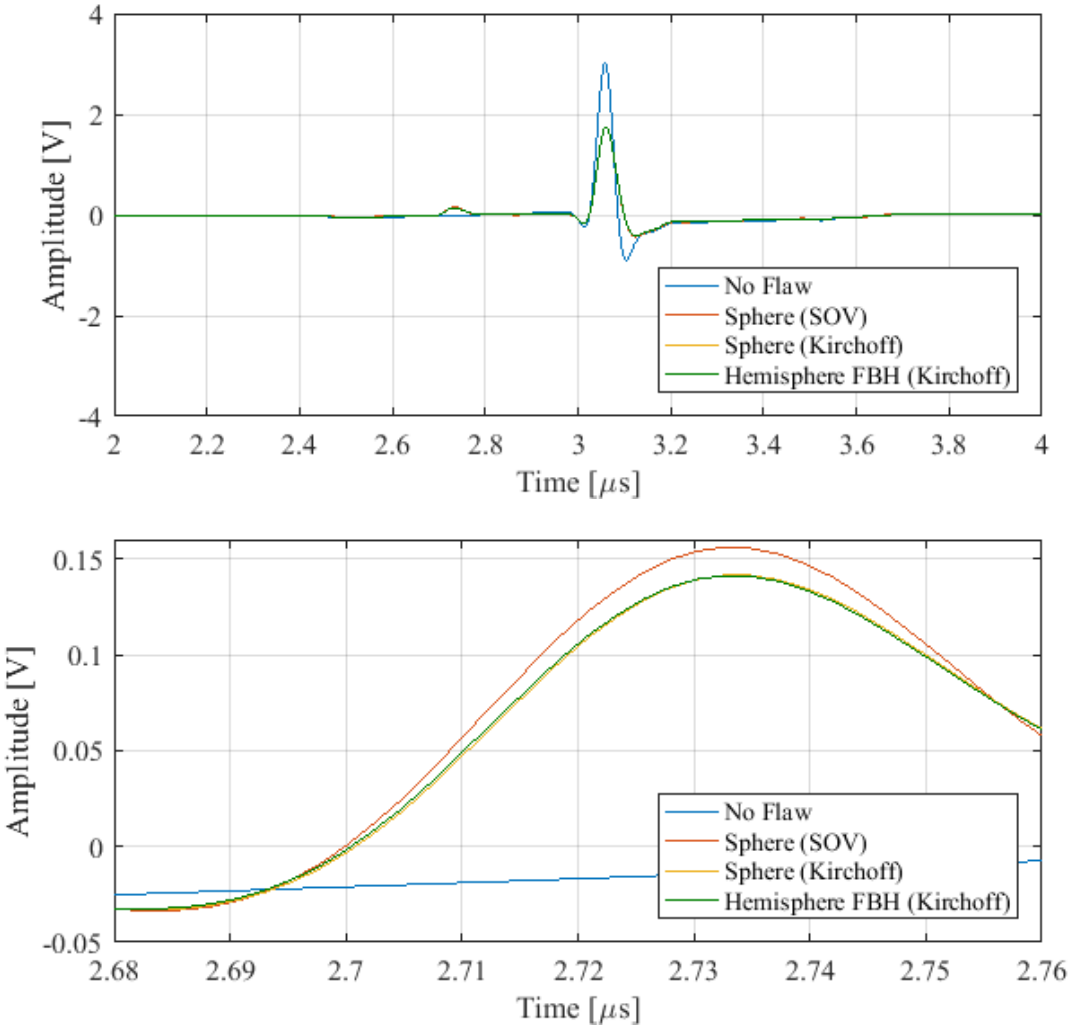

Figure 7.9 Simulated response amplitude in time domain showing all three scattering models are similar.

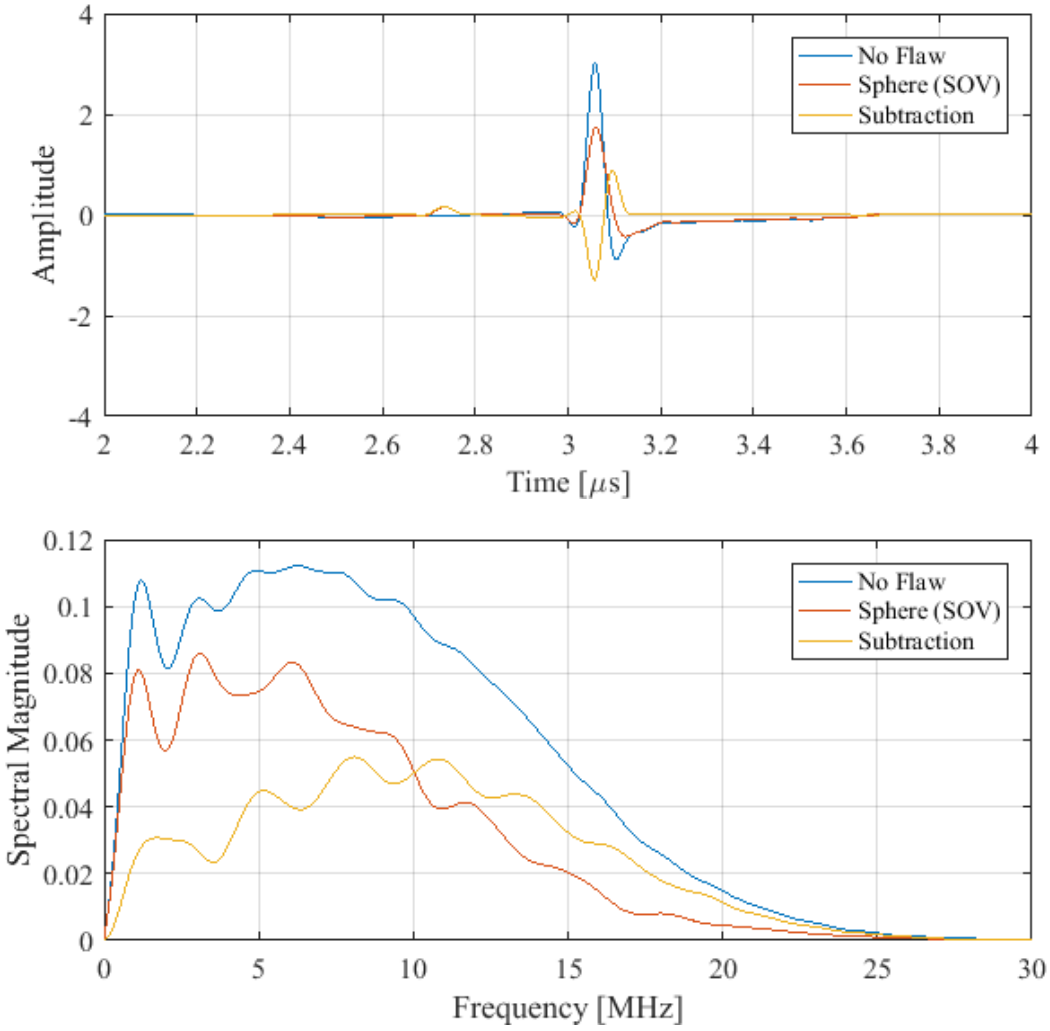

Figure 7.10 Simulated voltage response amplitude and spectral magnitude. Figure previously published [Eason et al. (2017c)].

7.2 Experiment

A manual direct coupled experimental measurement was completed on an A106B carbon steel 4-inch nominal calibration pipe specimen of 9.0 ± 0.5 mm thickness and 114.3 ± 1.3 mm outside diameter with a machined hemispherical pit of 2.00 ± 0.005 mm diameter. A 10 MHz longitudinal wave flat 6.3 mm manual ultrasonic contact transducer [Olympus V112] was coupled to the outside of the pipe in two locations: i) away from the hemispherical pit, and ii) directly above the hemispherical pit.

The measurements were collected with a bench-top pulser-receiver [Tecscan UTPR-CC-50] and a digital storage oscilloscope [LeCroy HDO4002]. The transducer was coupled to the pipe outside diameter with a spring loaded fixture and water based gel couplant. The transducer was actuated with a square pulse of 300V and 90.0 ns width with 45 Ω damping and a pulse-repetition frequency of 100 Hz.

The received signals were captured within a 6V amplitude window at a 2mV interval and within a 5 μs time window at a 0.4 ns interval resulting in 12500 points per signal. The received signals were captured without averaging with a 1 MHz high-pass filter at gain values of 0 dB, 7 dB, and 25 dB. All measurements were collected over a few minutes at a constant ambient temperature of 25°C. The same offset, Tukey windowing, padding, and Fourier transform process was applied.

The time domain and frequency plots for the 0 dB gain measurements are shown in Figure 7.11. The defect is difficult to observe in the time domain plot at 2.8 μs. However, a change in spectral frequency magnitude is present, and this change is even more apparent in the subtracted signal.

The time domain and frequency plots for the 7 dB gain measurements are shown in Figure 7.12. The gain was set to the maximum value while still avoiding saturation of the back-wall reflection. The defect is still difficult to observe in the time domain plot at 2.8 μs. A practically identical change in spectral frequency magnitude can be observed as compared to the 0 dB measurement.

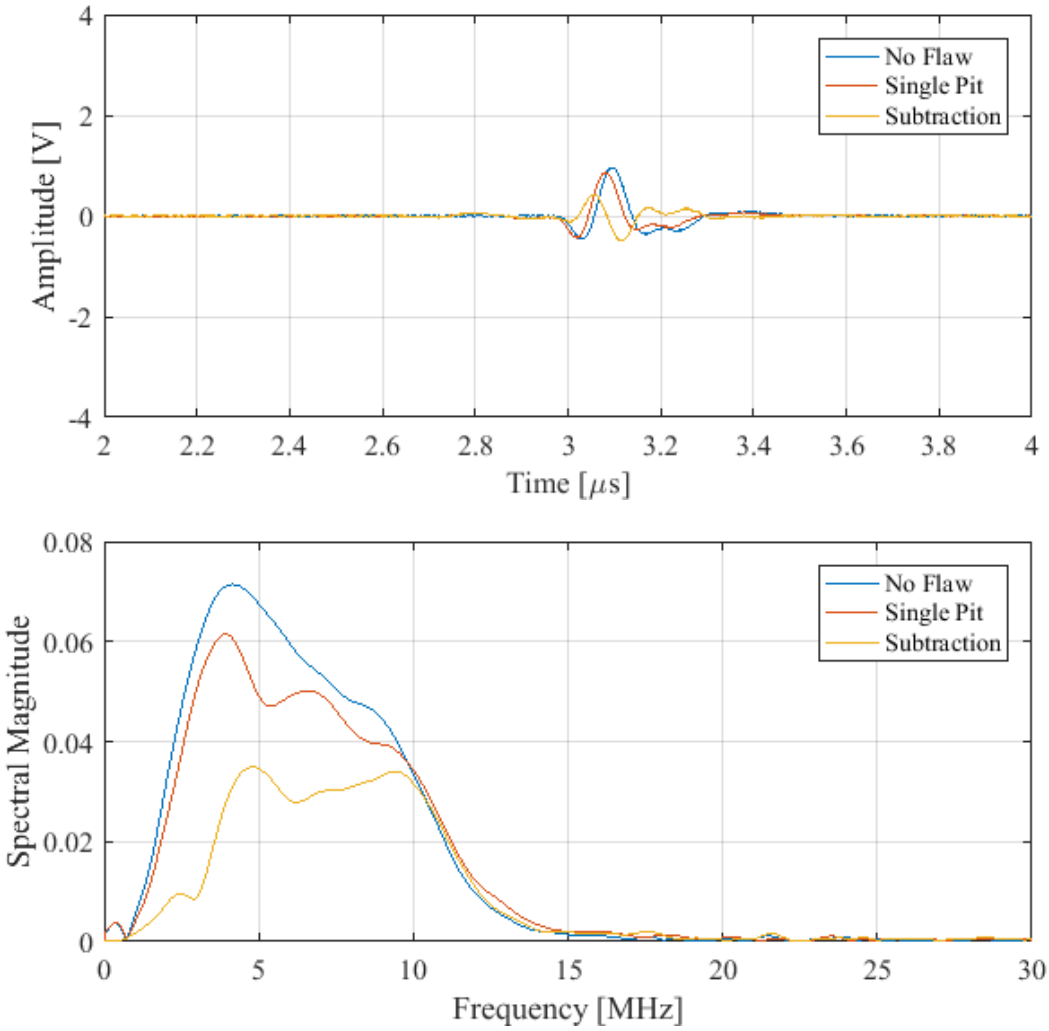

Figure 7.11 0 dB gain measurement voltage response amplitude and spectral magnitude.

The time domain and frequency plots for the 25 dB gain measurements are shown in Figure 7.13. The gain was set to the maximum value while still avoiding saturation of the defect reflection. The defect is observable in the time domain plot at 2.8 μs. However, the resulting spectral frequency magnitude plot is not useful as a result of the back-wall saturation.

The high frequency spectral components greater than 15 MHz are not present in Figures 7.11-7.13 as a result of the 10 MHz transducer bandwidth limitation to transmit and receive in this range.

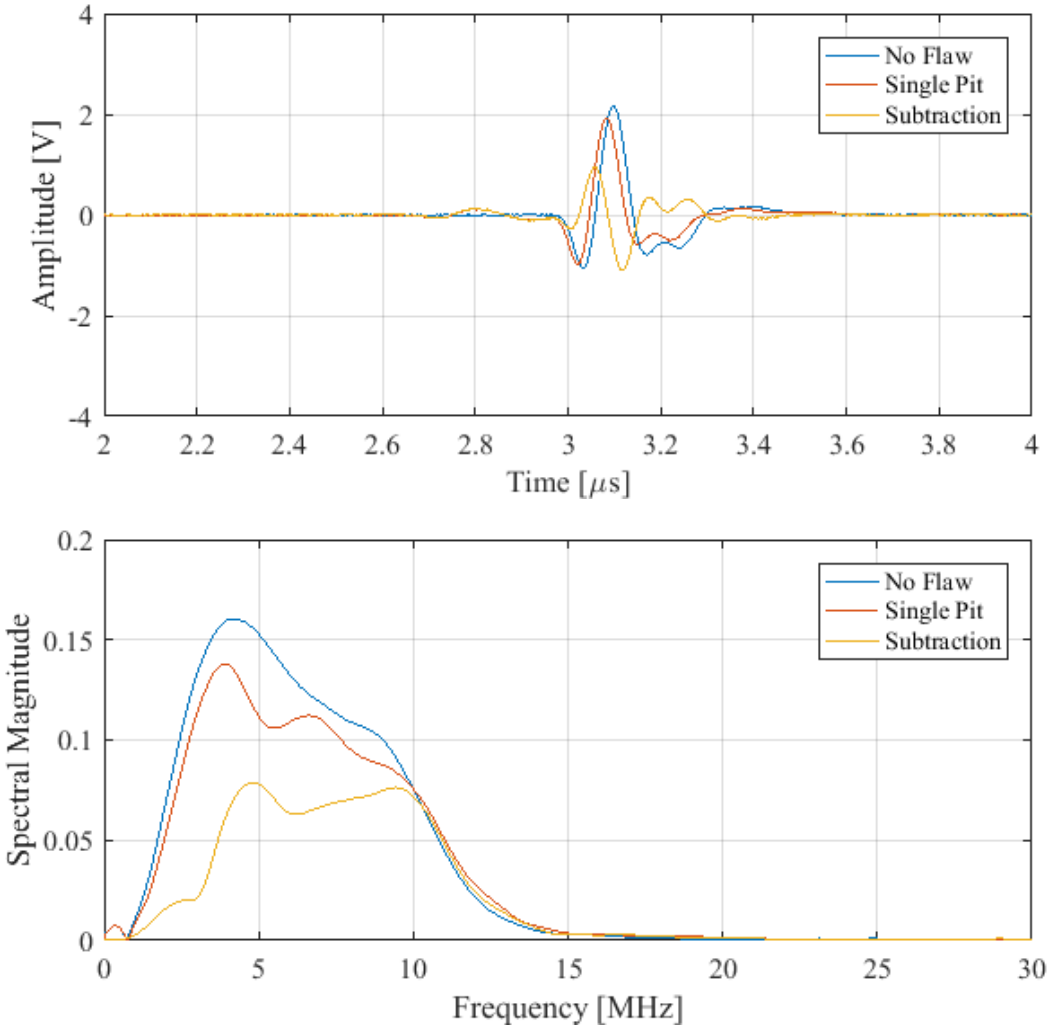

Figure 7.12 7 dB gain measurement voltage response amplitude and spectral magnitude. Figure previously published [Eason et al. (2017c)].

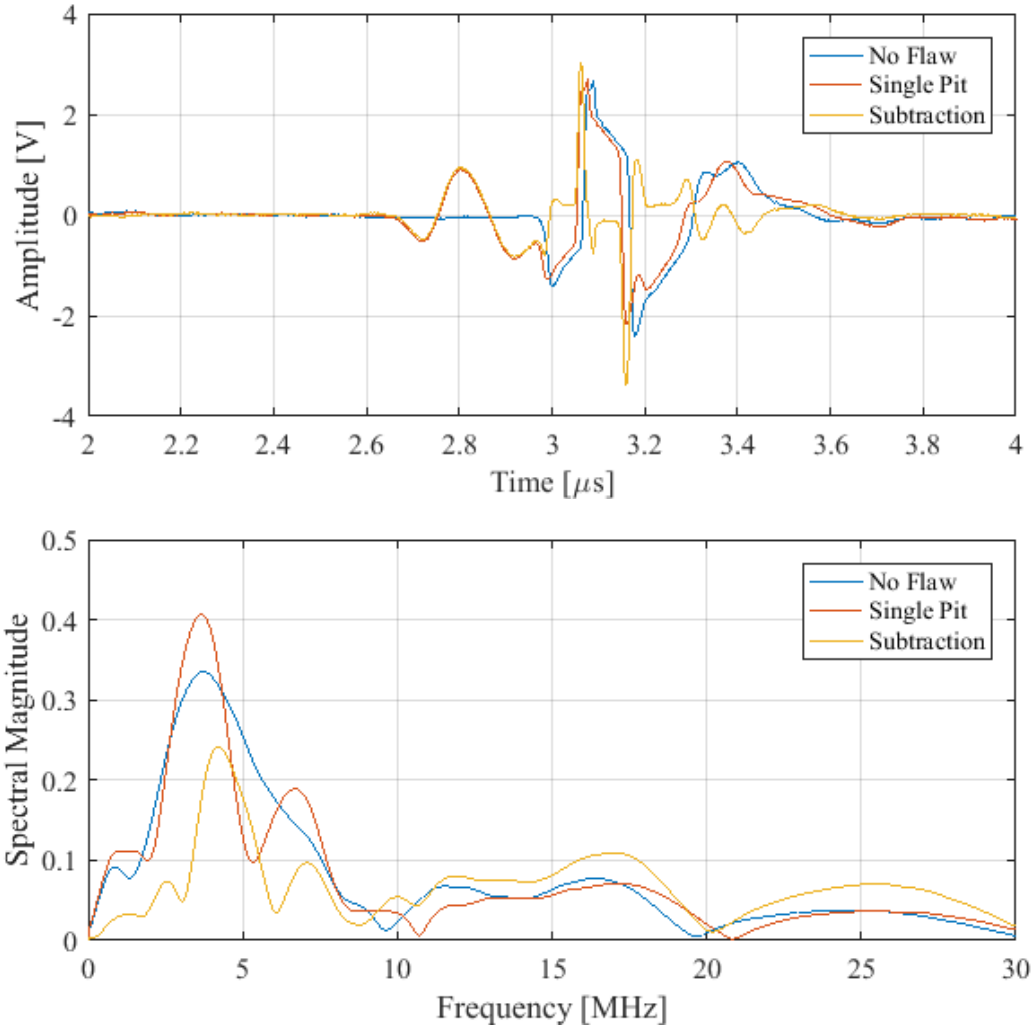

Figure 7.13 25 dB gain measurement voltage response amplitude and spectral magnitude.

7.3 Summary

A contact transducer simulation and experimental measurements were provided to evaluate the scattering of a hemispherical pit on a curved surface.

CHAPTER 8. ACCURACY, PRECISION, AND RELIABILITY OF ULTRASONIC THICKNESS MEASUREMENTS

The accuracy, precision, and reliability of structural health monitoring thickness measurement systems must be sufficient to provide a better understanding of the integrity risk associated with refining crude oils of higher acid concentration. It is prudent to first establish a method to statistically quantify the measurement uncertainty, then apply the method to a significant number of sensors in a baseline scenario on a smooth surface at ambient temperature before taking measurements in more extreme environments at elevated temperatures, for rough back-wall surfaces, and for system degradation over time. This chapter addresses sources of uncertainty in structural health monitoring ultrasonic thickness measurements, proposes a weighted censored relative likelihood analysis method to capture asymmetric measurement uncertainty, and demonstrates the method using sol-gel transducers [Barrow et al. (1996); Kobayashi et al. (2009); Kobayashi and Jen (2012)] in calibration of a measurement system and in establishing the baseline thickness measurement error accuracy and precision for a number of relatively simple time-of-flight thickness calculation methods.

To demonstrate uncertainty factor quantification, two longitudinal wave ultrasonic thickness structural health monitoring experiments are conducted i) on a flat calibration block at ambient temperature with forty four thick-film sol-gel transducers and various time-of-flight thickness calculation methods, and ii) on a curved pipe specimen with a flat bottom hole. In each experiment, as an initial calibration, the voltage response signals from each sensor are used to determine the common material velocity as well as the signal offset unique to each calculation method. Next, the measurement precision of the thickness error of each method is determined with a proposed weighted censored relative maximum likelihood statistical analysis technique incorporating the propagation of asymmetric measurement uncertainty. The results

are presented as upper and lower confidence limits analogous to the $a_{90/95}$ terminology used in industry recognized Probability-of-Detection assessments. This new statistical method may be used to quantify the propagation af asymmetric measurement uncertainty.

Finally, a reliability study of a structural health monitoring sensor system is presented to explore time domain independent and dependent sources of variability.

8.1 Background

A background on ultrasonic thickness measurements and factors influencing structural health monitoring ultrasonic thickness (SHM-UT) measurement uncertainty are discussed.

8.1.1 Ultrasonic Thickness Measurement

A bulk wave ultrasonic thickness measurement technique for corrosion monitoring can be applied with temporary or permanent coupling of a transducer to the outside surface of a pipe; the pipe wall thickness can be determined from the time difference between transducer excitation and reception of the reflected wave from the back-wall surface [Matthies (1998); Burch (2012)].

8.1.2 SHM-UT Measurement Uncertainty

Measurement uncertainty for permanently installed, fixed, structural health monitoring ultrasonic thickness measurement systems can be categorized as follows: accuracy of a single sensor measurement, precision among multiple measurements of a single sensor, precision of a single measurement among multiple sensors, and reliability of measurements over time. The accuracy of a single sensor measurement can be influenced by the sampling rate, transducer bandwidth, excitation frequency, time-of-flight calculation method [Barshan (2000)], as well as the velocity, offset, and temperature calibration. The precision among multiple measurements of a single sensor (over a short time period) can be described as measurement repetition uncertainty and can be influenced by system stability. The precision of a single measurement among multiple sensors (over a short time period) can be described as spatial variation among an array

of sensors and can be influenced by sensor fabrication consistency, coupling consistency, acoustic velocity material variation (caused by spatial temperature variation), and variation in the back-wall surface roughness [Jarvis and Cegla (2012); Benstock et al. (2014)]. The reliability of a single (or multiple) measurement(s) from a single (or array) of sensors can be described as temporal variation and can be influenced by piezoelectric aging, coupling degradation, electronics and cabling degradation, changing back-wall surface morphology, and acoustic velocity temporal variation (caused by temporal temperature variation). Other factors can also influence measurement uncertainty such as pulse-echo or pith-catch configuration, supply voltage, pipe geometry curvature, and the presence of a tapered back-wall [Matthies (1998)].

Only the following accuracy and precision sources of uncertainty are quantified in this chapter by comparing measurements with known true thickness reference values (over a short time period): sampling rate, time-of-flight calculation method, velocity and offset calibration, measurement repetition, and fabrication and coupling consistency.

8.2 Theory

The statistical theory on ultrasonic thickness measurement error includes: i) uncertainty analysis including location-scale distributions, ii) relative likelihood, iii) censored relative likelihood, and iv) the proposed weighted censored relative likelihood. Finally, specific details of the likelihood methodology applied to various measurements to generate asymmetric $a_{05/05}$ lower and $a_{95/95}$ upper confidence limits is described.

8.2.1 Ultrasonic Thickness Measurement Error

The measured thickness t_m is related to the bulk longitudinal wave speed c and the time-of-flight of a feature from the first back-wall reflection for a pulse-echo (single transducer) τ_{1PE} configuration as shown in Equation 8.1 and pitch-catch (two transducers) τ_{1PC} configuration as shown in Equation 8.2 where τ_o is a time offset and x_p is the center distance (pitch) between the two transducers neglecting pipe curvature. The wave speed c and time offset τ_o can be specified during initial calibration. The offset time is not necessary when multiple reflections

are present on a calibration block, but multiple reflections may not be present with a rough back-wall surface as a result of internal pipe corrosion [Matthies (1998)].

$$t_m = \frac{c\left(\tau_{1PE} - \tau_o\right)}{2} \tag{8.1}$$

$$t_m = \sqrt{\left(\frac{c\left(\tau_{1PC} - \tau_o\right)}{2}\right)^2 - \left(\frac{x_p}{2}\right)^2} \tag{8.2}$$

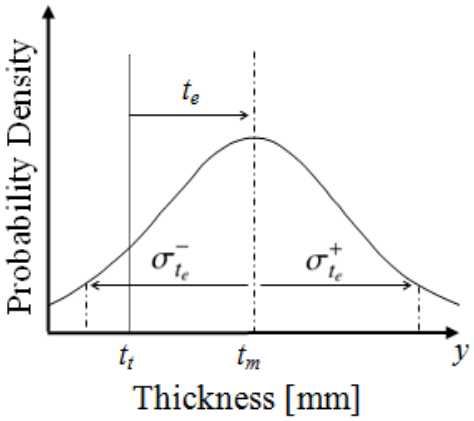

Figure 8.1 Thickness measurement Probability Density Function to demonstrate measurement accuracy represented as a thickness error t_e, and measurement precision represented as positive and negative thickness error uncertainty $\sigma^+_{t_e}$ and $\sigma^-_{t_e}$. The thickness error t_e can be positive or negative defined as the difference between measured thickness t_m and true thickness t_t as shown in Equation 8.3. Figure previously published [Eason et al. (2016a)].

The thickness measurement error for a pulse-echo configuration t_e is analogous to measurement accuracy as presented in Figure 8.1 and is defined in Equation 8.3 as the difference in measured thickness t_m and true thickness t_t. The uncertainty of the thickness measurement error σ_{t_e} is analogous to measurement precision as presented in Figure 8.1 and defined in Equation 8.4 with σ_c as the velocity uncertainty, σ_{τ_o} as the time offset uncertainty, σ_{t_t} as the true thickness dimensional uncertainty, and σ_{τ_1} as the time-of-flight measurement uncertainty. The measurement error uncertainty σ_{t_e} in Equation 8.4 is determined by propagation of uncertainty [Ku (1966)] while assuming correlation among terms is secondary such that covariance is neglected. A positive thickness measurement error $\sigma^+_{t_e}$ indicates a measured thickness

greater than the true thickness; a negative thickness measurement error $\sigma_{t_e}^{-}$ indicates a measured thickness less than the true thickness. The consequence of a positive or negative thickness measurement error is not the same in a corrosion monitoring application; therefore, measurement error asymmetry is of interest.

$$t_e = \frac{c\left(\tau_1 - \tau_o\right)}{2} - t_t \tag{8.3}$$

$$\sigma_{t_e}^{\pm} = \sqrt{\frac{\left(\tau_1 - \tau_o\right)^2 \sigma_c^{\pm 2}}{4} + \frac{c^2\left(\sigma_{\tau_1}^{\pm\,2} + \sigma_{\tau_o}^{\mp\,2}\right)}{4} + \sigma_{t_t}^{\mp 2}} \tag{8.4}$$

The resulting thickness measurement error uncertainty for a pitch-catch configuration is shown in Equation 8.5. For when x_p and σ_{x_p} are zero, Equation 8.5 would reduce to be the same as Equation 8.4.

$$\sigma_{t_e}^{\pm} = \sqrt{\frac{\left(\tau_1 - \tau_o\right)^4 c^2 \sigma_c^{\pm 2} + c^4\left(\tau_1 - \tau_o\right)^2\left(\sigma_{\tau_1}^{\pm\,2} + \sigma_{\tau_o}^{\mp\,2}\right) + {x_p}^2 \sigma {x_p}^{\mp 2}}{4\left(c^2\left(\tau_1 - \tau_o\right)^2 - {x_p}^2\right)} + \sigma_{t_t}^{\mp 2}} \tag{8.5}$$

8.2.2 Uncertainty Analysis

The uncertainty components in Equations 8.4 and 8.5 can be described as either Type B, the intrinsic measurement resolution limit, or as Type A, the natural variation that is present among a set of measurements [Taylor and Kuyatt (1994)]. Type A uncertainty can be modeled with location scale-distributions. Type B uncertainty can be incorporated into such distribution models with a censored relative likelihood analysis method.

8.2.2.1 Location-Scale Distributions

The probability density functions ϕ and cumulative distribution functions Φ of the Smallest Extreme Value (SEV), Largest Extreme Value (LEV), and Logistic (LGS) distributions are shown in Equations 8.6-8.11 with $z = \frac{y-\mu}{\sigma}$ as the normalized dispersion factor with y as an individual measured value, μ as the mean, and σ as the standard deviation [Meeker and Escobar (1998)]. The left-skewed (SEV), right-skewed (LEV), and symmetric (LGS) distributions have

closed form cumulative distribution functions that allow for a relatively efficient computation as compared with the Normal distribution.

$$\phi_{SEV} = e^{(z-e^z)} \tag{8.6}$$

$$\phi_{LEV} = e^{(-z-e^{-z})} \tag{8.7}$$

$$\phi_{LGS} = \frac{e^z}{(1+e^z)^2} \tag{8.8}$$

$$\Phi_{SEV} = 1 - e^{(-e^z)} \tag{8.9}$$

$$\Phi_{LEV} = e^{(-e^{-z})} \tag{8.10}$$

$$\Phi_{LGS} = \frac{e^z}{(1+e^z)} \tag{8.11}$$

8.2.2.2 Relative Likelihood

The industry standard for NDE reliability assessments [Annis (2009)] applies a relative likelihood method to quantify measurement error uncertainty for various location-scale distribution models. The likelihood L of a particular set of mean μ and deviation σ parameters is shown in Equation 8.12 as the product of the probability density f of each individual measurement y for n total measurements. A range of μ and σ parameters are analyzed with the resulting maximum likelihood value corresponding to $\hat{\mu}$ and $\hat{\sigma}$. The relative likelihood R is a normalization of the maximum likelihood as shown in Equation 8.13. A confidence region of the most likely μ and σ parameters corresponding to the relative likelihood values greater than α as derived from a χ^2 distribution with two degrees of freedom is shown in Equation 8.14 [Meeker and Escobar (1998)]. The industry recognized a_{90} confidence value can be determined as the cumulative distribution point from the maximum likelihood $\hat{\mu}$ and $\hat{\sigma}$ model, while the $a_{90/95}$ confidence value can be determined with the Delta method to establish Wald confidence intervals [Annis

(2009)]; alternatively, the $a_{90/95}$ confidence value can be determined using a simulation method similar to Monte Carlo to construct a set of distribution models with the μ and σ parameters from the relative likelihood confidence region perimeter [Eason et al. (2015b, 2016a,b)].

$$L(\mu,\sigma)=\prod_{i=1}^{n} f(y_i;\mu,\sigma)=\prod_{i=1}^{n}\left[\frac{1}{\sigma}\phi\left(\frac{y_i-\mu}{\sigma}\right)\right] \tag{8.12}$$

$$R(\mu,\sigma)=\frac{L(\mu,\sigma)}{L(\hat{\mu},\hat{\sigma})} \tag{8.13}$$

$$R(\mu,\sigma)>\exp\left(\frac{-\chi^2_{(1-\alpha;2)}}{2}\right)=\alpha \tag{8.14}$$

8.2.2.3 Censored Relative Likelihood

Instead of assuming a single point value for each measurement, the censored relative likelihood method uses an upper y_U and lower y_L confidence interval for each measurement as shown in Equation 8.15 with F as the cumulative distribution function. The censored likelihood method has been previously applied for the normal distribution [Vardeman and Lee (2005)] and extreme value distributions [Liu and Meeker (2015)] to account for measurement resolution and round-off error uncertainties.

$$L(\mu,\sigma)=\prod_{i=1}^{n}\left[F(y_{U_i};\mu,\sigma)-F(y_{L_i};\mu,\sigma)\right]=\prod_{i=1}^{n}\left[\Phi\left(\frac{y_{U_i}-\mu}{\sigma}\right)-\Phi\left(\frac{y_{L_i}-\mu}{\sigma}\right)\right] \tag{8.15}$$

8.2.2.4 Weighted Censored Relative Likelihood

The relative likelihood method does not capture an individual measurement data point confidence interval, and the censored relative likelihood method does not consider if an individual measurement data point mean has asymmetric uncertainty. However, the individual data point mean and asymmetric measurement confidence intervals are considered in the proposed weighted censored relative likelihood method [Eason et al. (2016a)] as described in

Equations 8.16 or 8.17 with κ as the weight parameter ranging from $\kappa = 0$ for no censoring (same as Equation 8.12) to $\kappa = 1$ for full censoring (same as Equation 8.15).

$$L(\mu, \sigma) = \prod_{i=1}^{n} \left[(1-\kappa) f(y_i) + \frac{\kappa}{2} \left[F(y_{U_i}) - F(y_{L_i}) \right] \right] \tag{8.16}$$

$$L(\mu, \sigma) = \prod_{i=1}^{n} \left[\frac{1-\kappa}{\sigma} \phi\left(\frac{y_i - \mu}{\sigma} \right) + \frac{\kappa}{2} \left[\Phi\left(\frac{y_{U_i} - \mu}{\sigma} \right) - \Phi\left(\frac{y_{L_i} - \mu}{\sigma} \right) \right] \right] \tag{8.17}$$

8.2.3 Applied Likelihood Methodology

The specific details of the applied likelihood uncertainty analysis method is described. First, the weighted ($\kappa = 0.5$) censored relative likelihood SEV, LEV, or LGS location-scale distribution model is identified to generate a confidence region ($\alpha = .05$) from the corresponding relative likelihood function. Then, a new set of potential distribution models are simulated from the μ and σ parameters on the confidence region perimeter. Finally, the most likely mean $\hat{\mu}$ from the maximum likelihood distribution is considered the most likely mean term $\overline{y} = \hat{\mu}$, and, the 95% upper and 5% lower confidence limits from the set of simulated distribution models $a_{95/95}$ and $a_{05/05}$ are used to determine the (possibly asymmetric) upper uncertainty $\sigma_{\overline{y}}^{+} = a_{95/95} - \overline{y}$ and lower uncertainty $\sigma_{\overline{y}}^{-} = \overline{y} - a_{05/05}$. This method is applied three times in course of determining thickness error uncertainty: velocity calibration, offset calibration, and thickness error. A demonstration of the steps in this method can be observed in Figures 8.4-8.6.

8.3 Accuracy and Precision - Flat Back-Wall Surface

An experiment and analysis was completed using sol-gel transducers in pulse-echo mode on a calibration block with a flat back-wall to demonstrate the weighted censored relative likelihood method for various thickness calculation algorithms [Eason et al. (2016a)].

8.3.1 Methodology

The flat back-wall experiment and analysis methodology are described including experimental setup, time-of-flight calculation methods, and considered uncertainty factors.

8.3.1.1 Experiment Setup

A total of forty four sol-gel sensor element transducers [Barrow et al. (1996); Kobayashi et al. (2009); Kobayashi and Jen (2012)] were directly deposited in 2 × 2 array groups onto a flat step calibration block with a 0.10 ± 0.005 mm step size from 24.00 mm to 25.00 mm as shown in Figure 8.2 and previously described [Eason et al. (2015a,b)]. The gain for each sensor was individually adjusted to maximize the first back-wall reflection amplitude without saturation. A total of 44 pulse-echo waveforms were collected for each of the sensor elements over a period of 90 minutes at constant indoor ambient temperature resulting in 1936 individual voltage response signals. The elements have a center frequency from 6.9 MHz to 9.1 MHz and a bandwidth from 72% to 79% at -6 dB. One sensor did not produce a response signal and was excluded from the analysis as an outlying data point.

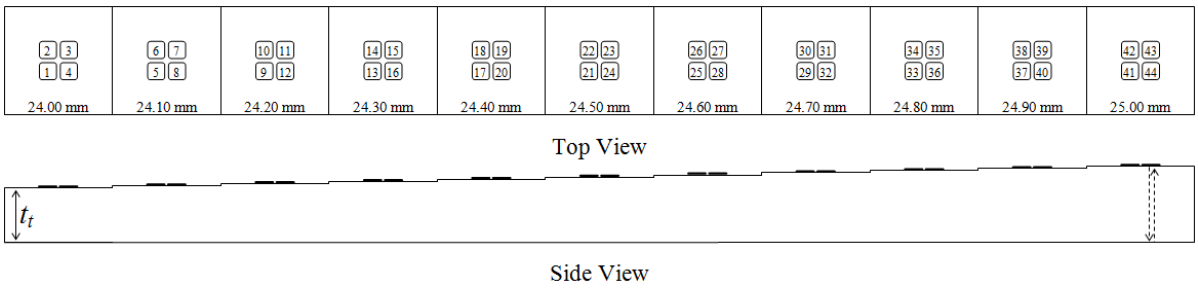

Figure 8.2 AISI 1018 carbon steel eleven step calibration block from 24.00 mm to 25.00 mm with 44 direct sol-gel transducers. Figure previously published [Eason et al. (2016a)].

8.3.1.2 Time-of-Flight Calculation Methods

While many different thickness calculation methods exist [Svilainis (2013)], this work addresses relatively simple time-of-flight methods; the initial focus is not to discover the most precise method, but rather, avoid the least precise among commonly used methods. A total of 87 time-of-flight measurement methods were investigated as described in Table 8.1 based on the voltage amplitude and arrival time of various signal features within a time gate region around the first, and sometimes second, back-wall reflection. The positive, negative, and zero-crossing

voltage measurement refers to features at a positive, negative, or zero voltage. The rectified voltage measurement refers to features of a rectified voltage signal. The voltage threshold refers to features at a positive (or negative) voltage as a percentage of the maximum (or minimum) peak voltage. The peak category refers to features at the maximum (or minimum) voltage. The first threshold category refers to the first feature on a voltage threshold. The mean threshold category refers to the mean of features on a voltage threshold. The peak threshold category refers to the feature on a voltage threshold immediately preceding a maximum (or minimum) peak feature.

Table 8.1 Time-of-flight Measurement Methods - Combinations Description

Voltage Measurement	**Voltage Threshold**	**Category**
Positive	75%	Peak
Negative	50%	Threshold - First
Zero-Crossing	25%	Threshold - Mean
Rectified	20%	Threshold - Peak
	15%	
	10%	
	5%	

Overlay plots of all 44 voltage response signals from a single sensor are shown in Figure 8.3. Features are identified within gated regions around the first and second back-wall reflections; slight variation of a feature is observable in Figure 8.3c as repetition uncertainty.

8.3.1.3 Considered Uncertainty Factors

The error propagation and likelihood methods applied to quantify the uncertainty components in Equations 8.4 and 8.5 are described in detail. Any variable with a j subscript indicates uniqueness to a particular calculation method; a k subscript indicates uniqueness to a particular sensor; an l subscript indicates uniqueness to a particular response signal; no subscript indicates applicability among all calculation methods, sensors, and response signals. The typical absolute and relative uncertainty values for this experiment are summarized in Table 8.2.

Repetition, Sampling Rate, and Dimensional Uncertainty For each of the 87 calculation method, and each of the 43 sensors, and each of the 44 voltage response signals, the

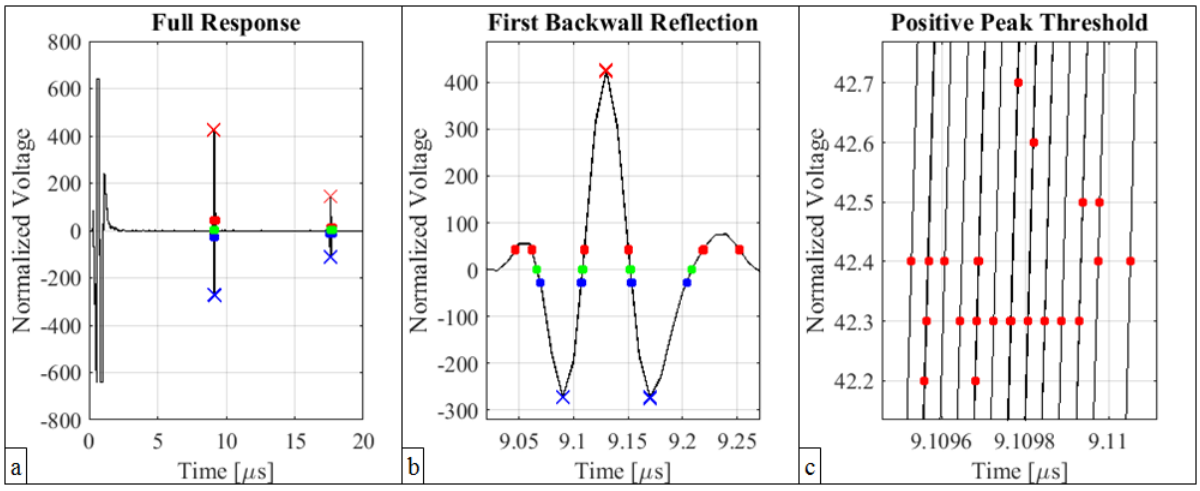

Figure 8.3 Overlay plots of 44 voltage response signals from a single sensor for a) the full response, b) a close view of the first back-wall reflection, and c) a very close view of the positive peak threshold features. The various features are observable as positive peak [×], 10% positive threshold [•], 10% zero-crossing [•], 10% negative threshold [•], and negative peak [×]. Figure previously published [Eason et al. (2016a)].

feature arrival point of the first back-wall reflection $\tau_{1_{jkl}}$ and the feature arrival point difference between the second and first back-wall reflections $\tau_{2-1_{jkl}}$ were captured. These feature arrival points were re-converted to time units by dividing the digitized points by the sampling rate of 100 MHz. The mean feature arrival times $\tau_{1_{jk}}$ and $\tau_{2-1_{jk}}$ of the 44 voltage response signals were captured along with the corresponding standard errors $\text{SE}_{\tau_{1\,jk}}$ and $\text{SE}_{\tau_{2-1\,jk}}$.

The measurement repetition uncertainty $\sigma^{\pm}_{R_{jk}}$ of a mean feature arrival time τ_{jk} is considered Type A and can be approximated by a t-distribution with $\alpha = 0.05$ and 43 degrees of freedom [Taylor and Kuyatt (1994)] as symmetric uncertainty $\sigma^{\pm}_{R_{jk}} = t_{(0.95,43)}\text{SE}_{\tau_{jk}}\sqrt{43} = 2.0168 \cdot \text{SE}_{\tau_{jk}}\sqrt{43}$.

The sampling rate uncertainty $\sigma^{\pm}_{S_j}$ of any mean feature is considered Type B for only the three peak calculation methods. For a single feature, the symmetric uncertainty $\sigma^{\pm}_{S_{1_j}} = 5$ ns; for the difference in two features, the symmetric uncertainty $\sigma^{\pm}_{S_{2-1_j}} = 10$ ns. For the non-peak methods, the sampling rate uncertainty $\sigma^{\pm}_{S_j} \approx 0$ ns as such methods are linearly interpolated between two points and the linear interpolation error $<<$ 1 ns.

Table 8.2 Individual Factor Uncertainty Ranges for Peak and Threshold Calculation Methods

FACTORS		AVERAGE UNCERTAINTY RANGE			
Name	Symbol	Peak Methods		Threshold Methods	
True Thickness	$\sigma_{t_t k}$	-.005–.005mm	-.02 – .02%	-.005–.005mm	-.02 – .02%
Sound Path	$\sigma_{d_{PE}k}$	-.010–.010mm	-.02 – .02%	-.010–.010mm	-.02 – .02%
Repetition	$\sigma_{R_{2-1}jk}$	-0.2 – 0.2ns	-.002–.002%	-0.8 – 0.8ns	-.01 – .01%
Sampling	$\sigma_{S_{2-1}jk}$	-10 – 10ns	-0.1 – 0.1%	$\sim$ 0ns	$\sim$ 0%
Feature Arrival	$\sigma_{\tau_{2-1}jk}$	-10 – 10ns	-0.1 – 0.1%	-0.8 – 0.8ns	-.01 – .01%
Velocity	σ_{cjk}	-7 – 7m/s	-0.1 – 0.1%	-2 – 2m/s	-.03 – .03%
Velocity	σ_{cj}	-41 – 16m/s	-0.7 – 0.3%	-48 – 26m/s	-0.8 – 0.4%
Repetition	σ_{R_1jk}	-0.1 – 0.1ns	-.001–.001%	-0.4 – 0.4ns	-.004–.004%
Sampling	σ_{S_1jk}	-5 – 5ns	-.06 – .06%	$\sim$ 0ns	$\sim$ 0%
Feature Arrival	σ_{τ_1jk}	-5 – 5ns	-.06 – .06%	-0.4 – 0.4ns	-.004–.004%
Offset	σ_{τ_ojk}	-11 – 7ns	-1.6 – 1.0%	-10 – 5ns	-1.5 – 0.7%
Offset	σ_{τ_oj}	-59 – 55ns	-8.5 – 8.1%	-42 – 66ns	-6.2 – 9.5%
Thickness	σ_{t_mjk}	-0.2 – 0.2mm	-0.7 – 0.7%	-0.2 – 0.1mm	-0.8 – 0.5%
Thickness Error	σ_{t_ejk}	-0.2 – 0.2mm	n/a	-0.2 – 0.1mm	n/a
Thickness Error	σ_{t_ej}	-0.2 – 0.2mm	n/a	-0.1 – 0.2mm	n/a

The true thickness t_{tk} of the calibration block ranges from 24.00 to 25.00 mm with a corresponding Type B symmetric uncertainty fabrication tolerance $\sigma^{\pm}_{t_t k} = 0.005$ mm. In pulse echo mode, the sound path distance $d_{PEk} = 2 \cdot t_{tk}$ ranges from 48.00 to 50.00 mm with a corresponding symmetric uncertainty $\sigma^{\pm}_{d_{PE}k} = 2 \cdot \sigma^{\pm}_{t_t k} = 0.01$ mm.

Velocity Uncertainty The common material velocity c can be obtained from a reference [Selfridge (1985)] or directly measured. The measured material velocity c_{jk} is described in Equation 8.18 and associated uncertainty $\sigma^{\pm}_{c\,jk}$ is described in Equation 8.19 where $\sigma^{\mp}_{\tau_{2-1}jk} = \sigma^{\mp}_{R_{2-1}jk} + \sigma^{\mp}_{S_{2-1}j}$. These terms are input to the previously described likelihood method with $y_i = c_{jk}$, $y_U = c_{jk} + \sigma^{+}_{c\,jk}$, and $y_L = c_{jk} - \sigma^{-}_{c\,jk}$ to generate the most likely material velocity c_j, positive uncertainty $\sigma^{+}_{c\,j}$, and negative uncertainty $\sigma^{-}_{c\,j}$ for each of the 87 calculation methods. The method with the smallest uncertainty range $(\sigma^{+}_{c\,j} - \sigma^{-}_{c\,j})$ was selected such that $c = 5909.9$ m/s, $\sigma^{+}_{c} = 7.1$ m/s, and $\sigma^{-}_{c} = 2.9$ m/s as the velocity and velocity uncertainty.

$$c_{jk} = \frac{d_{PEk}}{\tau_{2-1}{}_{jk}} \tag{8.18}$$

$$\sigma_{c\,jk}^{\pm} = c_{jk}\sqrt{\left(\frac{\sigma_{d_{PE}k}^{\pm}}{d_{PE}k}\right)^2 + \left(\frac{\sigma_{\tau_{2-1}jk}^{\mp}}{\tau_{2-1}jk}\right)^2} \tag{8.19}$$

Offset Uncertainty The response signal offset time τ_{oj} is to compensate for the slight difference among feature locations unique to each calculation method when considering only the first back-wall reflection. The offset time τ_{oj} is different, and much smaller, than a delay time that would need to be considered for any probe design without direct contact between the piezoelectric material and pipe surface and using only the first back-wall reflection. The measured offset time τ_{ojk} is described in Equation 8.20 and associated uncertainty $\sigma_{\tau_{ojk}}^{\pm}$ is described in Equation 8.21 where $\sigma_{\tau_1 jk}^{\pm} = \sigma_{R_1 jk}^{\pm} + \sigma_{S_1 j}^{\pm}$. These terms are input to the previously described likelihood method with with $y_i = \tau_{ojk}$, $y_U = \tau_{ojk} + \sigma_{\tau_{ojk}}^{+}$, and $y_L = \tau_{ojk} - \sigma_{\tau_{ojk}}^{-}$ to generate the most likely offset time τ_{oj}, positive uncertainty $\sigma_{\tau_{oj}}^{+}$, and negative uncertainty $\sigma_{\tau_{oj}}^{-}$ for each of the 87 calculation methods.

$$\tau_{ojk} = \tau_{1jk} - \frac{d_{PE}k}{c} \tag{8.20}$$

$$\sigma_{\tau_{ojk}}^{\pm} = \sqrt{{\sigma_{\tau_1 jk}^{\pm}}^2 + \left(\frac{d_{PE}k}{c}\right)^2 \left[\left(\frac{\sigma_{d_{PE}k}^{\mp}}{d_{PE}k}\right)^2 + \left(\frac{\sigma_c^{\pm}}{c}\right)^2\right]} \tag{8.21}$$

Thickness Measurement Uncertainty The thickness measurement t_{mjk} is described in Equation 8.22 and associated uncertainty $\sigma_{t_m jk}^{\pm}$ is described in Equation 8.23. The thickness measurement uncertainty $\sigma_{t_m j}$ provides an indication of measurement precision for each calculation method.

$$t_{mjk} = \frac{c\left(\tau_{1jk} - \tau_{oj}\right)}{2} \tag{8.22}$$

$$\sigma_{t_m jk}^{\pm} = \frac{1}{2}\sqrt{\left(\tau_{1jk} - \tau_{oj}\right)^2 \sigma_c^{\pm 2} + c^2\left({\sigma_{\tau_1 jk}^{\pm}}^2 + {\sigma_{\tau_{oj}}^{\mp}}^2\right)} \tag{8.23}$$

Thickness Measurement Error Uncertainty The thickness measurement error t_{ejk} is described in Equation 8.24 and associated uncertainty $\sigma_{t_{ejk}}^{\pm}$ is described in Equation 8.25.

These terms are input to the previously described likelihood method with $y_i = t_{ejk}$, $y_U = t_{ejk} + \sigma^+_{t_{ejk}}$, and $y_L = t_{ejk} - \sigma^-_{t_{ejk}}$ to generate the most likely thickness measurement error t_{ej}, positive uncertainty $\sigma^+_{t_{ej}}$, and negative uncertainty $\sigma^-_{t_{ej}}$ for each of the 87 calculation methods. These values provide an indication of measurement accuracy and precision for each calculation method. The 95% upper confidence limit from the set of simulated distribution models $a_{95/95_j} = t_{ej} + \sigma^+_{t_{ej}}$ is of most interest. This upper confidence limit represents the largest expected measurement error corresponding to a measured thickness greater than the true thickness, described as an over-reporting of the thickness.

$$t_{ejk} = \frac{c\left(\tau_{1jk} - \tau_{oj}\right)}{2} - t_{tk} \tag{8.24}$$

$$\sigma^{\pm}_{t_{ejk}} = \sqrt{\frac{\left(\tau_{1jk} - \tau_{oj}\right)^2 \sigma_c^{\pm 2}}{4} + \frac{c^2\left(\sigma^{\pm}_{\tau_{1jk}}{}^2 + \sigma^{\mp}_{\tau_{oj}}{}^2\right)}{4} + \sigma^{\mp}_{t_{tk}}{}^2} \tag{8.25}$$

8.3.2 Data

The average uncertainty range of each measured factor is shown in Table 8.2 for the peak calculation methods and the threshold calculation methods. The negative values indicate the uncertainty range less than the mean; the positive values indicate the uncertainty range greater than the mean. The uncertainty of measured factors are determined from propagation of measurement uncertainty. The measured true thickness, sound path, repetition, sampling, feature arrival, and velocity uncertainty values are assumed symmetric; the measured offset, thickness, and thickness error uncertainty values are allowed to be asymmetric. Some of the factors are not measured, but rather determined from the weighted censored relative likelihood method analysis; these non-measured factors and allowed to be asymmetric. The values in Table 8.2 are not an inclusive range among all measurements, but rather an average range to compare the typical magnitude among uncertainty factors.

The thickness error uncertainty will vary among calculation methods as displayed in Figure 8.4a for an accurate and precise calculation method and Figure 8.4b for a relatively imprecise method. The relative likelihood contour plot for the imprecise method from Figure 8.4b is

shown in Figure 8.5. Three cumulative distribution function plots for the imprecise method are shown in Figure 8.6; the thickness error measurement mean and associated asymmetric measurement uncertainty confidence limits, the maximum likelihood SEV model fit, the most likely (mean) value μ, the 95% upper confidence limit a_{95}, and the 95% lower confidence limit a_{05} are shown in Figure 8.6a; a sample of 8 distribution models from the set of location scale parameters on the relatively likelihood 95% confidence region perimeter to demonstrate the simulation of potential distribution models are shown in 8.6b; the complete set of potential distribution models and the associated 95% upper confidence limit $a_{95/95}$ and 95% lower confidence limit $a_{05/05}$ are shown in Figure 8.6c.

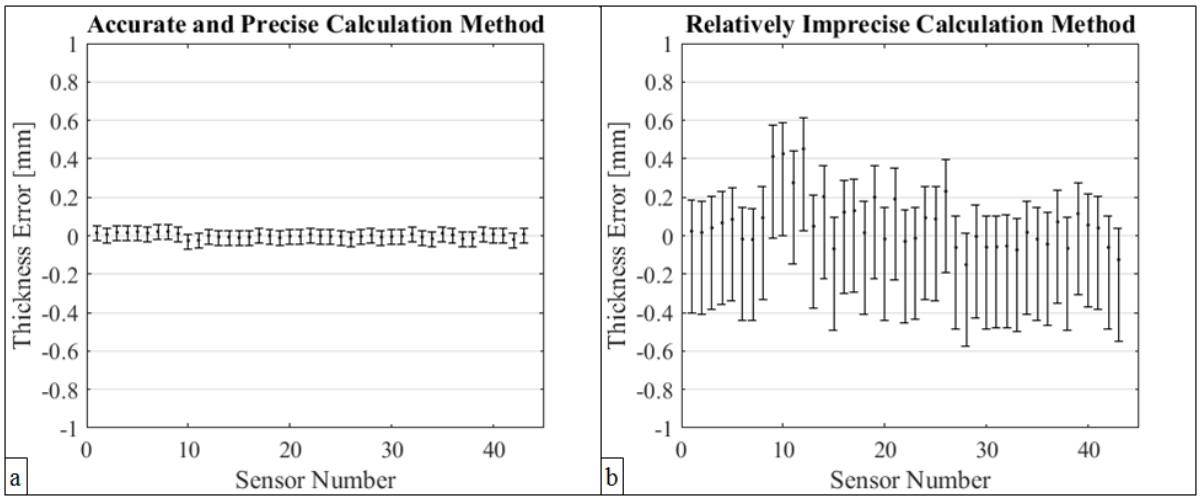

Figure 8.4 The thickness error calculation from the same voltage response signals for each of the 43 sensors are shown for a) an accurate and precise calculation method and b) a relatively imprecise calculation method. Figure previously published [Eason et al. (2016a)].

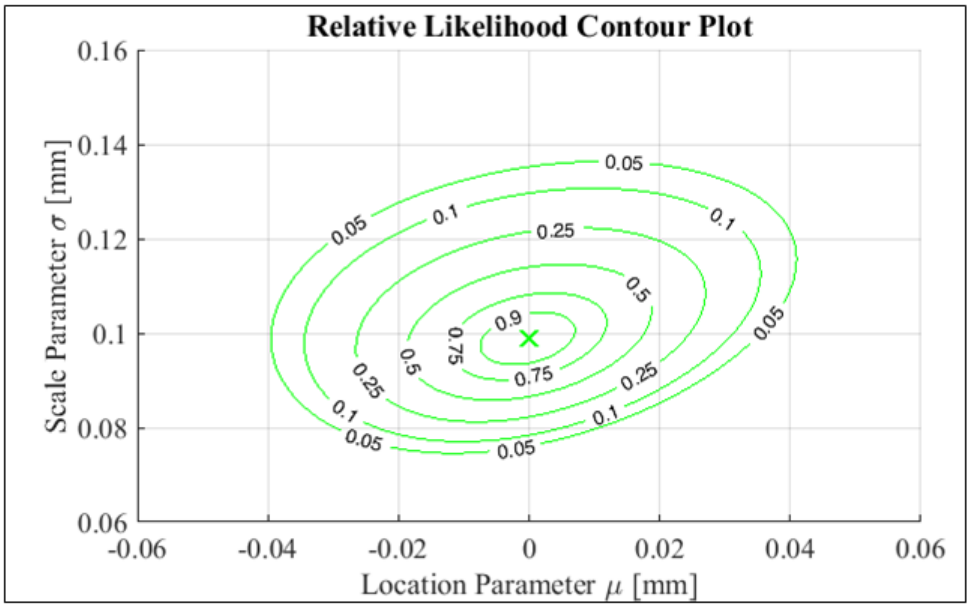

Figure 8.5 The relative likelihood contour plot for the relatively imprecise measurement method from Figure 8.4 is shown. The 95% confidence region perimeter can be taken as the set of location scale parameters μ and σ on the 0.05 contour line. Figure previously published [Eason et al. (2016a)].

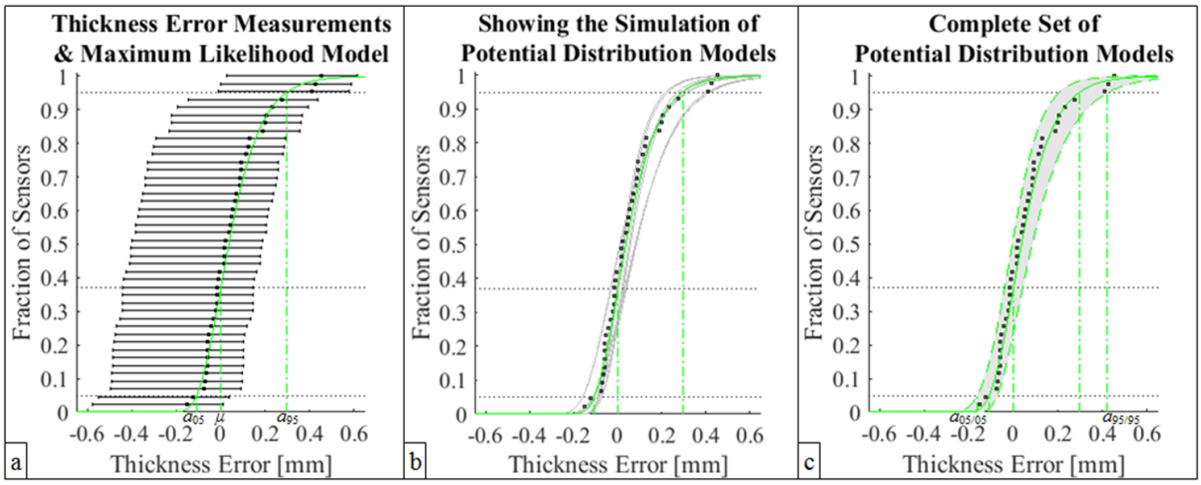

Figure 8.6 Three cumulative distribution function plots for the relatively imprecise measurement method from Figures 8.4 and 8.5 are shown. Plot a) includes the thickness error measurement point and associated asymmetric uncertainty confidence limits. Plot b) includes a sampling from the set of location scale parameters on the relatively likelihood 95% confidence region perimeter. Plot c) includes the complete set of potential distribution models and the associated 95% upper confidence limit $a_{95/95}$ and 95% lower confidence limit $a_{05/05}$. Figure previously published [Eason et al. (2016a)].

8.3.3 Results and Analysis

Four metrics can be considered to compare the accuracy and precision among various calculation methods: the upper confidence limit $\left[a_{95/95_j} = t_{ej} + \sigma^{+}_{t_{ej}}\right]$ corresponding to over-reporting of the thickness, the lower confidence limit $\left[a_{05/05_j} = t_{ej} - \sigma^{-}_{t_{ej}}\right]$ corresponding to under-reporting of the thickness, the average confidence limit $\left[\frac{1}{2}\left(a_{95/95_j} + a_{05/05_j}\right)\right]$, as well as the maximum confidence limit $\left[\max\left(\left|a_{95/95_j}\right|, \left|a_{05/05_j}\right|\right)\right]$. For a symmetric logistic distribution, all four metrics provide equivalent information, but for asymmetric largest and smallest extreme value distributions, the distinction between metrics is of interest. The thickness error confidence limits for each of the 87 calculation methods are organized by measurement category in Figure 8.7a for the maximum confidence limit, and in Figure 8.7b for the upper and lower confidence limits.

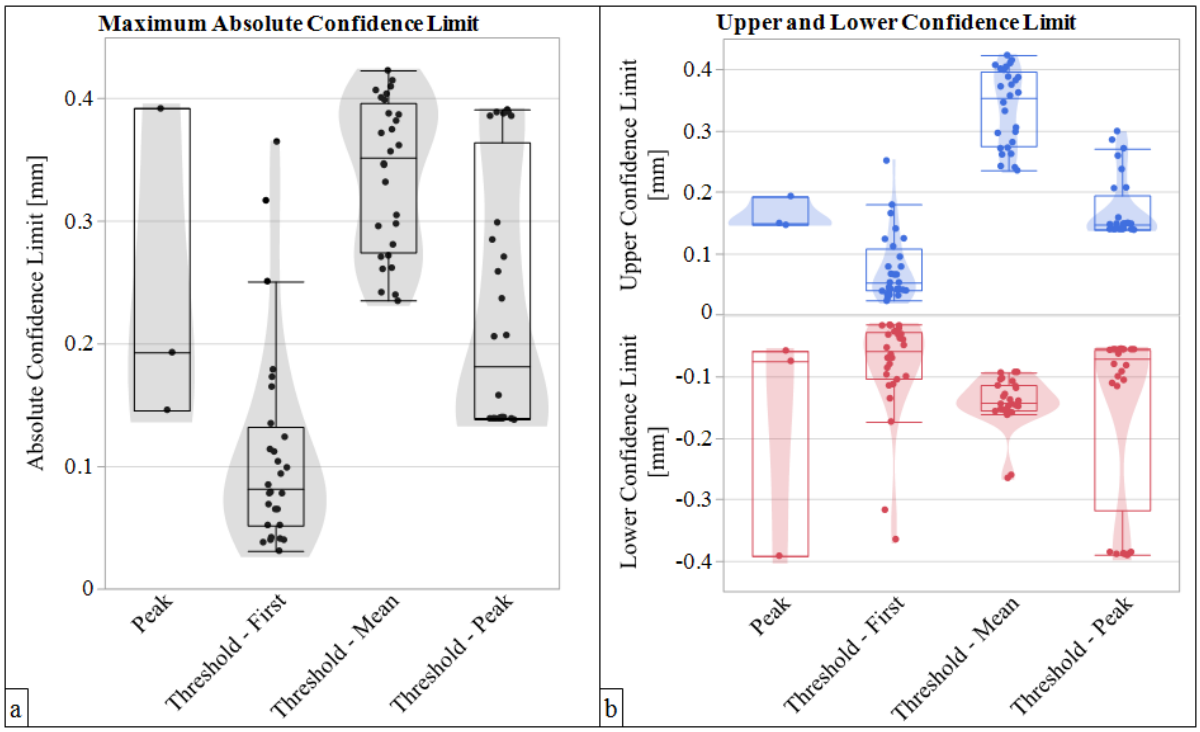

Figure 8.7 The a) thickness error absolute maximum confidence limit, and b) thickness error upper and lower confidence limit for each of the 87 calculation methods grouped by category are shown. Figure previously published [Eason et al. (2016a)].

In general, the first threshold methods are more precise and accurate, the peak and peak threshold methods are less precise, and the mean threshold methods are the least precise. The mean threshold methods relative lack of precision is exacerbated as the maximum confidence limits are upper confidence limits indicating a greater tendency for over-reporting of the thickness as opposed to a more conservative under-reporting of the thickness. Neither the voltage measurement nor the voltage threshold appear to have a significant influence on measurement accuracy and precision.

8.4 Accuracy and Precision - Flat-Bottom Hole

An experiment and analysis was completed using sol-gel transducers in pulse-echo and pitch-catch configuration on a calibration block with a flat-bottom hole (FBH) to demonstrate the weighted censored relative likelihood method for various thickness calculation algorithms [Eason et al. (2016b)].

8.4.1 Methodology

The FBH experiment and analysis methodology are described including experimental setup, time-of-flight calculation methods, and considered uncertainty factors.

8.4.1.1 Experimental Setup

The measurement piece was an A106B carbon steel 4-inch nominal calibration pipe of 13.50 ± 0.07 mm thickness and 114.40 ± 0.07 mm outside diameter with a machined flat-bottom hole (FBH) of 3.975 ± 0.002 mm diameter and 2.032 ± 0.002 mm depth as shown in Figure 8.8. The hole dimension uncertainty is the machining tolerance provided and validated by the manufacturer of the calibration block. A proprietary four element 2 × 2 sol-gel matrix transducer array with 4.00 ± 0.05 mm x 4.00 ± 0.05 mm square elements and 0.90 ± 0.05 mm spacing between element edges are characterized to have a central frequency around 8.5 to 10 MHz for each element [Eason et al. (2016b)]. The transducer was placed in five positions around the FBH as shown in Figure 8.9. From these five positions, a total of four different single element pulse-echo (PE) measurement configurations of A, B, C, and D, and a total of

nine different two element pitch-catch (PC) measurement configurations of E, F, G, Gr, H, Hr, I, J, and Jr were considered as categorized by perpendicular distance to the central ray path as shown in Table 8.3 and Figure 8.10 with r indicating the reverse path to distinguish configurations that are not symmetric. A total of 80 PE and PC combinations among five positions resulted in either four or eight measurements per configuration.

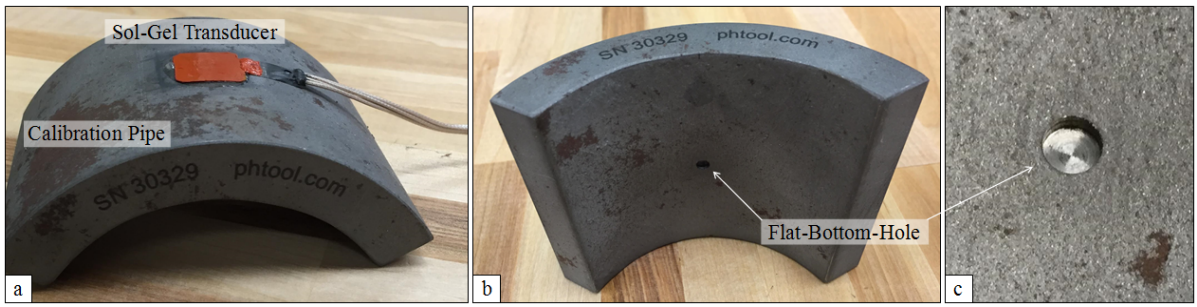

Figure 8.8 Picture of a) sol-gel transducer, b) calibration pipe, and c) flat-bottom hole (FBH). Figure previously published [Eason et al. (2016b)].

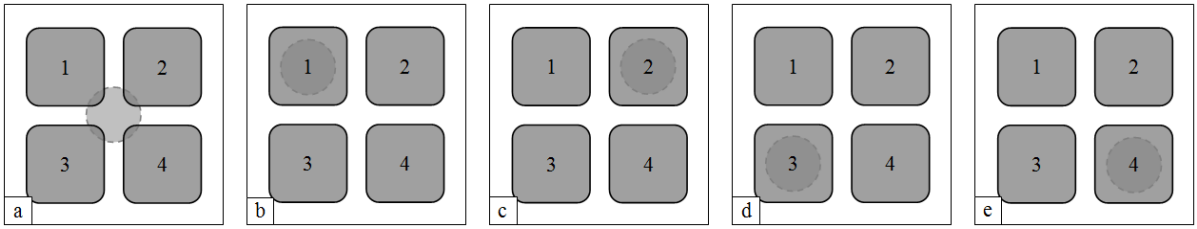

Figure 8.9 Measurement a) Position 0 - central FBH, b) Position 1 - FBH below element 1, c) Position 2 - FBH below element 2, d) Position 3 - FBH below element 3, and e) Position 4 - FBH below element 4. Figure previously published [Eason et al. (2016b)].

The measurements were collected with a benchtop pulser-receiver [Tecscan UTPRCC-50 SN 000065] and a digital storage oscilloscope [LeCroy HDO4002]. The transducer was coupled to the pipe outside diameter with a spring loaded fixture and water based gel couplant. The transducer was actuated with a square pulse of 100V and 45.0 ns width with 45 Ω damping and a pulse-repetition frequency of 500 Hz. The received signals were captured within a 6V amplitude window at a 2mV interval and within a 10 μs time window at a 0.4 ns interval

Table 8.3 Measurement Configuration and Perpendicular Distance from FBH to Ray Path

Measurement	Position 0	Position 1	Position 2	Position 3	Position 4
PE 1-1	(B) 3.5mm	(A) 0.0mm	(C) 4.9mm	(C) 4.9mm	(D) 7.1mm
PE 2-2	(B) 3.5mm	(C) 4.9mm	(A) 0.0mm	(D) 7.1mm	(C) 4.9mm
PE 3-3	(B) 3.5mm	(C) 4.9mm	(D) 7.1mm	(A) 0.0mm	(C) 7.1mm
PE 4-4	(B) 3.5mm	(D) 7.1mm	(C) 4.9mm	(C) 4.9mm	(A) 0.0mm
PC 1-2	(F) 2.5mm	(G) 0.0mm	(Gr) 0.0mm	(J) 4.9mm	(Jr) 4.9mm
PC 1-3	(F) 2.5mm	(G) 0.0mm	(J) 4.9mm	(Gr) 0.0mm	(Jr) 4.9mm
PC 1-4	(E) 0.0mm	(H) 0.0mm	(I) 3.5mm	(I) 3.5mm	(Hr) 0.0mm
PC 2-1	(F) 2.5mm	(Gr) 0.0mm	(G) 0.0mm	(Jr) 4.9mm	(J) 4.9mm
PC 2-3	(E) 0.0mm	(I) 3.5mm	(H) 0.0mm	(Hr) 0.0mm	(I) 3.5mm
PC 2-4	(F) 2.5mm	(J) 4.9mm	(G) 0.0mm	(Jr) 4.9mm	(Gr) 0.0mm
PC 3-1	(F) 2.5mm	(Gr) 0.0mm	(Jr) 4.9mm	(G) 0.0mm	(J) 4.9mm
PC 3-2	(E) 0.0mm	(I) 3.5mm	(Hr) 0.0mm	(H) 0.0mm	(I) 3.5mm
PC 3-4	(F) 2.5mm	(J) 4.9mm	(Jr) 4.9mm	(G) 0.0mm	(Gr) 0.0mm
PC 4-1	(E) 0.0mm	(Hr) 0.0mm	(I) 3.5mm	(I) 3.5mm	(H) 0.0mm
PC 4-2	(F) 2.5mm	(Jr) 4.9mm	(Gr) 0.0mm	(J) 4.9mm	(G) 0.0mm
PC 4-3	(F) 2.5mm	(Jr) 4.9mm	(J) 4.9mm	(Gr) 0.0mm	(G) 0.0mm

resulted in 25000 points per signal. The received signals were captured without averaging with a 2.5 MHz high-pass filter by increasing the gain until either the first reflected signal positive or negative peak reached 80% of the saturation level at a +2.24V or -2.65V threshold. Typical gain values were 42 dB for pulse-echo, 56 dB for pitch-catch adjacent, and 58 dB for pitch-catch diagonal. Each signal was captured 5 times over a few seconds resulting in a total of 400 FBH measurements as well as 80 initial and 80 final velocity calibration measurements away from the FBH. All 560 measurements were collected over a few hours at constant ambient temperature of 25 $\pm$ 1 °C measured from the lab thermostat.

8.4.1.2 Time-of-Flight Calculation Methods

Many thickness calculation methods exist [Svilainis (2013)]; a total of 63 calculation methods are considered and described as 1) the arrival time of Peak, First Threshold, Mean Threshold, and Peak Threshold features at 2) various voltage threshold levels as a percentage of peak amplitude for 3) positive, negative, zero-crossing, and rectified measurements.

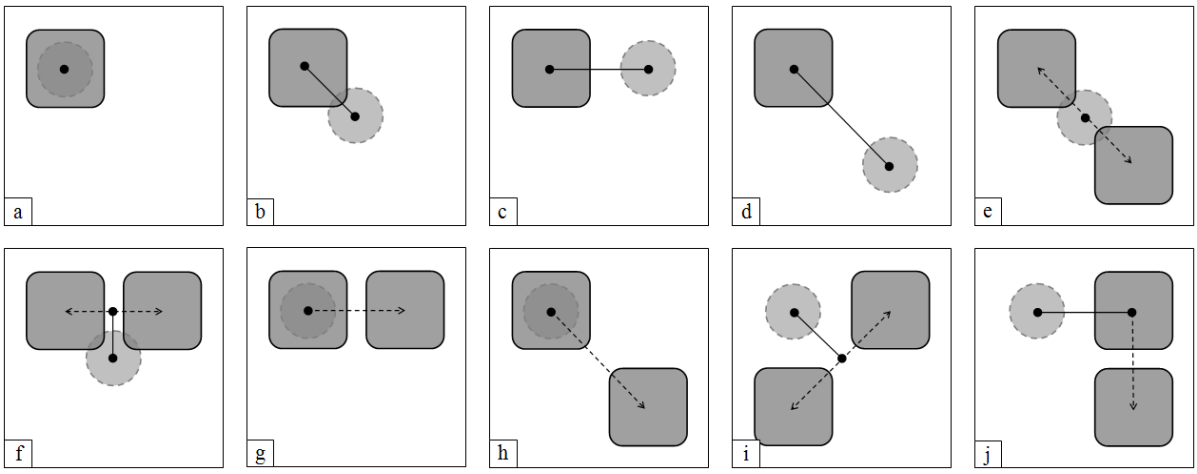

Figure 8.10 Measurement configurations with ray path direction as a dashed arrow line and perpendicular distance from ray path to the FBH as a solid line for (a)-(d) pulse-echo and (e)-(j) pitch-catch. Figure previously published [Eason et al. (2016b)].

8.4.1.3 Considered Uncertainty Factors

The same process as in the flat back-wall experiment was followed for the flat-bottom hole experiment to determine the same uncertainty factors: repetition, sampling rate, dimensional, velocity, offset, thickness measurement, and ultimately thickness measurement error.

8.4.2 Data

Signal features from the first and second flat-bottom hole and back-wall reflections can be observed in the voltage signal in Figure 8.11. The amplitude response from the flat-bottom hole may be compared with an analytical model [Sedov et al. (1992)] in future work.

8.4.3 Results and Analysis

The upper confidence limit $a_{95/95}$ corresponding to over-reporting of thickness is shown in Figure 8.12 for 63 calculation methods. This is a conservative presentation of results not to be confused with the median (or expected) thickness error. Configurations C, D, H, Hr, I, J, and Jr are relatively imprecise; almost none of the calculation methods for these configurations have an upper confidence limit less than the depth of the FBH at 2 mm.

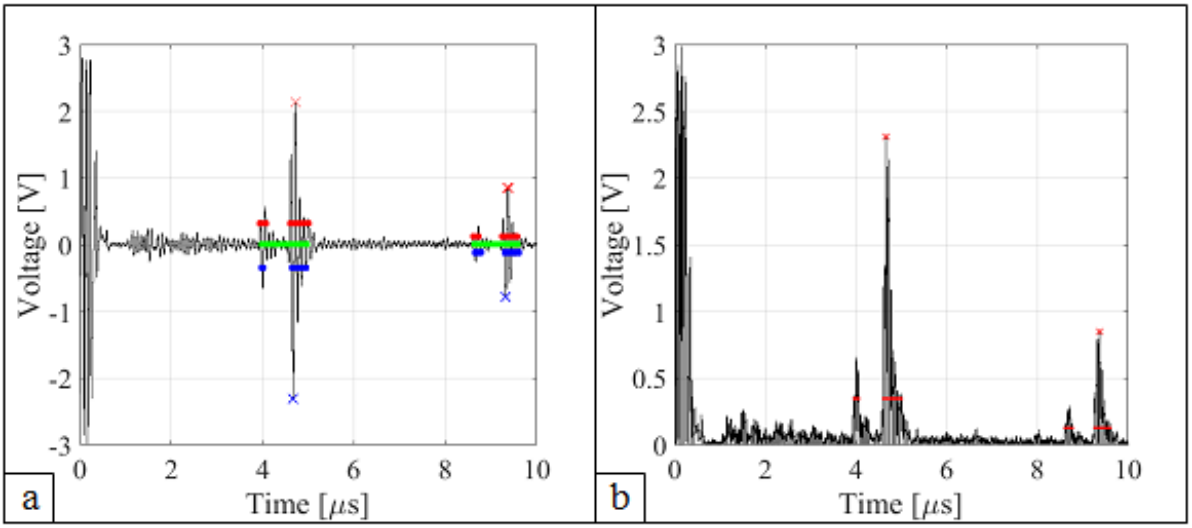

Figure 8.11 Voltage response signal from configuration B in a) full response and b) rectified format showing the first FBH reflection [4.0 μs] and first back-wall reflection [4.7 μs]. The features are observable as positive peak [×], 15% positive threshold [•], 15% zero-crossing [•], 15% negative threshold [•], and negative peak [×]. Figure previously published [Eason et al. (2016b)].

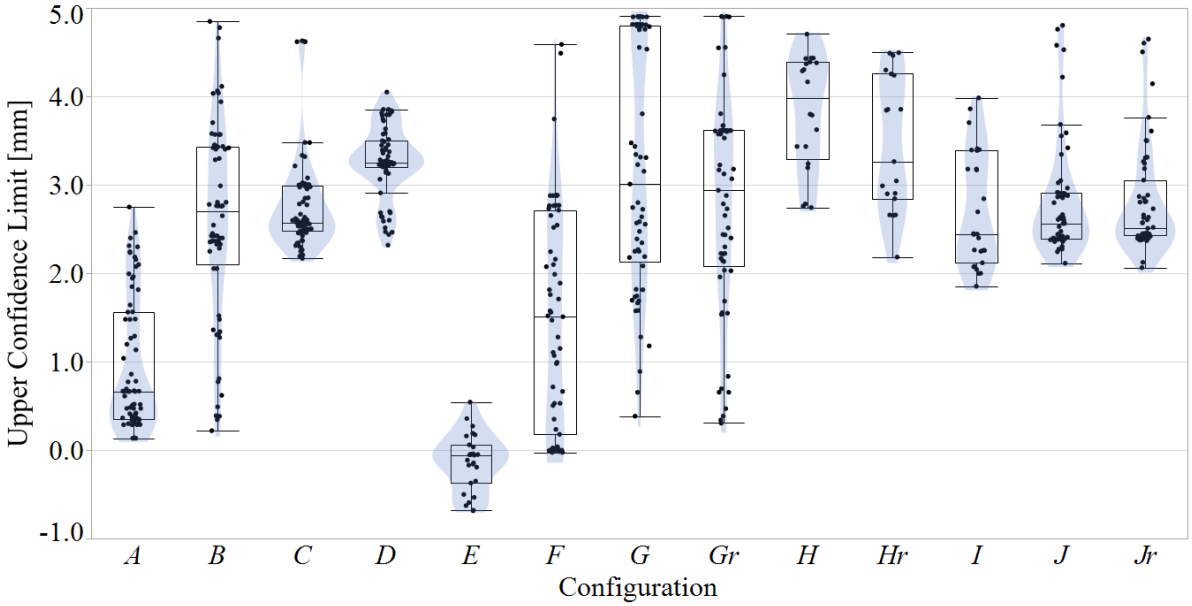

Figure 8.12 Thickness calculation method measurement error upper confidence limits grouped by configuration. Figure previously published [Eason et al. (2016a)].

The remaining configurations A, B, E, F, G, and Gr are relatively precise and shown in Figure 8.13 grouped by calculation method with the following observations: i) the only relatively precise methods for configurations B, G, and Gr, are categorized as First Threshold, ii) all methods are relatively precise for configuration E, however, this may be skewed due to a uniquely small sample size, and iii) the Peak and Peak Threshold methods are consistently relatively precise for configuration A, but not configuration F.

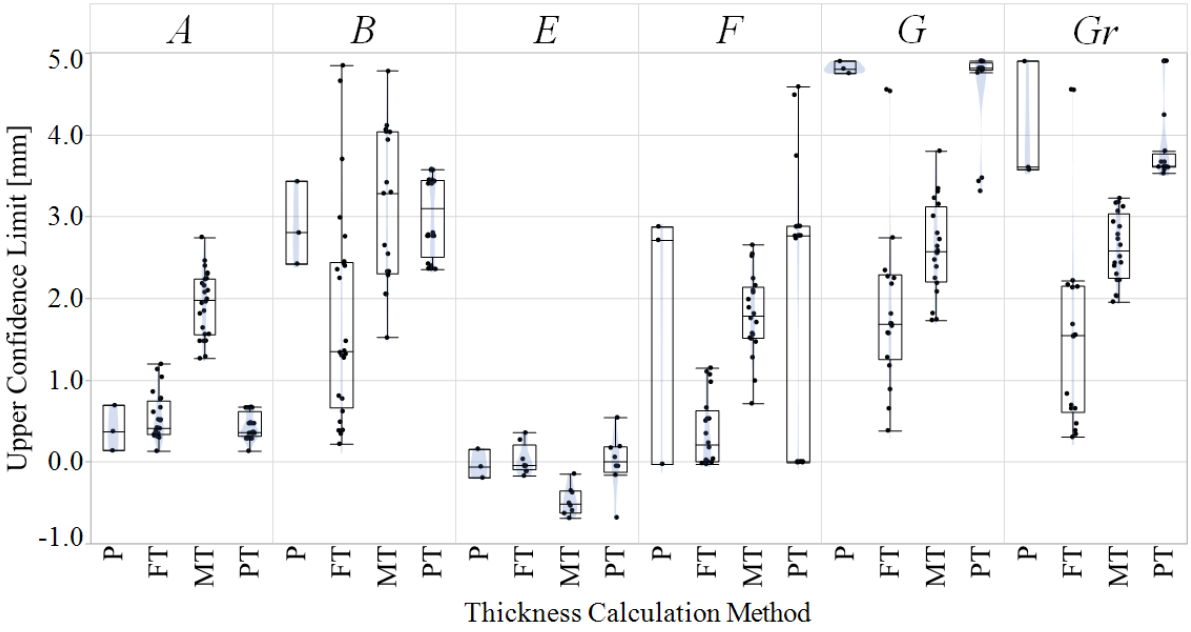

Figure 8.13 Thickness calculation method measurement error upper confidence limits grouped by configuration and method: P - Peak, FT - First Threshold, MT - Mean Threshold, PT - Peak Threshold. Figure previously published [Eason et al. (2016b)].

The upper confidence limit results are generally greater than in the flat back-wall example in Figure 8.7. A comparison of measured uncertainty factors from the flat back-wall to the flat-bottom hole experiments ares as follows: Sound Path Distance - increase to 0.5%, Repetition - increase to 0.08%, Sampling - decrease to 0.006%, Feature Arrival - similar at 0.1%, Measured Velocity - increase to 0.5%. The resulting Modeled Velocity, Offset, Thickness, and Thickness Error uncertainties are ultimately greater due to the increased thickness uncertainty in the calibration pipe as compared to the machined calibration block, in addition, there is a decrease in the number of measurements per model from 43 to either 16, 8, or 4. The underlying sys-

tematic increase in uncertainty present in this experiment is regardless of the introduced pitch distance uncertainty in pitch-catch configurations and regardless of the introduced influence of the FBH. The contribution from Sampling uncertainty is very small based on the digital storage oscilloscope 0.4 ns sampling interval relative to the feature arrival time for the peak calculation methods typically around 5 μs.

8.5 Reliability - System Degradation

There is a general industry need to integrate the spatial domain and time domain variability and uncertainty into the qualification process for SHM measurement systems. While there has been some recent effort in this space [Li et al. (2015); Aldrin et al. (2016); Forsyth (2016); Gianneo et al. (2016); Lindgren (2016); Meeker (2016); Schmitte et al. (2016)], a consensus on how to quantify the multi-parameter and multi-domain sources of independent and dependent variation and uncertainty does not currently exist; it is of interest to develop such a statistical framework.

A robust statistical framework is not provided in this work, however, a reliability evaluation for the degradation of an experimental structural health monitoring system with time domain data variability is described. A study was conducted to test the reliability of a set of 40 prototype sensors in an accelerated lifecycle environment. The purpose of the study was to determine if 90% of the sensors would survive beyond a specified lifetime. The analysis is based on known statistical methods (Meeker and Escobar, 1998) using JMP® commercial software (SAS Institute, 2014).

8.5.1 Methodology

Each of the 40 sensors had a signal reading collected every 12 hours up until 204 readings (2448 hours). At this point, the electronics system was upgraded, and all failed and surviving sensors were repaired, recalibrated, and reinstalled. The experiment continued to collect data on all 40 sensors every 12 hours up to 103 readings (1236 hours) under a similar accelerated lifecycle environment. A failed sensor has been defined conservatively as any sensor that produces an unacceptable signal based on any of the following signal characteristics: low signal to noise

ratio (Type N), low amplitude (Type A), excessive oscillations (Type R), and signal distortion (Type D).

8.5.2 Data

The initial experiment data prior to the repair is summarized in Table 8.4 and after the repair summarized in Table 8.5.

8.5.3 Analysis

A non-parametric plot of the initial data is shown in Figure 8.14. There are three occurrences around 600 hours, 1600 hours, and 1700 hours where many sensors failed within in a short period of time indicating the possibility of non-independent systematic failures. Such systematic failures could be the result of an unreliable common electronics grounding design that was ultimately repaired after 2448 hours. Therefore, any failure within 24 hours of a previous failure of the same mechanism was right censored in an attempt to provide a more independent failure data set as shown in Figure 8.14.

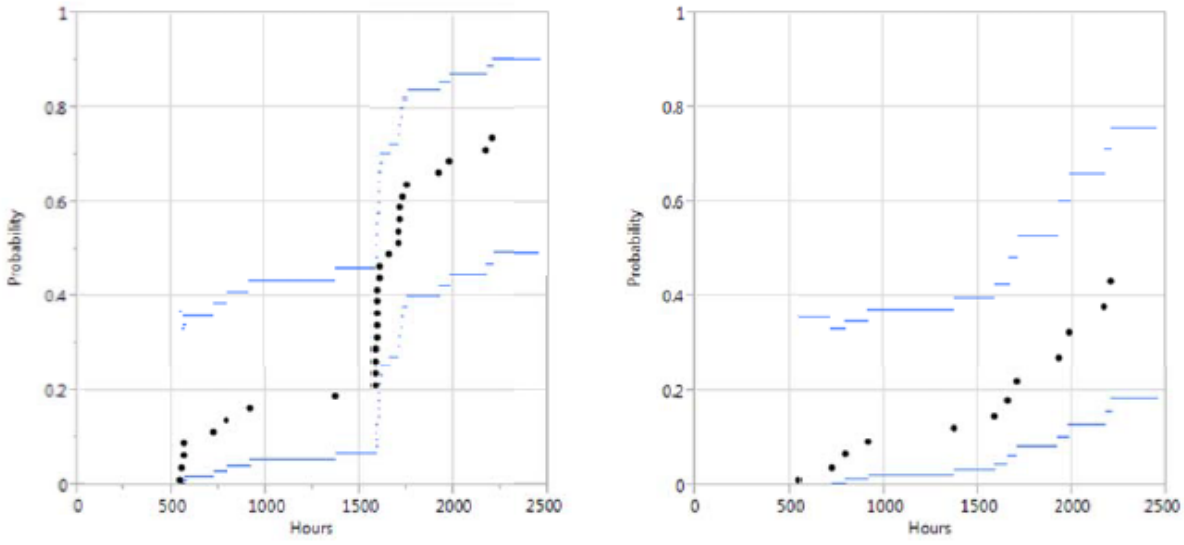

Figure 8.14 Plots for non-parametric dependent (left) and non-parameteric independent (right) initial data.

Table 8.4 Initial Failure Data

Sensor Name	Failure [Reading Number]	Failure [Hours]	Censor	Failure
311	45	540	None	Type R
209	46	552	None	Type R
214	47	564	None	Type R
218	47	564	None	Type R
316	60	720	None	Type N
310	66	792	None	Type N
301	76	912	None	Type A
201	114	1368	None	Type A
307	132	1584	None	Type R
313	132	1584	None	Type R
315	132	1584	None	Type R
317	132	1584	None	Type R
208	133	1596	None	Type R
213	133	1596	None	Type R
210	133	1596	None	Type R
217	133	1596	None	Type R
308	133	1596	None	Type R
207	134	1608	None	Type R
212	134	1608	None	Type R
211	138	1656	None	Type R
318	142	1704	None	Type R
220	142	1704	None	Type R
206	143	1716	None	Type R
205	143	1716	None	Type R
304	144	1728	None	Type R
203	146	1752	None	Type R
202	160	1920	None	Type R
306	165	1980	None	Type R
302	181	2172	None	Type R
309	184	2208	None	Type R
320	204	2448	Right	None
204	204	2448	Right	None
215	204	2448	Right	None
216	204	2448	Right	None
219	204	2448	Right	None
303	204	2448	Right	None
305	204	2448	Right	None
312	204	2448	Right	None
314	204	2448	Right	None
319	204	2448	Right	None

Table 8.5 Failure Data After Repair

Sensor Name	Failure [Reading Number]	Failure [Hours]	Censor	Failure
208	0	0	Left	Type A
320	0	0	Left	Type A
206	5	60	None	Type A
310	13	156	None	Type N
318	13	156	None	Type R
301	23	276	None	Type N
209	24	288	None	Type A
201	24	288	None	Type A
207	24	288	None	Type A
203	56	672	None	Type A
212	65	780	None	Type A
213	85	1020	None	Type A
202	85	1020	None	Type A
220	93	1116	None	Type A
211	100	1200	None	Type R
311	103	1236	Right	None
214	103	1236	Right	None
218	103	1236	Right	None
316	103	1236	Right	None
307	103	1236	Right	None
313	103	1236	Right	None
315	103	1236	Right	None
317	103	1236	Right	None
210	103	1236	Right	None
217	103	1236	Right	None
308	103	1236	Right	None
205	103	1236	Right	None
304	103	1236	Right	None
306	103	1236	Right	None
302	103	1236	Right	None
309	103	1236	Right	None
204	103	1236	Right	None
215	103	1236	Right	None
216	103	1236	Right	None
219	103	1236	Right	None
303	103	1236	Right	None
305	103	1236	Right	None
312	103	1236	Right	None
314	103	1236	Right	None
319	103	1236	Right	None

Multiple failure distribution models were fit to the independent failure data set for the following scenarios: i) ignoring failure mechanism, ii) isolating failure mechanism Type A, iii) isolating failure mechanism Type N, and iv) isolating failure mechanism Type R. The best fit distribution for each scenario is shown in Figure 8.15. The fit of the Weibull distribution for each scenario is adequate as shown in Figure 8.16.

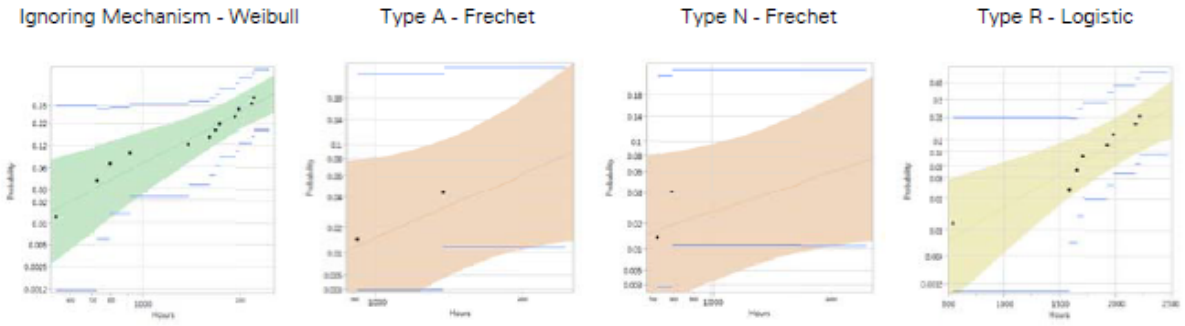

Figure 8.15 Initial data best fit distributions for specific failure mechanisms.

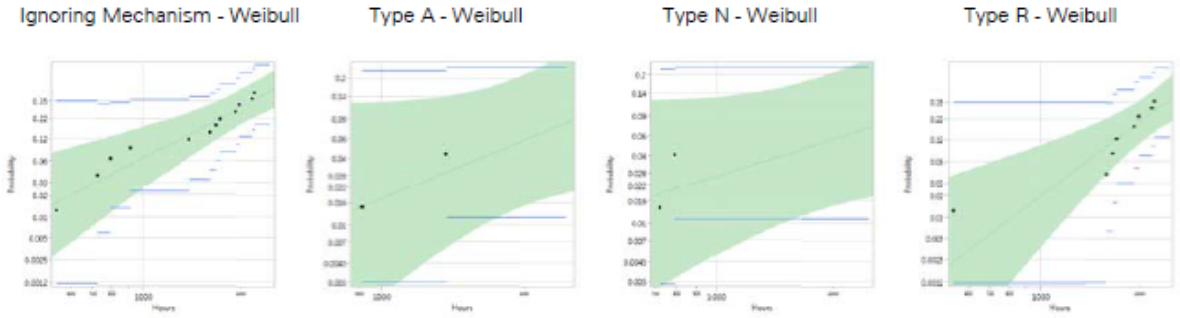

Figure 8.16 Initial data Weibull distribution for specific failure mechanisms.

The failure modes have been combined using the best fit distribution models to each failure mechanism as well as using Weibull distributions for each failure mechanism as shown in Figure 8.17.

The experiment continued after the electronics and sensors were repaired at 2448 hours. The repair data was analysed in a similar fashion by approximating an independent data set and then fitting distributions to different failure mechanism scenarios as shown in Figures 8.18-8.21.

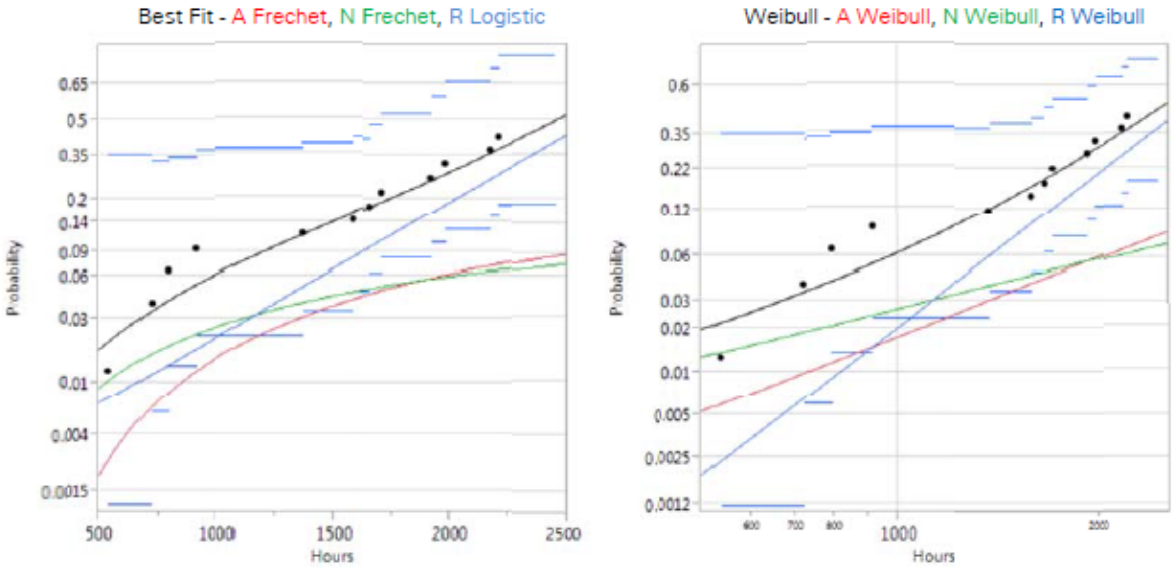

Figure 8.17 Initial data combined failure models.

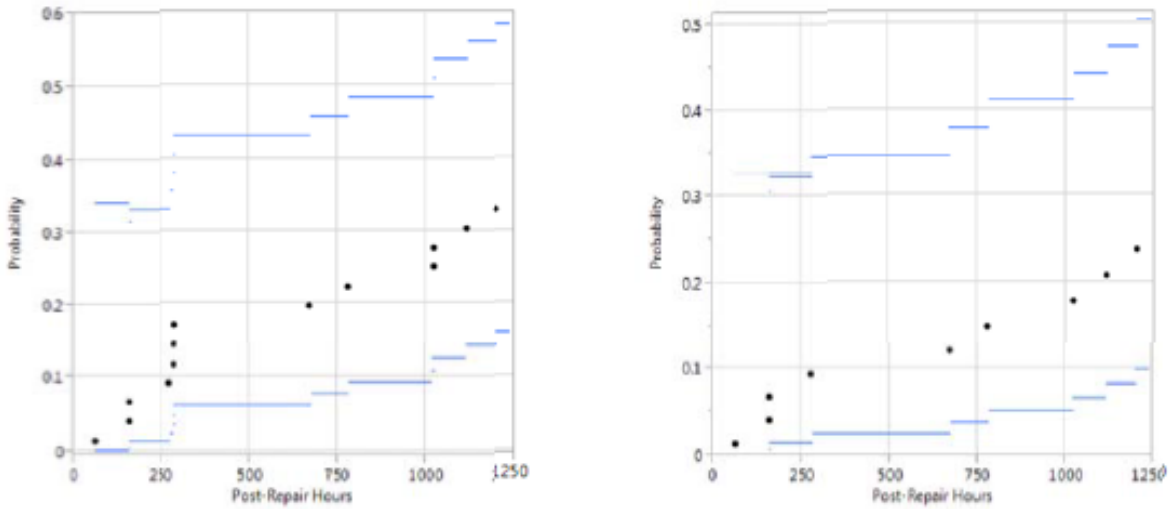

Figure 8.18 Plots for non-parametric dependent (left) and non-parametric independent (right) repair data.

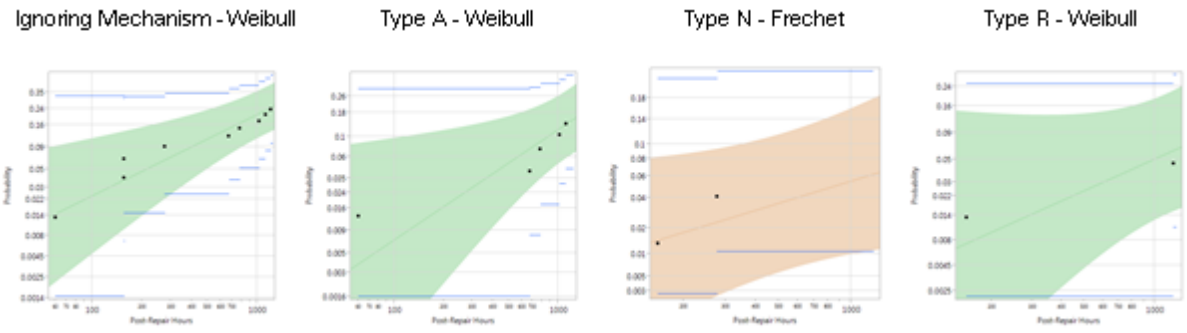

Figure 8.19 Repair data best fit distributions for specific failure mechanisms.

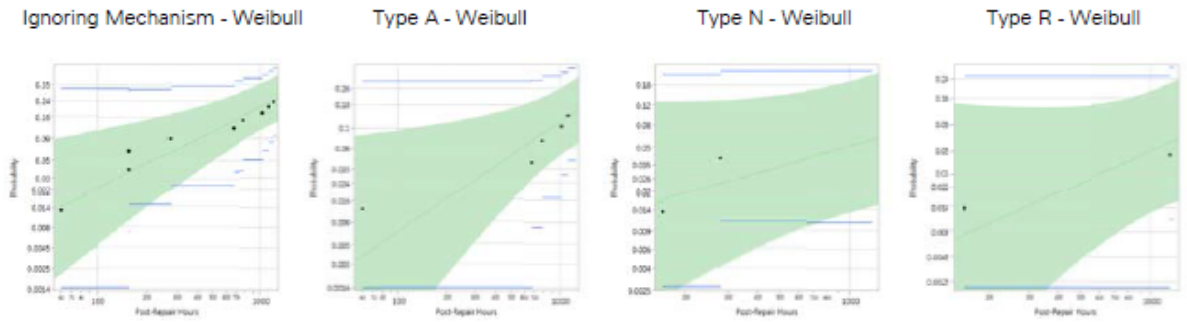

Figure 8.20 Repair data Weibull distribution for specific failure mechanisms.

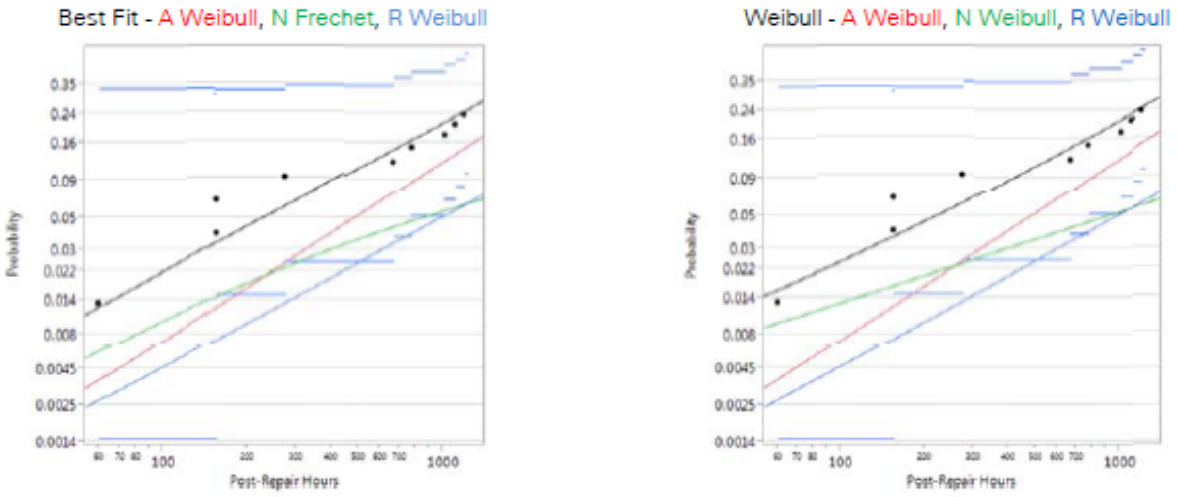

Figure 8.21 Repair data combined failure models.

8.5.4 Results

The estimated 10% failure quantile $t_{0.10}$ information from all scenarios is shown in Table 8.6 for best fit and Weibull distributions.

Table 8.6 Initial and Repair Dataset 10% Failure Quantiles

Scenario				$t_{0.10}$ Lower 95%	$t_{0.10}$ Estimate	$t_{0.10}$ Upper 95%
Initial	Best Fit	Ignore	Weibull	825	1182	1692
		A	Frechet	982	2730	7592
		N	Frechet	646	3405	17941
		R	Logistic	1258	1671	2084
		Combined		766	1262	1759
	Weibull	Ignore	Weibull	825	1182	1692
		A	Weibull	1127	2717	6548
		N	Weibull	775	3355	14518
		R	Weibull	1228	1594	2067
		Combined		781	1244	1707
Repair	Best Fit	Ignore	Weibull	183	441	1061
		A	Weibull	410	862	1809
		N	Frechet	152	3127	64362
		R	Weibull	433	1961	8890
		Combined		71	459	847
	Weibull	Ignore	Weibull	183	441	1061
		A	Weibull	410	862	1809
		N	Weibull	211	2955	41297
		R	Weibull	433	1961	8890
		Combined		61	463	864

There are four scenarios where the best fit distribution is not Weibull: Initial Type A, Initial Type N, Initial Type R, and Repair Type N. All four of these scenarios can be compared to a Weibull distribution as shown in Table 8.6. All four scenarios are very similar in terms of mean and 95% confidence intervals. As a result, the combined failure mechanism scenarios are also very similar for the initial data and the repair data. Therefore, it is reasonable to use Weibull distributions to approximate all scenarios. The estimated model parameters assuming a Weibull distribution for all scenarios are shown in Table 8.7.

Table 8.7 Model Parameter Values for Different Scenarios Assuming Weibull Distribution

Scenario		Failures	β			α		
			Lower 95%	Estimate	Upper 95%	Lower 95%	Estimate	Upper 95%
Initial	Ignore	12	1.36	2.37	3.72	2414	3054	4875
	A	2	0.79	1.78	-	1134	9616	81625
	N	2	0.48	1.12	-	670	25212	948620
	R	8	2.22	3.49	8.22	2287	3034	4025
	Combine	12	-	-	-	-	-	-
Repair	Ignore	9	0.49	0.98	1.72	2073	4338	25176
	A	5	0.68	1.25	7.18	1242	5240	22107
	N	2	0.26	0.62	-	149	114026	87085395
	R	2	0.45	1.05	-	383	16834	740695
	Combine	9	-	-	-	-	-	-

8.5.4.1 Initial Reliability

In an accelerated lifecycle environment, based on the initial test, the sensor system will have 90% survivability between 781 and 1707 hours with 95% confidence using the Weibull distribution combined failure mechanism model.

The 10% failure quantile of the combined failure mechanism model is very similar to the 10% failure quantile of the model that ignores damage mechanisms at between 825 and 1692 hours. The Weibull distribution of the ignored damage mechanism scenario results in a β parameter of 2.37, indicating an overall wear-out failure mechanism. Taking a closer look, by isolating the possible failure mechanisms, the wear-out is dominated by the Type R mechanism with a β parameter of 3.49 (as well as the having the majority of failures). The Type A mechanism and Type N mechanism fail at a more random pace with β parameters of 1.78 and 1.12 respectively. There are no Type D failures.

The failure behavior for similar electronics systems is expected to be random. Even the attempt to censor systematic failures to mimic independent failure behavior does not result in the expected random failure behavior. The observed wear-out failure mode indicates a possible design flaw.

8.5.4.2 Repair Effectiveness

A repair was completed after 1236 hours to address the systematic failures related to grounding and prevent Type R failures. Post-repair, the 90% survivability was lower between 61 and 864 hours with 95% confidence using the Weibull distribution combined failure mechanism model. This indicates that the repair did not fully return the sensor and electronics system to the original state of quality. The 10% failure quantile of the combined failure mechanism model is very similar to the 10% failure quantile of the model that ignores damage mechanisms at between 183 and 1064 hours. The Weibull distribution of the ignored damage mechanism scenario results in a β parameter of 0.98, indicating a more random failure mechanism. Taking a closer look, by isolating the possible failure mechanisms, the random failure is common among Type A, Type N, and Type R failures with β parameters of 1.25, 0.62, and 1.05 respectively. Again, there are no Type D failures.

Another approach is to compare the 10% failure quantile of each individual failure mechanism before and after the repair. Type R failures have an estimated 90% survivability of 1594 hours before the repair and 1961 hours after the repair, but this improvement may not be statistically significant as the confidence intervals have a large overlap. Type A failures have an estimated 90% survivability of 2717 hours before the repair and 862 hours after the repair, but this decline may not be statistically significant as the confidence intervals overlap. Type N failures have an estimated 90% survivability of 3355 hours before the repair and 2955 hours after the repair, but this decline may not be statistically significant as the confidence intervals have a large overlap.

The repair to fix the electronics grounding was likely not effective at returning the system to its original state of quality as observed by a decrease in 90% survivability time; but the repair may have corrected a design flaw that was causing wear-out failures as observed with the decrease in β parameter of the overall system and more clearly observed with the decrease in β parameter and an increase in survival time of the isolated Type R failure mechanism. The post-repair failure behavior was more typical of similar electronics systems indicating that a significant design flaw may have been corrected with the repair.

8.6 Summary

This chapter proposed a weighted censored relative likelihood method to capture asymmetric measurement uncertainty as applied to a sol-gel ultrasonic thickness structural health monitoring measurement system. This new statistical method may be used to quantify the propagation af asymmetric measurement uncertainty. The upper and lower confidence limits of measurements collected on calibration blocks over a short time period at ambient temperature were presented for two experiments.

Finally, a statistical reliability evaluation of experimental structural health monitoring data with time domain variability was described.

CHAPTER 9. PROGNOSIS

Regarding prognosis information, a pipe failure condition is based on the material behavior relation between stress and strain. Various material models may be applicable: high strength steel is typically linear-elastic, low-strength and medium-strength steel is typically elastic-plastic or fully plastic, and metals at high temperature are typically viscoplastic [Anderson (2005)]. The rate of wall thinning is not necessarily uniform over the internal surface, and in the extreme case, a single pit can initiate and grow, possibly in high temperature environments [Garverick (1994); Godard (1984); Wu et al. (2004b)]. While NDE methods can be used to detect such pitting corrosion; the pipe failure criteria will define the necessary NDE detection threshold. This threshold must be met by the NDE or SHM technique with consideration for measurement uncertainty. Elastic and plastic failure criteria for steel pipe with uniform and localized pitting corrosion is investigated via analytical and finite element methods.

9.1 Uniform Corrosion

The case of uniform corrosion is represented by a pipe with uniform wall thickness.

9.1.1 Pipe Geometry

Consider an infinitely long cylindrical pipe of isotropic material with an average diameter D and wall thickness t under internal pressure p with no external loading at a constant and uniform temperature. The pipe can be represented by a plane-strain model as shown in Figure 9.1. The thin-wall approximation is not applied.

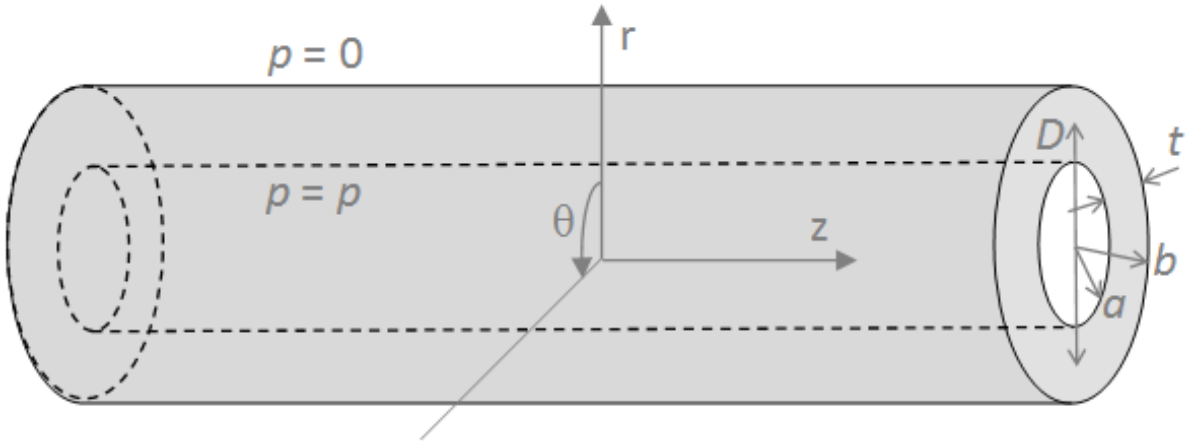

Figure 9.1 Schematic of pipe geometry and loading model.

9.1.2 Linear-Elastic Material

A linear-elastic material model is considered for analytical and finite element stress analysis methodologies.

9.1.2.1 Analytical Methodology

The linear-elastic stress field, defined as the stress tensor $\boldsymbol{\sigma}(r)$, and yield condition, defined as the von Mises yield criterion σ_Y, are derived from deformation geometry, momentum balance, and linear-elastic material model equations [Sadd (2009)]. The derivation is shown via reduction with an axisymmetric plane-strain condition. The thin-wall approximation is not applied.

First consider the axisymmetric dispalement u, strain ϵ, and stress σ fields for plane-strain as shown in Equation 9.1. Normal strains ϵ_r ϵ_θ ϵ_z and shear strains $\epsilon_{\theta z}$ ϵ_{zr} $\epsilon_{r\theta}$ are defined by the geometric relations as shown in Equations 9.2-9.7.

$$\begin{array}{llllll} u_r(r) & u_\theta = 0 & u_z = 0 & & & \\ \epsilon_r & \epsilon_\theta & \epsilon_z & \epsilon_{\theta z} & \epsilon_{zr} & \epsilon_{r\theta} \\ \sigma_r & \sigma_\theta & \sigma_z & \sigma_{\theta z} & \sigma_{zr} & \sigma_{r\theta} \end{array} \tag{9.1}$$

$$\epsilon_r = \frac{\partial u_r}{\partial r} = \frac{du_r}{dr} \tag{9.2}$$

$$\epsilon_\theta = \frac{1}{r}\left(\frac{\partial u_\theta}{\partial \theta} + u_r\right) = \frac{u_r}{r} \tag{9.3}$$

$$\epsilon_z = \frac{\partial u_z}{\partial z} = 0 \tag{9.4}$$

$$\epsilon_{\theta z} = \frac{1}{2}\left(\frac{\partial u_\theta}{\partial z} + r\frac{\partial u_z}{\partial \theta}\right) = 0 \tag{9.5}$$

$$\epsilon_{zr} = \frac{1}{2}\left(\frac{\partial u_z}{\partial r} + \frac{\partial u_r}{\partial z}\right) = 0 \tag{9.6}$$

$$\epsilon_{r\theta} = \frac{1}{2}\left(\frac{1}{r}\frac{\partial u_r}{\partial \theta} + \frac{\partial u_\theta}{\partial r} - \frac{u_\theta}{r}\right) = 0 \tag{9.7}$$

The material model relation between stress and strain is provided by Hooke's Law in Equation 9.8 with resulting shear stresses $\sigma_{\theta z}$ σ_{zr} $\sigma_{r\theta}$ shown to be zero in Equations 9.9-9.11.

$$\varepsilon_{ij} = \frac{1+\nu}{E}\sigma_{ij} - \frac{\nu}{E}\sigma_{kk}\delta_{ij} + \alpha\Delta T\delta_{ij} \tag{9.8}$$

$$\sigma_{\theta z} = \frac{E}{1+\nu}\epsilon_{\theta z} = 0 \tag{9.9}$$

$$\sigma_{zr} = \frac{E}{1+\nu}\epsilon_{zr} = 0 \tag{9.10}$$

$$\sigma_{r\theta} = \frac{E}{1+\nu}\epsilon_{r\theta} = 0 \tag{9.11}$$

Applying the zero longitudinal strain ϵ_z from Equation 9.4 to Hooke's Law in Equation 9.8 results in Equation 9.12 and a relation for longitudinal stress σ_z in Equation 9.13.

$$\epsilon_z = \frac{1+\nu}{E}\sigma_z - \frac{\nu}{E}\left(\sigma_r + \sigma_\theta + \sigma_z\right) = 0 \tag{9.12}$$

$$\sigma_z = \nu\sigma_r + \nu\sigma_\theta \tag{9.13}$$

Substituting Equation 9.13 into Hooke's Law in Equation 9.8 as a function of Young's modulus E, Poisson's ratio ν, and coefficient of thermal expansion α, results in the relation for radial strain ϵ_r in Equation 9.14 and circumferential strain ϵ_θ in Equation 9.15.

$$\epsilon_r = \frac{1+\nu}{E}\left(\left(1-\nu\right)\sigma_r - \nu\sigma_\theta\right) \tag{9.14}$$

$$\epsilon_\theta = \frac{1+\nu}{E}\left(\left(1-\nu\right)\sigma_\theta - \nu\sigma_r\right) \tag{9.15}$$

Taking the derivative of Equation 9.15 with respect to r results in Equation 9.16.

$$\frac{d\epsilon_\theta}{dr} = \frac{1+\nu}{E}\left(\left(1-\nu\right)\frac{d\sigma_\theta}{dr} - \nu\frac{d\sigma_r}{dr}\right) \tag{9.16}$$

A differential element can be used to derive the conservation of momentum equation as shown in Equation 9.17.

$$\frac{\partial\sigma_r}{\partial r} + \frac{1}{r}\frac{\partial\sigma_{r\theta}}{\partial\theta} + \frac{\partial\sigma_{rz}}{\partial z} + \frac{\sigma_r - \sigma_\theta}{r} + b_r = 0 \tag{9.17}$$

Equation 9.17 can be reduced to find the relation for radial stress σ_θ as shown in Equation 9.18 as well as the derivative with respect to r as shown in Equation 9.19.

$$\sigma_\theta = r\frac{d\sigma_r}{dr} + \sigma_r \tag{9.18}$$

$$\frac{d\sigma_\theta}{dr} = r\frac{d^2\sigma_r}{dr^2} + 2\frac{d\sigma_r}{dr} \tag{9.19}$$

Substitution of Equation 9.3 into Equation 9.2 will result in Equation 9.20.

$$\epsilon_r = \frac{d}{dr}\left(r\epsilon_\theta\right) = \epsilon_\theta + r\frac{d\epsilon_\theta}{dr} \tag{9.20}$$

Substitution of Equations 9.14-9.16 into Equation 9.20 will result in Equation 9.21 and simplified to Equation 9.22.

$$\frac{1+\nu}{E}\left(\left(1-\nu\right)\sigma_r - \nu\sigma_\theta\right) = \frac{1+\nu}{E}\left(\left(1-\nu\right)\sigma_\theta - \nu\sigma_r\right) + r\left(\frac{1+\nu}{E}\left(\left(1-\nu\right)\frac{d\sigma_\theta}{dr} - \nu\frac{d\sigma_r}{dr}\right)\right) \tag{9.21}$$

$$\sigma_r - \sigma_\theta = r\left((1-\nu)\frac{d\sigma_\theta}{dr} - \nu\frac{d\sigma_r}{dr}\right) \tag{9.22}$$

Substitution of Equations 9.18 and 9.19 into Equation 9.22 will result in Equation 9.23 and simplified to Equation 9.24

$$\sigma_r - \left(r\frac{d\sigma_r}{dr} + \sigma_r\right) = r\left((1-\nu)\left(r\frac{d^2\sigma_r}{dr^2} + 2\frac{d\sigma_r}{dr}\right) - \nu\frac{d\sigma_r}{dr}\right) \tag{9.23}$$

$$\frac{d^2\sigma_r}{dr^2} + \frac{3}{r}\frac{d\sigma_r}{dr} = 0 \tag{9.24}$$

The radial stress second order differential equation in Equation 9.24 can be solved with the characteristic equation $\sigma_r = r^a$ and constants A and B as shown in Equation 9.25 as well as the derivative with respect to r as shown in Equation 9.26.

$$\sigma_r = A + \frac{B}{r^2} \tag{9.25}$$

$$\frac{d\sigma_r}{dr} = -2\frac{B}{r^3} \tag{9.26}$$

The circumferential stress is obtained by substitution of Equations 9.25 and 9.26 into Equation 9.18 as shown in Equation 9.27.

$$\sigma_\theta = -2\frac{B}{r^2} \tag{9.27}$$

The longitudinal stress is obtained by substitution of Equation 9.25 and Equation 9.27 into Equation 9.13 as shown in Equation 9.28.

$$\sigma_z = 2\nu A \tag{9.28}$$

Boundary conditions are applied at the inside radius a where $\sigma_r \mid_{r=a} = -p$ and at the outside radius b where $\sigma_r \mid_{r=a} = 0$ resulting in the stress tensor $\boldsymbol{\sigma}(r)$ shown in Equation 9.29.

$$\boldsymbol{\sigma}(r) = \frac{p}{\left(\frac{b}{a}\right)^2 - 1} \begin{bmatrix} 1 - \left(\frac{b}{r}\right)^2 & 0 & 0 \\ 0 & 1 + \left(\frac{b}{r}\right)^2 & 0 \\ 0 & 0 & 2\nu \end{bmatrix} \tag{9.29}$$

The von Mises yield criterion σ_Y in terms of principal stresses $\sigma_I = \sigma_r$, $\sigma_{II} = \sigma_\theta$, and $\sigma_{III} = \sigma_z$ is described in Equations 9.30-9.32.

$$\sigma_Y = \sqrt{\frac{1}{2}\left((\sigma_I - \sigma_{II})^2 + (\sigma_{II} - \sigma_{III})^2 + (\sigma_{III} - \sigma_I)^2\right)} \tag{9.30}$$

$$\sigma_Y = \sqrt{{\sigma_r}^2 + {\sigma_\theta}^2 + {\sigma_z}^2 - \sigma_r\sigma_\theta - \sigma_\theta\sigma_z - \sigma_z\sigma_r} \tag{9.31}$$

$$\sigma_Y = \frac{p\sqrt{3\left(\frac{b}{r}\right)^4 + (2\nu - 1)^2}}{\left(\frac{b}{a}\right)^2 - 1} \tag{9.32}$$

9.1.2.2 Analytical Results

Four pipes with various diameter to thickness ratios $\frac{D}{t} = \frac{b+a}{b-a}$ shown in Figure 9.2 are considered. The corresponding normalized principal component and von Mises stresses are plotted in Figure 9.3 for $\nu = 0.3$. The largest absolute maximum normalized principal component and von Mises stresses occur at $r = a$; such stresses are plotted in Figure 9.4 for a range of diameter to thickness ratios. Only internal pressure loading is considered; static loads such as pipe weight and support reactions, and dynamic loads such as thermal induced strain and vibration are neglected.

The largest absolute maximum normalized principal component and von Mises stresses occur at $r = a$; such stresses are plotted in Figure 9.4 for a range of diameter to thickness ratios. Only internal pressure loading is considered; static loads such as pipe weight and support reactions, and dynamic loads such as thermal induced strain and vibration are neglected.

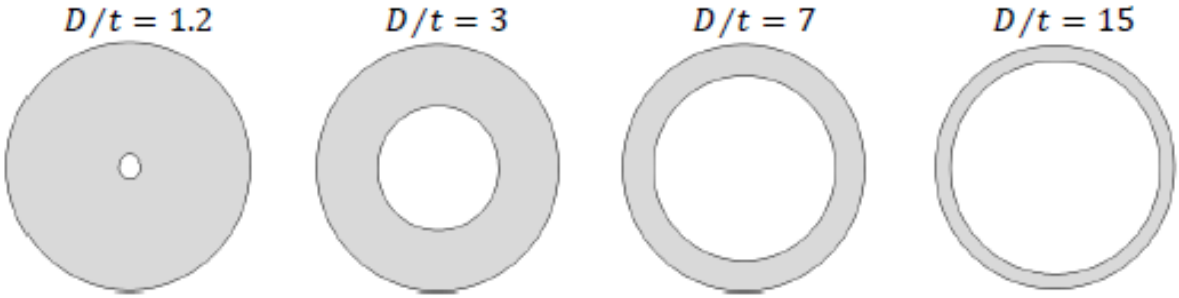

Figure 9.2 Schematic of pipe diameter to thickness ratio cases.

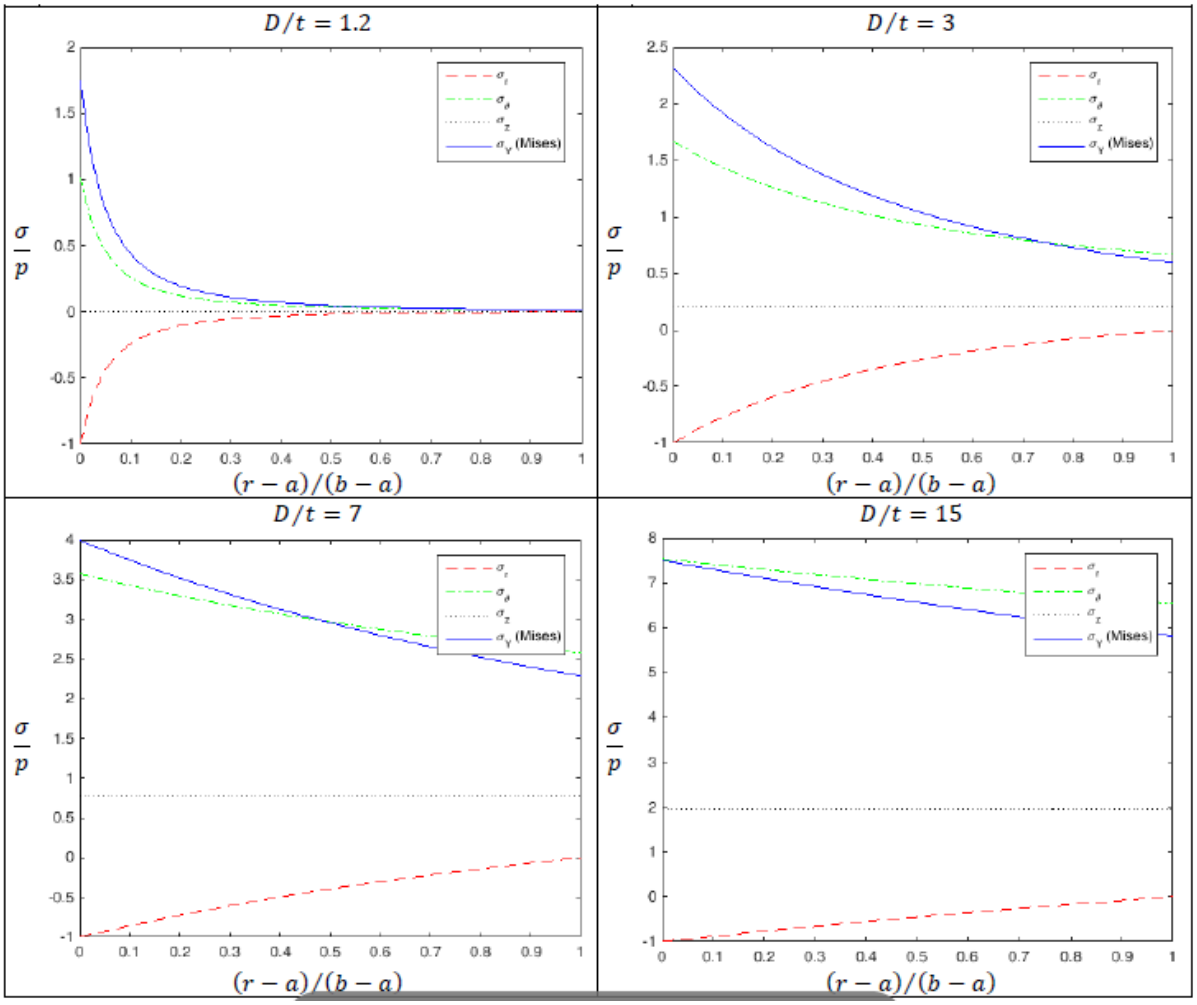

Figure 9.3 Normalized principal component and von Mises stress plots.

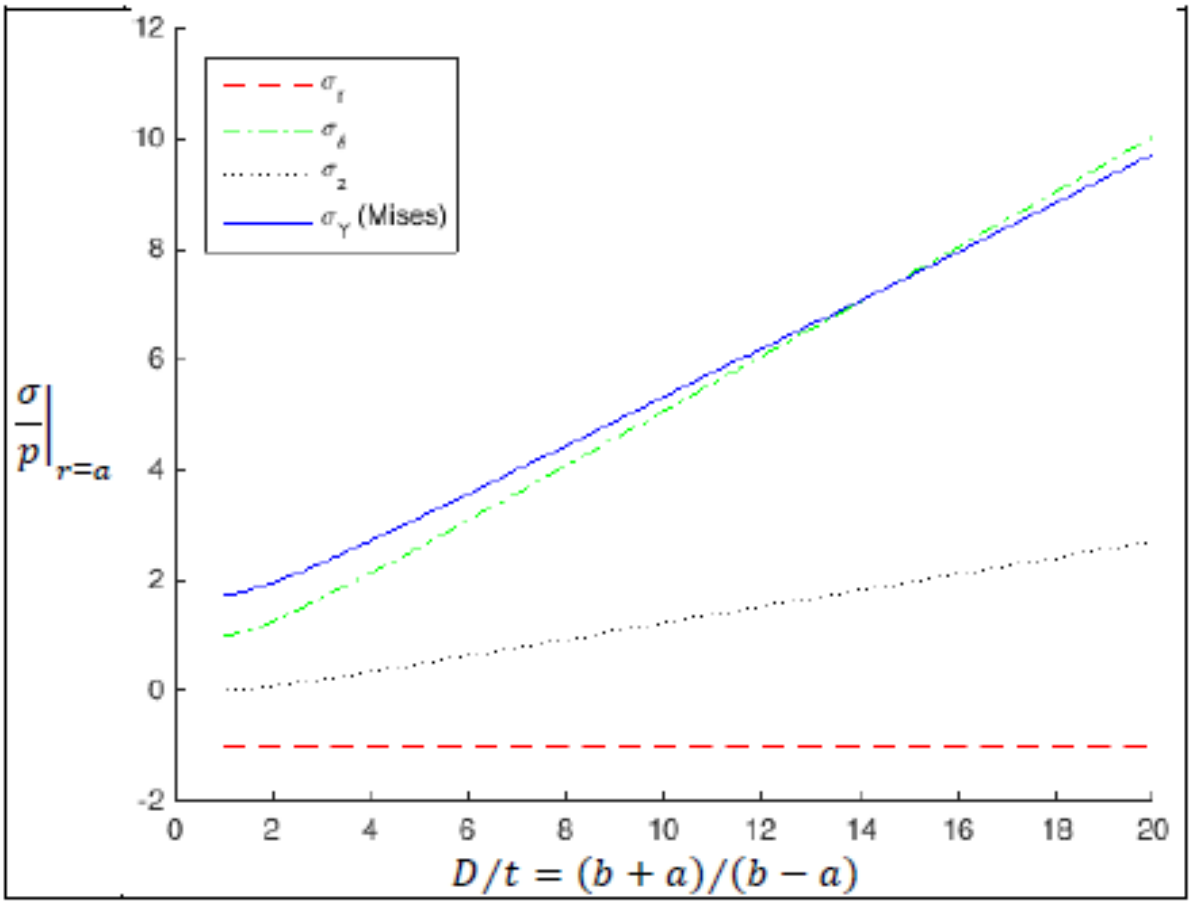

Figure 9.4 Absolute maximum principal component and von Mises stress plot.

9.1.2.3 Finite Element Methodology

The uniform corrosion case can be solved analytically; however, a Finite Element Methodology (FEM) [Zienkiewicz et al. (2005)] solution is presented for comparison. While even a one dimensional axisymmetric model would be sufficient, a two dimensional plane-strain model of a one quarter cross-section $\frac{D}{t} = 7$ pipe was created to provide better visualization. Four quadrilateral element types of linear and quadratic order with and without reduced integration were considered (CPE4R, CPE4, CPE8R, and CPE8) [Dassault Systemes (2015)]. A unity pressure load condition was applied on the inside radius boundary, a zero perpendicular displacement symmetric boundary condition was applied on the radial boundaries, and a free boundary condition naturally occurs on the outside radius boundary as shown in Figure 9.5 along with the various mesh densities considered. A Poisson ratio of $\nu = 0.3$ was the only material condition applied.

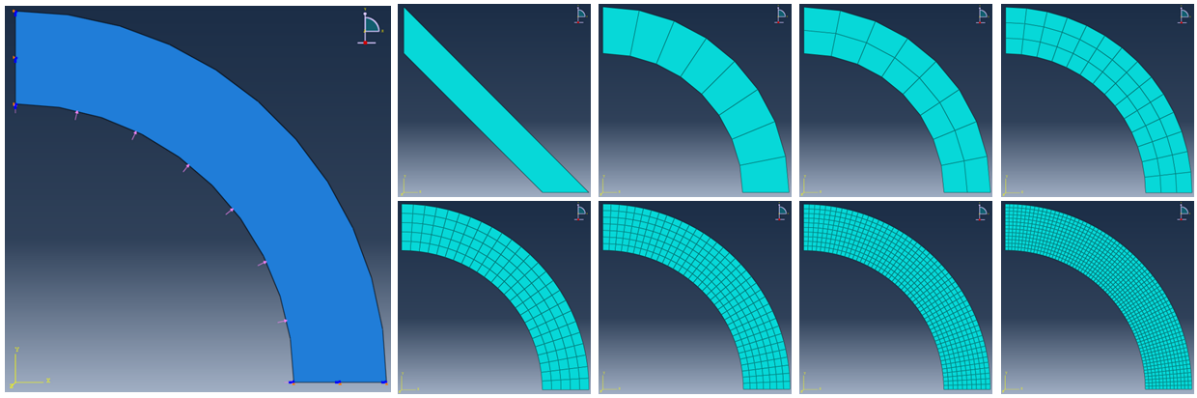

Figure 9.5 Two dimensional plane-strain geometry, boundary conditions, and mesh densities.

9.1.2.4 Finite Element Results

The finite element normalized von Mises stress is compared to the analytical solution for various mesh densities along the normalized radial distance for linear and quadratic order elements with and without reduced integration as shown in Figures 9.6 and 9.7. The overall error decreases as the number of nodes increase as expected. In regard to radial distribution, the error is the smallest at integration points as observable in the number and location of valley

points that coincide with the various mesh densities. Also, the relative error is largest at the boundaries for most element types. The reduced integration quadratic elements tend to not have the largest relative error at $r = a$, this is the radial distance of interest when looking for the maximum von Mises stress value. The mesh convergence for L_2 total error and error at $r = a$ is shown in Figure 9.8. The individual component stress errors are plotted in Figure 9.9 for the reduced integration quadratic model with the highest mesh density.

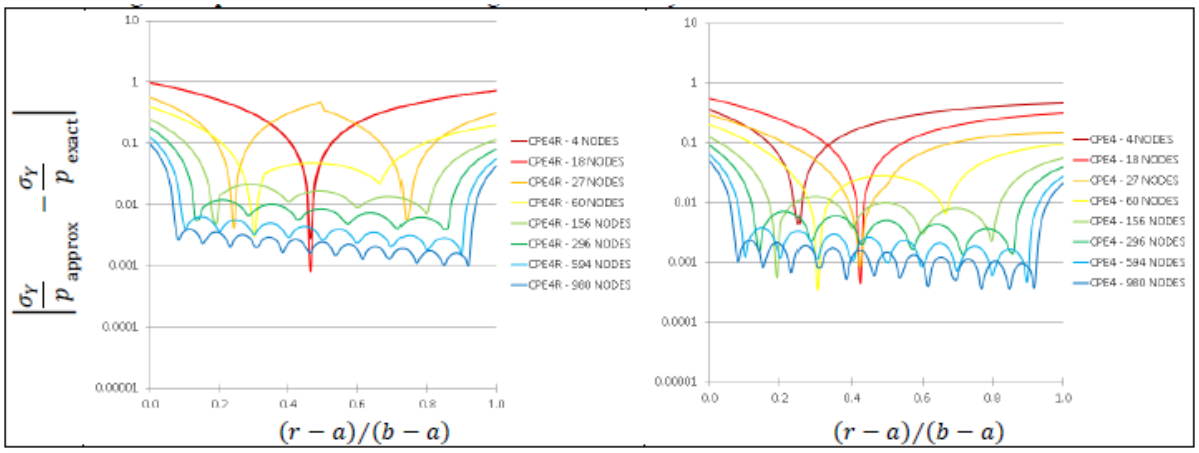

Figure 9.6 Normalized von Mises stress error for reduced (left) and full integration (right) linear elements.

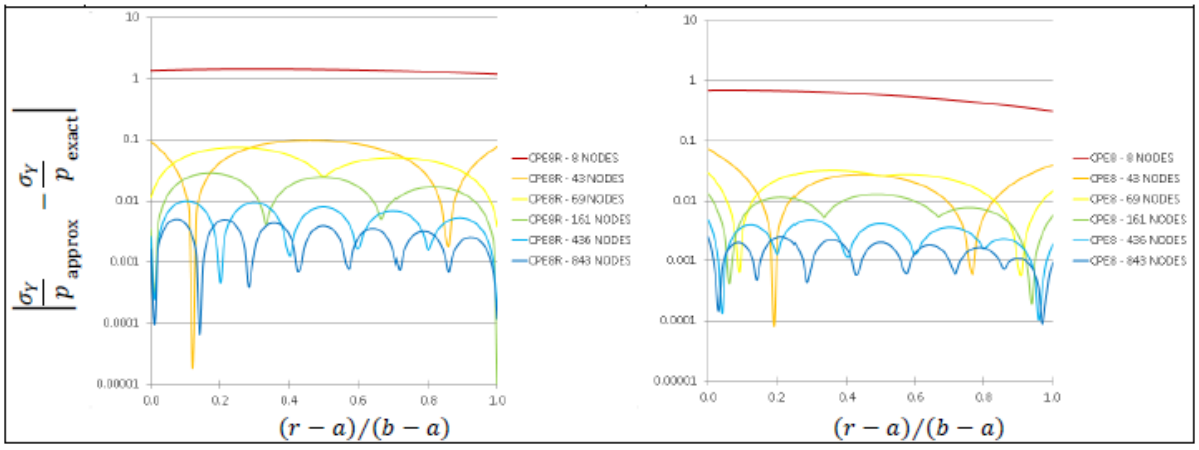

Figure 9.7 Normalized von Mises stress error for reduced (left) and full integration (right) quadratic elements.

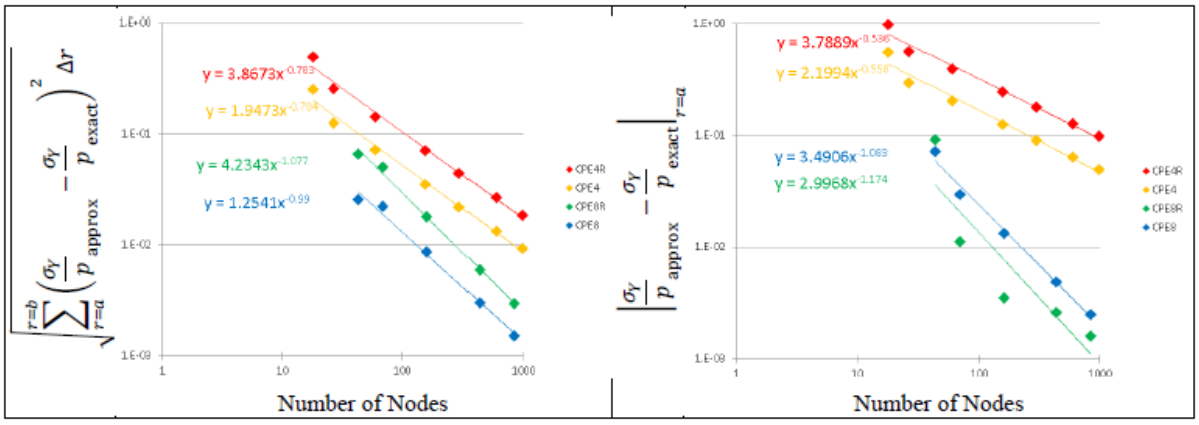

Figure 9.8 Showing mesh convergence for total error (left) and error at the inside radius location (right).

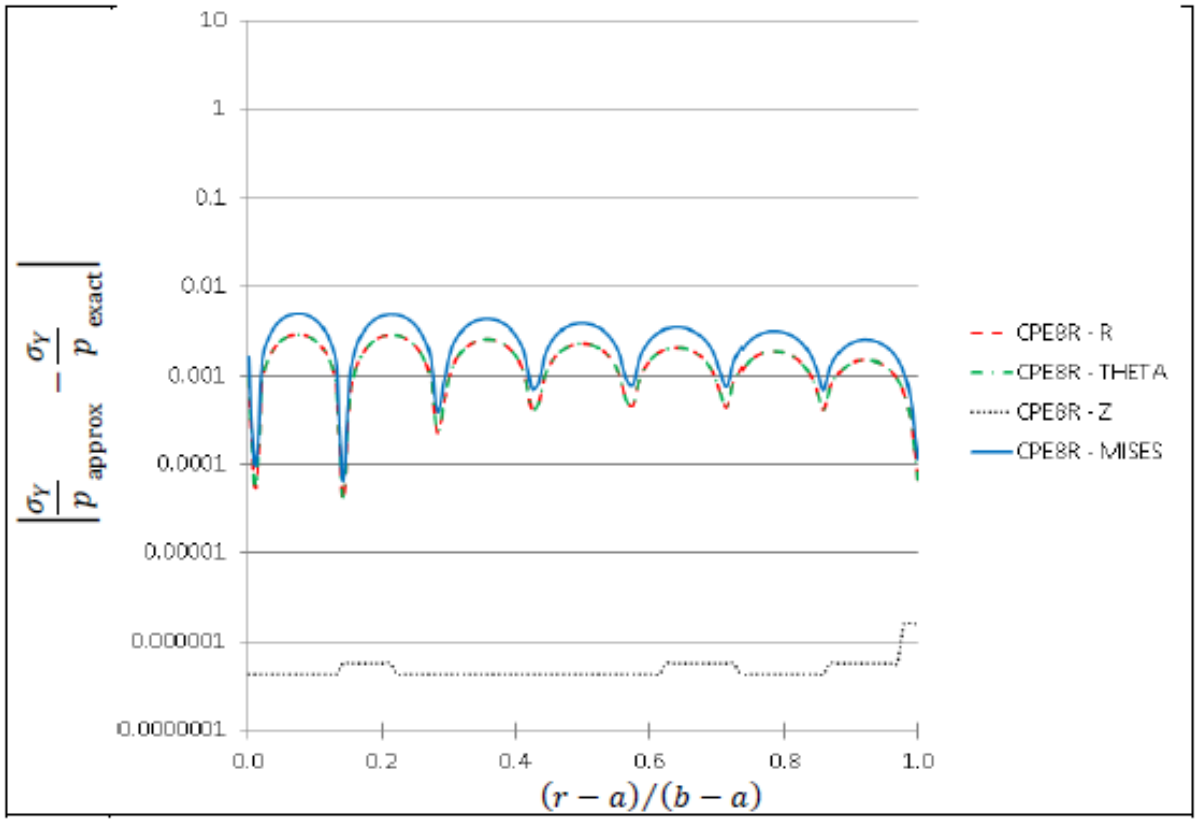

Figure 9.9 Normalized component stress error for quadratic order reduced integration elements.

9.1.3 Plastic Material

A plastic material model is considered for analytical and finite element stress analysis methodologies.

9.1.3.1 Analytical Methodology

A material being loaded into the plastic regime (beyond the yield stress state) will not return to original dimensional form and will have realized a permanent deformation upon unloading. The material yield stress state is increased as a result of the plastic deformation. The isotropic hardening model implies that the increase in yield stress state is equal relative to each principal stress component. This is analogous to a von Mises yield surface keeping the same central point and shape, but only increasing in size [Lubliner (2005)]. The isotropic hardening material relation between stress and strain can be represented over the entire elastic and plastic loading regime by piecewise functions shown in Figure 9.10 described as Elastic/Perfectly Plastic (Figure 9.10 Red and Equation 9.33), Elastic/Linear-Hardening (Figure 9.10 Blue and Equation 9.34), and Elastic/Power-Hardening (Figure 9.10 Green and Equation 9.35) as well as a first order continuous Ramberg-Osgood relation (Figure 9.10 Yellow and Equation 9.36) [Ramberg and Osgood (1943); Dowling (1999)]. When studying material failure at the ultimate tensile strength limit, it is reasonable to consider only the plastic strain deformation and neglect elastic strain.

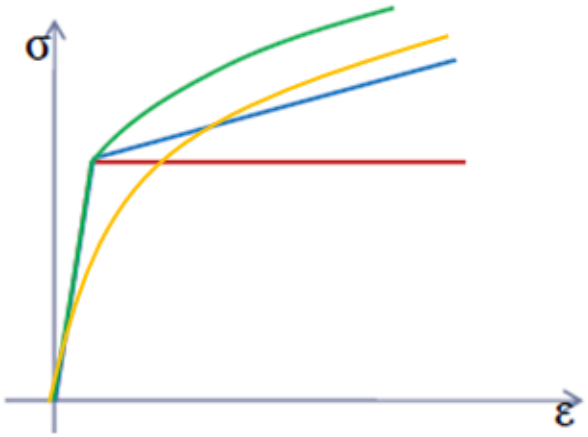

Figure 9.10 Elastic-plastic stress strain model curves.

$$\left\{ \begin{array}{ll} \sigma = E\epsilon & \sigma \leq \sigma_Y \\ \sigma = \sigma_Y & \epsilon \geq \frac{\sigma_Y}{E} \end{array} \right\} \tag{9.33}$$

$$\left\{ \begin{array}{ll} \sigma = E\epsilon & \sigma \leq \sigma_Y \\ \sigma = (1-\delta)\,\sigma_Y + \delta E\epsilon & \sigma \geq \sigma_Y \end{array} \right\} \left[\delta E = \frac{\sigma - \sigma_Y}{\epsilon - \epsilon_Y} \right] \tag{9.34}$$

$$\left\{ \begin{array}{ll} \sigma = E\epsilon & \sigma \leq \sigma_Y \\ \sigma = H_1 \epsilon^{n_1} & \sigma \geq \sigma_Y \end{array} \right\} \tag{9.35}$$

$$\sigma = H {\epsilon_p}^n \tag{9.36}$$

An attempt is made to derive an analytical solution from the deformation geometry, momentum balance, and Power-Hardening/Ramberg-Osgood plastic material model equations [Ramberg and Osgood (1943); Dowling (1999); Lubliner (2005); Sadd (2009)]. The same axisymmetric plane-strain condition can be considered as for the linear-elastic material behavior. Elastic strain ϵ_e and plastic strain ϵ_p are both considered in 9.37. Substitution of the Ramberg-Osgood stress-strain relation in Equation 9.36 [Ramberg and Osgood (1943)] into Equation 9.37 results in Equation 9.38.

$$\epsilon = \epsilon_e + \epsilon_p \tag{9.37}$$

$$\epsilon = \frac{\sigma}{E} + \left(\frac{\sigma}{H} \right)^{\frac{1}{n}} \tag{9.38}$$

Now, neglecting elastic strain, the Ramberg-Osgood relation takes the Power-Harding form in Equation 9.39.

$$\sigma = H\epsilon^n \tag{9.39}$$

The secant moduli E_s is described in Equation 9.40 by substituting the non-linear stress-strain relation from Equation 9.39.

$$E_s\left(\boldsymbol{\sigma}\right) = \frac{\sigma_{11}}{\epsilon_{11}} = \frac{\sigma_r}{\epsilon_r} = \frac{H {\epsilon_r}^n}{\epsilon_r} = H {\epsilon_r}^{n-1} \tag{9.40}$$

The secant moduli E_s is related to the shear secant moduli G_s as shown in Equation 9.41 with the stress-strain relation based on secant moduli shown in Equation 9.42.

$$\frac{1}{2G_s\left(\boldsymbol{\sigma}\right)} = \frac{1}{2G} + \frac{3}{2}\left[\frac{1}{E_s\left(\boldsymbol{\sigma}\right)} - \frac{1}{E}\right] \tag{9.41}$$

$$\varepsilon_{ij} = \frac{1}{2G_s\left(\boldsymbol{\sigma}\right)}\left(\sigma ij - \frac{1}{3}\sigma_{kk}\delta_{ij}\right) - \frac{6\nu - 3}{9E}\sigma_{kk}\delta_{ij} \tag{9.42}$$

Applying $\epsilon_z = 0$ from Equation 9.4 and solving Equation 9.42 for σ_z in combination with Equations 9.40 and 9.41 result in Equations 9.43 and 9.44.

$$\begin{aligned}\epsilon_r = &-\left(3EG\epsilon_r - 3GH{\epsilon_r}^n + EH{\epsilon_r}^n\right)\cdot \\ &\left(\frac{\left(EH{\epsilon_r}^n\sigma_r - EH{\epsilon_r}^n\sigma_\theta + GH{\epsilon_r}^n\sigma_r + 5GH{\epsilon_r}^n\sigma_\theta + 3EG\epsilon_r\sigma_r - 3EG\epsilon_r\sigma_\theta - 8GH{\epsilon_r}^n\sigma_r\nu - 4GH{\epsilon_r}^n\sigma_\theta\nu\right)}{4EGH{\epsilon_r}^n\left(2GH{\epsilon_r}^n - 3EG\epsilon_r - EH{\epsilon_r}^n + 2GH{\epsilon_r}^n\nu\right)}\right)\end{aligned} \tag{9.43}$$

$$\begin{aligned}\epsilon_\theta = &-\left(3EG\epsilon_r - 3GH{\epsilon_r}^n + EH{\epsilon_r}^n\right)\cdot \\ &\left(\frac{\left(EH{\epsilon_r}^n\sigma_r - EH{\epsilon_r}^n\sigma_\theta - 5GH{\epsilon_r}^n\sigma_r - GH{\epsilon_r}^n\sigma_\theta + 3EG\epsilon_r\sigma_r - 3EG\epsilon_r\sigma_\theta + 4GH{\epsilon_r}^n\sigma_r\nu + 8GH{\epsilon_r}^n\sigma_\theta\nu\right)}{4EGH{\epsilon_r}^n\left(2GH{\epsilon_r}^n - 3EG\epsilon_r - EH{\epsilon_r}^n + 2GH{\epsilon_r}^n\nu\right)}\right)\end{aligned} \tag{9.44}$$

While a clean analytical solution has not been achieved, the problem has been simplified to a set of four non-linear ordinary differential equations as a function of r in Equations 9.18, 9.20, 9.43, and 9.44 with the four unknowns ϵ_r, ϵ_θ, σ_r, and σ_θ.

9.1.3.2 Finite Element Methodology and Results

A finite element method can be applied with a non-linear relation between stress and strain prescribed by adjusting the material model relation. Additional material properties need to be included in addition to the Poisson ratio of $\nu = 0.3$ used to describe the elastic model. A relatively low-strength, low-carbon A106-B steel [ASTM (2014)] was applied with a yield strength of $\sigma_Y = 240$ MPa, an ultimate strength of $\sigma_U = 415$ MPa, and an elastic modulus of $E = 200$ GPa. Neglecting elastic strain, the Ramberg-Osgood relation is the same as the Power-Hardening relation as previously shown in Equation 9.39. Typical Power-Harding parameters for low-carbon steel ($H_1 = 600$ MPa; $n_1 = 0.21$) [Callister (2005)] were converted

to Ramberg-Osgood parameters (α offset $= EH^{-n_1}\sigma_Y^{n_1-1} = 687$; $n = \frac{1}{n_1}$) [Ramberg and Osgood (1943); Dassault Systemes (2015)], and implemented as a "Plastic Deformation" material condition [Dassault Systemes (2015)].

The two dimensional plane-strain geometry model was not analyzed for the case of uniform corrosion plastic behavior; rather, the full three dimensional stress model described in the next section was applied. The failure criteria was established as the internal pressure resulting in the von Mises stress to equal the ultimate strength $\sigma_U = 415$ MPa. The uniform corrosion results are plotted alongside the isolated pit corrosion results in Figure 9.16.

9.2 Isolated Pit Corrosion

The case of isolated pit corrosion is represented by a pipe with single hemispherical pit of varying depth. In the model, the edges of the pit are infinitely sharp which will lead to an infinite stress concentration under elastic loading; this infinitely sharp geometry does not exist in real pits.

9.2.1 Pipe Geometry

Consider a pipe geometry of $\frac{D}{t} = 7$ under three different isolated pit corrosion conditions: 25%, 50%, and 75% wall loss. A cross-section image of the pipe is shown in Figure 9.14 and one quarter of a three dimensional model section is shown in Figure 9.11.

9.2.2 Linear-Elastic Material

A linear-elastic material model is considered for analytical and finite element stress analysis methodologies.

9.2.2.1 Analytical Methodology

The analytical solution for this geometry is not trivial as the elasticity partial differential equations [Sadd (2009)] cannot be reduced to ordinary differential equations as a function of r as is the case of uniform corrosion.

9.2.2.2 Finite Element Methodology

While an analytical solution is not obvious, the finite element methodology can be applied to discretized three dimensional geometries and solve the weak form of the partial differential elasticity equations [Zienkiewicz et al. (2005)]. The previously described two dimensional plane-strain model was expanded to a full three dimensional model. The ability to converge three dimensional meshes was limited; therefore, the two dimensional plane-strain error analysis results at $r = a$ was used to prescribe a hexagonal quadratic order reduced integration element type (C3D20R) [Dassault Systemes (2015)]. A unity pressure load condition was applied on the inside radius surface of the cylinder and on the pit face surface; a zero perpendicular displacement symmetric boundary condition was applied on the vertical boundary, horizontal boundary, and longitudinal boundary intersecting the pit; a zero perpendicular displacement was applied on the longitudinal boundary opposite the pit to mimic far-field behavior as a "plane-strain" boundary condition; a free boundary condition naturally occurs on the outer radial surface boundary; all boundary conditions are shown in Figure 9.11 along with the various geometries considered.

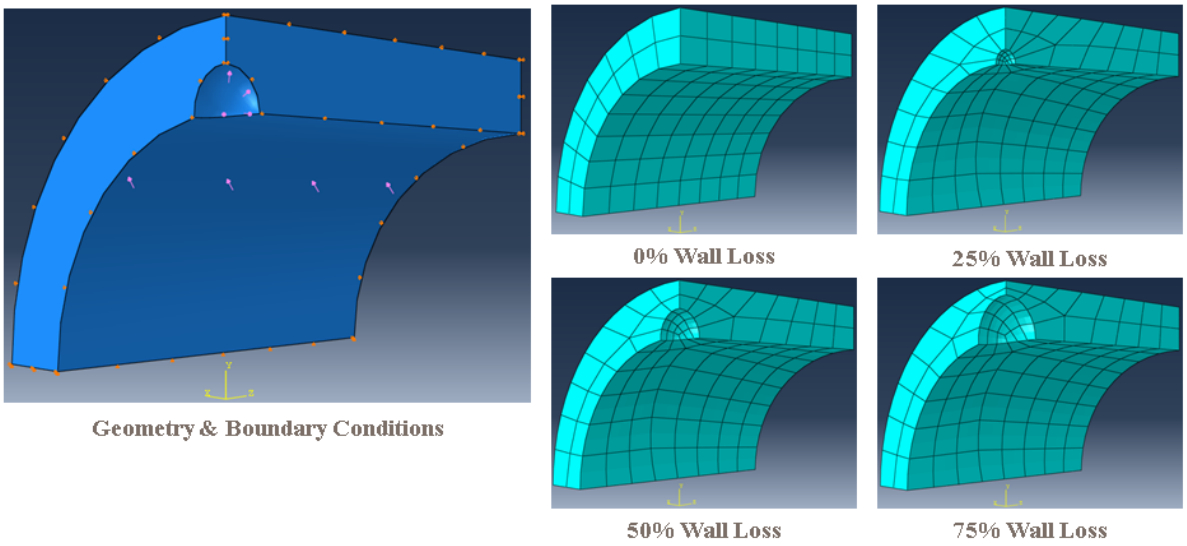

Figure 9.11 Three dimensional stress geometries, boundary conditions, and mesh densities.

9.2.2.3 Finite Element Results

The normalized von Mises stress field results are shown in Figures 9.12, 9.14, and 9.16. In Figure 9.12, the same contour color range is applied in order to visualize the relative increase in stress concentration. The highest stress concentrations occur at the edge of the pit and inside surface. Only the relative stress values at this location among the three pit geometries are of interest; the actual reported stress values are inherently false as the pit edges are infinitely sharp which will lead to an infinite stress concentration under elastic loading.

9.2.3 Plastic Material

A plastic material model is considered for analytical and finite element stress analysis methodologies.

9.2.3.1 Analytical Methodology

Similar to the elastic case, the analytical solution for this geometry is not obvious because the strain definition, momentum balance, and non-linear material model partial differential equations [Dowling (1999); Sadd (2009)] cannot be reduced to ordinary differential equations as a function of r as is the case of uniform corrosion.

9.2.3.2 Finite Element Methodology and Results

The same finite element model geometry, element type, mesh density, and boundary conditions were used as in the liner elastic case. The "Plastic Deformation" [Dassault Systemes (2015)] material condition was applied with the same parameters in the plastic uniform corrosion case. The failure criteria was established as the internal pressure such that the von Mises stress equals the ultimate strength $\sigma_U = 415$ MPa. The von Mises stress field results are shown in Figure 9.13 and plotted in Figure 9.16. In Figure 9.13, the same contour color range is applied showing that the location of the stress concentration does not occur at the infinitesimal edge between the pit wall and inside surface as in the case of elastic deformation; this edge is now allowed to yield and plastically deform. Instead, the highest stress concentrations occur at the deepest point in the pit.

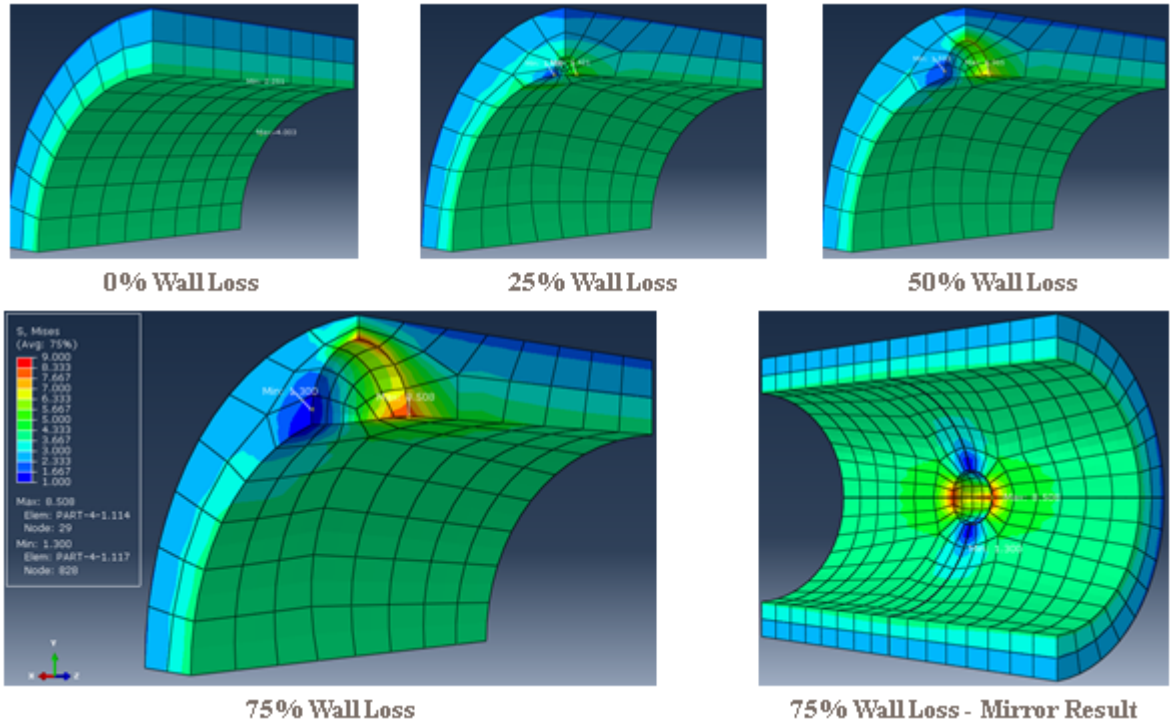

Figure 9.12 Linear elastic material normalized von Mises stress results.

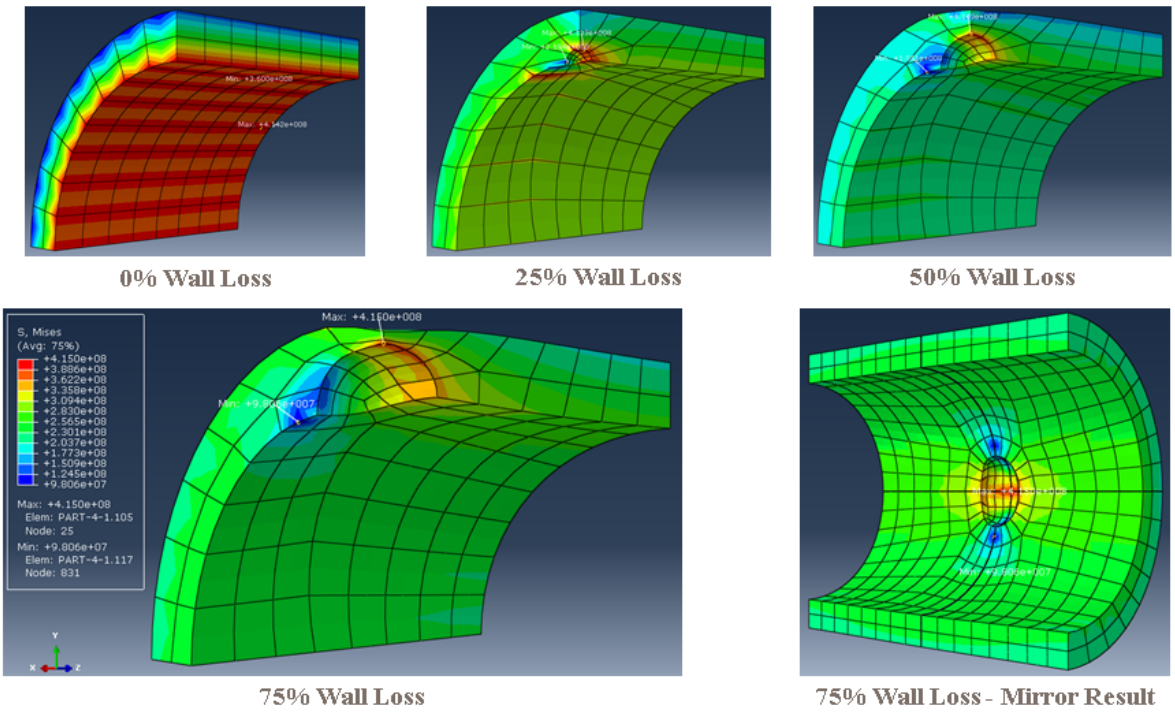

Figure 9.13 Plastic material von Mises stress results.

9.3 Discussion

The cases of uniform and isolated pit corrosion, linear-elastic and plastic material models, and analytical and finite element solution method combinations are summarized in Table 9.1.

Table 9.1 Summary of Cases Evaluated

Corrosion Type	Material Model	Solution Method	Results Status
Uniform	Linear-Elastic	Analytical	General solution provided.
		Finite Element	Demonstrated the method with 2D plane-strain model. Provided convergence results.
	Plastic	Analytical	General solution possible, but unable to solve non-linear ODE. Reduced problem provided.
		Finite Element	Demonstrated method with 3D stress. Unable to provide convergence results with node limit.
Isolated Pit	Linear-Elastic	Analytical	General solution not trivial. Geometry does not allow reduction of full field PDEs to ODEs.
		Finite Element	Demonstrated method with 3D stress. Unable to converge due to infinitesimal edge.
	Plastic	Analytical	General solution not trivial. Geometry does not allow reduction of full field PDEs to ODEs.
		Finite Element	Demonstrated method with 3D stress. Unable to provide convergence results with node limit.

The linear-elastic isolated pit corrosion is compared to an equivalent uniform corrosion metal loss based on the maximum pit depth as shown in Figure 9.14. The reported maximum von Mises stress values are at the edge of the pit wall and inside surface wall as shown in Figure 9.12. These stress values are false as the edges of the pit are infinitely sharp which will lead to an infinite stress concentration under elastic loading. This type of error can be observed from the reported relation at 25% wall loss that goes against intuition where the isolated pit has a larger normalized von Mises stress than a comparable uniform corrosion wall loss. A further refinement of the isolated pit mesh was not completed due to a limitation in the number of available node values, but regardless, the maximum stress value of this model will not converge.

The linear-elastic and plastic material isolated pit corrosion is compared to an equivalent uniform corrosion metal loss based on the maximum pit depth as shown in Figure 9.16; the

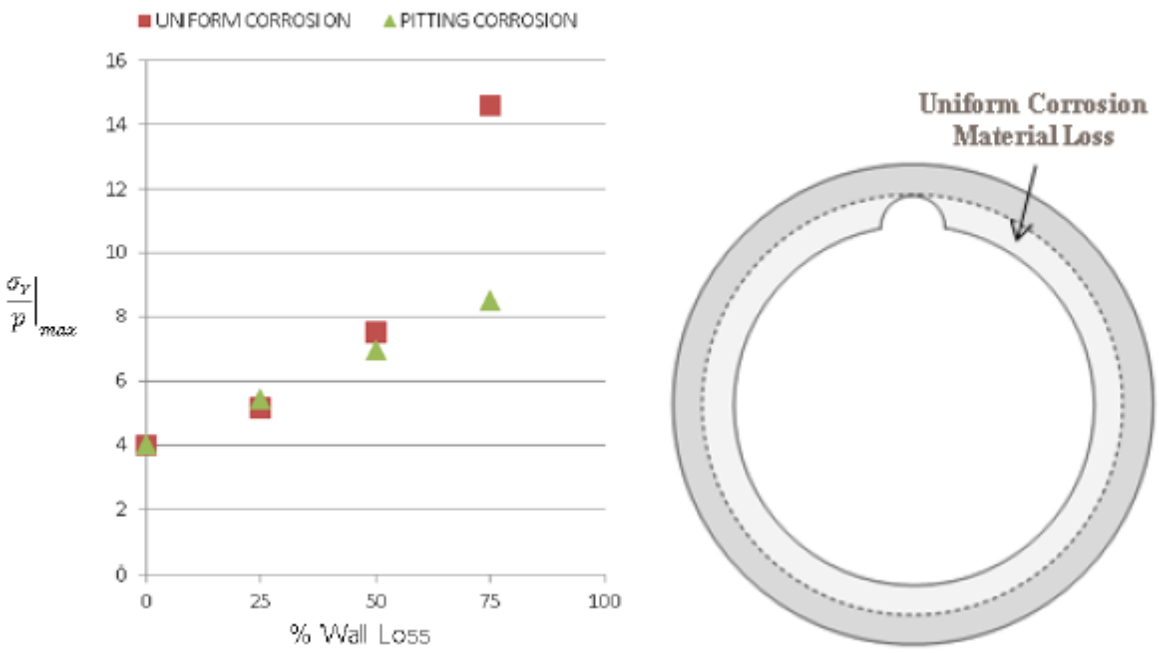

Figure 9.14 A comparison of internal pressure at failure for linear-elastic uniform corrosion and linear-elastic isolated pit corrosion.

failure criteria for elastic and plastic material are based on the material yield stress and ultimate stress values correspondingly. As the ultimate stress is greater than the yield stress, all cases of plastic material fail at a higher internal pressure than linear-elastic material. Unlike the isolated pit elastic results, the plastic results are more intuitive where a single isolated pit will result in failure at a higher pressure as compared to an equivalent uniform wall loss. The maximum von Mises stress location for the plastic isolated pit is at the maximum pit depth as shown in Figure 9.13. The maximum stress location is not at the infinitesimal edge between the pit wall and inside surface as in the case of elastic material. In the plastic case, this edge is now allowed to yield and plastically deform. A further refinement of the plastic material isolated pit mesh was not completed due to a limitation in the number of available node values, but if completed, the maximum stress value of this model may converge.

In general, the three dimensional stress mesh densities are too coarse. A rigorous convergence test was not completed for any of the three dimensional models due to the limited number of available nodes. The maximum displacement convergence could be investigated

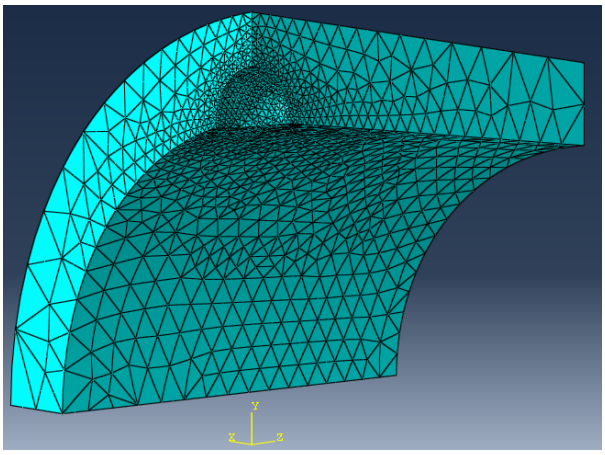

Figure 9.15 A possible gradient mesh density.

for the linear-elastic case and the maximum stress convergence could be investigated for the plastic case. It would also be prudent to make the model larger to investigate (and possibly eliminate) the plane-strain zero perpendicular displacement boundary condition. Finally, there is also clear evidence in Figure 9.13 of hour-glassing in the case of uniform corrosion 0% wall loss. The reduced order integration elements exhibit this hour-glassing effect due to the under-constrained nature of reduced integration elements with a combination of an insufficient number of elements. The full integration elements were attempted, and provided a visually more appealing result; however, the full integration elements were less accurate at $r = a$ in the elastic case for both two dimensional plane-strain and full three dimensional stress models. The best approach in the future would be to increase the mesh density in a gradient manner as shown in Figure 9.15 such that the density is greatest at the location of the pit. As seen in the case of two dimensional plane-strain error analysis, there should be at least two element rows in the radial direction for linear or quadratic element orders.

Also, the finite element results are not general, and based on specific geometry and material values. The results are not directly transferable to other geometries and materials.

Finally, the failure criteria result only considers the internal pressure loading and is not conservative. Static loads such as pipe weight and support reactions, and dynamic loads such as thermal induced strain and vibration, were neglected; these loads may be very significant in low pressure and large diameter applications.

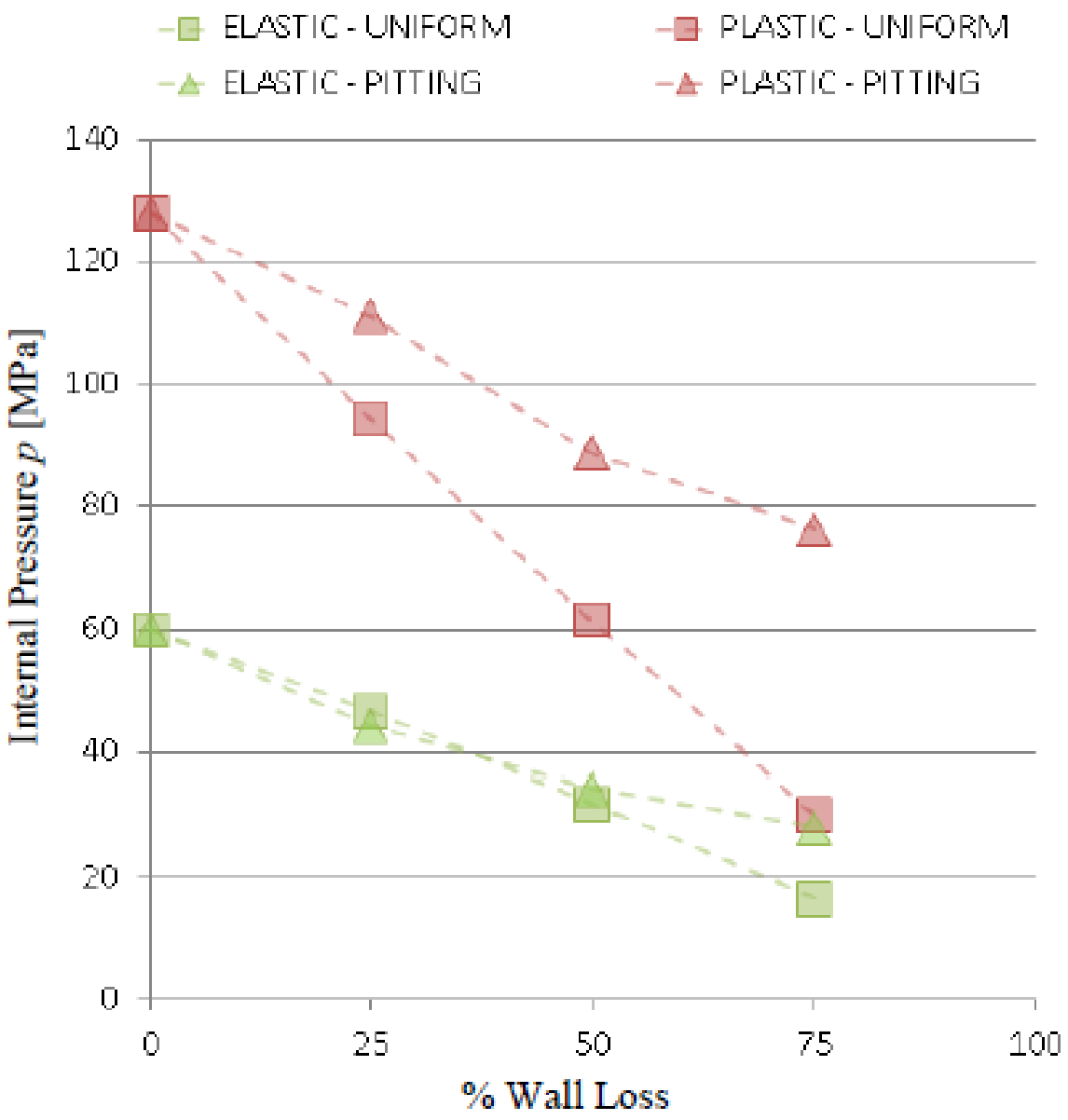

Figure 9.16 A comparison of internal pressure at failure for linear-elastic and plastic materials for uniform corrosion and isolated pit corrosion mechanisms.

9.4 Summary

Progress was made on the case combinations of uniform and isolated pit corrosion, linear-elastic and plastic material models, and analytical and finite element solution methods as summarized in Table 9.1. The various geometry and material model cases may be applied to generate prognosis information with input from NDE or SHM data with consideration for measurement uncertainty.

CHAPTER 10. CONCLUSION

Naphthenic acid corrosion occurs at high temperatures in oil refinery plants and can be difficult to predict as discussed in Chapter 1 as the research motivation. Also described were i) crude oil trends related to corrosion, ii) the principals of naphthenic acid corrosion, and iii) Non-Destructive Evaluation (NDE) and Structural Health Monitoring (SHM) technology design considerations and parameters.

A general review of NDE background material was summarized in Chapter 2 for optical, electromagnetic, radiographic, acoustic emission, ultrasonic, and other methods. The characteristics of the various measurement methods were classified and compared for a high temperature corrosion monitoring application. Ultimately, a permanently installed bulk wave ultrasonic thickness (UT) SHM technology was determined to be an applicable method to monitor localized high-temperature internal pitting corrosion of steel pipe. A review of commercially available UT SHM bulk wave technology and a brief discussion on guided wave technology was included, as well as a review of rough surface elastic wave scattering.

A sensor produced by the sol-gel ceramic fabrication process has the potential to be deployed to monitor such pitting corrosion, and to help investigate the mechanisms causing such corrosion. Thid sol-gel sensor technology was described in Chapter 3. In addition, the propagating longitudinal and shear elastic wave beam profile generated by a thick-film sol-gel transducer was experimentally characterized using the dynamic photoelastic visualization method; images of the wave-field were compared with semi-analytical modeling results. This thick-film transducer type was also characterized using an electric circuit model as described in Appendix 1.

After transducer characterization, various elastic wave propagation and flat surface reflection bounding case scenarios for the ultrasonic bulk wave corrosion monitoring application were modeled with elastodynamic simulation software in Chapter 4.

In Chapter 5, the classic elastic wave scattering theory for an embedded spherical cavity was reviewed. New scattering theory from the seismology community for a hemisphere in a stress-free half-space boundary was extended with the derivation of a far-field scattering amplitude term of interest in NDE measurement applications. This theory extension was applied to a hemispherical pit geometry to represent initial localized corrosion. Data from this new scattering theory was compared with immersion measurement experimental results by applying principals from the Thompson-Gray measurement model for a flat surface in Chapter 5, and for a curved pipe surface in Chapter 6. This initial model validation work may provide a basis for a possible new hemispherical pit geometric reference standard for ultrasonic NDE corrosion applications. The hemispherical pit scattering work was extended to experimental measurements and semi-analytical elastodynamic modeling in Chapter 7 for a contact measurement configuration.

In Chapter 8, the UT SHM measurement accuracy, precision, and reliability were described with a new weighted censored relative likelihood methodology to consider the propagation of asymmetric uncertainty in quantifying thickness measurement error. This new statistical method was experimentally demonstrated and applied to thickness measurement data obtained in pulse-echo and pitch-catch configurations for various time-of-flight thickness calculation methods. A reliability analysis of a structural health monitoring sensor system was presented to investigate time domain independent and dependent sources of variability.

Finally, the plastic behavior of a corroded steel pipe was modeled with analytical and finite element methods to generate prognosis information in Chapter 9.

The overall hypothesis investigated was to understand if such sol-gel sensor technology can be used to monitor localized high-temperature corrosion with acceptable measurement accuracy and precision as defined in Table 1.1.

10.1 Novel Contributions

The following is a brief summary of the novel contributions in this dissertation.

- Demonstration of the laboratory photoelastic optical imaging technique and associated image processing to characterize the incident longitudinal and shear wave beam profile of a thick-film sol-gel transducer.
- Extension of elastic wave scattering theory to derive a far-field scattering amplitude term for the case of a hemispherical pit, initial work towards experimental validation of such theory, and the potential basis for a new hemispherical pit calibration reference standard.
- Development and demonstration of a weighted censored relative likelihood statistical analysis method to determine ultrasonic thickness measurement accuracy and precision considering propagation of asymmetric uncertainty.

10.2 Future Work

Extensions of the current work to be considered in future studies are grouped by characterization, scattering, statistics, and prognosis.

10.2.1 Characterization

Regarding sol-gel transducer characterization, future work could be to find the necessary complex material parameter values for the Lukacs Model analysis, complete an analysis for the Mason Circuit, Redwood, KLM, and Reeder-Winslow Models, and collect real electrical impedance values from a network analyzer on various sol-gel transducers to compare with the theoretical models and identify which model is the most representative.

The photoelastic imaging technique measures the dynamic stress in a transparent material as a two dimensional planar elastic field. While work has been completed to generate a three dimensional field via tomographic imaging from the Schlieren visualization method [Caliano et al. (2012)], a tomogram has yet to be generated from ultrasound photoelastic images. It

would a natural extension to generate a three dimension beam profile from a traditional contact transducer as well as a sol-gel transducer to quantify beam profile antisymmetry with a photoelastic tomographic imaging technique to capture both longitudinal and shear wave modes.

10.2.2 Scattering

Discrepancies between theory and measurement from the hemispherical pit from on a flat plate or curved surface could be a result of measurement error, incorrect theory, or incorrect methods to transfer the received voltage to scattering amplitude. The following items could be further explored in future model validation studies:

- The ideal velocity ratio values may be too large by taking the field maximum ideal velocity ratio value at each frequency. This does not completely consider scattering from the half-space boundary; evaluation of a -6dB average, >10% integral average, or other method to determine the ideal velocity ratio values may be more accurate.

- Further investigate the scale factor and shift factor adjustment process as a result of measurement system linearity over a range of dB gain values to account for the normalizing variable L in Equation 5.69.

- Further investigate the sensitivity error bar generation method shown in Figures 5.32 and 5.33.

- Evaluate over a broader range of ka values using different transducers or different diameter hemispherical pits.

- Reconfigure immersion experiment to have steel block back-wall interface with air such that the acoustic impedance reflection ratio is more truly a stress-free half-space $R \approx 1$ to better match the theory to be validated. The current configuration with water has as acoustic impedance reflection ratio $R \approx 0.9$ and is not truly a stress-free half-space as some of the longitudinal wave mode energy is transmitted through the back-wall, and through the hemispherical pit.

- Investigate the definition and use of water path distance as compared to physical distance for the following steps in the scattering amplitude validation process: i) the initial calibration block design simulation, ii) generating of the acoustic/elastic transfer function, iii) defining the Multi-Gaussian beam model, iv) determining the reference spectrum, v) collecting the reference measurement, and vi) collecting the pit measurement.

- Evaluate using different materials other than A106B carbon steel to test the hemispherical pit scattering amplitude theory at longitudinal to shear wave speed ratios besides ≈ 1.82.

- Evaluate at different temperatures to understand if the approach is transferable to higher temperature applications for precise measurement of pits in materials with greater material wave speed and attenuation uncertainty as a result of bulk and gradient spatial temperature variations.

- Investigate the sensitivity of the current theory, or explore other methods, considering other pit geometries such as hemiellipsoidal pits or multiple pits.

- For the curvature immersion experiment in Chapter 6, further investigate the influence of curvature regarding the acoustic/elastic function. Consider various specimen radius to beam area ratios.

- For the curvature immersion experiment in Chapter 6, complete the analysis using a system function gathered from the front-wall (instead of the first back-wall).

- For the curvature immersion experiment in Chapter 6, gather more accurate attenuation measurement coefficient values by taking measurements on a sample with a greater thickness to curvature ratio.

- For the curvature immersion experiment in Chapter 6, further investigate the $L = 0.1$ cm and $ka = 1$ shift normalization factors.

- For the curvature immersion experiment in Chapter 6, explore an attenuation curvature correction to address the discrepancy shown in Figure 6.42.

Finally, the amplitude response from the FBH experimental measurements may be compared with an analytical model [Sedov et al. (1992)] in future work.

10.2.3 Statistics

There is still a need to develop a robust statistical framework to quantify the multi-parameter and multi-domain sources of independent and dependent variation and uncertainty in structural health monitoring systems.

Future work could also be to apply the weighted censored relative likelihood statistical analysis technique to quantify asymmetric measurement precision of additional thickness calculation methods under different environmental conditions such as high temperature, rough back-wall surface, and system degradation with an intended application to monitor naphthenic acid corrosion in refineries. This could also be a use case to consider time domain sources of uncertainty and explore the relation between independent and dependent sources of variability and uncertainty. The resulting concept would be that the uncertainty of measurements in more extreme environments could be quantified for various factors such as temperature, surface roughness, and system degradation. In addition, various pitch-catch and transducer array configurations and different thickness calculation methods could be considered.

Specifically regarding the reliability study, recommended future work would be to retest a new sensor and electronics system that has incorporated the better grounding design from the start of the test in an effort to obtain a more accurate initial reliability prediction of the overall improved system.

10.2.4 Prognosis

The current prognosis analysis could be extended as follows:

- Increase the number of nodes in the three dimensional models for i) mesh convergence, ii) investigation of the plane-strain boundary, and iii) to eliminate of hour-glassing.
- Consider various diameter-to-thickness pipe geometries.
- Consider various mechanical material properties.

- Investigate other degradation profiles and stress concentrations such as a hemiellipsoidal pit, or combinations of pits.
- Investigate other plastic material behavior models such as a high temperature viscoplasticity model.

APPENDIX A. CIRCUIT MODELING

An understanding of piezoelectric transducer behavior in an attempt to characterize the performance of thick-film sol-gel transducers is based primarily on Kino's transducer characterization work [Kino (1987)], but complimented with other general piezoelectric transducer characterization references [Meeker (1996); Lu (2012); Sherrit and Mukherjee (2012)], as well as specific examples of air-backed thick-film transducer impedance characterization [Maréchal et al. (2006); Dorey et al. (2007); Pardo et al. (2010); Ali et al. (2015); Mahmood et al. (2015)].

There are various circuit models available to characterize an air backed thick-film sol-gel transducer: Three-Port-Network, Mason Circuit, Redwood, KLM, Reeder Winslow [Reeder and Winslow (1969)], and a model specifically for air-back thick-film sol-gel transducers [Lukacs et al. (1999, 2000)]. This work considers only the Three-Port-Network and Lukacs Models.

A.1 Three-Port-Network Model

The Three-Port-Network Model is used to characterize an air-backed thick-film sol-gel transducer. The theory is first introduced followed by the model analysis.

A.1.1 Theory

A piezoelectric transducer can be modeled in one dimension as a three-port-network as shown in Figure A.1 with the corresponding set of relations in matrix form in Equation A.1 with F_1 as the external force applied to the back-surface of the transducer, F_2 as the external force applied to the front-surface of the transducer, v_1 as the particle velocity at the back-surface of the transducer, v_2 as the particle velocity at the front-surface of the transducer, V_3 as the voltage across the transducer, I_3 as the current across the transducer, Z_C as the material acoustic impedance of the transducer, $\overline{\beta}_a$ as as the stiffened acoustic propagation constant, l

as the transducer thickness, h as the transmitting constant, ω as the angular frequency, and C_0 as the clamped (zero strain) capacitance of the transducer [Kino (1987)].

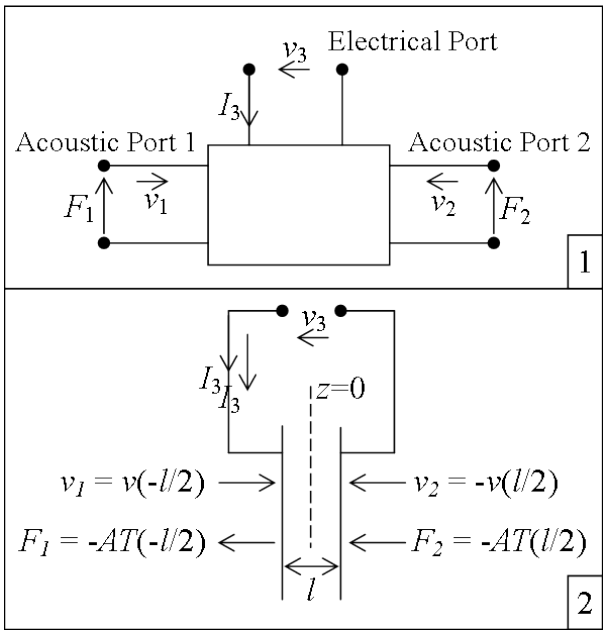

Figure A.1 The 1) transducer modeled as a three-port black box and the 2) relation of three--port notation to the physical parameters of the transducer. Based on similar figure previously published [Kino (1987)].

$$\begin{bmatrix} F_1 \\ F_2 \\ V_3 \end{bmatrix} = -j \begin{bmatrix} Z_c \cot\left(\overline{\beta}_a l\right) & Z_c \operatorname{cosec}\left(\overline{\beta}_a l\right) & \frac{h}{\omega} \\ Z_c \operatorname{cosec}\left(\overline{\beta}_a l\right) & Z_c \cot\left(\overline{\beta}_a l\right) & \frac{h}{\omega} \\ \frac{h}{\omega} & \frac{h}{\omega} & \frac{1}{\omega C_0} \end{bmatrix} \begin{bmatrix} v_1 \\ v_2 \\ I_3 \end{bmatrix} \tag{A.1}$$

The Equation A.1 relations are used to model the transducer electrical impedance Z_3 as shown in Equation A.2 with k_T as the piezoelectric coupling constant for a transversely clamped material, Z_1 as the backing material acoustical impedance, and Z_2 as the substrate material acoustical impedance.

$$Z_3 = \frac{1}{j\omega C_o}\left[1 + {k_T}^2 \frac{j\left(Z_1 + Z_2\right) Z_C \sin \overline{\beta}_a l - 2{Z_C}^2\left(1 - \cos \overline{\beta}_a l\right)}{\left[\left({Z_C}^2 + Z_1 Z_2\right) \sin \overline{\beta}_a l - j\left(Z_1 + Z_2\right) Z_C \cos \overline{\beta}_a l\right] \overline{\beta}_a l}\right] \tag{A.2}$$

The angular frequency ω is described in Equation A.3 with f as the frequency corresponding to transducer vibration.

$$\omega = 2\pi f \tag{A.3}$$

The clamped (zero-strain) capacitance of the transducer C_0 is described in Equation A.4 with ε^S as the transducer material dielectric constant of permittivity with zero or constant strain, and A as the transducer electrode surface area.

$$C_0 = \frac{\varepsilon^S A}{l} \tag{A.4}$$

The transducer material dielectric constant of permittivity with zero or constant strain ε^S is described in Equation A.5 with e as the piezoelectric stress constant, c^E as elastic constant in the presence of a constant or zero electrical field, and K as the piezoelectric coupling constant.

$$\varepsilon^S = \frac{e^2}{c^E K^2} \tag{A.5}$$

The piezoelectric coupling constant K is described in Equation A.6 with c^D as stiffened elastic constant.

$$K = \sqrt{\frac{c^D}{c^E} - 1} \tag{A.6}$$

The piezoelectric coupling constant for a transversely clamped material k_T is described in Equation A.7.

$$k_T = \sqrt{1 - \frac{c^E}{c^D}} \tag{A.7}$$

The stiffened acoustic propagation constant $\overline{\beta}_a$ is described in Equation A.8 with $\rho_{m0} \equiv \rho$ as the transducer mass density in the stationary state.

$$\overline{\beta}_a = \omega\sqrt{\frac{\rho_{m0}}{c^D}} \tag{A.8}$$

An example of the real and imaginary electrical impedance model and experimental data for a piezoelectric transducer can be found in literature [Kino (1987)].

A.1.2 Analysis

For an air-backed sol-gel transducer with $Z_1 = 0$, the terms in Equations A.2-A.8 can be combined such that the transducer electrical impedance Z_3 is described in Equation A.9 as a function of frequency f, substrate acoustic impedance Z_2, transducer geometry A and l, and transducer material properties Z_c, e, c^D, c^E, and ρ.

$$Z_3 = \frac{l\left(c^E - c^D\right)}{2\pi f A e^2}\left[\left(\frac{c^D - c^E}{2\pi f l c^D\sqrt{\frac{\rho}{c^D}}}\right)\left(\frac{2{Z_c}^2\left[\cos\left(2\pi f l\sqrt{\frac{\rho}{c^D}}\right)-1\right]+Z_2 Z_c \sin\left(2\pi f l\sqrt{\frac{\rho}{c^D}}\right)j}{{Z_c}^2\sin\left(2\pi f l\sqrt{\frac{\rho}{c^D}}\right)-Z_2 Z_c\cos\left(2\pi f l\sqrt{\frac{\rho}{c^D}}\right)j}+1\right)\right]j \quad \text{(A.9)}$$

The analysis is applied to an longitudinal mode air-backed thick-film sol-gel transducer of 4.0 mm $\times$ 4.0 mm square dimension. The transducer material properties for PZT-5A are described in Table A.1 [Kino (1987)] with the elastic constant subscript 33 referring to the longitudinal elastic constant relating longitudinal stress and strain components in the z-direction and the piezoelectric stress constant subscript $z3$ referring to the ratio of the longitudinal stress in the z-direction to the E field in the z-direction.

A central frequency f_0 of 10MHz and a central piezoelectric material thickness l_0 of 150 μm is established based on the characteristic range of properties from available sol-gel transducers. The real and imaginary transducer electrical impedance for the Three-Port-Network Model with Equation A.9 and Table A.1 is shown in Figure A.2. The general pattern of the theoretical model in Figure A.2 is consistent with the typical general pattern of the theoretical model and collected data [Kino (1987)]. The real and imaginary transducer electrical impedance values for a thickness range from $l = 0$ to $l = 2l_0$ are shown in Figure A.3. The real transducer electrical impedance for a range of thickness values from $l = 0$ to $l = 2l_0$ is shown in Figure A.4.

Table A.1 Three-Port-Network Model Material and Geometry Properties

PZT-5A Elastic constant (zero electric field)	$c^E{}_{33}$	1.11×10^{11}	N/m^2
PZT-5A Elastic constant (stiffened)	$c^D{}_{33}$	1.47×10^{11}	N/m^2
PZT-5A Piezoelectric stress constant	e_{z3}	15.8	C/m^2
PZT-5A Density	ρ	7750	kg/m^3
Backing Acoustic Impedance - Air	Z_1	0	kg/m^2s
Transducer Acoustic Impedance - PZT	Z_c	3.4×10^7	kg/m^2s
Substrate Acoustic Impedance - Steel	Z_2	4.6×10^7	kg/m^2s
Electrode Surface Area	A	1.6×10^{-5}	m^2

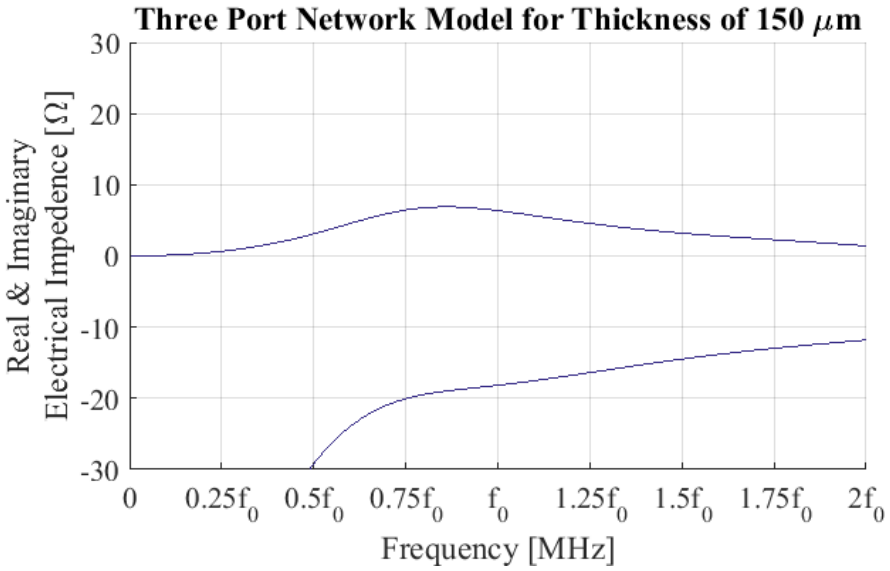

Figure A.2 The real and imaginary electrical impedance for a Three-Port-Network model with Equation A.9, Table A.1, a central frequency f_0 of 10MHz, and a transducer thickness l_0 of 150 μm.

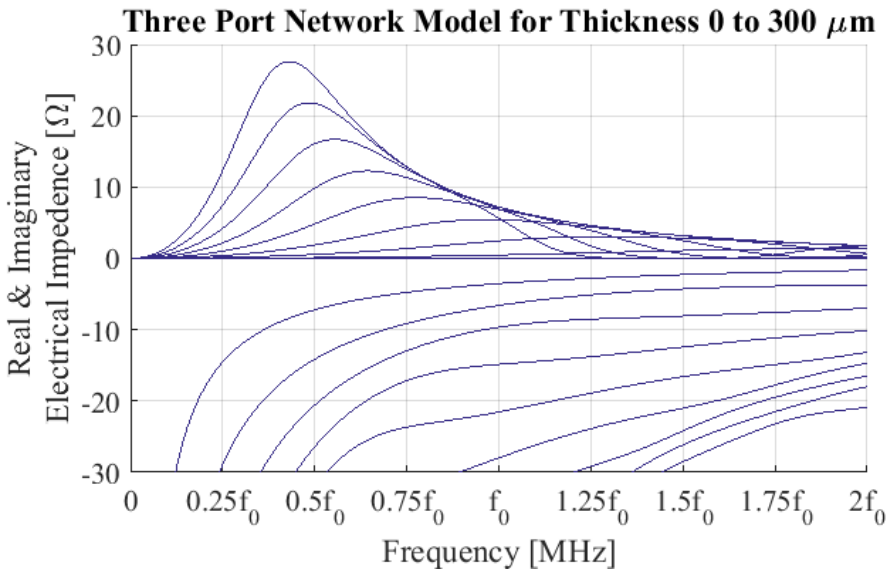

Figure A.3 The real and imaginary electrical impedance for a Three-Port-Network model with Equation A.9, Table A.1, a central frequency f_0 of 10MHz, and a transducer thickness range from 0 to 300 μm.

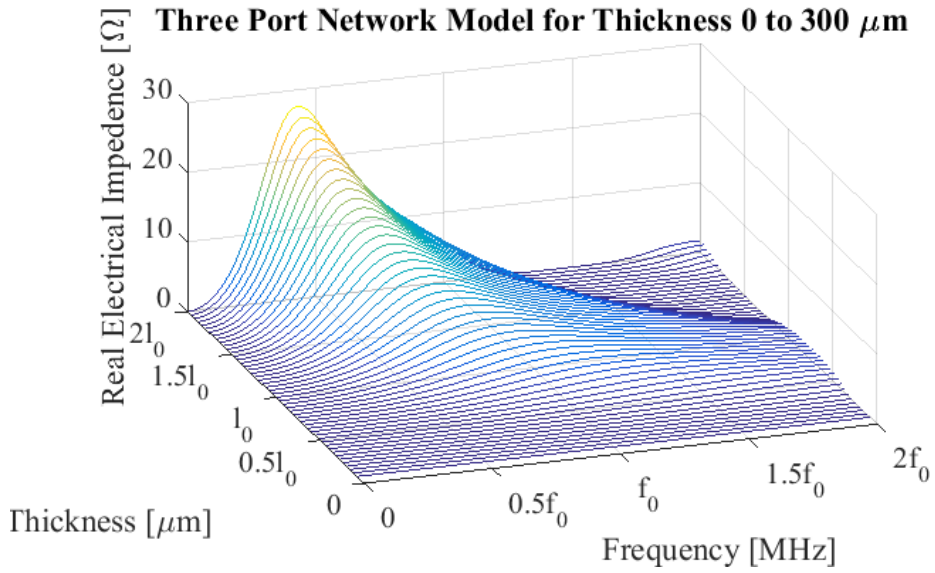

Figure A.4 The real electrical impedance for a Three-Port-Network model with Equation A.9, Table A.1, a central frequency f_0 of 10MHz, and a transducer thickness range from 0 to 300 μm.

A.2 Lukacs Model

The Lukacs Model is used to characterize an air-backed thick-film sol-gel transducer. The theory is first introduced followed by the model analysis.

A.2.1 Theory

The Lukacs Model theory is based on an air-backed thick-film sol-gel transducer as described in Figure A.5. The electrical impedance Z_3 of the transducer is described in Equations A.10-A.13 [Lukacs et al. (1999, 2000)] with Z^* as a complex impedance offset to account for stray inductance during measurements, β_p^S as the inverse permittivity of the piezoelectric material at constant strain, l_p and l_s as the thickness of the piezoelectric material and substrate material, h_p as the piezoelectric transmitting constant, v_p and v_s as the velocity of the piezoelectric material and substrate material, c_p^D and c_s^D as the stiffened elastic constant of the piezoelectric material and substrate material, and with u_{ss}, u_L, and u_R shown only as intermediate variables.

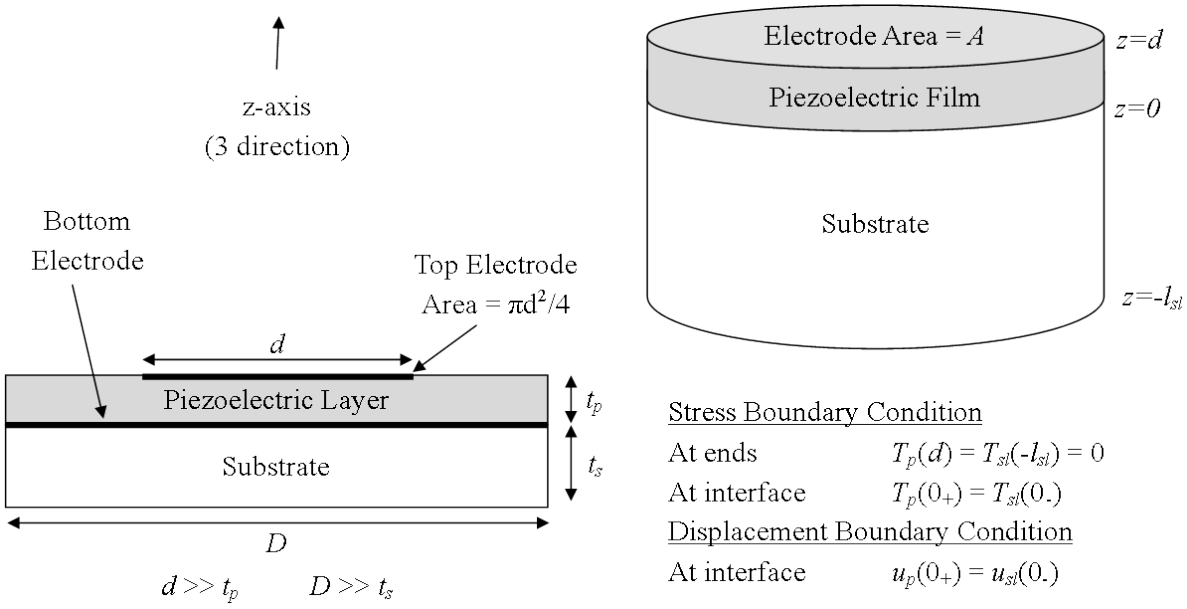

Figure A.5 Lukacs Model transducer schematic and boundary conditions. Based on similar figure previously published [Lukacs et al. (1999)].

The transducer electrical impedance Z_3 in Equations A.10-A.13 is derived using the one-dimensional wave equation and linear piezoelectric equations with the following geometric conditions: the top electrode diameter must be much larger than the thickness of the piezoelectric material in order to only excite the thickness-mode resonance, the diameter of the substrate must be much larger than its thickness in order to prevent lateral-mode excitation, any energy that reverberates within the substrate must remain within the near-field of the transducer until it has been sufficiently dissipated (depends on elastic stiffness of piezoelectric and substrate layers), and finally, the electrodes must be thin with respect to the thickness of the piezoelectric film.

$$Z_3 = Z^* + \frac{j}{\omega A}\left\{-\beta_p^S l_p + h_p \frac{u_L}{u_R}\sin\left(\frac{\omega l_p}{v_p}\right) - h_p u_{ss}\left[\frac{c_p^D \omega}{v_p}\frac{u_L}{u_R} - h_p\right]\left[\cos\left(\frac{\omega l_p}{v_p}\right) - 1\right]\right\} \tag{A.10}$$

$$u_{ss} = \frac{v_s}{c_s^D \omega \tan\left(\frac{\omega l_s}{v_s}\right)} \tag{A.11}$$

$$u_L = \frac{h_p v_p}{\omega c_p^D} + u_{ss} h_p \sin\left(\frac{\omega l_p}{v_p}\right) \tag{A.12}$$

$$u_R = \cos\left(\frac{\omega l_p}{v_p}\right) + \frac{u_{ss} c_p^D \omega}{v_p}\sin\left(\frac{\omega l_p}{v_p}\right) \tag{A.13}$$

The velocity of the piezoelectric material v_p is described in Equation A.14 with ρ_p as the piezoelectric material density in the stationary state.

$$v_p = \sqrt{\frac{c_p^D}{\rho_p}} \tag{A.14}$$

The stiffened elastic constant of the substrate material c_s^D is described in Equation A.15 with ρ_s as the substrate material density in the stationary state.

$$c_s^D = {v_s}^2 \rho_s \tag{A.15}$$

The inverse permittivity of the piezoelectric material at constant strain β_p^S is described in Equation A.16 with ε_p^S as piezoelectric material dielectric constant of permittivity with zero or constant strain.

$$\beta_p^S = \frac{1}{\varepsilon_p^S} \tag{A.16}$$

The piezoelectric transmitting constant h_p is described in Equation A.17 with e_p as the piezoelectric material piezoelectric stress constant.

$$h_p = \frac{e_p}{\varepsilon_p^S} \tag{A.17}$$

A.2.2 Analysis

The terms in Equations A.3, A.5, A.6, and A.10–A.17 can be combined while neglecting the complex electrical impedance offset Z^* such that the transducer electrical impedance Z_3 can be described as a function of frequency f, geometry A, l_p, and l_s, substrate material properties ρ_s and v_s, and piezoelectric material properties e_p, c_p^D, c_p^E, and ρ_p.

The Lukacs Model requires the complex form of the substrate and piezoelectric material properties, and unfortunately these values are not readily available. Therefore, the analysis did not result in true impedance values when only the real form of the substrate and piezoelectric material properties were used. Regardless, this erroneous analysis without the complex form of the material properties is applied to the same longitudinal mode air-backed thick-film sol-gel transducer of 4.0 mm × 4.0 mm square dimension, with the same transducer material properties for PZT-5A and steel substrate properties as described in Table A.2 [Kino (1987)], and the same central frequency f_0 of 10MHz and a central piezoelectric material thickness $l_p = l_0$ of 150 μm.

The real and imaginary transducer electrical impedance for the Lukacs Model with Equation A.10 and Table A.2 is shown in Figure A.6. As previously described, the values in Figure A.6 are erroneous as complex material properties were not used.

The real and imaginary transducer electrical impedance values for a thickness range from $l_p = 0$ to $l_p = 2l_0$ are shown in Figure A.7. The real transducer electrical impedance for a range of thickness values from $l_p = 0$ to $l_p = 2l_0$ is shown in Figure A.8.

Table A.2 Lukacs Model Material and Geometry Properties

PZT-5A Elastic constant (zero electric field)	$c^E_{p\,33}$	1.11×10^{11}	N/m^2
PZT-5A Elastic constant (stiffened)	$c^D_{p\,33}$	1.47×10^{11}	N/m^2
PZT-5A Piezoelectric stress constant	$e_{p_{z3}}$	15.8	C/m^2
PZT-5A Density	ρ_p	7750	kg/m^3
Steel Density	ρ_s	7900	kg/m^3
Steel Longitudinal Velocity	v_s	5900	m/s
Electrode Surface Area	A	1.6×10^{-5}	m^2
Steel Substrate Thickness	l_s	1×10^{-4}	m

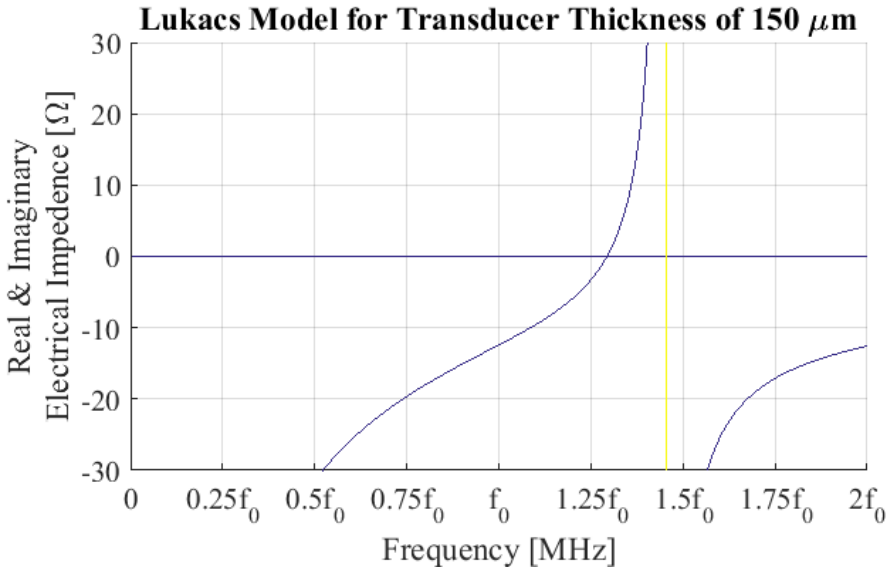

Figure A.6 The real and imaginary electrical impedance for a Lukacs model with Equation A.10, Table A.2, a central frequency f_0 of 10MHz, and a transducer thickness l_0 of 150 μm.

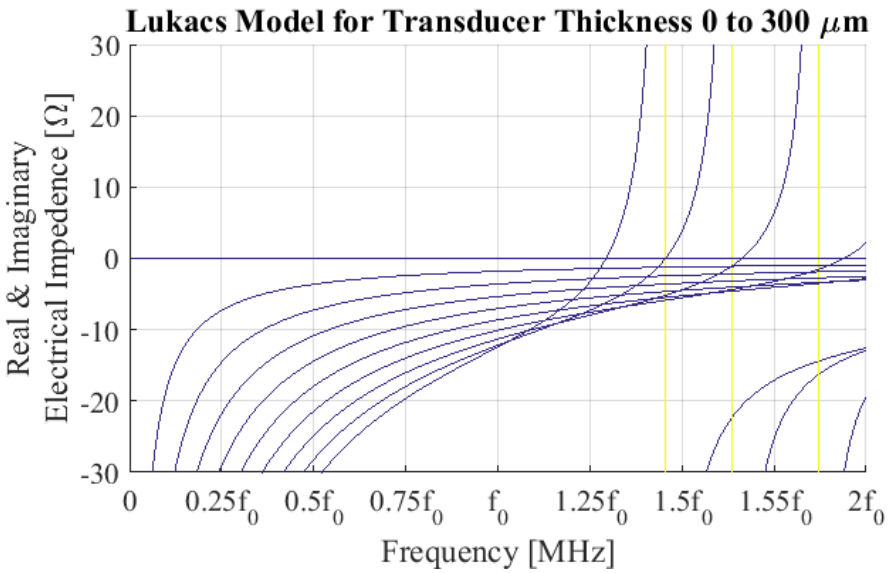

Figure A.7 The real and imaginary electrical impedance for a Lukacs model with Equation A.10, Table A.2, a central frequency f_0 of 10MHz, and a transducer thickness range from 0 to 300 μm.

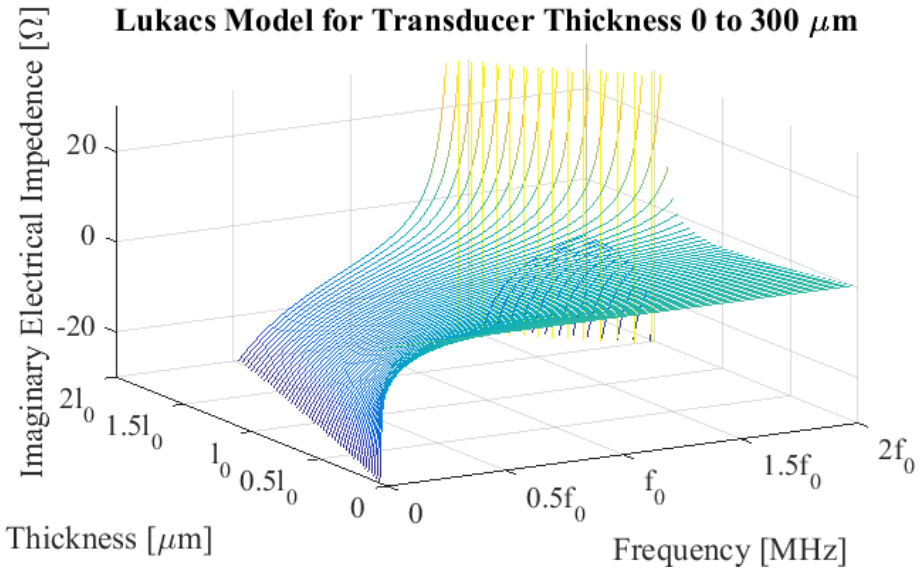

Figure A.8 The real electrical impedance for a Lukacs model with Equation A.10, Table A.2, a central frequency f_0 of 10MHz, and a transducer thickness range from 0 to 300 μm.

A.3 Summary

Various transducer models were presented and analyzed for an air-backed thick-film sol-gel transducer application. The Three-Port-Network Model appears to have a realistic pattern for real and imaginary impedance values. The Lukacs Model analysis is not applicable as only the real piezoelectric material parameters were used instead of the required complex piezoelectric material parameters.

APPENDIX B. TRADEMARKS

CALIPERAY is a registered trademark of MISTRAS Group, Inc.

COSASCO is a registered trademark of Rohrback Cosasco Systems, Inc.

EMERSON is a registered trademark of Emerson Electric Co.

GE is a registered trademark of General Electric Company

JMP is a registered trademark of SAS Institute Inc.

MATLAB is a registered trademark of The MathWorks, Inc.

MISTRAS is a registered trademark of MISTRAS Group, Inc.

PANAMETRICS is a registered trademark of GE Infrastructure Sensing, Inc.

PERMASENSE is a registered trademark of Permasense Limited

RIGHTRAX is a registered trademark of GE Inspection Technologies, LP General Electric Company

SMART PIMS is a registered trademark of Sensor Networks, Inc.

SOUNDSAFE is a registered trademark of Sonotech, Inc.

ULTRACORR is a registered trademark of Rohrback Cosasco Systems, Inc.

BIBLIOGRAPHY

A3 Monitoring (2014). spotOn U. https://www.a3monitoring.com/assets/leaflet-u.pdf.

Albach, P. H. and Bond, L. J. (1990). Numerical simulation of elastic wave scattering from three-dimensional axisymmetric surface features. In Thompson, D. O. and Chimenti, D. E., editors, *Review of Progress in Quantitative Nondestructive Evaluation Volume 9*, pages 53–60. Plenum Press (New York).

Aldrin, J. C., Annis, C., Sabbagh, H. A., and Lindgren, E. A. (2016). Best practices for evaluating the capability of nondestructive evaluation (NDE) and structural health monitoring (SHM) techniques for damage characterization. In Chimenti, D. E. and Bond, L. J., editors, *42nd Annual Review of Progress in Quantitative Nondestructive Evaluation Volume 35*, volume 1706, pages 200002 1–10, Minneapolis. AIP Publishing.

Ali, M. G. S., Elsayed, N. Z., and Eid, E. A. (2015). An approach to design broadband air backed piezoelectric sensor. *Arch. Acoust.*, 40(1):3–10.

Alleyne, D. N., Pavlakovic, B., Lowe, M. J. S., and Cawley, P. (2001). Rapid, long range inspection of chemical plant pipework using guided waves. In Thompson, D. O. and Chimenti, D. E., editors, *Review of Progress in Quantitative Nondestructive Evaluation Volume 20*, volume 557, pages 180–187, Ames. American Institute of Physics.

Alobaidi, W. M., Alkuam, E. A., Al-Rizzo, H. M., and Sandgren, E. (2015). Applications of ultrasonic techniques in oil and gas pipeline industries : a review. *Am. J. Oper. Res.*, 5(4):274–287.

Alvisi, P. P. and Lins, V. F. C. (2011). An overview of naphthenic acid corrosion in a vacuum distillation plant. *Eng. Fail. Anal.*, 18(5):1403–1406.

American Petroleum Institute (2007). Fitness-For-Service - API 579-1/ASME FFS-1. Technical report, American Petroleum Institute, Washington, D.C.

American Petroleum Institute (2011). Damage Mechanisms Affecting Fixed Equipment in the Refining Industry - API 571. Technical report, American Petroleum Institute, Washington, D.C.

An, Z.-w., Jin, S.-j., Lian, G.-x., and Wang, X.-m. (2014). Investigation of the directivity of ultrasonic scattering field using dynamic photoelastic technique. In *Symposiom on Piezoelectricity, Acoustic Waves, and Device Applications*, pages 408–411, Beijing. IEEE.

Anderson, T. L. (2005). *Fracture Mechanics: Fundamentals and Applications*. CRC Press, Boca Raton, 3rd edition.

Annis, C. (2009). MIL-HDBK-1823A - Nondestructive Evaluation System Reliability Assessment. Technical report, U.S. Department of Defense, Wright-Patterson Air Force Base.

ASTM (2014). A106 - Standard Specification for Seamless Carbon Steel Pipe for High-Temperature Service. Technical report, ASTM International, West Conshohocken.

Avila-Carrera, R. and Sanchez-Sesma, F. J. (2006). Scattering and diffraction of elastic P- and S-waves by a spherical obstacle: A review of the classical solution. *Geofis. Int.*, 45(1):3–21.

Baborovsky, V. M., Marsh, D. M., and Slater, E. A. (1973). Schlieren and computer studies of the interaction of ultrasound with defects. *Nondestruct. Test.*, 6(4):200–207.

Bagavathiappan, S., Lahiri, B. B., Saravanan, T., Philip, J., and Jayakumar, T. (2013). Infrared thermography for condition monitoring – A review. *Infrared Phys. Technol.*, 60:35–55.

Banerjee, S. and Kundu, T. (2008). Semi-analytical modeling of ultrasonic fields in solids with internal anomalies immersed in a fluid. *Wave Motion*, 45(5):581–595.

Bardier, C., Dusseaux, R., Edee, K. S., and Granet, G. (2004). Scattering of a plane wave by one-dimensional dielectric random rough surfaces–study with curvilinear coordinate method. *Waves Random Media*, 14(1):61–74.

Barrow, D. A., Petroff, T. E., and Sayer, M. (1996). Method for Producing Thick Ceramic Films by a Sol Gel Coating Process. U.S. Patent 5,585,136.

Barshan, B. (2000). Fast processing techniques for accurate ultrasonic range measurements. *Meas. Sci. Technol.*, 11(1):45–50.

Bass, F. G. and Fuks, I. M. (1979). *Wave Scattering from Statistically Rough Surfaces*. Pergamon Press, New York, 1st edition.

Beckmann, P. and Spizzichino, A. (1963). *The Scattering of Electromagnetic Waves from Rough Surfaces*. Pergamon Press, New York, 1st edition.

Beissner, R. and Birring, A. (1988). Nondestructive Evaluation Methods for Characterization of Corrosion. Technical report, Southwest Research Institute - Nondestructive Testing Information Analysis Center, San Antonio.

Bennett, J. M. and Mattsson, L. (1989). *Introduction to Surface Roughness and Scattering*. Optical Society of America, Washington, D.C., 1st edition.

Benstock, D., Cegla, F. B., and Stone, M. (2014). The influence of surface roughness on ultrasonic thickness measurements. *J. Acoust. Soc. Am.*, 136(6):3028–3039.

Berkeley Springs (2016). The Eagle Array - Pipeline Integrity: Remote Condition Monitoring. http://bsisentry.com/images/productpages/eagle_array/EA-brochure.pdf.

Bickerstaff, R., Vaughn, M., Stoker, G., Hassard, M., and Garrett, M. (2002). Review of Sensor Technologies for In-line Inspection of Natural Gas Pipelines. Technical report, Sandia National Laboratories, Albuquerque.

Biryukov, S. V., Gulyaev, Y. V., Krylov, V., and Plessky, V. (1995). *Surface Acoustic Waves in Inhomogeneous Media*. Springer-Verlag, New York, 1st edition.

Bourlier, C., Déchamps, N., and Berginc, G. (2005). Comparison of asymptotic backscattering models (SSA, WCA, and LCA) from one-dimensional Gaussian ocean-like surfaces. *IEEE Trans. Antennas Propag.*, 53(5):1640–1652.

Bovankovich, J. C. (1994). On-line corrosion monitoring for process plant control. *Mater. Perform.*, 33(11):57.

Brath, A. J., Simonetti, F., Nagy, P. B., and Instanes, G. (2017). Guided wave tomography of pipe bends. *IEEE Trans. Ultrason. Ferroelectr. Freq. Control*, 64(5):847–858.

Bray, D. E. and Stanley, R. K. (1997). *Nondestructive Evaluation: A Tool in Design, Manufacturing, and Service*. CRC Press, Boca Raton, revised edition.

Brune, D. (1997). *Surface Characterization: A User's Sourcebook*. Scandinavian Science Publisher, Oslo, 1st edition.

Budimir, M., Mohimi, A., Selcuk, C., and Gan, T.-H. (2011). High temperature NDE ultrasound transducers for condition monitoring of superheated steam pipes in nuclear power plants. In *20th International Conference Nuclear Energy for New Europe*, pages 502 1–8, Bovec.

Burch, S. F. (2012). HOIS recommended practice for precision thickness measurements for corrosion monitoring. Technical report, ESR Technology, Warrington.

Caliano, G., Savoia, A. S., and Iula, A. (2012). An automatic compact schlieren imaging system for ultrasound transducer testing. *IEEE Trans. Ultrason. Ferroelectr. Freq. Control*, 59(9):2102–2110.

Callister, W. D. (2005). *Fundamentals of Materials Science and Engineering: An Integrated Approach*. John Wiley & Sons, 2nd edition.

Calmon, P., Mahaut, S., Chatillon, S., and Raillon, R. (2006). CIVA: An expertise platform for simulation and processing NDT data. *Ultrason.*, 44:e975–e979.

Calvo, D. C., Rudd, K. E., Zampolli, M., Sanders, W. M., and Bibee, L. D. (2010). Simulation of acoustic scattering from an aluminum cylinder near a rough interface using the elastodynamic finite integration technique. *Wave Motion*, 47(8):616–634.

Cawley, P., Cegla, F., and Stone, M. (2013). Corrosion monitoring strategies–choice between area and point measurements. *J. Nondest. Eval.*, 32(2):156–163.

Cawley, P., Lowe, M. J. S., Alleyne, D. N., Pavlakovic, B., and Wilcox, P. (2003). Practical long range guided wave inspection-applications to pipes and rail. *Mater. Eval.*, 61(1):66–74.

Cegla, F. B., Cawley, P., Allin, J., and Davies, J. (2011). High-temperature (>500C) wall thickness monitoring using dry-coupled ultrasonic waveguide transducers. *IEEE Trans. Ultrason. Ferroelectr. Freq. Control*, 58(1):156–167.

Chandler-Wilde, S. N., Heinemeyer, E., and Potthast, R. (2006). Acoustic scattering by mildly rough unbounded surfaces in three dimensions. *SIAM J. Appl. Math.*, 66(3):1002–1026.

Cheeke, J. D. N. (2012). *Fundamentals and Applications of Ultrasonic Waves*. CRC Press, Boca Raton, 2nd edition.

Clebsch, A. (1863). As to the reflection on a spherical surface. *J. Pure Appl. Math.*, 61:195–262.

Cocheril, Y. and Vauzelle, R. (2007). A new ray-tracing based wave propagation model including rough surfaces scattering. *Prog. Electromagn. Res.*, 75:357–381.

Cosasco (2016). Ultracorr 2 - Wall Thickness Monitor. https://www.cosasco.com/documents/Datasheets/Ultracorr 2 RevA.pdf.

Dassault Systemes (2015). ABAQUS 6.14 Student Edition. Computer Program.

Davies, J. and Cawley, P. (2009). The application of synthetic focusing for imaging crack-like defects in pipelines using guided waves. *IEEE Trans. Ultrason. Ferroelectr. Freq. Control*, 56(4):759–771.

Davies, S. J., Edwards, C., Taylor, G. S., and Palmer, S. B. (1993). Laser-generated ultrasound: its properties, mechanisms and multifarious applications. *J. Phys. D: Appl. Phys.*, 26(3):329–348.

Demma, A., Cawley, P., Lowe, M., Roosenbrand, A. G., and Pavlakovic, B. (2004). The reflection of guided waves from notches in pipes: a guide for interpreting corrosion measurements. *NDT & E Int.*, 37(3):167–180.

Deschamps, G. A. (1972). Ray techniques in electromagnetics. *Proc. IEEE*, 60(9):1022–1035.

Didascalou, D., Döttling, M., Geng, N., and Wiesbeck, W. (2003). An approach to include stochastic rough surface scattering into deterministic ray-optical wave propagation modeling. *IEEE Trans. Antennas Propag.*, 51(7):1508–1515.

Dorey, R. A., Dauchy, F., Wang, D., and Berriet, R. (2007). Fabrication and characterisation of annular thickness mode piezoelectric micro ultrasonic transducers. *IEEE Trans. Ultrason. Ferroelectr. Freq. Control*, 54(12):2462–2468.

Dowling, N. E. (1999). *Mechanical Behavior of Materials: Engineering Methods for Deformation, Fracture, and Fatigue.* Prentice Hall, Upper Saddle River, 2nd edition.

Drinkwater, B. W. and Wilcox, P. D. (2006). Ultrasonic arrays for non-destructive evaluation: A review. *NDT & E Int.*, 39(7):525–541.

Duran, O., Althoefer, K., and Seneviratne, L. D. (2007). Automated pipe defect detection and categorization using camera/laser-based profiler and artificial neural network. *IEEE Trans. Autom. Sci. Eng.*, 4(1):118–126.

Eason, T. J., Bond, L. J., Engle, B. J., and Lozev, M. G. (2017a). Elastic wave scattering amplitude from a single hemispherical pit. *Ultrason.*, in review.

Eason, T. J., Bond, L. J., and Lozev, M. G. (2015a). Structural health monitoring of localized internal corrosion in high temperature piping for oil industry. In Chimenti, D. E. and Bond, L. J., editors, *41st Annual Review of Progress in Quantitative Nondestructive Evaluation Volume 34*, volume 1650, pages 863–873, Boise. AIP Publishing.

Eason, T. J., Bond, L. J., and Lozev, M. G. (2015b). Ultrasonic thickness structural health monitoring photoelastic visualization and measurement accuracy for internal pipe corrosion. In Meyendorf, N. G., editor, *SPIE Smart Materials and Nondestructive Evaluation for Energy Systems*, volume 9439, pages 94390M 1–16, San Diego. SPIE.

Eason, T. J., Bond, L. J., and Lozev, M. G. (2016a). Structural health monitoring ultrasonic thickness measurement accuracy and reliability of various time-of-flight calculation methods. In Chimenti, D. E. and Bond, L. J., editors, *42nd Annual Review of Progress in Quantitative*

Nondestructive Evaluation Volume 35, volume 1706, pages 200003 1–11, Minneapolis. AIP Publishing.

Eason, T. J., Bond, L. J., and Lozev, M. G. (2016b). Ultrasonic sol-gel arrays for monitoring high temperature corrosion. In *19th World Conference on Non-Destructive Testing*, pages 19528 1–9, Munich. ndt.net.

Eason, T. J., Bond, L. J., and Lozev, M. G. (2017b). Elastic wave far-field scattering amplitude from a hemispherical pit. In *EURODYN*, Rome. paper accepted.

Eason, T. J., Bond, L. J., and Lozev, M. G. (2017c). Ultrasonic scattering from a hemispherical pit theory and experimental measurement precision. In Chimenti, D. E. and Bond, L. J., editors, *43rd Annual Review of Progress in Quantitative Nondestructive Evaluation Volume 36*, volume 1806, pages 070004 1–10, Atlanta. AIP Publishing.

Eclipse Scientific (2014). Ultrasonic Photoelastic Visualization System Data Sheet. http://www.eclipsescientific.com/Products/Training/Photoelastic/ESPhotoElastic Data Sheet.pdf.

Einspruch, N. G., Witterholt, E. J., and Truell, R. (1960). Scattering of a plane transverse wave by a spherical obstacle in an elastic medium. *J. Appl. Phys.*, 806(5):806–818.

Elfouhaily, T. M. and Guérin, C.-A. (2004). A critical survey of approximate scattering wave theories from random rough surfaces. *Waves Random Media*, 14(4):R1–R40.

Elfouhaily, T. M. and Johnson, J. T. (2007). A new model for rough surface scattering. *IEEE Trans. Geosci. Remote Sens.*, 45(7):2300–2308.

Elschner, J. and Hu, G. (2015). Elastic scattering by unbounded rough surfaces: solvability in weighted Sobolev spaces. *Appl. Anal.*, 94(2):251–278.

Ensminger, D. and Bond, L. J. (2012). *Ultrasonics: Fundamentals, Technologies, and Applications.* CRC Press Taylor & Francis Group, Boca Raton, 3 edition.

ESR Technology (2014). HOIS Interactive Knowledge Base. http://hois-ikb.esrtechnology.com.

Fiaz, M. A., Frezza, F., Pajewski, L., Ponti, C., and Schettini, G. (2012). Scattering by a circular cylinder buried under a slightly rough surface: The cylindrical-wave approach. *IEEE Trans. Antennas Propag.*, 60(6):2834–2842.

Forsyth, D. S. (2016). Structural health monitoring and probability of detection estimation. In Chimenti, D. E. and Bond, L. J., editors, *42nd Annual Review of Progress in Quantitative Nondestructive Evaluation Volume 35*, volume 1706, pages 200004 1–6, Minneapolis. AIP Publishing.

Franceschetti, G. and Riccio, D. (2006). *Scattering, Natural Surfaces, and Fractals.* Academic Press, Burlington, 1st edition.

Frankel, G. S. (1998). Pitting corrosion of metals a review of the critical factors. *J. Electrochem. Soc.*, 145(6):2186–2198.

Fung, A. K. (2015). *Backscattering From Multiscale Rough Surfaces with Application to Wind Scatterometry.* Artech House, Norwood, 1st edition.

Fung, A. K. and Chen, K. S. (2010). *Microwave Scattering and Emission Model for Users.* Artech House, Boston, 1st edition.

Galvagni, A. and Cawley, P. (2013). Permanently installed guided wave pipeline monitoring. In Thompson, D. O. and Chimenti, D. E., editors, *39th Annual Review of Progress in Quantitative Nondestructive Evaluation Volume 32*, volume 1511, pages 159–166, Denver. American Institute of Physics.

Gan, F., Tian, G., Wan, Z., Liao, J., and Li, W. (2016). Investigation of pitting corrosion monitoring using field signature method. *Meas.*, 82:46–54.

Garverick, L., editor (1994). *Corrosion in the Petrochemical Industry.* ASM International, Materials Park, 1st edition.

GE Oil & Gas (2017). Predictive Corrosion Management – Specification Sheet – GEA-32848. https:// www.ge.com/digital/sites/default/files/GE-Digital-Corrosion-Inspection-Solution-with-Predix-Spec-Sheet.pdf.

GE Sensing & Inspection Technologies (2009). Rightrax HT Specifications – Online Corrosion Monitoring System – GEIT-20212EN. http://www.ge-mcs.com/download/ultrasound/corrosion-monitoring/GEIT-20212EN_rightrax-ht-specifications.pdf.

Gianneo, A., Carboni, M., and Giglio, M. (2016). Reliability aspects and multi-parameter POD formulation for guided wave based SHM techniques. In *19th World Conference on Non-Destructive Testing*, pages 19534 1–11, Munich. ndt.net.

Gilbert, F. and Knopoff, L. (1960). Seismic scattering from topographic irregularities. *J. Geophys. Res.*, 65(10):3437–3444.

Gilbert, M. S. and Johnson, J. T. (2003). A study of the higher-order small-slope approximation for scattering from a Gaussian rough surface. *Waves Random Media*, 13(2):137–149.

Ginzel, E. and Stewart, D. (2004). Photo-elastic visualisation of phased array ultrasonic pulses in solids. In *16th World Conference on Non-Destructive Testing*, Montreal. ndt.net.

Ginzel, E. and Zhenshun, Z. (2006). Quantification of ultrasonic beams using photoelastic visualisation. *NDT.net*, 11(5).

Godard, H. P. (1984). Localized Corrosion. In *Corosion Basics: An Introduction*, chapter 5. National Association of Corrosion Engineers, 1st edition.

Graff, K. F. (1975). *Wave Motion in Elastic Solids*. Courier Corporation, 1st edition.

Grandin, R. and Gray, T. (2017). UTSim2 validation. In Chimenti, D. E. and Bond, L. J., editors, *43rd Annual Review of Progress in Quantitative Nondestructive Evaluation Volume 36*, volume 1806, pages 150007 1–8, Atlanta. AIP Publishing.

Gros, X. E. (1996). Non-destructive Testing Techniques. In *NDT Data Fusion*, chapter 3, pages 43–81. Butterworth-Heinemann, 1st edition.

Guérin, C.-A., Soriano, G., and Elfouhaily, T. M. (2004). Weighted curvature approximation: numerical tests for 2D dielectric surfaces. *Waves Random Media*, 14(3):349–363.

Guo, L.-X., Liang, Y., Li, J., and Wu, Z.-S. (2011). A high order intergral SPM for the conducting rough surface scattering with the tapered wave incidence-TE case. *Prog. Electromagn. Res.*, 114:333–352.

Gutzeit, J. (2006). *Crude Unit Corrosion Guide - A Complete How To Manual*. PCC Process Corrosion Consultants, Gulf Breeze, 2nd edition.

Hall, G. (1977). Ultrasonic wave visualization as a teaching aid in non-destructive testing. *Ultrason.*, 15(2):57–69.

Hall, K. G. (1982). Observing ultrasonic wave propagation by stroboscopic visualization methods. *Ultrason.*, 20(4):159–167.

Hansen, P., Alismail, H., Browning, B., and Rander, P. (2011a). Stereo visual odometry for pipe mapping. In *IEEE/RSJ International Conference on Intelligent Robots and Systems*, pages 4020–4025, San Francisco. IEEE.

Hansen, P., Alismail, H., Rander, P., and Browning, B. (2011b). Monocular visual odometry for robot localization in LNG pipes. In *IEEE International Conference on Robotics and Automation*, pages 3111–3116, Shanghai. IEEE.

Hansen, P., Alismail, H., Rander, P., and Browning, B. (2013). Pipe mapping with monocular fisheye imagery. In *IEEE/RSJ International Conference on Intelligent Robots and Systems*, pages 5180–5185, Tokyo. IEEE.

Hanstead, P. D. (1972). Ultrasonic visualization. *Br. J. NDT*, 14(6):162–169.

Hanstead, P. D. (1974). A new ultrasonic focusing system for materials inspection. *J. Phys. D: Appl. Phys.*, 7(2):226–245.

Harris, F. J. (1978). On then use of windows for harmonic analysis with the discrete fourier transform. *Proc. IEEE*, 66(1):51–83.

He, Y., Tian, G., Zhang, H., Alamin, M., Simm, A., and Jackson, P. (2012). Steel corrosion characterization using pulsed eddy current systems. *IEEE Sens. J.*, 12(6):2113–2120.

Heidemann, E. and Hoesch, K. H. (1937). Optical investigations of ultrasonic fields in liquids and glasses. *J. Phys.*, 104(3-4):197–206.

Hinds, G. and Turnbull, A. (2010). Novel multi-electrode test method for evaluating inhibition of underdeposit corrosion–part 1: sweet conditions. *Corros.*, 66(4):046001 1–10.

Holmes, C., Drinkwater, B. W., and Wilcox, P. D. (2005). Post-processing of the full matrix of ultrasonic transmitreceive array data for non-destructive evaluation. *NDT & E Int.*, 38(8):701–711.

Hsueh, C.-H. and Wu, C.-C. (2010). Fabrication of lead zirconium titanium and silica composite films on copper/polyimide flexible substrates. *Smart Mater. Struct.*, 19(12):124005 1–8.

Huang, B. S., Yin, W. F., Sang, D. H., and Jiang, Z. Y. (2012). Synergy effect of naphthenic acid corrosion and sulfur corrosion in crude oil distillation unit. *Appl. Surf. Sci.*, 259:664–670.

Huang, H.-L., Cao, G., and Shen, I. (2014). Hydrothermal synthesis of lead zirconate titanate (PZT or Pb(Zr0.52Ti0.48)O3) nano-particles using controlled ramping and cooling rates. *Sens. Actuators A: Phys.*, 214:111–119.

Huthwaite, P., Ribichini, R., Cawley, P., and Lowe, M. J. S. (2013). Mode selection for corrosion detection in pipes and vessels via guided wave tomography. *IEEE Trans. Ultrason. Ferroelectr. Freq. Control*, 60(6):1165–1177.

Hyde, M. W., Basu, S., Spencer, M. F., Cusumano, S. J., and Fiorino, S. T. (2013). Physical optics solution for the scattering of a partially-coherent wave from a statistically rough material surface. *Opt. Express*, 21(6):6807–6825.

Ilyinski, A. S. and Slepyan, A. Y. (1993). *Propagation, Scattering, and Dissipation of Electromagnetic Waves*. Peter Peregrinus Institution of Electrical Engineers, London, 1st edition.

Imperatore, P., Iodice, A., and Riccio, D. (2009). Electromagnetic wave scattering from layered structures with an arbitrary number of rough interfaces. *IEEE Trans. Geosci. Remote Sens.*, 47(4):1056–1072.

Iowa State University (2014). NDT Education Resource Center. https://www.ndt-ed.org.

Ishamaru, A. (1978). *Wave Propagation and Scattering in Random Media*. IEEE Press, 1st edition.

Jackson, D. R. and Richardson, M. D. (2006). *High-frequency seafloor acoustics*. Springer, New York, 1st edition.

Jarvis, A. J. C. (2013). *Simulation of Ultrasonic Monitoring to Improve Corrosion Characterization within High Temperature Environments*. Doctor of philosophy, Imperial College London.

Jarvis, A. J. C. and Cegla, F. B. (2012). Application of the distributed point source method to rough surface scattering and ultrasonic wall thickness measurement. *J. Acoust. Soc. Am.*, 132(3):1325–1335.

Jarvis, A. J. C. and Cegla, F. B. (2014). Scattering of near normal incidence SH waves by sinusoidal and rough surfaces in 3-D: comparison to the scalar wave approximation. *IEEE Trans. Ultrason. Ferroelectr. Freq. Control*, 61(7):1179–1190.

Jiang, X., Kim, K., Zhang, S., Johnson, J., and Salazar, G. (2014). High-temperature piezoelectric sensing. *Sens.*, 14(1):144–169.

Jin, Y. Q. (2005). *Theory and Approach of Information Retrievals from Electromagnetic Scattering and Remote Sensing*. Springer Netherlands, Dordrecht, 1st edition.

Jirarungsatian, C. and Prateepasen, A. (2010). Pitting and uniform corrosion source recognition using acoustic emission parameters. *Corros. Sci.*, 51(1):187–197.

Johnson, G. and Truell, R. (1965). Numerical computations of elastic scattering cross sections. *J. Appl. Phys.*, 36(11):3466–3475.

Joshi, S. M. (2011). *Quantifying Three Dimensional Effects in Acoustic Rough Surface Scattering*. Master of science, University of Texas at Austin.

Kawasue, K. and Komatsu, T. (2013). Shape measurement of a sewer pipe using a mobile robot with computer vision. *Int. J. Adv. Robot. Syst.*, 10(52):1–7.

Kažys, R., Voleišis, A., and Voleišien, B. (2008). High temperature ultrasonic transducers: review. *Ultratarsas (Ultrasound)*, 63(2):7–17.

Khair, K. R., Datta, S. K., and Shah, A. H. (1989a). Amplification of obliquely incident seismic waves by cylindrical alluvial valley of arbitrary cross-sectional shape. Part I. Incident P and SV waves. *Bull. Seismol. Soc. Am.*, 79(3):610–630.

Khair, K. R., Datta, S. K., and Shah, A. H. (1989b). Three dimensional scattering of elastic waves by surface corrosion pits. In Thompson, D. O., editor, *Review of Progress in Quantitative Nondestructive Evaluation Volume 8*, pages 63–70, La Jolla. Springer-Verlag US.

Kino, G. S. (1987). *Acoustic Waves: Devices, Imaging, and Analog Signal Processing*. Simon & Schuster, Englewood Cliffs, 1st edition.

Kirk, K. J., Mcnab, A., Cochran, A., Hall, I., and Hayward, G. (1999). Ultrasonic arrays for monitoring cracks in an industrial plant at high temperatures. *IEEE Trans. Ultrason. Ferroelectr. Freq. Control*, 46(2):311–319.

Kobayashi, M. and Jen, C. K. (2012). Transducers for non-destructive evaluation at high temperatures. In Nakamura, K., editor, *Ultrasonic Transducers: Materials and Design for Sensors, Actuators and Medical Applications*, chapter 13, pages 408–443. Woodhead Publishing Limited, Cambridge, 1st edition.

Kobayashi, M., Jen, C. K., Bussiere, J. F., and Wu, K.-T. (2009). High-temperature integrated and flexible ultrasonic transducers for nondestructive testing. *NDT & E Int.*, 42(2):157–161.

Kraft, D. W. (1971). Scattering of elastic waves from a spherical cavity in a solid medium. *J. Appl. Phys.*, 42(8):3019–3024.

Krautkramer, J. and Krautkramer, H. (2013). *Ultrasonic Testing of Materials*. Springer Science & Business Media, 4th edition.

Ku, H. (1966). Notes on the use of propagation of error formulas. *J. Res. Natl. Bur. Stand., Sect. C: Eng. Instrum.*, 70C(4):263–273.

Kuo, C.-H. (2008). *Full Wave 2D Modeling of Scattering and Inverse Scattering for Layered Rough Surfaces with Buried Objects*. Doctor of philosophy, University of Michigan.

Kurkcu, H. (2008). *High-Frequency Scattering by Infinite Rough Surfaces*. Doctor of philosophy, University of Minnesota.

Kwun, H., Kim, S. Y., and Light, G. M. (2003). The magnetostrictive sensor technology for long range guided wave testing and monitoring of structures. *Mater. Eval.*, 61(1):80–84.

Lackner, G. and Tscheliesnig, P. (2004). Field testing of flat bottomed storage tanks with acoustic emission - a review on the gained experience. *J. Acoust. Emiss.*, 22:201–207.

Lai, Z. (2007). *Electromagnetic Wave Propagation Over Large Rough Surfaces at Low Grazing Angles*. Doctor of philosophy, University of Massachusetts Amherst.

Laredo, G. C., López, C. R., Álvarez, R. E., and Cano, J. L. (2004). Naphthenic acids, total acid number and sulfur content profile characterization in Isthmus and Maya crude oils. *Fuel*, 83(11-12):1689–1695.

Lechleiter, A. and Ritterbusch, S. (2010). A variational method for wave scattering from penetrable rough layers. *IMA J. Appl. Math.*, 75(3):366–391.

Lee, J.-J. and Langston, C. A. (1983). Three-dimensional ray tracing and the method of principal curvature for geometric spreading. *Bull. Seismol. Soc. Am.*, 73(3):765–780.

Lee, V. W. (1978). Displacements Near a Three-Dimensional Hemispherical Canyon Subjected to Incident Plane Waves. Technical Report CE 78-16, U.S. Geological Survey & U.S. Nuclear Regulatory Commission, Los Angeles.

Lee, V. W. (1982). A note on the scattering of elastic plane waves by a hemispherical canyon. *Soil Dyn. Earthq. Eng.*, 1(3):122–129.

Lee, V. W. (1984). Three-dimensional diffraction of plane P, SV & SH waves by a hemispherical alluvial valley. *Soil Dyn. Earthq. Eng.*, 3(3):133–144.

Lee, V. W. and Zhu, G. (2014). A note on three-dimensional scattering and diffraction by a hemispherical canyon I: Vertically incident plane P-wave. *Soil Dyn. Earthq. Eng.*, 61-62:197–211.

Leffler, W. L. (2008). *Petroleum Refining in Nontechnical Language*. PennWell Books, Tulsa, 4th edition.

Leinov, E., Lowe, M. J. S., and Cawley, P. (2016). Ultrasonic isolation of buried pipes. *J. Sound Vib.*, 363:225–239.

Leonard, K. R. and Hinders, M. K. (2003). Guided wave helical ultrasonic tomography of pipes. *J. Acoust. Soc. Am.*, 767(2):767–774.

Li, J. and Rose, J. L. (2006). Natural beam focusing of non-axisymmetric guided waves in large-diameter pipes. *Ultrason.*, 44(1):35–45.

Li, J. M., Lu, L., Lai, M. O., and Ralph, B. (2003). *Image-based Fractal Description of Microstructures*. Kluwer Academci Publishers, Boston, 1st edition.

Li, M., Spencer, F. W., and Meeker, W. Q. (2015). Quantile probability of detection: distinguishing between uncertainty and variability in nondestructive testing. *Mater. Eval.*, 73(1):89–95.

Li, S. Y., Kim, Y.-G., Jung, S., Song, H.-S., and Lee, S.-M. (2007). Application of steel thin film electrical resistance sensor for in situ corrosion monitoring. *Sens. Actuators B: Chem.*, 120(2):368–377.

Liao, D. and Dogaru, T. (2012). Full-wave characterization of rough terrain surface scattering for forward-looking radar applications. *IEEE Trans. Antennas Propag.*, 60(8):3853–3866.

Lindgren, E. A. (2016). SHM reliability and implementation a personal military aviation perspective. In Chimenti, D. E. and Bond, L. J., editors, *42nd Annual Review of Progress in*

Quantitative Nondestructive Evaluation Volume 35, volume 1706, pages 200001 1–6, Minneapolis. AIP Publishing.

Liu, P. and Jin, Y. Q. (2004). Numerical simulation of bistatic scattering from a target at low altitude above rough sea surface under an EM-wave incidence at low grazing angle by using the finite element method. *IEEE Trans. Antennas Propag.*, 52(5):1205–1210.

Liu, S. and Meeker, W. Q. (2015). Statistical methods for estimating the minimum thickness along a pipeline. *Technometrics*, 57(2):164–179.

Liu, X., Tao, S., and Shen, Y. (1997). Preparation and characterization of nanocrystalline α-Fe2O3 by a sol-gel process. *Sens. Actuators B: Chem.*, 40(2-3):161–165.

Liu, Z. and Kleiner, Y. (2013). State of the art review of inspection technologies for condition assessment of water pipes. *Meas.*, 46(1):1–15.

Lowe, M. J. S., Alleyne, D. N., and Cawley, P. (1998). Defect detection in pipes using guided waves. *Ultrason.*, 36(1-5):147–154.

Lowe, P. S., Sanderson, R., Boulgouris, N. V., and Gan, T. H. (2016). Hybrid active focusing with adaptive dispersion for higher defect sensitivity in guided wave inspection of cylindrical structures. *Nondestruct. Test. Eval.*, 31(3):219–234.

Lozev, M. G., Smith, R. W., and Grimmett, B. B. (2005). Evaluation of methods for detecting and monitoring of corrosion damage in risers. *Trans. ASME J. Press. Vessel Technol.*, 127(3):244–254.

Lu, H. (2012). *Design, Fabrication, and Testing of High-Frequency High-Numerical-Aperture Annular Array Transducer fro Improved Depth-of-Field Photoacoustic Microscopy*. Master of science, University of Alberta.

Lubbers, J. and Graaff, R. (1998). A simple and accurate formula for the sound velocity in water. *Ultrasound Med. Biol.*, 24(7):1065–1068.

Lubliner, J. (2005). *Plasticity Theory*. Courier Corporation, revised edition.

Lukacs, M., Olding, T., Sayer, M., Tasker, R., and Sherrit, S. (1999). Thickness mode material constants of a supported piezoelectric film. *J. Appl. Phys.*, 85(5):2835–2843.

Lukacs, M., Sayer, M., and Foster, S. (2000). Single element high frequency (<50 MHz) PZT sol gel composite ultrasound transducers. *IEEE Trans. Ultrason. Ferroelectr. Freq. Control*, 47(1):148–159.

Lunn, N., Dixon, S., and Potter, M. D. G. (2017). High temperature EMAT design for scanning or fixed point operation on magnetite coated steel. *NDT & E Int.*, 89:74–80.

Luo, W. and Rose, J. L. (2007). Phased array focusing with guided waves in a viscoelastic coated hollow cylinder. *J. Acoust. Soc. Am.*, 121(4):1945–1955.

MacLauchlan, D., Clark, S., Cox, B., Doyle, T., Grimmett, B., Hancock, J., Hour, K., and Rutherford, C. (2004). Recent advancements in the applicaiton of EMATS to NDE. In *16th World Conference on Non-Destructive Testing*, Montreal. ndt.net.

Mahmood, A., Naeem, A., Kaya, M. Y., Yasin, M., Mensur-Alkoy, E., and Alkoy, S. (2015). Effect of Co/Mg ratio on the phase, microstructure, dielectric and impedance properties of lead zirconate titanate. *J. Mater. Sci.: Mater. Electron.*, 26(12):10123–10131.

Majumder, M., Gangopadhyay, T. K., Chakraborty, A. K., Dasgupta, K., and Bhattacharya, D. K. (2008). Fibre Bragg gratings in structural health monitoring-Present status and applications. *Sens. Actuators A: Phys.*, 147(1):150–164.

Makinde, W., Favretto-Cristini, N., and de Bazelaire, E. (2005). Numerical modelling of interface scattering of seismic wavefield from a random rough interface in an acoustic medium: comparison between 2D and 3D cases. *Geophys. Prospect.*, 53(3):373–397.

Maradudin, A. A., editor (2007). *Light Scattering and Nanoscale Surface Roughness*. Springer Science & Business Media, New York, 1st edition.

Maréchal, P., Levassort, F., Holc, J., Tran-Huu-Hue, L.-P., Kosec, M., and Lethiecq, M. (2006). High-frequency transducers based on integrated piezoelectric thick films for medical imaging. *IEEE Trans. Ultrason. Ferroelectr. Freq. Control*, 53(8):1524–1533.

Matsuda, O., Larciprete, M. C., Voti, R. L., and Wright, O. B. (2015). Fundamentals of picosecond laser ultrasonics. *Ultrason.*, 56:3–20.

Matthies, K. (1998). *Thickness Measurement with Ultrasound*. DGZfP German Society of Nondestructive Testing, Berlin, 1st edition.

Meeker, T. R. (1996). Publication and proposed revision of ANSI/IEEE standard 176-1987 – ANSI/IEEE standard on piezoelectricity. *IEEE Trans. Ultrason. Ferroelectr. Freq. Control*, 43(5):717–771.

Meeker, W. Q. (2016). Probability of detection in structural health monitoring. Conference Presentation. 43rd Annual Review of Progress in Quantitative Nondestructive Evaluation. Atlanta. 19 July 2016.

Meeker, W. Q. and Escobar, L. A. (1998). *Statistical Methods for Reliability Data*. John Wiley & Sons, Hoboken, 1st edition.

Mishael, S. J., Dean, F. W. H., and Fowler, C. (2004). Practical applications of hydrogen permeation monitoring. In *CORROSION 2004*, pages 04476 1–12, New Orleans. NACE International.

Mistras (2016). Caliperay - Remote Thickness Tracking – Brochure. http://www.caliperay.com/publications/CALIPERAY_Brochure.pdf.

Motamedi, M., Faramarzi, F., and Duran, O. (2012). New concept for corrosion inspection of urban pipeline networks by digital image processing. In *IECON 2012 - 38th Annual Conference on IEEE Industrial Electronics Society*, pages 1551–1556, Montreal. IEEE.

Mow, C.-C. and Pao, Y.-H. (1971). The Diffraction of Elastic Waves and Dynamic Stress Concentrations. Technical report, United States Air Force Project Rand, Santa Monica.

Mu, J., Zhang, L., and Rose, J. L. (2007). Defect circumferential sizing by using long range ultrasonic guided wave focusing techniques in pipe. *Nondestruct. Test. Eval.*, 22(4):239–253.

Nagy, P. B., Simonetti, F., and Instanes, G. (2014). Corrosion and erosion monitoring in plates and pipes using constant group velocity Lamb wave inspection. *Ultrason.*, 54(7):1832–1841.

Ness, J. K. (1994). *Efficient inversion of Fourier and Laplace domain boundary element solutions for elastodynamic scattering.* Doctor of philosophy, Iowa State University.

Ness, S., Sherlock, C. N., Moore, P. O., and McIntire, P., editors (1996). *Nondestructive Testing Handbook - Volume 10 - Nondestructive Testing Overview.* American Society for Nondestructive Testing, 2nd edition.

Ogilvy, J. A. (1991). *Theory of Wave Scattering From Random Rough Surfaces.* Adam Hilger, Bristol, 1st edition.

Ono, Y., Kobayashi, M., Lévesque, D., Song, L., Sivagnanasundaram, M., and Jen, C. K. (2007). High frequency ($>$ 30 MHz) flexible broadband transducers. In *2007 IEEE Ultrasonics Symposium*, pages 92–95, New York. IEEE.

Ounaies, Z. (1995). *Sol-Gel and Microwave Processing of PZT Materials for Sensor and Actuator Applications.* Doctor of philosophy, The Pennsylvania State University.

Pao, Y.-H. (1983). Elastic waves in solids. *Trans. ASME J. Appl. Mech.*, 50(4B):1152–1164.

Pao, Y.-H. and Mow, C.-C. (1962). On the Scatteirng of Plane Compressional Waves by a Spherical Obstacle. Technical report, MITRE Corporation, Bedford.

Pao, Y.-H. and Mow, C.-C. (1963). Scattering of plane compressional waves by a spherical obstacle. *J. Appl. Phys.*, 34(3):493–499.

Papadakis, E. P. (1966). Ultrasonic diffraction loss and phase change in anisotropic materials. *J. Acoust. Soc. Am.*, 40(4):863–876.

Pardo, L., Jimenez, R., Garcia, A., Brebol, K., Leighton, G., and Huang, Z. (2010). Impedance measurements for determination of elastic and piezoelectric coefficients of films. *Adv. Appl. Ceram.*, 109(3):156–161.

Permasense (2015). WT210 WiHART Sensor Datasheet.

Permasense (2016). ET210 WiHART Sensor Datasheet.

Pettit, J. R., Walker, A. E., and Lowe, M. J. S. (2015). Improved detection of rough defects for ultrasonic nondestructive evaluation inspections based on finite element modeling of elastic wave scattering. *IEEE Trans. Ultrason. Ferroelectr. Freq. Control*, 62(10):1797–1808.

Pike, E. R. and Sabatier, P., editors (2001). *Scattering, Two-Volume Set: Scattering and Inverse Scattering in Pure and Applied Science*. Academic Press, San Diego, 1st edition.

Pinel, N. and Boulier, C. (2013). *Electromagnetic Wave Scattering from Random Rough Surfaces: Asymptotic Models*. John Wiley & Sons, Hoboken, 1st edition.

Placko, D. and Kundu, T. (2007). *DPSM for Modeling Engineering Problems*. Wiley-Interscience, Hoboken, 1st edition.

Priyada, P., Margret, M., Ramar, R., Shivaramu, R., Menaka, M., Thilagam, L., Venkataraman, B., and Raj, B. (2011). Intercomparison of gamma scattering, gammatography, and radiography techniques for mild steel non-uniform corrosion detection. *Rev. Sci. Instrum.*, 82(3):035115 1–8.

Qing, W. (2010). Processing high TAN crude: part I. *Petrol. Technol. Quart.*, 15(5):35–43.

Qu, D. R., Zheng, Y. G., Jing, H. M., Jiang, X., and Ke, W. (2005). Erosion-corrosion of Q235 and 5Cr1/2Mo steels in oil with naphthenic acid and/or sulfur compound at high temperature. *Mater. Corros.*, 56(8):533–541.

Qu, D. R., Zheng, Y. G., Jing, H. M., Yao, Z. M., and Ke, W. (2006). High temperature naphthenic acid corrosion and sulphidic corrosion of Q235 and 5Cr1/2Mo steels in synthetic refining media. *Corros. Sci.*, 48(8):1960–1985.

Raghavan, A. and Cesnik, C. E. S. (2007). Review of guided-wave structural health monitoring. *Shock Vib. Dig.*, 39(2):91–114.

Ramberg, W. and Osgood, W. R. (1943). Description of Stress-Strain Curves by Three Parameters. Technical report, National Advisory Committee for Aeronautics, Washington, D.C.

Rayleigh, J. W. S. B. (1877). *Theory of Sound*. Macmillan, London, 1st edition.

Reeder, T. M. and Winslow, D. K. (1969). Characteristic of microwave acoustic transducers for volume wave excitation. *IEEE Trans. Microw. Theory Tech.*, 17(11):927–941.

Retaureau, G. J. (2006). *Detection of Surface Corrosion By Ultrasonic Backscattering*. Master of science, Georgia Institute of Technology.

Rettig, T. W. and Felsen, M. J. (1976). Acoustic emission method for monitoring corrosion reactions. *Corros.*, 32(4):121–126.

Rizzo, P. (2013). NDE/SHM of underwater structures: a review. *Adv. Sci. Technol.*, 83:208–216.

Rokhlin, S. I., Zoofan, B., and Kim, J.-Y. (1999). Microradiographic characterization of pitting corrosion damage and fatigue life. In Thompson, D. O. and Chimenti, D. E., editors, *Review of Progress in Quantitative Nondestructive Evaluation Volume 18*, pages 1795–1804, Snowbird. Kluwer Academic Plenum Publishers.

Ropital, F. (2009). Current and future corrosion challenges for a reliable and sustainable development of the chemical, refinery, and petrochemical industries. *Mater. Corros.*, 60(7):495–500.

Rose, J. L. (2002). A baseline and vision of ultrasonic guided wave inspection potential. *J. Press. Vessel Technol.*, 124(3):273–282.

Rose, J. L. (2004). *Ultrasonic Waves in Solid Media*. Cambridge University Press, New York, 1st edition.

Rose, J. L., Jiao, D., and Spanner Jr., J. (1996). Ultrasonic guided wave NDE for piping. *Mater. Eval.*, 54(11):1310–1313.

Royer, R. A. and Unz, R. F. (2002). Use of electrical resistance probes for studying microbiologically influenced corrosion. *Corros.*, 58(10):863–870.

Russ, J. (1994). *Fractal Surfaces*. Springer Science & Business Media, 1st edition.

Sachse, W. (1979). Visualization of transducer-produced sound fields in solids. In *ARPA/AFML Review of Progress in Quantitative NDE, July 1977–June 1978*, pages 63 388–392, La Jolla.

Sadd, M. H. (2009). *Elasticity: Theory, Applications, and Numerics*. Academic Press, 2nd edition.

Safizadeh, M. S. and Azizzadeh, T. (2012). Corrosion detection of internal pipeline using NDT optical inspection system. *NDT & E Int.*, 52:144–148.

Sanchez-Sesma, F. and Campillo, M. (1991). Diffraction of P, SV, and Rayleigh waves by topographic features: a boundary integral formulation. *Bull. Seismol. Soc. Am.*, 81(6):2234–2253.

Sanchez-Sesma, F. J. (1983). Diffraction of elastic waves by three-dimensional surface irregularities. *Bull. Seismol. Soc. Am.*, 73(6):1621–1636.

Sanchez-Sesma, F. J. and Esquivel, J. A. (1979). Ground motion on alluvial valleys under incident plan SH waves. *Bull. Seismol. Soc. Am.*, 69(4):1107–1120.

Sanchez-Sesma, F. J. and Luzón, F. (1995). Seismic response of three-dimensional alluvial valleys for incident P, S, and Rayleigh waves. *Bull. Seismol. Soc. Am.*, 85(1):269–284.

Sanchez-Sesma, F. J. and Rosenblueth, E. (1979). Ground motion at canyons of arbitrary shape under SH waves. *Earthq. Eng. Struct. Dyn.*, 7(5):441–450.

SAS Institute (2014). JMP Pro 10. Computer Program.

Sato, H. and Fehler, M. C. (1998). *Seismic Wave Propagation and Scattering in the Heterogeneous Earth*. AIP Press, Woodbury, 1st edition.

Schmerr, L. W. (2015). *Fundamentals of Ultrasonic Phased Arrays*. Springer International Publishing, New York, 1st edition.

Schmerr, L. W. (2016). *Fundamentals of Ultrasonic Nondestructive Evaluation: A Modeling Approach*. Springer International Publishing, 2nd edition.

Schmerr, L. W. and Song, S.-J. (2007). *Ultrasonic Nondestructive Evaluation Systems - Models and Measurements*. Springer Science & Business Media, New York, 1st edition.

Schmitte, T., Orth, T., and Kersting, T. (2012). Visualization of phased-array sound fields and flaw interaction using the photoelastic effect. In Thompson, D. O. and Chimenti, D. E., editors, *Review of Progress in Quantitative Nondestructive Evaluation Volume 31*, volume 1430, pages 1976–1983, Burlington. American Institute of Physics.

Schmitte, T., Weingarten, W., Chichkov, N., Orth, T., Kersting, T., Wadas, M., and Spies, M. (2016). An innovative pipe end inspection system and POD analysis of its capability. Conference Presentation. 19th World Conference on Non-Destructive Testing. Munich. 14 June 2016.

Scruby, C. B. and Drain, L. E. (1990). *Laser Ultrasonics Techniques and Applications*. CRC Press, New York, 1st edition.

Scully, J. R. (1998). The polarization resistance method for determination of instantaneous corrosion rates: a review. In *CORROSION 1998*, pages 304 1–18, San Diego. NACE International.

Searfass, C. T., Pheil, C., Sinding, K., Tittmann, B. R., Baba, A., and Agrawal, D. K. (2016). Bismuth titanate fabricated by spray-on deposition and microwave sintering for high-temperature ultrasonic transducers. *IEEE Trans. Ultrason. Ferroelectr. Freq. Control*, 63(1):139–146.

Sedov, A., Schmerr, L. W., and Song, S. J. (1992). Ultrasonic scattering by a flat-bottom hole in immersion testing: An analytical model. *J. Acoust. Soc. Am.*, 92(1):478–486.

Selfridge, A. R. (1985). Approximate Material Properties in Isotropic Materials. *IEEE Trans. Sonics Ultrason.*, 32(3):381–394.

Sensor Networks (2016). smartPIMS – Permanently Installed Monitoring Systems. http://sensornetworkscorp.com/wp-content/uploads/2017/03/SNI-smartPIMS-02.20.17.pdf.

Sensorlink (2015). UltraMonit – In Situ – System Description. http://sensorlink.no/files/2015/04/Ultramonit-in-SITU_2015_LOW.pdf.

Sensorlink (2016a). PipeMonit Swarm. http://sensorlink.no/files/2016/08/600100-242-10_01-PipeMonit-Swarm-Technical-Brochure.pdf.

Sensorlink (2016b). UltraMonit Retrofit. http://sensorlink.no/files/2009/11/600100-242-13_01-Ultramonit-Retrofit_A4_2016.pdf.

Sezawa, K. (1927). Scattering of elastic wave and some allied problems. Technical report, Tokyo Imperial University, Japan.

Shelke, A., Das, S., and Kundu, T. (2010). Distributed point source method for modeling scattered ultrasonic fields in the presence of an elliptical cavity. *Struct. Health Monit.*, 9(6):527–539.

Sherrit, S. and Mukherjee, B. K. (2012). Characterization of Piezoelectric Materials for Transducers. In Bharadwaja, S. S. N. and Dorey, R. A., editors, *Dielectric and Ferroelectric Reviews*, page 45. Research Signpost, 1st edition.

Shi, F., Lowe, M., Xi, X., and Craster, R. (2016). Diffuse scattered field of elastic waves from randomly rough surfaces using an analytical Kirchhoff theory. *J. Mech. Phys. Solids*, 92:260–277.

Shih, J.-L., Kobayashi, M., and Jen, C.-K. (2010). Flexible metallic ultrasonic transducers for structural health monitoring of pipes at high temperatures. *IEEE Trans. Ultrason. Ferroelectr. Freq. Control*, 57(9):2103–2110.

Slavcheva, E., Shone, B., and Turnbull, A. (1999). Review of naphthenic acid corrosion in oil refining. *Br. Corros. J.*, 34(2):125–131.

Smith, R. L., Reynolds, W. N., and Wadley, H. N. G. (1981). Ultrasonic attenuation and microstructure in low-carbon steels. *Met. Sci.*, 15(11-12):554–558.

Sobczyk, K. (1985). *Stochastic Wave Propagation*. Elsevier, New York, 1st edition.

Sonotec (2016). Stationary Ultrasonic Wall Thickness Measurement – Sonowall S for Non-Destructive Testing – Flyer. http://www.sonotecusa.com/fileadmin/media/ENG/Produkte/Zerstoerungsfreie_Material_Pruefung/sonowall_s/fl_sonowall_s_us_sonotec.pdf.

Sophian, A., Tian, G. Y., Taylor, D., and Rudlin, J. (2001). Electromagnetic and eddy current NDT: a review. *Insight*, 43(5):1–5.

Spencer, M. F. (2014). *The Scattering of Partially Coherent Electromagnetic Beam Illumination from Statistically Rough Surfaces*. Doctor of philosophy, Air Force Institute of Technology.

Stanic, N., De Haan, C., Tirion, M., Langeveld, J. G., and Clemens, F. H. L. R. (2013). Comparison of core sampling and visual inspection for assessment of concrete sewer pipe condition. *Water Sci. Technol.*, 67(11):2458–2466.

Sun, H. and Pipe, K. P. (2012). Perturbation analysis of acoustic wave scattering at rough solid-solid interfaces. *J. Appl. Phys.*, 111(2):023510 1–6.

Sun, Z., Zhang, L., and Rose, J. L. (2005). Flexural torsional guided wave mechanics and focusing in pipe. *J. Press. Vessel Technol.*, 127(4):471–478.

Svilainis, L. (2013). Review of high resolution time of flight estimation techniques for ultrasonic signals. In *52nd Annual Conference of the British Institude of Non-Destructive Testing*, pages 1–12, Telford.

Tabatabaeenejad, S. A. (2008). *Forward and Inverse Models of Electromagnetic Scattering from Layered Media with Rough Interfaces*. Doctor of philosophy, University of Michigan.

Tanase, T., Kobayashi, Y., and Konno, M. (2004). Preparation of lead zirconate titanate thin films with a combination of self-assembly and spin-coating techniques. *Thin Solid Films*, 457:264–269.

Tateiba, M. and Tsang, L. (1996). *Electromagnetic scattering by rough surfaces and random media*. EMW Publishing, Cambridge, 1st edition.

Tayeb, G. and Enoch, S. (2004). Combined fictitious-sources–scattering-matrix method. *J. Opt. Soc. Am. A: Opt. Image Sci. Vis.*, 21(8):1417–1423.

Taylor, B. N. and Kuyatt, C. E. (1994). NIST Technical Note 1297 - Guidelines for Evaluating and Expressing the Uncertainty of NIST Measurement Results. Technical report, United States Department of Commerce Technology Administration - National Institute of Standards and Technology - Physics Laboratory, Gaithersburg.

Tennyson, R. C., Banthia, N., Rivera, E., Huffman, S., and Sturrock, I. (2007). Monitoring structures using long gauge length fibre optic sensors. *Can. J. Civ. Eng.*, 34(3):422–429.

Thomas, M. (2006). *Analysis of Rough Surface Scattering Problems.* Doctor of philosophy, University of Reading.

Thomas, T. R. (1982). *Rough Surfaces.* Longman Group, New York, 1st edition.

Thompson, D. R. (2003). Local and non-local curvature approximation: a new asymptotic theory for wave scattering. *Waves Random Media*, 13(4):321–337.

Thompson, R. B. (1990). Physical Principles of Measurements with EMAT Transducers. In Thurston, R. N. and Pierce, A. D., editors, *Ultrasonic Measurement Methods*, chapter 4, pages 157–200. Academic Press, San Diego, 1st edition.

Thompson, R. B. and Gray, T. A. (1983). A model relating ultrasonic scattering measurements through liquid–solid interfaces to unbounded medium scattering amplitudes. *J. Acoust. Soc. Am.*, 74(4):1279–1290.

Tran, B. M. (2013). *Three Transdimensional Factors for the Conversion of 2D Acoustic Rough Surface Scattering Model Results for Comparison with 3D Scattering.* Master of science, University of Texas at Austin.

Trifunac, M. D. (1971). Surface motion of a semi-cylindrical alluvial valley for incident plane SH waves. *Bull. Seismol. Soc. Am.*, 61(6):1755–1770.

Trifunac, M. D. (1973). Scattering of plane SH waves by a semi-cylindrical canyon. *Earthq. Eng. Struct. Dyn.*, 1(3):267–281.

Tsang, L. and Kong, J. A. (2001). *Scattering of Electromagnetic Waves: Advanced Topics.* J. Wiley, New York, 1st edition.

Tsang, L., Kong, J. A., and Ding, K. H. (2000). *Scattering of Electromagnetic Waves: Theories and Applications*. J. Wiley, New York, 1st edition.

Tsang, L., Kong, J. A., Ding, K. H., and Ao, C. O. (2001). *Scattering of Electromagnetic Waves: Numerical Solutions*. J. Wiley, New York, 1st edition.

U.S. Chemical Safety Board (2015). U.S. Chemical Safety Board Investigations. http://www.csb.gov/investigations/.

van der Heijden, S. J., Ramsaran, D., Augustijn, C. M., and Engel, M. P. L. (2016). Flexible ultrasonic transducer and a transducer block. WIPO Patent PCT/NL2015/050910.

Van Velsor, J. K., Gao, H., and Rose, J. L. (2007). Guided-wave tomographic imaging of defects in pipe using a probabilistic reconstruction algorithm. *Insight*, 49(9):532–537.

Vardeman, S. B. and Lee, C.-S. (2005). Likelihood-based statistical estimation from quantized data. *IEEE Trans. Instrum. Meas.*, 54(1):409–414.

Veilleux, J., Kruger, S. E., Wu, K.-T., and Blouin, A. (2013). Multi-element, high-temperature integrated ultrasonic transducers for structural health monitoring. In Peters, K. J., Ecke, W., and Matikas, T. E., editors, *SPIE Smart Sensor Phenomena, Technology, Networks, and Systems Integration*, volume 8693, pages 86930I 1–8, San Diego. SPIE.

Velichko, A. and Wilcox, P. D. (2010). A generalized approach for efficient finite element modeling of elastodynamic scattering in two and three dimensions. *J. Acoust. Soc. Am.*, 128(3):1004–1014.

Vinogradov, S. A. (2009). Magnetostrictive transducer for torsional guided waves in pipes and plates. *Mater. Eval.*, 67(3):333–341.

Voronovich, A. G. (1994). *Wave Scattering from Rough Surfaces*. Springer-Verlag, New York, 1st edition.

Washimori, S., Mihara, T., and Tashiro, H. (2012). Investigation of the sound field of phased array using the photoelastic visualization technique and the accurate FEM. *Mater. Trans.*, 53(4):631–635.

Weaver, P. M., Stevenson, T., Quast, T., Bartl, G., Schmitz-Kempen, T., Woolliams, P., Blumfield, A., Stewart, M., and Cain, M. G. (2015). High temperature measurement and characterisation of piezoelectric properties. *J. Mater. Sci.: Mater. Electron.*, 26(12):9268–9278.

Whitehouse, D. J. (2002). *Handbook of Surface and Nanometrology*. CRC Press, Boca Raton, 1st edition.

Wilcox, P. D. and Velichko, A. (2010). Efficient frequency-domain finite element modeling of two-dimensional elastodynamic scattering. *J. Acoust. Soc. Am.*, 127(1):155–165.

Wold, K. and Sirnes, G. (2007). FSM technology - 16 years of field history-experience, status and further developments. In *CORROSION 2007*, page 07331, Nashville. NACE International.

Wolf, H. A., Schilowitz, A. M., and Smeets, N. A. (2016). New tuning fork corrosion sensor with high sensitivity. In *CORROSION 2016*, pages 7737 1–12, Vancouver. NACE International.

Wu, K., Sun, Z., Jen, C., and Bussière, J. F. (2010). NDT of Pipes and Plates at High Temperatures. Technical report, National Research Council Canada - Industrial Materials Institute, Quebec.

Wu, X., Jing, H., Zheng, Y., Yao, Z., and Ke, W. (2004a). Erosion-corrosion of various oil-refining materials in naphthenic acid. *Wear*, 256(1-2):133–144.

Wu, X. Q., Jing, H. M., Zheng, Y. G., Yao, Z. M., and Ke, W. (2004b). Study on high-temperature naphthenic acid corrosion and erosion-corrosion of aluminized carbon steel. *J. Mater. Sci.*, 39(3):975–985.

Wyatt, R. C. (1972). Visualization of pulsed ultrasound using stroboscopic photoelasticity. *Nondestruct. Test.*, 5(6):354–358.

Wyatt, R. C. (1974). A compact stroboscopic spark light source with short flash duration and low time jitter. *J. Phys. E: Sci. Instrum.*, 7(6):437–440.

Wyatt, R. C. (1975). Imaging ultrasonic probe beams in solids. *Br. J. NDT*, 17(5):133–140.

Xiu, D. and Shen, J. (2007). An efficient spectral method for acoustic scattering from rough surfaces. *Commun. Comput. Phys.*, 2(1):54–72.

Yamamoto, K. (2012). Optical visualization of acoustic fields: the schlieren technique , the Fresnel method and the photoelastic method applied to ultrasonic transducers. In Nakamura, K., editor, *Ultrasonic Transducers: Materials and Design for Sensors, Actuators and Medical Applications*, chapter 10, pages 314–328. Elsevier, 1st edition.

Ye, H. and Jin, Y.-Q. (2005). Parameterization of the tapered incident wave for numerical simulation of electromagnetic scattering from rough surface. *IEEE Trans. Antennas Propag.actions on Antennas and Propagation*, 53(3):1234–1237.

Ying, C. F. and Truell, R. (1956). Scattering of a plane longitudinal wave by a spherical obstacle in an isotropically elastic solid. *J. Appl. Phys.*, 27(9):1086–1097.

Yu, C.-W. (2008). *Scattering of a plane harmonic SH wave by a completely embedded corrugated scatterer*. Doctor of philosophy, University of Southern California.

Zhang, H. and Bond, L. J. (1989). Ultrasonic scattering by spherical voids. *Ultrason.*, 27(2):116–119.

Zhang, J., Drinkwater, B. W., and Wilcox, P. D. (2011). Longitudinal wave scattering from rough crack-like defects. *IEEE Trans. Ultrason. Ferroelectr. Freq. Control*, 58(10):2171–2180.

Zhang, J., Drinkwater, B. W., Wilcox, P. D., and Hunter, A. J. (2010). Defect detection using ultrasonic arrays : The multi-mode total focusing method total focusing method. *NDT & E Int.*, 43(2):123–133.

Zhang, Q. Q., Djuth, F. T., Zhou, Q. F., Hu, C. H., Cha, J. H., and Shung, K. K. (2006). High frequency broadband PZT thick film ultrasonic transducers for medical imaging applications. *Ultrason.*, 44:e711–e715.

Zhao, Y., Wang, G.-C., and Lu, T.-M. (2000). *Characterization of Amorphous and Crystalline Rough Surface – Principles and Applications*. Academic Press, San Diego, 1st edition.

Zhu, H., Bond, L. J., and Albach, P. H. (1992). Experimental examination of mode conversion at hemispherical surface indentations. *Ultrason.*, 30(5):301–310.

Zhu, Y.-K., Tian, G.-Y., Lu, R.-S., and Zhang, H. (2011). A review of optical NDT technologies. *Sens.*, 11:7773–7798.

Zienkiewicz, O. C., Taylor, R. L., and Zhu, J. Z. (2005). *The Finite Elemnt Method: Its Basis and Fundamentals*. Elsevier Butterworth-Heinemann, 6th edition.

Zscherpel, U., Onel, Y., and Ewert, U. (2000). New concepts for corrosion inspection of pipelines by digital industrial radiology (DIR). In *15th World Conference on Non-Destructive Testing*, pages 1–8, Rome. ndt.net.